Dynamics of Galaxy Evolution: Insights from the Circumgalactic Medium and Supermassive Black Hole Mergers

by

Vida Saeedzadeh
B.Sc., Iran University of Science and Technology, 2014
M.Sc., Alzahra University, 2018

A Dissertation Submitted in Partial Fulfillment of the
Requirements for the Degree of

DOCTOR OF PHILOSOPHY

in the Department of Physics and Astronomy

Dynamics of Galaxy Evolution: Insights from the Circumgalactic Medium and Supermassive Black Hole Mergers

by

Vida Saeedzadeh
B.Sc., Iran University of Science and Technology, 2014
M.Sc., Alzahra University, 2018

Supervisory Committee

Dr. A. Babul, Supervisor
(Department of Physics and Astronomy)

Dr. S. Ellison, Departmental Member
(Department of Physics and Astronomy)

Dr. A. Suleman, Outside Member
(Department of Mechanical Engineering)

Abstract

Galaxy groups, with their complex environments, provide a laboratory for studying a range of physical processes. These processes span from large-scale structure statistics, which constrain our theories of the evolution of the Universe, to physical processes associated with galaxy formation. The conditions and processes arising in these group environments play a crucial role in galaxy evolution. Notably, over half of the Universe's galaxies reside within these groups, and some of the most massive galaxies known are formed within these systems. Therefore, understanding the interplay within galaxy groups is crucial for obtaining a comprehensive view of galaxy evolution. Understanding how galaxies grow and evolve in these systems requires a detailed understanding of the processes that affect the gaseous halo in which they are embedded and their interactions with other galaxies. This dissertation focuses on two main areas: (i) investigating the gas reservoir around galaxies and (ii) using dual and binary supermassive black holes (SMBHs) as tracers of galaxy mergers to study the evolution of their host galaxies in different stages of SMBHs mergers.

Using high-resolution, state-of-the-art cosmological simulations, the research presented in this dissertation examines the multiphase structure of the circumgalactic medium (CGM) surrounding the central group galaxy. My findings show that the CGM around these galaxies is multiphase with its structure heavily influenced by infalling or orbiting satellite galaxies. My investigation into the CGM's origin and evolution identifies two primary cooling mechanisms: filamentary inflows and condensations from rapidly cooling density perturbations. While current high-resolution simulations offer valuable insights into the CGM's multiphase structure, they only begin to uncover its complexity. Achieving a deeper understanding requires simulations of even higher resolution, which poses a significant challenge due to the computational cost of increasing resolution across the entire simulation domain. To address this, I have employed the GIZMO N-body+hydrodynamics simulation code to develop a novel model that enhances resolution specifically in the CGM area, without affecting the resolution inside galaxies. This targeted approach allows for more precise and realistic modeling of the CGM's spatial and dynamic structures while avoiding increasing the resolution in galaxies within the simulations.

In the second part of my dissertation, I delve into the dynamics of SMBH mergers, exploring the characteristics and evolution of their host galaxies during periods of active accretion and the SMBH-SMBH merger process. Leveraging the advanced SMBH model in the Romulus simulations – which accurately tracks SMBH dynamics – I compare the properties and occurrence rates of dual active galactic nuclei (AGNs) against those of single AGNs. This

investigation includes examining the conditions that give rise to dual AGNs and comparing the properties of their host galaxies with those hosting single AGNs. Moreover, by creating catalogs of merging SMBHs that emit low-frequency gravitational waves, I connect studying galaxy evolution with the growing field of gravitational wave astronomy. My findings show that the binary SMBHs detectable by Pulsar Timing Arrays (PTA) predominantly reside in low-redshift, early-type galaxies, which are marked by their high stellar mass, low star formation rates, and significant halo masses. This evidence suggests that nano-Hertz gravitational wave sources are most commonly found in massive early-type galaxies situated at the centers of groups and clusters.

Table of Contents

List of Tables

List of Figures

List of Abbreviations

AGN: Active Galactic Nuclei

AHF: Amiga Halo Finder

BGG: Brightest Group Galaxy

CMB: Cosmic Microwave Background

CGM: Circumgalactic Medium

COS: Cosmic Origins Spectrograph

CPTA: Chinese Pulsar Timing Array

DF: Dynamical Friction

EM: Electromagnetic

EPTA: European Pulsar Timing Array

GALEX: Galaxy Evolution Explorer

GW: Gravitational Wave

HST: Hubble Space Telescope

IGM: Intergalactic Medium

IGrM: Intra-Group Medium

InPTA: Indian Pulsar Timing Array

IPTA: International Pulsar Timing Array

ISCO: Innermost Stable Circular Orbit

ISM: Interstellar Medium

Kpc: Kiloparsec

LISA: Laser Interferometer Space Antenna

LVK: LIGO-Virgo-KAGRA

Mpc: Megaparsec

NANOGrav: North American Nanohertz Observatory for Gravitational Waves

PTA: Pulsar Timing Array

SF: Star Formation

SGWB: Stochastic Gravitational Wave Background

SKA: Square Kilometre Array

SMBH: Supermassive Black Hole

SMBBH: Supermassive Binary Black Hole

SFR: Star Formation Rate

SDSS: Sloan Digital Sky Survey

SNe: Supernovae

SPH: Smoothed Particle Hydrodynamics

sSFR: Specific Star Formation Rate

ΛCDM: Λ Cold Dark Matter

Acknowledgements

I would like to thank:

Arif Babul, for your patience, mentoring, and for the invaluable knowledge you have taught me. I would especially like to thank you for teaching me the art of critical thinking, the importance of continually asking questions, and the skill of making clear arguments. These lessons are more than just academic skills for me; they are invaluable life lessons.

Sara Ellison and Afzal Suleman, for insightful discussions and for asking questions that prompted me to think more deeply and see the bigger picture during my Ph.D. research.

Belaid Moa, for making research joyful and giving me life advice when I needed it the most.

My life partner, Mohammad Reza, there are not enough words to thank you for your support, your patience, and for always encouraging me through the ups and downs of my Ph.D. process. You were a shoulder for me to cry on and a reason for me to laugh; you believed in me more than I believed in myself. Finishing this journey would have been impossible without you.

Doug Rennehan, for your infinite support, unwavering encouragement, and for answering all my questions until the last day. You made discussions about simulations fun and helped me see new perspectives on various topics. I am so grateful to have a friend like you.

Ondrea, Bobore, Eleanora, Isabel, and Guillaume, for showing me that you can have a close, deep friendship even if you are from very different places. Your friendship warmed my heart and kept me sane during the pandemic.

Elham, Ramin and Faezeh, for being my home away from home. You are my safe place and were always there for me no matter what.

Sasha and Mercedes, For being accepting, making me feel included during my days at UBC, and for opening the office door for me!

Allison Man and Douglas Scott for making me feel welcome at UBC.

Kim Venn, for being the light of my working weekdays with your shining energy.

My father, who taught me that the sky is the limit, never doubted me, and encouraged me to dream big.

My brothers and sisters, Amir, Ehsan, Firoozeh and Aida, who always believed in me and encouraged me. Even though far away, their support and presence kept me going.

Life's a stage for our singular craft, each displays
Where every soul its own melody plays and then strays
The stage stands eternal, steadfast in its grace
Fortunate be the tune that in hearts finds its embrace
Jaleh Esfahani

Dedication

I dedicate this dissertation to the brave Iranian women who fight for their rights and freedom every single day.

WOMAN
LIFE
FREEDOM

Chapter 1

Introduction

Modern cosmology is rooted in the early observations of an expanding Universe (Hubble, 1929). In the 1920s, using the 100-inch telescope at Mount Wilson, Edwin Hubble made an extraordinary discovery. He found that a nebula previously thought to be part of the Milky Way was in fact a distant galaxy – a revelation that first introduced humanity to the existence of other galaxies in the Universe. More importantly, by measuring the distances and velocities of galaxies, Hubble discovered that they were receding from us, with more distant galaxies moving away at faster speeds, thereby providing the first observational evidence for an expanding Universe. This finding laid the groundwork for the Big Bang theory which suggests that the Universe originated from an extremely hot and dense singularity about 13.8 billion years ago and has been continuously expanding since then.

In the subsequent decades, scientists further developed the Big Bang theory. Today, the Λ Cold Dark Matter (ΛCDM) model of cosmology is the latest incarnation of our understanding of the origin of the Cosmos. This model builds upon the Big Bang theory by proposing that the majority of the Universe's mass is composed of dark matter. Cold dark matter [1] is believed to be slow-moving particles that interact only through gravity and does not emit or scatter electromagnetic radiation. The Λ in the model's name refers to dark energy, a hypothetical force thought to be accelerating the Universe's expansion. The ΛCDM model, suggests a composition of 70% dark energy, 25% dark matter, and 5% ordinary matter in terms of the Universe's total mass-energy density (Ade et al., 2016) and successfully explains its large-scale structure and evolution.

According to the ΛCDM model, the Universe was intensely hot, remarkably smooth, and essentially homogeneous at the beginning. The infant Universe consisted of a tightly coupled plasma of photons and matter, forming a dense and nearly uniform mixture. The

[1] Dark matter can be also warm and cold depending on its velocity, but the current model of cosmology favors cold dark matter.

initial conditions of this early plasma are thought to have been established during a period of rapid expansion known as inflation, occurring only a fraction of a second after the Big Bang. It is theorized that quantum fluctuations in the field driving inflation were responsible for seeding the density fluctuations in this primordial plasma, which eventually led to the formation of the large-scale structures observed in the Universe today (e.g. Edwards & Heath, 1976)

About 380,000 years after the Big Bang, as the Universe expanded, its density decreased significantly compared to earlier epochs. Simultaneously, the temperature dropped from the initial billions of Kelvin to around 3000 Kelvin, enabling protons and electrons to combine and form neutral hydrogen atoms. This decoupling of electrons and photons marked the onset of the "Dark Ages", a period devoid of light sources like stars, characterized instead by vast clouds of neutral hydrogen.

The decoupling had two effects: photons could now freely travel through the increasingly transparent universe, forming what we now observe as the Cosmic Microwave Background (CMB); and baryonic [2] matter was free to coalesce under the effect of gravity. During this era, dark matter begins gravitational collapse in overdense regions and forms dark matter structures which are referred to as halos. Ordinary matter particles could feel the gravitational attraction from the dark matter halos and fall toward them. Unlike dark matter, which is collisionless ordinary matter being collisional undergoes shocks as it collides with other infalling ordinary matter, converting its kinetic energy into thermal energy. This process leads to a state of hydrostatic equilibrium, where the gas pressure balances the gravitational pull, and to the establishment of virial equilibrium [3] within the entire system. For galaxy formation to occur, this hot gas needs to lose thermal energy. The most important mechanisms for this energy loss are two-body processes within the gas where it loses its energy in the form of radiation through radiative cooling. These processes include collisional ionization, recombination, collisional excitation, and bremsstrahlung, depending on the gas's temperature and metallicity. As the gas in the center of the dark matter halo cools and leaves equilibrium, the process of creating stars begins. Stars then form galaxies. However, a large fraction of the gas remains too hot to condense and form stars. This gas stays in a hot, diffuse gaseous form that is cocooning a galaxy and is referred to as the circumgalactic medium (CGM).

The first generation of stars were born in low-mass galaxies. As galaxies evolve, some of

[2] In astronomy, baryons or baryonic matter refers to all matter that is not dark matter.

[3] It is also referred to as the halo being virialized. Virialization occurs when the kinetic energy is half of the potential energy in the system, $K = -\frac{1}{2}U$

the massive stars reach the end of their lives and die in a core-collapse supernova explosion, and then their remnants collapse under their own gravity and form a black hole. After a black hole has formed, it can grow by accreting mass from its surroundings. Supermassive black holes (SMBH) of millions of solar masses may form by accreting gas and merging with other black holes. The black hole mergers are ubiquitous in the Universe since all galaxies are thought to host SMBHs in their center (e.g. Kormendy & Ho, 2013).

In the hierarchical structure formation paradigm, cosmic structures are built up through successive mergers, starting with smaller galaxies merging and forming more and more massive structures. The galaxy groups and galaxy clusters are at the peak of the hierarchical assembly of galaxies (e.g. Springel, 2005).

Galaxy groups are a group of a few to tens of individual galaxies gravitationally bound together. They provide a laboratory to study a range of physical processes spanning from large-scale structure statistics constraining our theories of the evolution of the universe to physical processes associated with galaxy formation and evolution. Most galaxy groups host a dominant brightest group galaxy (BGG) near their halo center. BGGs are among the most luminous and massive galaxies in the universe and are typically found at the minimum of the gravitational potential of their host halo. Understanding how these massive galaxies grow and evolve requires a detailed understanding of the processes that affect the gaseous halo they are embedded in and their interaction with other galaxies. The goal of my research is twofold: (i) to advance our understanding of the structure of the BGGs circumgalactic medium and (ii) to use binary SMBHs as tracers of galaxy mergers to study the evolution of their host galaxies in different stages.

1.1 The Circumgalactic Medium

The circumgalactic medium (CGM) plays a crucial role in the evolutionary paths of galaxies, serving as the interface linking the galaxys interstellar medium (ISM) with the broader distribution of gas in the intergalactic medium (IGM) and the intragroup medium (IGrM). The CGM is both a source and a buffer, mediating the large-scale inflow of gas that fuels galaxies. Gas accreted into the halo surrounding the galaxy mixes in the CGM before it settles onto the galaxy.

There are also processes through which gas is expelled from a galaxy. Massive stars, at the end of their lifespan, undergo core-collapse supernova (SNe) explosions, causing galactic-scale winds or outflows. Additionally, SMBHs located at the centers of galaxies occasionally enter an active phase, giving rise to outflows driven by the active galactic nucleus (AGN).

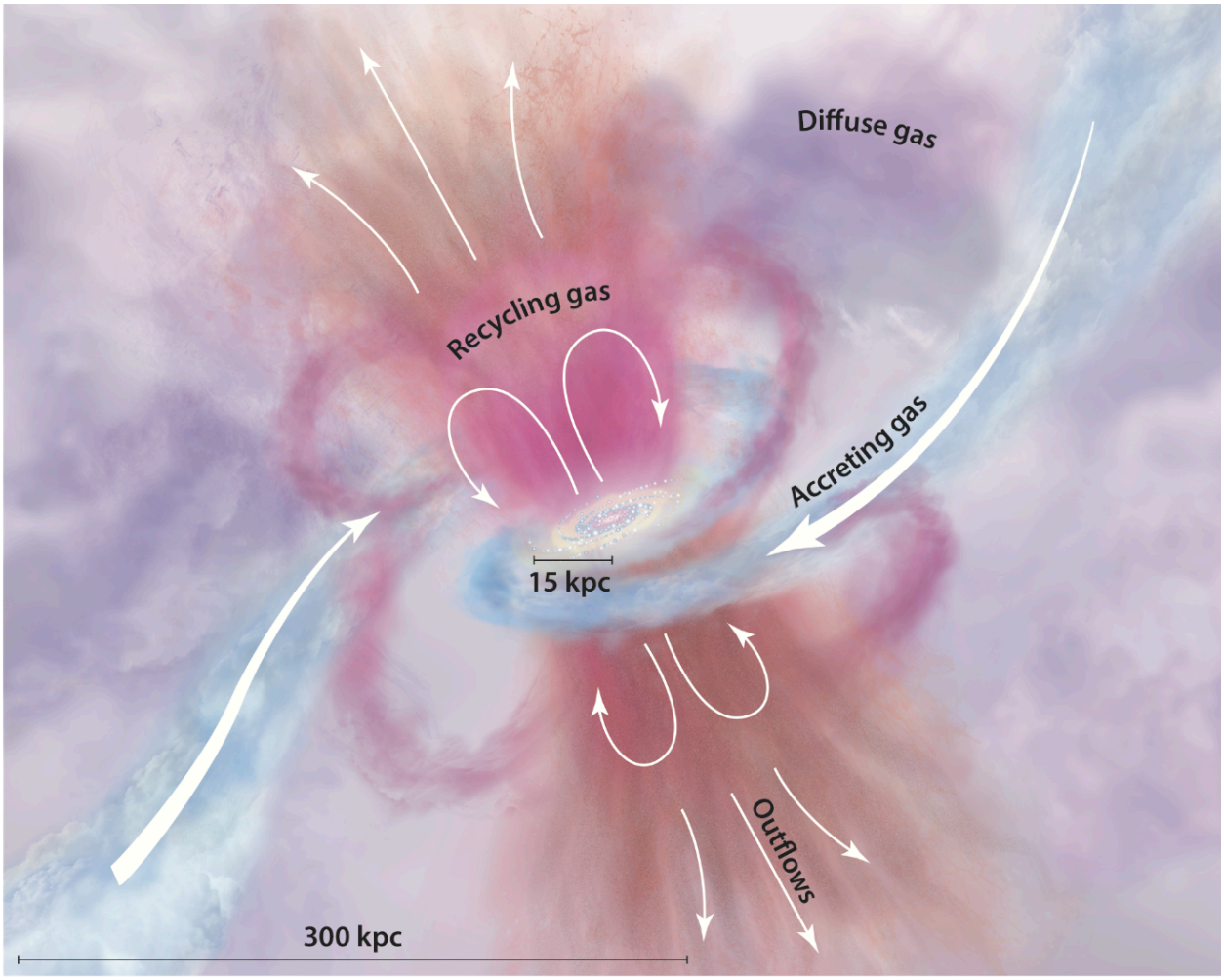

Figure 1.1: A schematic illustration of the CGM from Tumlinson et al. (2017). The diagram highlights the complexity of processes feeding and affecting CGM around galaxies. Filamentary cold accretion streams, depicted in blue, feed the galaxy with gas from the IGM. Outflows, which propel gas away from the galaxy, are represented in orange and pink hues. The recycling of gas previously expelled from the galaxy into the CGM is indicated by the circular arrows. The diffuse gas, shown in purple, encompasses contributions from all the aforementioned processes (i.e. accretion and outflows), having mixed over time.

These processes are responsible for expelling gas and metals from galaxies, thereby enriching the CGM. The gas that leaves the galaxy can either diffuse and mix with the CGM, cool and settle back onto the galaxy, or escape the halo. This dynamic interplay underscores the CGM's undeniable crucial role in the evolutionary narrative of galaxies (e.g. Sokołowska et al., 2018). Fig. 1.1 shows a schematic representing the complex fate of gas within the CGM.

The conceptualization of the CGM, originally referred to as the "Galactic corona", dates back to 1956. It was Lyman Spitzer who first proposed the existence of a diffuse, hot galactic corona, that maintains the pressure confinement of cooler clumps of gas (Spitzer, 1956). This early hypothesis laid the groundwork for subsequent explorations into the nature and properties of the CGM through the spectroscopy of intervening absorption lines in quasar spectra. In the late 1960s, Bahcall & Spitzer (1969) expanded upon this concept, proposing that "most of the absorption lines observed in quasi-stellar sources with multiple absorption redshifts are caused by gas in extended halos of normal galaxies".

Building on these foundational ideas, the following decades witnessed significant advancements in CGM research, propelled by increasingly sophisticated observational techniques and instruments. Initially, the study of CGM relied on the sparse absorption in quasar spectra, which was linked to the foreground galaxies and their extended halos, providing early insights into the nature of galactic halos (e.g. Bergeron, 1986; Lanzetta et al., 1995; Tripp et al., 2000; Chen et al., 2001). The turn of the century saw a further leap in CGM research, driven by large spectroscopic surveys of galaxies with well-determined physical properties (e.g., Sloan Digital Sky Survey - SDSS), all sky UV surveys (e.g., Galaxy Evolution Explorer - GALEX), and the improved sensitivity of UV spectrographs (e.g., Cosmic Origins Spectrograph - COS). Since these developments, CGM studies have not only deepened our understanding of its properties, but have also systematically connected gas absorption properties to galaxy properties in statistically meaningful samples (e.g. Cooksey et al., 2010; Prochaska et al., 2011a; Tumlinson et al., 2013; Liang & Chen, 2014; Lehner et al., 2015).

These pioneering observations have shown that the CGM is a turbulent, multiphase medium, teeming with enriched gas exhibiting varying ionization states, temperatures, densities, and kinematics (e.g. Prochaska et al., 2011b; Tumlinson et al., 2011a, 2017; Faucher-Giguere & Oh, 2023). In the CGM, clumpy cold ($T < 10^4$ K) dense gas is embedded in a hot ($T \geq 10^6$ K) X-ray emitting medium (e.g. Heitsch & Putman, 2009; Bordoloi et al., 2014; Armillotta et al., 2017). The hot gas component of the CGM is indicated by the presence of the highest ionization species, such as OVII and OVIII, with strong transitions in the soft X-ray region (~ 20 Å). Furthermore, ultraviolet absorption lines from quasars have uncovered

a significant reservoir of HI and metals within the CGM, existing at temperatures ranging from 10^4 to $10^{5.5}$ K (Burchett et al., 2018; Stocke et al., 2019), attesting to the existence of both cool and warm gas phases. The detection of OVI at the interface of the cooler regions suggests a gradation to a warm-hot gas layer (Putman et al., 2012; Scannapieco, 2017; Armillotta et al., 2017; Bordoloi et al., 2017), further supporting the model of a clumpy, multiphase circumgalactic medium.

Contemporary research has thus demonstrated the ubiquitous and multiphase nature of CGM (e.g. Thom et al., 2012; Werk et al., 2013; Bordoloi et al., 2014; Prochaska et al., 2017) and showed its strong dependence on some galaxy properties such as stellar mass (e.g. Tumlinson et al., 2011b; Bordoloi et al., 2014), star formation activity (Tumlinson et al., 2011b; Borthakur et al., 2013; Heckman et al., 2017; Prochaska et al., 2017), black hole activity (Berg et al., 2018), and environment (Pointon et al., 2017; Nielsen et al., 2018).

Star formation and stellar feedback directly influence galaxy halo gas by depleting and enriching the gas reservoirs. The cooling gas from the CGM can form molecular clouds that collapse and form stars in galaxies. On the other hand, when a massive star dies, an enormous amount of energy and metals [4] are injected as stellar feedback to the surrounding gas on kpc [5] scales, enriching and heating the CGM. These processes alter the halo gas's overall properties, such as its temperature, density, and metallicity (e.g. Oppenheimer & Davé, 2006; Agertz & Kravtsov, 2016)

Another critical process influencing the CGM is the feedback from active galactic nuclei (AGN). When a galaxy's central supermassive black hole actively accretes material, it enters the AGN phase, exerting significant energy and radiation on its surroundings (Fabian, 2012). The physics governing the coupling of energy produced by AGN to its surrounding environment is not yet fully understood, though existing theories propose categorizing AGN feedback into two modes to explain it (e.g. Buff & McCray, 1974; Ciotti & Ostriker, 1997; Murray et al., 2005): (1) radiative (or wind/quasar mode) and (2) kinetic (or radio jet/maintenance mode), differentiated by the nature of the energy outflow near the black hole. The radiative mode requires high accretion rates (e.g. Narayan & Yi, 1994; Trump et al., 2011), and its influence is on galactic scales. Conversely, the kinetic mode occurs when the black hole accretes at a lower rate and has powerful jets. These jets inflate bubbles into the CGM and extend even further into the IGrM, keeping the gas in a hot state that prevents accretion (Fabian, 2012). The radio-mode feedback, combined with radiation from

[4] In astronomy, metals are any element heavier than helium.

[5] Astronomical scales and distances are based on the parsec, where 1 pc = $3.086 \times 10^1 3$ km.In these units, 1 kpc = 10^3 pc, and 1 Mpc = 10^6 pc

the AGN, keeps the CGM hot, buoyant, and consistently ionized (McNamara & Nulsen, 2007; Bower et al., 2017; Hani et al., 2018).

The environment surrounding a galaxy plays a crucial role in shaping the characteristics of its CGM as well. Galaxies in denser environments, such as clusters or groups, encounter interactive processes that significantly influence the CGM. Galaxy interactions result in the release of a huge amount of cold gas into the central region of halos altering the properties of CGM. The excess amounts of gas in the center also trigger starbursts and AGN activity (Cox et al., 2006; Torrey et al., 2012; Ellison et al., 2011, 2013; Moreno et al., 2015), which themselves have important impacts on the CGM.

The aforementioned physical processes have notable impacts on the state of the CGM. However, understanding the nature, structure, and dynamics of this multiphase medium, despite considerable efforts over the past few years, remains elusive. With these processes as a backdrop, there are several mechanisms have been proposed to explain the multiphase structure of the CGM: (i) debris from ram pressure stripping and tidal disruption of satellite galaxies (e.g. Murakami & Babul 1999; McCarthy et al. 2008; Sun et al. 2009; Franchetto et al. 2021; Jung et al. 2022); (ii) byproducts of cooling due to mixing between the diffuse CGM and the multiphase stellar and/or AGN-driven galactic outflows (Huang et al., 2020a,b; Schneider et al., 2020; Rennehan, 2021), as well as mixing between the diffuse CGM and the interstellar gas dredged (uplifted) out of the galaxy by active galactic nucleus (AGN) jets (e.g. Revaz et al. 2008; Pope et al. 2010; Scannapieco & Brüggen 2015; Schneider & Robertson 2017; Qiu et al. 2020); to (iii) the byproducts of induced positive density perturbations within the CGM that result in localized regions of rapidly cooling gas which condense out of the general medium and form in-situ cool clouds (e.g. Maller & Bullock, 2004; Sharma et al., 2010, 2012a; Choudhury & Sharma, 2016; Prasad et al., 2015, 2017; Voit et al., 2015; Li et al., 2015).[6] I will explain each of these proposals briefly in the next few paragraphs.

Proposal (i) suggests that the gas lost from gas-rich satellite galaxies due to ram pressure stripping or tidal disruption disperses into the CGM and contributes to its multiphase structure (Murakami & Babul, 1999; Sun et al., 2009; Franchetto et al., 2021). When a galaxy passes through a gaseous medium, such as the CGM of a massive central galaxy, it will encounter a headwind known as "ram pressure". The strength of this headwind is set by the gas density of the local medium and its relative speed with the satellite galaxy. Gunn & Gott 1972 proposed that ram pressure can remove gas from a galaxy when its strength

[6]In literature, phenomenology is often associated with labels "condensations" and "precipitation". In this thesis, "condensations" refers to cool-cold clouds forming in-situ out of localized regions of rapidly cooling density perturbations. Precipitation refers to cold clouds that fall or rain down onto the central galaxy.

exceeds the galaxys own local gravitational restoring pressure. This action is known as "ram pressure stripping" and is more effective in lower mass galaxies, where gravitational restoring pressures are generally lower, and for galaxies moving through more massive host halos, where ram pressures are generally higher. The ram pressure stripped gas from satellite galaxies is generally less hot than the CGM of the central galaxy, therefore, contributing to the multiphase structure of the medium (e.g. Campitiello et al., 2021; Tonnesen et al., 2011; Yun et al., 2019; Murakami & Babul, 1999)

Proposal (ii) addresses the formation of the CGM's multiphase structure through the interplay between stellar and AGN outflows and the CGM. Observations have shown the coexistence of multiple phases of gas in the same outflows (Veilleux et al., 2020), with the cold and cool phases often dominating the total mass. Taking M82 as an example, in addition to the hot X-ray plasma, outflowing gas has been observed at every wavelength probed, from soft X-ray emission (e.g. Strickland et al., 2004), to cool (T $\sim 10^4$ K) ionized gas (e.g. McKeith et al., 1995; Westmoquette et al., 2009), to neutral hydrogen and cold molecular outflows (e.g. Walter et al., 2002; Leroy et al., 2015; Martini et al., 2018). The interaction of these multiphase outflows with the CGM is thought to contribute to the CGM's multiphase structure.

Additionally, the uplift of the interstellar medium (ISM) by AGN jets and lobes contributes to the CGM's multiphase structure. This phenomenon suggests that as cavities inflate and rise away from the AGN, they uplift cool material from the galaxy's ISM into the CGM (Revaz et al., 2008; Pope et al., 2010). This upward displacement of cool gas adds further complexity to the CGM, enriching it with the cold gas phase and reinforcing its multiphase nature. These observations and studies collectively indicate that the interaction of outflows with the CGM is a significant factor in creating and maintaining its multiphase composition.

Proposal (iii) centers on the concept of a thermal instability leading to the condensation of gas within the CGM, contributing to its multiphase structure. Linear stability analyses and experiments with idealized simulations show that small-amplitude density perturbations in a thermally balanced, stratified diffuse CGM can become thermally unstable and prone to condensation when the median cooling time ($t_{\rm cool}$) to free-fall time ($t_{\rm ff}$) ratio drops below 10 (Sharma et al., 2012b; Gaspari et al., 2012; Voit et al., 2015; Prasad et al., 2015; Li et al., 2015; Choudhury & Sharma, 2016)). Here, $t_{\rm cool} \equiv E_{\rm thermal}/[n_e^2 \Lambda]$ represents the cooling time, with Λ being the radiative cooling function and n_e the electron number density. The free-fall time $t_{\rm ff} \equiv \sqrt{2r/g(r)}$ is calculated at a radius r, where $g(r) = GM(< r)/r^2$ denotes the gravitational acceleration. These density perturbations form cool-cold clouds, giving rise to

a multiphase structure in the CGM (e.g. Sharma et al., 2010, 2012b; McCourt et al., 2012; Meece et al., 2015; Choudhury & Sharma, 2016).

All in all, the mechanisms discussed above illustrate that the structure and properties of the CGM emerge from complex gas physics. Consequently, numerical simulations of galaxy formation are a powerful tool for studying the origin and evolution of the CGM's multiphase structure. However, given the CGM cold phase has a very low volume filling factor, capturing the formation of the multiphase medium in simulations requires very high resolution (approaching $\sim$ 1 pc; Hummels et al., 2019). Such high resolution has so far remained in the domain of idealized simulations because cosmological simulations cannot have such a fine resolution due to computational costs. While idealized simulations offer controlled experiments and very high resolutions, they lack the dynamic nature of realistic cosmological simulations. For instance, in cosmological environments, density perturbations can arise from mergers, substructure motions, AGN outbursts, and winds, whereas idealized simulations primarily seed perturbations through turbulence triggered by AGN jets (Prasad et al., 2017). Furthermore, cosmological simulations allow for the introduction of thermally unstable gas into the CGM through ram pressure stripping and tidal disruption by infalling substructures, a feature often missing in idealized models due to the absence of a realistic growth history of galaxy groups. Thus, considering cosmological processes in CGM studies is crucial for understanding its origin, the evolution of its multiphase structure, and its role in galaxy evolution.

Recent advancements in the resolution of cosmological simulations (e.g. Tremmel et al., 2017; Pillepich et al., 2019; Hopkins et al., 2018) have provided unique opportunities to investigate the multiphase CGM. These improvements involve various approaches, including code redesigns that enhance mass resolution only in a halos circumgalactic environment (cf. Hummels et al., 2019; Suresh et al., 2019; van de Voort et al., 2019; Peeples et al., 2019) or leveraging more efficient codes and greater computing resources to achieve higher overall resolutions (cf. Tremmel et al., 2019; Fiacconi et al., 2017; Hafen et al., 2019; Nelson et al., 2019a; Fielding et al., 2020; Tamfal et al., 2022).

Such high-resolution simulations open a new era of studying properties of the CGM that have never been explored before. In Chapter 2, I use the high-resolution Romulus suite of cosmological simulations (Tremmel et al., 2017, 2019), which fall into the second category and have overall high resolution, to examine the formation and evolution of the CGM around massive galaxies. In Chapter 3, I develop a model to enhance resolution only in the CGM of galaxies.

1.2 Dual and Binary Supermassive Black Holes

Spectroscopy of the nuclei of nearby galaxies, using the Hubble Space Telescope (HST), has revealed evidence of supermassive black holes (SMBHs) across many galaxies. These observations lead to the compelling conclusion that SMBHs, with masses ranging from approximately 10^6 to $10^9\,M_\odot$, are ubiquitous in various types of galaxies (Kormendy & Richstone, 1995; Kormendy & Gebhardt, 2001). This led to the revelation that the mass of SMBHs is correlated with key properties of their host galaxies, such as stellar velocity dispersion (σ_*), luminosity (L_{host}), and stellar mass (M_*), indicating that larger SMBHs are typically found in galaxies with greater σ_*, L_{host}, and M_* (e.g. Magorrian et al., 1998; Ferrarese & Merritt, 2000; Gebhardt et al., 2000; Häring & Rix, 2004; Beifiori et al., 2012; Kormendy & Ho, 2013).

Therefore, there are very likely mechanisms enabling communication between the host galaxy and its central SMBH. One such mechanism could involve the transfer of matter from the host galaxy to the SMBH. Galaxy interactions and mergers are known to trigger substantial gas inflows into galaxies' central region (Di Matteo et al., 2005). Multi-wavelength observations have provided evidence that these interactions do, to some extent, feed the central SMBH and activate it as an AGN (Silverman et al., 2011; Ellison et al., 2011; Mechtley et al., 2016a; Goulding et al., 2018; Koss et al., 2018).

In recent years, there has been significant interest in exploring the idea that galaxy mergers fuel the growth of SMBHs, particularly through investigating simultaneous accretion events on SMBHs within merging galaxies. Numerical simulations suggest that during a galaxy merger, both SMBHs can become active (Hopkins et al., 2006; Capelo et al., 2015, 2017), undergoing accretion well before their final coalescence. This process can lead to the formation of dual AGNs, with separations ranging from $0.1 - 100$ kpc. Consequently, there has been a surge in efforts to find and characterize dual AGNs, from both theoretical and observational standpoints (De Rosa et al., 2019). The detection and characterization of dual AGNs are not only crucial for understanding the formation and accretion history of SMBHs across cosmic epochs but also for shedding light on the processes of galaxy assembly (Comerford et al., 2009).

Observationally, many dual AGNs have been discovered serendipitously (e.g. Bianchi et al., 2008; Green et al., 2010; Huang et al., 2014). However, systematic searches have recently begun to more comprehensively address the statistical properties of dual AGNs, including both their occurrence and characteristics. These searches typically fall into two categories: (i) Blind searches, which utilize surveys to identify two AGNs in close proximity

or within a single galaxy, for example through spectroscopic signatures (e.g. Comerford et al., 2013; Hwang et al., 2020; Kim et al., 2020). (ii) Assisted searches, where the focus is on finding companions near already detected AGNs (e.g. Koss et al., 2012; Silverman et al., 2020). In both types of searches, after initial candidate selection, further verification is required through multi-wavelength observations to conclusively confirm the dual nature of the identified systems (e.g. Rosario et al., 2011; Comerford et al., 2012; Rubinur et al., 2019; Foord et al., 2020).

Among the observed samples of dual AGNs, some controversial conclusions have arisen, likely due to the different selection functions employed by various observational techniques. For instance, a number of studies have reported a higher fraction of dual AGNs in galaxies with closer separations, suggesting that galaxy interactions play a significant role in triggering AGN activity (e.g. Ellison et al., 2011; Silverman et al., 2011; Liu et al., 2012; Satyapal et al., 2014; Kocevski et al., 2015; Koss et al., 2012, 2018). Conversely, there are also studies that find no enhanced AGN activity in merging galaxies compared to a control sample of inactive galaxies (e.g. Cisternas et al., 2011; Mechtley et al., 2016b). These uncertainties highlight the importance of the detection and characterization of dual and binary SMBHs for understanding their formation and accretion history.

Numerical simulations, including both cosmological simulations and isolated simulations of mergers, play a pivotal role in studying the dual AGNs and binary SMBHs. These simulations are also instrumental in exploring the formation, evolution, and properties of the host galaxies in such systems. Idealized merger simulations have high resolution and can resolve sub-kpc scales, which are crucial for tracking the dynamics of SMBHs and systematically studying the evolution of their parameters, such as mass, spin, merger times, etc. However, these simulations can only simulate individual systems and, as such, cannot predict statistical aspects of dual AGNs, such as the fraction of AGN pairs relative to the total number of AGNs.

In contrast to idealized merger simulations, cosmological simulations offer a broader perspective by modeling galaxy mergers and systems of multiple AGNs. They serve as a crucial counterpart to observational studies by enabling the estimation of the dual AGN fraction relative to single AGNs. However, these simulations face their own challenges. Not all cosmological simulations are capable of producing AGN pairs with separations down to kpc scales. This is primarily due to two factors: (i) the requirement for large simulation volumes with high resolution, which are computationally expensive; and (ii) the limitation of most current black hole models in effectively tracking black holes to the resolution limit during a galaxy merger.

When two galaxies merge, their central SMBH goes through a long journey. They start with tens of kpc separation from each other, then gradually lose their orbital energy and sink to the center of the new galaxy due to the dynamical friction (DF) exerted by the gas, stars, and dark matter around them (e.g. Chandrasekhar, 1943a; Ostriker, 1999). As these SMBHs approach a sub-pc separation, they form a binary system. At this stage, their energy loss is driven through other mechanisms, including gravitational wave emission (e.g. Sesana, 2013), scattering with stars (Quinlan, 1996; Sesana et al., 2007; Vasiliev et al., 2015), gas drag from a surrounding circumbinary disk (Haiman et al., 2009), or three-body scattering with a third BH (e.g. Bonetti et al., 2018).

Cosmological simulations, however, due to resolution limits cannot feasibly include detailed treatment of the BH binary dynamics. Once the two SMBH reach the innermost region of the remnant galaxy, the gravitational potential close to the resolution limit becomes noisy. Such a noisy potential can unrealistically scatter the SMBH away from its halo center. To avoid this unexpected scattering of the BHs around the galaxy's center, large-volume cosmological simulations usually pin (or reposition) the black holes at the minimum potential of halos (e.g. Crain et al., 2009; Sijacki et al., 2015; Davé et al., 2019). Consequently, during a merger, the central black holes of the merging galaxies are often instantaneously merged as soon as the two merging galaxies are identified as one galaxy by the halo finder. This premature merging happens relatively early in the process, hindering the direct tracing of the dynamics and growth of two black holes throughout the merger.

In the last decade, addressing these challenges, emerging works have integrated subgrid[7] modeling of dynamical friction self-consistently into cosmological simulations. This approach aims to simulate black hole dynamics more realistically, moving away from the artificial repositioning approximation. These advancements include implementing dynamical friction, either from gas (Dubois et al., 2013) or from stars and dark matter (Hirschmann et al., 2014; Tremmel et al., 2015; Chen et al., 2022a). Both approaches have been successful in stabilizing black holes at the centers of halos. The development of black hole models that more accurately follow the dynamics of black holes has opened new avenues for studying dual AGNs and binary SMBHs within cosmological simulations.

Parallel to these advancements in simulations, significant progress in gravitational wave (GW) astronomy has opened new avenues for probing the SMBH binaries' evolution. Merging SMBHs can produce GW signals detectable at low-frequency bands from a few nano-Hertz

[7]In hydrodynamical simulations, subgrid models are used to represent physical processes occurring below the numerical grid-scale (i.e., the resolution scale), such as star formation, stellar feedback, black hole dynamics, and AGN feedback.

to milli-Hertz range. In the milli-Hertz frequency range, upcoming GW detectors, such as Laser Interferometer Space Antenna (LISA; Amaro-Seoane et al., 2017; Baker et al., 2019), can probe signal from the SMBHs of masses in the range $\sim 10^4$- 10^7 $M_\odot$. The nano-Hertz GW signal from sources with masses above 10^8 $M_\odot$ can be detected and characterized using the timing data from several extremely well-studied millisecond pulsars (Sesana et al., 2008b; Foster & Backer, 1990). A GW propagating into space affects the travel time of photons, an effect that is measurable in millisecond pulsars which are very precise cosmic clocks. The detection of gravitational waves from these systems offers a unique opportunity to probe the final stages of SMBH mergers. These signals are the target of the International Pulsar Timing Array (IPTA) collaboration [8] (Antoniadis et al., 2022).

The recent evidence of the stochastic GW background (SGWB) by IPTA in the nano-Hertz range promises to open an exciting new window into the evolving population of binary SMBHs. This leads to an interesting investigation of not only the characteristics of the binary SMBHs but also their host galaxies. Numerical simulations specifically play an important role in this area of study, offering insights into the environments where SMBH mergers occur and in narrowing down the potential host galaxies for more focused observational scrutiny (Rosado & Sesana, 2014; Goldstein et al., 2019; Volonteri et al., 2003, 2020; Muhamed Kozhikkal et al., 2023). This synergy between numerical simulations and GW observations is set to significantly enhance our understanding of SMBH mergers and their cosmic context.

1.3 Romulus simulations

In my analysis in Chapters 2, 4, and 5, I use the Romulus hydrodynamic cosmological simulations. This section will detail the aspects of the Romulus simulations that are relevant to my studies.

Romulus is a suite of simulations run with the Tree + Smooth Particle Hydrodynamics (Tree + SPH) code ChaNGa (Menon et al., 2015; Wadsley et al., 2017). ChaNGa uses standard physics modules that have been previously used and thoroughly tested in GASOLINE/GASOLINE2 codes (Wadsley et al., 2004, 2008; Stinson et al., 2006; Shen et al., 2010a). This includes modules handling UV background radiation, star formation, stellar feedback, and turbulent diffusion (Shen et al., 2010b), as well as low temperature metal

[8] IPTA collaboration comprises the European Pulsar Timing Array (EPTA; Desvignes et al., 2016), the North American Nanohertz Observatory for Gravitational Waves (NANOGrav; McLaughlin, 2013), the Indian Pulsar Timing Array Project (InPTA; Joshi et al., 2018) and the Parkes Pulsar Timing Array (PPTA; Manchester et al., 2013). Along with the IPTA Collaboration, the Chinese Pulsar Timing Array (CPTA; Xu et al., 2023a) are also making measurements in this band.

line cooling and improved treatment of both weak and strong shocks. SMBH formation, dynamics, growth, and feedback models are, however, novel (Tremmel et al., 2015, 2017).

The ROMULUS suite comprises one uniform cosmological volume and three group/cluster-scale zoom-in[9] simulations. ROMULUSG1 and ROMULUSG2 are zoom-in simulations of galaxy groups and ROMULUSC is a zoom-in simulation of a massive group/low-mass cluster (Tremmel et al., 2019). ROMULUS25 is a simulation of a cosmological volume of a periodic cube with a length of 25 Mpc per side including a large uniform sample of group galaxies (Tremmel et al., 2017).

All simulations in the ROMULUS suite have the same hydrodynamics, sub-grid physics, resolution, and background cosmology. The background cosmology corresponds to a ΛCDM universe with cosmological parameters consistent with results from Planck (Ade et al., 2016): $\Omega_{\rm m} = 0.309$, $\Omega_\Lambda = 0.691$, $\Omega_{\rm b} = 0.0486$, $H_0 = 67.8\,{\rm kms^{-1}Mpc^{-1}}$, and $\sigma_8 = 0.82$. The ROMULUS simulations are among the highest resolution cosmological simulations run to z = 0, with a Plummer equivalent gravitational force softening of 250 pc (or 350 pc spline kernel), and a maximum SPH resolution of 70 pc. Unlike many similar cosmological runs, the dark matter distribution is oversampled, such that 3.375 times more dark matter particles than gas particles are simulated, resulting in a dark matter and gas mass resolution of $3.39 \times 10^5 {\rm M}_\odot$ and $2.12 \times 10^5 {\rm M}_\odot$, respectively. This is an important shift from the standard approach of simulating the same number of gas and dark matter particles, as it allows for decreased numerical noise and more accurate black hole dynamics (Tremmel et al., 2015).

1.3.1 Halo Extraction

Halos and subhalos are identified and processed using the Amiga Halo Finder (AHF) (Knebe et al., 2008; Knollmann & Knebe, 2009). These structures exist in a nested hierarchy, with halos at the uppermost level and subhalos nested within them. AHF detects these structures by identifying density peaks in an adaptively smoothed density field and then determines all particles (including dark matter, gas, stars, and black holes) that are gravitationally bound to these peaks. This method extends through the hierarchy, progressively identifying larger structures. Once the halos are identified, their centers are determined using the shrinking sphere method (Power et al., 2003).

[9] In cosmological zoom-in simulations, a higher resolution is used in regions of interest (zoom-in regions), while the resolution in the rest of the box is degraded, thus permitting faster computational times and higher resolution.

1.3.2 Star Formation and Gas Physics

Star formation (SF) and supernova (SNe) feedback are critical processes in the evolution of galaxies. However, these processes occur on scales well below the resolution of any cosmological simulation, necessitating the use of subgrid models. ROMULUS follows the same SF and feedback subgrid model as Stinson et al. (2006) where they are regulated by several key parameters.

The cold gas requires to have a density more than $n_* = 0.2\mathrm{m_p/cm^3}$, and temperature less than $T_* = 10^4\mathrm{K}$, to be allowed to form stars. The probability of creating a star particle from gas is given by

$$p = \frac{m_{gas}}{m_*}(1 - exp(-c_*\Delta t/t_{\mathrm{dyn}})), \tag{1.1}$$

where $t_{\mathrm{dyn}} = \sqrt{3\pi/(32G\rho)}$ is the local dynamical time, the characteristic timescale is taken as $\Delta t = 10^6 yr$ for star formation, and $c_* = 0.15$ is the star formation efficiency, a free parameter fine-tuned in Tremmel et al. (2017) to reproduce scaling relations for Milky Way-sized and dwarf galaxies. Star particles are assumed to follow a Kroupa initial mass function (Kroupa, 2001) to compute metal enrichment.

Supernova feedback is implemented as a thermal injection with 75% coupling eciency following the blastwave model from Stinson et al. (2006). Gas cooling is regulated by metal abundance as in Guedes et al. (2011) as well as SPH hydrodynamics and both thermal and metal diffusion as described in Shen et al. (2010a) and Governato et al. (2015).

An important limitation of the ROMULUS simulations worth noting is that they only include low temperature metal cooling rather than a full implementation of metal line cooling, a major coolant for higher temperature gas in groups and clusters. Metal line cooling has been shown to affect the accretion of gas onto galaxies in the centers of massive halos, though feedback from AGN is also critically important in regulating this process (van de Voort et al., 2011). The decision to use just low-temperature metal cooling was made following the results of Christensen et al. (2014), who found that in case of no molecular hydrogen physics, including metal line cooling results in overcooling of the gas in galaxies. Christensen et al. (2014) also show that ISM models that include both metal lines and H_2 physics result in galaxies with star formation histories and outow rates more similar to primordial cooling runs than to simulations with metal lines and no H_2. Other possible solutions to the overcooling problem consider: (i) boosting supernovae feedback to mitigate overcooling while allowing for metal line cooling, (ii) allowing metal line cooling only in hot, diffuse gas. The first solution was disfavoured because it results in unrealistic ISM or CGM, as shown by Sokołowska

et al. 2016, 2018. The second solution is also not very attractive because it introduces a new level of complexity since it requires determining the different gas phases in CGM and distinguishing between CGM and ISM. Given the severe aws in both of these solutions, the metal line cooling is not included in ROMULUS.

1.3.3 Black Hole Physics

One of the key advancements in the ROMULUS simulations, compared to other cosmological simulations, is the innovative and sophisticated approach to black hole seeding, fueling, feedback and dynamics. The following provides a detailed summary of this model.

Seed Formation

Unlike many other cosmological simulations (e.g., Schaye et al., 2015; Weinberger et al., 2017; Pillepich et al., 2018; Nelson et al., 2019b; Davé et al., 2019) that SMBH seeding depends on a halo or a galaxy to exceed a certain mass threshold for a SMBH to form, in ROMULUS SMBH seeding only depends on local gas properties (Tremmel et al., 2017). As a result, the SMBHs in ROMULUS can form in lower mass halos (10^{8-10} $M_\odot$) and at higher redshifts ($z > 5$, Tremmel et al., 2017).

A SMBH seed forms by converting a gas particle, already selected to form a star (see §1.3.2), into a SMBH seed instead if it meets the following criteria:

- Low mass fraction of metals ($Z < 3 \times 10^{-4}$)
- Density 15 times that of the SF threshold (3 m_p/cm^3)
- Temperature between 9500 K and 10000 K

These criteria identify dense rapidly collapsing regions (i.e., collapsing faster than the star formation timescale, as they have not yet formed stars) that are most likely capable of growing SMBHs in early Universe.

Once formed, the initial mass of each SMBH seed in the ROMULUS simulations is set to 10^6 $M_\odot$. Although this is higher than most theoretical estimates suggest (Johnson et al., 2012; Volonteri, 2012), it's justified considering that early growth rates of SMBH seeds can exceed 0.1 $M_\odot yr^{-1}$, influenced by environmental factors and processes below the resolution limit of the simulations (e.g. Hosokawa et al., 2013; Schleicher et al., 2013). In reality, a spectrum of SMBH seed masses would likely emerge early on. However, due to the unresolved nature of these processes in the simulation, it's not possible to differentiate where a larger SMBH seed

should grow. This chosen mass is also sufficiently large in comparison to the dark matter and gas particle masses in ROMULUS, ensuring that the dynamics of all SMBHs are well resolved (Tremmel et al., 2015).

Black Hole Dynamics and Mergers

In the ROMULUS simulations, the dynamics of SMBHs are significantly advanced through the incorporation of a sub-grid approach for modeling dynamical friction (DF). DF is the force exerted by the gravitational wake caused by a massive object, like an SMBH, moving through an extended medium (Chandrasekhar, 1943a; Binney & Tremaine, 2008) leading to the decay of its orbit towards the center of massive galaxies (Governato et al., 1994; Kazantzidis et al., 2005). However, this effect is challenging to resolve in cosmological simulations due to numerical noise and limited gravitational force resolution. ROMULUS employs a sub-grid model that accounts for the unresolved DF from stars and dark matter that the SMBHs ought to be experiencing (Tremmel et al., 2015). This approach has been shown to produce realistically sinking SMBHs (Tremmel et al., 2015). For each SMBH in the simulation, this force is estimated by assuming a locally isotropic velocity distribution and integrating Chandrasekhar's equation (Chandrasekhar, 1943b) from the 90-degree deflection radius (r_{90}) to the SMBH's gravitational softening length (ϵ_g). The resulting acceleration is

$$\mathbf{a}_{DF} = -4\pi G^2 \, M_\bullet \, \rho(v < v_{BH}) \, \ln\Lambda \, \frac{\mathbf{v}_{BH}}{v_{BH}^3}, \tag{1.2}$$

Unlike common techniques in cosmological simulations that reposition or push the SMBH along its local potential gradient leading to nearly immediate SMBH mergers during galaxy interactions, Romulus' approach allows for a realistic and temporally extended process of SMBH sinking and merging (e.g. Crain et al., 2009; Sijacki et al., 2015; Davé et al., 2019). This sophisticated approach to SMBH dynamics allows the ROMULUSsimulations to track the dynamics and interactions of SMBHs during and after galaxy mergers, down to sub-kpc scales. As a result, the merger rates of SMBHs are realistically decoupled from galaxy mergers, leading to more accurate predictions of SMBH growth and behavior. This methodology also facilitates the natural production of dual and offset AGN as well as binary SMBHs.

In order for two SMBHs to merge, they must be within a distance of two gravitational softening lengths (0.7 kpc) and possess a low enough relative velocity to be mutually bound; i.e. $\frac{1}{2}\,\Delta\mathbf{v}^2 < \Delta\mathbf{a}\cdot\Delta\mathbf{r}$, where $\Delta\mathbf{v}$ and $\Delta\mathbf{a}$ are the differences in velocity and acceleration of the two black holes, and $\Delta\mathbf{r}$ is the distance between them (Bellovary et al., 2011; Tremmel et al.,

2017)[10]. The separation limit of two gravitational softening lengths is deemed appropriate because once the separation drops below this limit, the simulation's ability to accurately track the SMBH pair's dynamics becomes less reliable.

When two SMBH merge, the resulting SMBH is assigned a velocity that conserves momentum, and its mass is the sum of the masses of its progenitors. Mergers are one of the two processes driving the growth of SMBHs. I explain the other process in the next section.

Black Hole Accretion and Feedback

The other process by which SMBHs grow is via the accretion of gas. In the ROMULUS simulations, the accretion of gas onto SMBHs is governed by a modified version of the Bondi-Hoyle accretion formula (Bondi 1952, for modifications see Tremmel et al. 2017), which takes into account the additional angular momentum support present in rotating gas. Due to the limitations in resolving the Bondi radius, even in high-resolution simulations like ROMULUS, the actual properties of dense cool gas surrounding the SMBH are not accurately captured. This unresolved multiphase structure of the gas typically leads to an underestimation of gas densities and an overestimation of temperatures near the SMBH, resulting in artificially lower accretion rate estimates. To address this, ROMULUS employs a density-dependent boost factor, following the approach of Booth & Schaye (2009), to compensate for the unresolved multiphase structure and its impact on gas accretion. The accretion equation has the following form:

$$\dot{M}_\bullet = \alpha \times \begin{cases} \frac{\pi (G M_\bullet)^2 \rho_{\rm gas}}{(v_{bulk}^2 + c_s^2)^{3/2}} & \text{if } v_{bulk} > v_\theta \\ \\ \frac{\pi (G M_\bullet)^2 \rho_{\rm gas} c_s}{(v_\theta^2 + c_s^2)^2} & \text{if } v_{bulk} < v_\theta \end{cases} , \alpha = \begin{cases} (\frac{n}{n_{th,*}})^\beta & \text{if } n \geq n_{th,*} \\ \\ 1 & \text{if } n \leq n_{th,*} \end{cases} , \tag{1.3}$$

where $\rho_{\rm gas}$ is the ambient gas density, c_s is the ambient sound speed, v_θ is the local rotational velocity of surrounding gas, and v_{bulk} is the bulk velocity relative to the SMBH. All ambient quantities are calculated using the 32 nearest gas particles. The introduction of v_θ and v_{bulk} terms in the above aims to remedy the neglect of gas bulk motion and angular momentum in the original Bondi-Hoyle formulation. The model compares the tangential velocity of gas (representing angular momentum) to the overall bulk motion, reverting to the standard Bondi-Hoyle model when rotational motion is not dominant. The accretion

[10]Note that there is a typographical error in the criterion for gravitationaly bound criteria in Tremmel et al. (2017).

model includes a boost factor, alpha, which increases with density to reflect the multiphase nature of the gas, calculated by comparing the number density of nearby gas particles to the threshold for star formation, $n_{th,*} = 0.2\,\mathrm{m_p/cm^3}$. For lower densities, it is assumed that the gas is not sufficiently multiphase to require such a boost (Booth & Schaye, 2009). How much this boost increases with density is governed by β, a free parameter, which after calibrating against a series of observed black hole scaling relations is set to 2 (Tremmel et al., 2017).

Feedback from accreting SMBHs in ROMULUS is modeled by converting a fraction of the accreted mass into energy, which is then transferred to nearby gas particles. The thermal energy deposition rate is given by

$$\dot{E}_{\bullet,th} = \epsilon_r \epsilon_f \dot{M}_\bullet c^2 \tag{1.4}$$

where ϵ_r is the radiative efficiency and ϵ_f is the gas coupling efficiency.These are free parameters assumed to be 10% and 2%, respectively. The thermal energy is imparted isotropically to the 32 nearest gas particles, with the energy being distributed among these gas particles according to the smoothing kernel. More detailed discussions on free parameter calibration and the feedback model can be found in Tremmel et al. (2017).

1.4 Dissertation Overview

This dissertation is presented in two parts:

Part I comprises two projects focusing on the circumgalactic medium of galaxies. Chapter 2 presents a detailed analysis of the origin and evolution of the multiphase structure of the CGM around massive galaxies using the state-of-the-art, high-resolution ROMULUS cosmological simulation. This study has been published in the Monthly Notices of the Royal Astronomical Society (MNRAS). In Chapter 3, I describe the development of a novel model to enhance resolution in the CGM region surrounding a galaxy, without increasing the resolution within the galaxies themselves. This targeted approach aims to avoid the necessity of evolving galaxies in simulations at very high resolution while enabling more accurate and realistic modeling of the spatial and dynamic structures in the CGM.

Part II includes investigations of merging SMBHs at various stages of their evolution. First, in Chapter 4, using the ROMULUS cosmological simulations, I study SMBHs that are actively accreting and are in close separation, so appearing as luminous dual AGNs. This chapter focuses on the conditions leading to dual luminous AGNs, as opposed to single luminous AGNs, and compares the properties of their host galaxies. At the time of writing this dissertation, this work has been accepted for publication in the Astrophysical Journal

(ApJ). Using the same simulation in Chapter 5, I explore the properties of host galaxies of binary SMBHs that emit nanohertz gravitational waves, detectable by pulsar timing arrays (PTA). Exploring the characteristics of their host galaxies in simulations assists in narrowing down the field of potential host galaxies for more targeted observational scrutiny. This study has been published in MNRAS.

Finally, Chapter 6 concludes the dissertation with a summary of the overall conclusions drawn from each topic.

PART I: The Gaseous Reservoirs Shaping Galactic Destinies

Chapter 2

Cool and gusty, with a chance of rain: Dynamics of multiphase CGM around massive galaxies in the ROMULUS simulations

Originally published in Monthly Notices of the Royal Astronomical Society: Volume 525, Issue 4, November 2023, Pages 56775701. Reproduced by permission of Oxford University Press. https://doi.org/10.1093/mnras/stad2637

Authors: Vida Saeedzadeh[1], S. Lyla Jung[2], Douglas Rennehan[3], Arif Babul[1,11], Michael Tremmel[4], Thomas R. Quinn[5], Zhiwei Shao[6], Prateek Sharma[7], Lucio Mayer[8], E. OSullivan[9], S. Ilani Loubser[10]

[1]Department of Physics and Astronomy, University of Victoria, 3800 Finnerty Road, Victoria, BC, V8P 1A1, Canada
[2]Research School of Astronomy & Astrophysics, Australian National University, Canberra, ACT 2611, Australia
[3]Center for Computational Astrophysics, Flatiron Institute, 162 5th Ave, New York, NY 10010, USA
[4]School of Physics, University College Cork, College Road, Cork T12 K8AF, Ireland
[5]Astronomy Department, University of Washington, Box 351580, Seattle, WA, 98195-1580, USA
[6]Department of Astronomy, School of Physics and Astronomy, Shanghai Jiao Tong University, Shanghai 200240, China
[7]Department of Physics and Joint Astronomy Program, Indian Institute of Science, Bangalore 560012, India
[8]Institute for Computational Science, University of Zürich, Winterthurerstrasse 190, 8057 Zürich, Switzerland
[9]Center for Astrophysics | Harvard & Smithsonian, 60 Garden Street, Cambridge, MA 02138, USA
[10]Centre for Space Research, North-West University, Potchefstroom 2520, South Africa
[11]Infosys Visiting Chair Professor, Indian Institute of Science, Bangalore 560012, India

Abstract: Using high-resolution ROMULUS simulations, we explore the origin and evolution of the circumgalactic medium (CGM) in the region $0.1 \leq R/R_{500} \leq 1$ around massive central galaxies in group-scale halos. We find that the CGM is multiphase and highly dynamic. Investigating the dynamics, we identify seven patterns of evolution. We show that these are robust and detected consistently across various conditions. The gas cools via two pathways: (1) filamentary cooling inflows and (2) condensations forming from rapidly cooling density perturbations. In our cosmological simulations, the perturbations are mainly seeded by orbiting substructures. The condensations can form even when the median $t_{\rm cool}/t_{\rm ff}$ of the X-ray emitting gas is above 10 or 20. Strong amplitude perturbations can provoke runaway cooling regardless of the state of the background gas. We also find perturbations whose local $t_{\rm cool}/t_{\rm ff}$ ratios drop below the threshold but which do not condense. Rather, the ratios fall to some minimum value and then bounce. These are weak perturbations that are temporarily swept up in satellite wakes and carried to larger radii. Their $t_{\rm cool}/t_{\rm ff}$ ratios decrease because $t_{\rm ff}$ is increasing, not because $t_{\rm cool}$ is decreasing. For structures forming hierarchically, our study highlights the challenge of using a simple threshold argument to infer the CGM's evolution. It also highlights that the median hot gas properties are suboptimal determinants of the CGM's state and dynamics. Realistic CGM models must incorporate the impact of mergers and orbiting satellites, along with the CGM's heating and cooling cycles.

2.0.1 Introduction

It is largely accepted that conditions and processes arising in galaxy group environments must play a crucial role in galaxy evolution. Owing to higher galaxy density and relatively low galaxy velocity dispersion (cf. O'Sullivan et al. 2017a; Werner & Mernier 2020; Lovisari & Ettori 2021 and references therein), group galaxies, both central and satellites, have a higher vulnerability to mergers and tidal interactions. These galaxies are also subjected to ram pressure stripping (McCarthy et al., 2008) and cooling flows due to their being immersed in an ocean of hot X-ray emitting plasma. After all, not only do a substantial fraction of galaxies in the Universe ($> 50\%$; Eke et al. 2006) reside in groups, some of the most massive galaxies in the cosmos are also forged in group environments (cf. Rennehan et al. 2020; Jung et al. 2022 and references therein).

In spite of this, groups have received far less attention than individual galaxies or the more massive galaxy clusters. One reason for this is that they are difficult to detect in X-ray observations due to their low surface brightness; they are also difficult to identify reliably in optical catalogs due to their relatively small galaxy number density contrast

(Pearson et al., 2017; O'Sullivan et al., 2017a). There is change afoot, however. In part, this is due to recent and upcoming compilations that promise high fidelity group catalogs. These include the multiwavelength Complete Local-Volume Groups Sample (CLoGS; e.g. O'Sullivan et al. 2017a, 2018; Kolokythas et al. 2019, 2022) and galaxy group catalogs from the 2MASS Redshift Survey (Lambert et al., 2020), the REFINE survey (Sarron & Conselice, 2021), the eROSITA Final Equatorial-Depth Survey (Liu et al., 2022), etc. The heightened attention is also in part due to improving group detection algorithms (e.g. Ibrahem et al., 2015; Duarte & Mamon, 2015; Yang et al., 2021; Xu et al., 2022) and the increasingly sophisticated cosmological galaxy formation simulations that are now able to reproduce the observed stellar properties of group galaxies as well as facilitate new insights into group-scale processes and their impact on galaxies (see the recent review by Oppenheimer et al. 2021a as well as the recent study by Jung et al. 2022 for a summary discussion of the relevant simulations.)

One such set is the Romulus suite of cosmological hydrodynamic simulations (Tremmel et al., 2017, 2019; Butsky et al., 2019; Chadayammuri et al., 2020; Jung et al., 2022) comprising one uniform cosmological volume (25 Mpc per side) and three group-scale zoom simulations. Recently, Jung et al. (2022) examined the kinematic and photometric properties of the brightest group galaxies (hereafter, BGGs) in Romulus groups. They found that the distribution of their properties, the trends exhibited by and the correlations among them, are in very good agreement with the observations. Like the observed BGGs, the Romulus BGGs include both quenched and star forming galaxies; early-type elliptical galaxies and late-type disk galaxies; fast-rotators and slow-rotators; etc. Jung et al. (2022) also follow the evolution of BGGs transforming from late- to early-type in the aftermath of mergers. More interestingly, they also find "galaxy rejuvenation" where quenched early-type BGGs transition into late-type star-forming galaxy (see also Jackson et al. 2022.)

The latter is, at first glance, surprising and tempting to dismiss as an artefact, but recent results from the Multi Unit Spectroscopic Explorer (MUSE; Olivares et al. 2022) suggest that the re-emergence of gaseous disks and star forming disks/rings around BGGs, at least on a small scale, is not uncommon (see also Loubser et al. 2022; Lagos et al. 2022). Moreover, Weinmann et al. (2006) find that ($\sim 40 - 50\%$) of the central galaxies in galaxy groups are star-forming late-type galaxies. In fact, a significant minority of galaxies has been shown to have disky morphology even at the highest stellar mass ($M_* > 10^{11.4}$ $M_\odot$) (e.g. Conselice 2006; Ogle et al. 2016, 2019) and even early-type BGGs have been shown to contain non-trivial amount of cold gas (Werner et al., 2014; O'Sullivan et al., 2018). The presence of cold gas and gaseous disks, rejuvenations, and the ongoing star formation all indicate that BGGs

must be receiving influx of gas from their surroundings every so often. In the present paper, we focus on the reservoir of gas cocooning the ROMULUS BGGs (hereafter, the circumgalactic medium or the CGM) and seek to identify the different modes of gas influx. In the process, we also investigate the nature of the CGM and the origin of structure therein. As it turns out, all of these are inter-linked.

The nature and the dynamics of the CGM and the impact of these on galaxy formation is a highly topical subject. Observations of CGM surrounding BGGs and giant elliptical galaxies find that this reservoir comprises gas with a broad range of kinematics, ionization states, temperatures, densities, and phases (e.g. Werner et al., 2014; Werk et al., 2016; Lakhchaura et al., 2018; O'Sullivan et al., 2018; Zahedy et al., 2019; Olivares et al., 2022). Among the many riddles linked to this rich diversity, the origin of cold ($\sim 10^4$ K) gas co-existing alongside warm-hot ($\sim 10^6 - 10^7$ K) gas in the CGM of quiescent galaxies is particularly puzzling. Possible explanations of the phenomenon run the gamut from (i) debris from ram pressure stripping and tidal disruption of satellite galaxies (e.g. Murakami & Babul 1999; McCarthy et al. 2008; Sun et al. 2009; Franchetto et al. 2021; Jung et al. 2022); (ii) byproducts of cooling due to mixing between the diffuse CGM and the multiphase stellar and/or AGN-driven galactic outflows (Huang et al., 2020a,b; Schneider et al., 2020; Rennehan, 2021), as well as mixing between the diffuse CGM and the interstellar gas dredged (uplifted) out of the galaxy by active galactic nucleus (AGN) jets (e.g. Revaz et al. 2008; Pope et al. 2010; Scannapieco & Brüggen 2015; Schneider & Robertson 2017; Qiu et al. 2020); to (iii) the byproducts of induced positive density perturbations within the CGM that result in localized regions of rapidly cooling gas which condense out of the general medium and form in-situ cool clouds (e.g. Maller & Bullock 2004; Sharma et al. 2010, 2012a; Choudhury & Sharma 2016; Prasad et al. 2015, 2017; Voit et al. 2015; Li et al. 2015).[2] The key to sorting through these various mechanisms, and the way in which they impact the evolution of the galaxies is to undertake a detailed study of the baryon cycles and the physics underlying these cycles in these systems (cf. Donahue & Voit, 2022; Faucher-Giguere & Oh, 2023, and references therein).

For systems that assemble hierarchically over the cosmic timescales, one way of quantifying the importance of the different origin mechanisms and more generally, of acquiring better insight into the dynamics of the CGM, is to track its evolution in self-consistent, cosmological hydrodynamic simulations of galaxy evolution. However, investigating the CGM

[2]In literature, the phenomenology is often associated with labels "condensations" and "precipitation". In this paper, "condensations" refers to cool-cold clouds forming in-situ out of localized regions of rapidly cooling density perturbations. Precipitation refers to cold clouds that fall or rain down onto the central galaxy.

using cosmological simulations is very challenging because most current cosmological simulations typically under-resolve lower density structures, like the CGM (Hummels et al., 2019). This is due to two main constraints: (i) an effective ceiling on the maximum resolution due to practical considerations (e.g., the computational costs in terms of time and resources), and (ii) the intentional design of the codes to prioritize and direct computational resources towards high density structures.

There are, however, concerted ongoing efforts to improve the treatment of the CGM. One promising approach involves code redesign (cf. Hummels et al., 2019; Suresh et al., 2019; van de Voort et al., 2019; Peeples et al., 2019) that allows the mass resolution in a halos circumgalactic environment to be boosted above the halos base resolution. The other approach leverages more efficient codes, faster computers and greater computing resources to push to higher resolutions overall (cf. Tremmel et al., 2019; Fiacconi et al., 2017; Hafen et al., 2019; Nelson et al., 2019a; Fielding et al., 2020; Tamfal et al., 2022). Our ROMULUS suite of simulations fall in the latter category. In fact, most of the studies cited above that follow the evolution of cosmologically realistic halos rely on higher resolution globally, the only exceptions being Suresh et al. (2019), van de Voort et al. (2019) and Peeples et al. (2019).

To be sure, both approaches have limitations. For one, neither class of simulations have achieved convergence. Nonetheless, the effort represents significant improvement. Also, we note that at present the computational expenses involved typically limit the size of the halos that can be investigated, or restrict the runs from being continued past some time point, or require some other compromises. For example, all except Nelson et al. (2020) and the ROMULUS analyses limit themselves to halos of mass $M_{vir} \sim 10^{12}$ $M_\odot$ or lower.

Here, we expand on prior ROMULUS studies (Tremmel et al., 2017, 2019; Butsky et al., 2019; Chadayammuri et al., 2020; Jung et al., 2022) to investigate the origin and the dynamics of the CGM in the radial range $0.1 \leq R/R_{500} \leq 1$ around the central galaxies in group-scale halos with present-day ($z = 0$) masses in the range 2.3×10^{12} $M_\odot \leq M_{200} \leq 1 \times 10^{14}$ $M_\odot$. When we speak of the CGM, this is the gas that we are referring to — unless we explicitly say otherwise. We exclude the gas inside $0.1R_{500}$ from current study because gas dynamics in this "inner CGM" is considerably more complex. For one, it undergoes repeated heating and cooling episodes which give rise to variations in the central temperature, cooling times, gas velocities, etc. We will explore the evolution of the "inner CGM" in a follow-up paper. This paper is organized as follows: In Section 2.0.1, we explain our analysis methodology and present some preliminary results. In Section 2.0.2, we discuss the nature of the CGM and investigate its origin. We then explore the dynamics of the multiphase CGM in Section 2.0.3.

Halo ID	$M_{200}\|_{z=0}$ [$M_\odot$]	z_a	M_{200} [$M_\odot$]	M_{500} [$M_\odot$]	$M_{*,R_{gal}}$ [$M_\odot$]	$M_{*,50\ kpc}$ [$M_\odot$]	R_{200} [kpc]	R_{500} [kpc]	R_{gal} [kpc]
C	1.1e+14	0.70	5.9e+13	4.6e+13	8.0e+11	9.2e+11	629.8	428.5	23.0
52024	1.8e+13	0.29	1.3e+13	1.0e+13	2.0e+11	2.5e+11	451.7	304.6	15.2
G1	1.4e+13	0.25	1.6e+13	1.1e+13	2.6e+11	3.3e+11	488.9	317.7	15.9
49510	1.2e+13	0.36	1.1e+13	8.2e+12	1.7e+11	2.2e+11	417.5	276.6	12.1
99966	6.3e+12	0.31	5.9e+12	3.9e+12	1.1e+11	1.3e+11	342.2	219.8	12.1
38182	4.4e+12	0.44	4.0e+12	2.8e+12	1.0e+11	1.1e+11	286.3	187.2	11.0
91655	2.3e+12	0.26	2.1e+12	1.7e+12	1.1e+11	1.4e+11	247.9	171.3	13.3
77876	2.3e+12	0.25	2.1e+12	1.8e+12	1.0e+11	1.3e+11	251.2	174.2	11.0

Table 2.1: Properties of the eight ROMULUS halos that we use as foil for the discussion in this study. Halos are ordered by halo mass M_{200} at z = 0. z_a is the redshift at which the halos were analyzed. M_{200} (M_{500}) is the the total mass at z_a within R_{200} (R_{500}). $M_*(< R_{gal})$ is the total stellar mass contained within the central galaxy's radius R_{gal} (see text for definition of R_{gal}) and $M_*(< 50$ kpc) is stellar mass within 50 kpc of the halo center at z_a.

We summarize and discuss our results in Section 2.0.5 and give final concluding remarks in Section 2.0.6.

Analysis Methods and Initial Findings

We use three of the ROMULUS simulations: ROMULUS25, which is a $(25\,\mathrm{Mpc})^3$ cosmological volume simulation, as well as ROMULUSC and ROMULUSG1, which are two zoom simulations of individual group-scale systems. All three simulations share the same background cosmology[3], sub-grid physics and ROMULUS galaxy formation model (Tremmel et al., 2017, 2019; Butsky et al., 2019; Chadayammuri et al., 2020; Jung et al., 2022). Also, all three simulations are run using Tree+Smoothed Particle Hydrodynamics (Tree+SPH) code CHANGA (Menon et al., 2015; Wadsley et al., 2017).

The details about the ROMULUS simulations, including a thorough discussion of the hydrodynamics code and the galaxy formation model used, the sub-grid physics incorporated therein, the various modeling choices adopted, as well as the simulations' unique features, have been described extensively in a number of published papers. In the interest of brevity, we do not repeat this account here and instead, refer interested readers to Tremmel et al. (2015, 2017, 2019, 2020); Sanchez et al. (2019); Butsky et al. (2019); Chadayammuri et al.

[3]The background cosmology corresponds to a ΛCDM universe with cosmological parameters consistent with Ade et al. (2016) results: $\Omega_m = 0.309$, $\Omega_\Lambda = 0.691$, $\Omega_b = 0.0486$, $H_0 = 67.8\,\mathrm{km\ s^{-1}Mpc^{-1}}$, and $\sigma_8 = 0.82$.

(2020); and Jung et al. (2022). The latter especially offers a concise yet complete summary. Here, instead, we concentrate on providing a clear description of the approach we take in analyzing the simulations.

There is, however, one aspect that is important to highlight: The resolution of all the groups extracted from ROMULUS simulations is the same regardless of whether they are drawn from zoom or cosmological simulations. They are all characterized by a Plummer equivalent gravitational force softening of 250 pc (or 350 pc spline kernel), a maximum SPH resolution of 70 pc, and gas and dark matter particle masses of 2.12×10^5 $M_\odot$ and 3.39×10^5 $M_\odot$, respectively.

Together, the ROMULUS simulations yield a sample numbering in a few tens of halos in the mass range of interest. These are among the highest resolution group-scale halos simulated using cosmologically realistic initial conditions.

Halo catalogue and substructure definition

The output files for all the ROMULUS simulations discussed in this study were processed in an identical manner: The halos and subhalos were extracted and processed using the Amiga Halo Finder (Knebe et al., 2008; Knollmann & Knebe, 2009, AHF), and tracked across time with TANGOS (Pontzen & Tremmel, 2018).

The halos and subhalos exist in a nested hierarchy, with the halos being the top-level structures and the subhalos embedded therein. AHF finds these structures by locating peaks in an adaptively smoothed density field, identifying all particles (dark matter, gas, stars, and black holes) that are gravitationally bound to each peak, and then proceeding up the hierarchy to find successively larger structures. Once the halos are identified, their centers are found by applying the shrinking sphere approach (Power et al., 2003) to the distribution of bound particles associated with each of the halos.

The halo masses (M_Δ) are determined by constructing a sphere of radius R_Δ about each of the halo centers such that the mean interior density is $\langle \rho_{m,\Delta}(z) \rangle = \Delta \cdot \rho_{crit}(z)$ where $\rho_{crit} = 3H^2(z)/8\pi G$ is the critical cosmological density and Δ is a constant. (see, for example, Babul et al., 2002). Throughout this study, we refer to (M_{200}, R_{200}) and (M_{500}, R_{500}) which correspond to $\Delta = 200$ and $\Delta = 500$ respectively. For the assumed cosmology in ROMULUS simulations $M_{500}/M_{200} \sim 0.7$ and $R_{500}/R_{200} \sim 0.68$.

The above prescription is only appropriate for the halos. In the case of subhaloes, AHF tracks the local density profile as a function of distance from the peak center. At some point, the external gravitational field becomes dominant and correspondingly, the behaviour of the

density profile changes. The distance from the peak where this happens marks the size of the subhalo, and the mass enclosed is recorded as the subhalo's mass.

As noted in §2.0.1, in this study we are interested in the CGM surrounding the massive central galaxies in group-scale halos. Consequently, we restrict ourselves to halos in our simulations with $z = 0$ masses $M_{200} \geq 2 \times 10^{12}$ $M_\odot$ (cf Jung et al., 2022).

Central galaxy selection criterion

Next, we are specifically interested in the evolution of the quiescent CGM, that is the dynamics of the CGM in the absence of shocks and other disturbances due to major mergers and massive interlopers (see, for example, Poole et al., 2006). We therefore examine each of the halos of interest and locate a 5 Gyrs window over the redshift range $0 \leq z \leq 1.5$ during which the volume inside R_{500} is undisturbed by a major (1:10 or larger) merger. We set our epoch of analysis (hereafter, z_a) at two Gyrs after the start of the window. Our analysis of the gas dynamics in group-scale halos that undergo major mergers shows that it rarely takes longer than two Gyrs for the gas inside R_{500} to relax. In order to identify the origins and the fate of the CGM gas at the time of analysis, z_a, we consider the evolution of the gas starting from 5 Gyrs prior (we explain the choice of 5 Gyrs in §2.0.3) to z_a to 3 Gyrs after.

Since the halos are generally dynamically relaxed during the period of study, the massive galaxies in the halos are always located at the halo center. We determine the galaxies' baryonic properties by looking at the gas, stellar and black hole particles within spheres of different sizes centered on the halo centers. To further restrict ourselves to massive central galaxies (hereafter, BGGs), we only investigate systems that host central galaxies with $M_*(< R_{gal}) \geq 10^{11}$ $M_\odot$, where R_{gal} is the galaxy's radius. We follow Hafen et al. (2019) and define a central galaxy's radius as $R_{gal} = 4R_{*,0.5}$, where $R_{*,0.5}$ is the half mass radius for all star particles within $0.15R_{200}$.

There are 19 such systems across all of the ROMULUS simulations and although we have analyzed all 19, we have selected eight for detailed investigation and as foil for our discussion. The basic characteristics of these eight halos are listed in Table2.1. We emphasize that these should be regarded as illustrative. They were chosen because their halo and BGG masses, as well as the number and properties of the subhalos orbiting inside $R_{500}(z_a)$ sample the range spanned by the full sample, and because their CGM properties reflect the diversity present in our sample. For example, we wanted to ensure that the sample included both cool core and non-cool core groups. We emphasize that the findings and behaviours that we highlight are general and observed in all the halos.

For completeness, we point out that the cool core/non-cool core classification criterion for observed groups is *not* the same as that for clusters. For the latter, it is based on entropy or the cooling time of the intracluster medium in the cluster core. Groups, however, are classified on the basis of their observed temperature profiles: Those that exhibit central temperature drop are designated "cool core (CC)" while those with flat or centrally peaked temperature profiles are labelled "non-cool core (NCC)". We refer interested readers to O'Sullivan et al. (2017a) for further details. The classification of ROMULUS groups is discussed in Jung et al. (2022) and their temperature profiles are shown in Fig. 12 of that paper.

The circumgalactic gas surrounding the BGGs

The main focus of this study is to determine where the gas in the CGM around massive galaxies at the time of analysis, $z_{\rm a}$, has come from, to identify the different types of structures present, and ascertain the fate of these CGM subcomponents. We will do this via particle tracking analysis applied to the individual gas resolution elements of the CGM. Particle tracking leverages the fact that Lagrangian hydrodynamic codes, like CHANGA, provide access to the full time history of these resolution elements and the fact that mass exchange between gas elements is not permitted. It has previously been used to study gas inflow onto galaxies and their halos, as well as the impact of galactic winds; it has also been used to study the gas and metal content of the intragroup medium and most recently, the CGM around Milky Way-like and lower mass halos (cf. Kereš et al., 2005; Oppenheimer et al., 2010; Liang et al., 2016; Anglés-Alcázar et al., 2017; Hafen et al., 2019; Esmerian et al., 2021, and references therein).

An assessment of the gas properties (e.g., temperature, entropy, cooling time, etc.) surrounding the BGGs in the ROMULUS groups shows that at any given radius, these typically span a broad distribution. This is illustrated in Fig. 2.1, where we show the distribution of the local gas cooling time at $z_{\rm a}$, as a function of halocentric distance, in our eight illustrative halos. Here, $t_{\rm cool} \equiv E_{\rm thermal}/[n_e^2\Lambda]$, where Λ is the radiative cooling function and n_e is electron number density.

The grey shading in each of the panels illustrates the distribution of *all* the gas inside R_{500} of the identified halos, including the cool, potentially star-forming gas (hereafter, the interstellar medium or the ISM) within the BGG. Operationally, we divided the panels into equal-sized pixels, binned the gas particles in these pixels, and converted the resulting count into a fraction relative to the total number of gas particles within R_{500}. The contrast

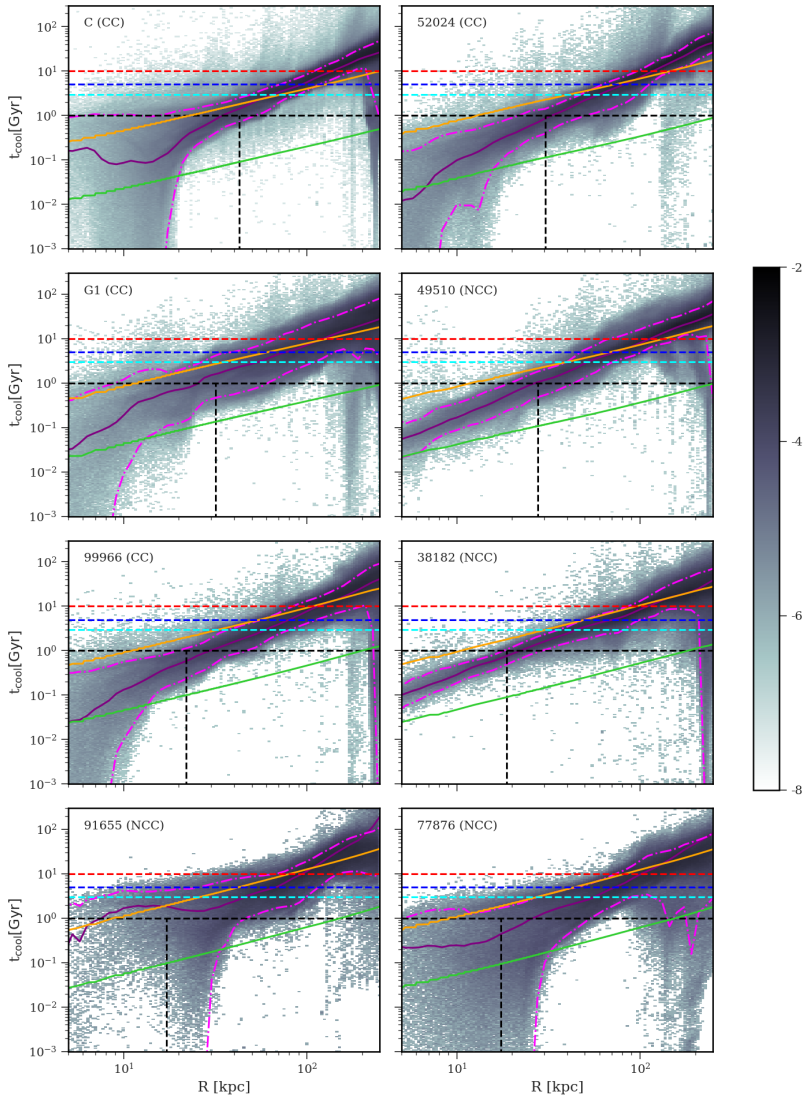

Figure 2.1: The distribution of $t_{\rm cool}$ for gas within R_{500} in eight ROMULUS halos used in this study at $z_{\rm a}$. The grey pixels show $t_{\rm cool}$ versus the radius of *all* gas. The pixels' contrast is determined by the logarithm of the ratio of gas particles in each pixel to the total gas particles within R_{500} of each halo. The purple line in each panel is the median $t_{\rm cool}$ for the hot ($T > 10^6$ K) gas. The dashed horizontal lines corresponds to $t_{\rm cool} = 10$ (red), $= 5$ (blue), $= 3$ (cyan) and $= 1$ (black).The magenta dotted-dashed lines show the upper and lower values of $t_{\rm cool}$ bounding 90% of non-ISM gas. Black vertical line shows $r = 0.1\ R_{500}$ for each halo. As discussed in the text, we designate the gas at $0.1 \leq R/R_{500} \leq 1$ as the CGM. The orange line shows $t_{\rm cool}/t_{\rm ff} = 20$ and green line shows $t_{\rm cool}/t_{\rm ff} = 1$. The significance of these thresholds is discussed in the text.

of the shading is determined by the logarithm of the fraction: larger the fraction, darker the shading. Additionally, the horizontal dashed lines in each of the panels correspond to cooling timescales of 10 Gyrs (red), 5 Gyrs (blue), 3 Gyrs (cyan), and 1 Gyr (black). The purple curve is the median $t_{\rm cool}$ for the hot (T $> 10^6$ K) gas; the vertical black dashed line corresponds to $0.1{\rm R}_{500}$; and the two magenta dot-dashed lines show the upper and lower values of $t_{\rm cool}$ bounding 90% of the non-ISM gas.[4] As for the orange and green diagonal lines, we will discuss these in §2.0.1.

The CGM

The panels in Fig. 2.1 show several features worth noting. We first start by considering all the gas in the radial range $0.1 \leq {\rm R/R}_{500} \leq 1$. We find that no more than 10% (20%) of the gas has cooling time of less than 1 Gyr (3 Gyrs). Generally, the non-ISM CGM gas in all halos is distributed in a band about the median hot gas $t_{\rm cool}$ curve. Still, even if we set aside the cool dense ISM-like gas in the satellite and the central galaxies *and* further exclude the gas in the two tails of the distribution, the remaining 90% (bracketed by the two magenta dot-dashed lines) includes gas whose cooling times range from $\sim 0.3-0.4$ to $\sim 2-3$ times the median *at the same radius*. Moreover, we also find occasional deep downward extensions plunging cooling times as much as $10^{-3}\times$, or even $10^{-4}\times$ lower, as well as upward extensions from the median band reaching $\sim$100$\times$ larger, than the hot gas median. Such large dynamic ranges in $t_{\rm cool}$ has also been reported by Esmerian et al. (2021) and Nelson et al. (2020) in simulations of Milky Way-mass (FIRE-2) as well as group-scale ($M_{200} \sim 10^{13.5}\ M_\odot$) halos (TNG50), respectively. As for the origin of the dips and peaks, we will discuss these further in greater detail in §2.0.2 & §2.0.3. Here we simply note that the former are due to gas recently stripped from the satellites while the latter are due to shock-heated gas.

Secondly, although we have explicitly indicated that we will focus on gas in the radial range $0.1 \leq {\rm R/R}_{500} \leq 1$ around BGGs, we cannot ignore the fact that in many of the halos, bulk of the gas — and this includes the non-ISM gas — inside $0.1{\rm R}_{500}$ has short ($<$ 1 Gyr) cooling time. Consequently during periods of low AGN activity, one expects the emergence of a global cooling flow. Chadayammuri et al. (2020) noted this trend in ROMULUS C system (see their Fig. 7 and 8), and we see it in *all* other ROMULUS groups as well (see §2.0.3). Inevitably, these flows are disrupted by AGN outbursts (e.g. see panel for halo 91655 in Fig. 2.1) but when present, they extend beyond $0.1{\rm R}_{500}$ and impact the dynamics of the gas of interest (cf. §2.0.3).

[4]Specifically, we exclude any gas that is bound to central and satellite galaxies *and* whose temperature is less than $5 \times 10^4 K$ and hydrogen number density greater than $0.1\,{\rm cm}^{-3}$.

Next, we turn to the solid orange diagonal lines. This line corresponds to $t_{\rm cool}/t_{\rm ff} = 20$, where $t_{\rm ff} \equiv \sqrt{2r/g(r)}$ is the free-fall time at radius r and $g(r) = GM(<r)/r^2$. We consider this quantity because linear stability analyses and experiments with idealized simulations find that small-amplitude density perturbations in stratified diffuse CGM in global thermal balance are thermally unstable and susceptible to condensation whenever the median $t_{\rm cool}/t_{\rm ff}$ drops below 10.[5] Condensing perturbations will form cool-cold clouds, giving rise to multiphase structure in the CGM (cf.Sharma et al. 2010, 2012a; McCourt et al. 2012; Meece et al. 2015; Choudhury & Sharma 2016). And, while there is observational support for this thermal instability picture from, for example, studies of the galaxy cluster cores, some of these same observational studies suggest a higher $t_{\rm cool}/t_{\rm ff}$ value for the onset of the instability (e.g., ~ 20; Hogan et al. 2017; Pulido et al. 2018; Babyk et al. 2018). Recently, a theoretical reanalysis by Choudhury & Sharma (2016) suggests that this value depends on the detailed shape of the gravitational potential well (due, for example, to the central galaxy within the halo; see also Voit & Donahue, 2015; Prasad et al., 2018) and can be as much as a factor of 2 higher in realistic group/cluster cores. Guided by these findings, we adopt $t_{\rm cool}/t_{\rm ff} = 20$ (solid orange line) as our threshold (in §2.0.5, we discuss how our findings change if our threshold is raised to 30 or lowered to 10.) An examination of the panels in Fig. 2.1 shows that in all except halo 91655 (which is undergoing active AGN heating), the purple curve lies below the solid orange curve (or equivalently, $(t_{\rm cool}/t_{\rm ff})_{\rm med} \leq 20$) out to ~ 60 kpc. In other words, gas density perturbations within the central ~ 60 kpc of these group-scale halos ought to be prone to condensation.

The green solid line corresponds to $t_{\rm cool}/t_{\rm ff} = 1$. Voit (2021) suggests that once the perturbations' local $t_{\rm cool}/t_{\rm ff}$ drops below $t_{\rm cool}/t_{\rm ff} = 1$, they will condense and form cool-cold clouds. We will discuss the distinction between local and global values of $t_{\rm cool}/t_{\rm ff}$ in §2.0.1.

In Fig. 2.2, we show the distribution of the local $t_{\rm cool}/t_{\rm ff}$ at $z_{\rm a}$ for *all* the gas inside $\rm R_{500}$, including the cool, potentially star-forming ISM gas, in halos under consideration. The grey shading has the same meaning as in Fig. 2.1; the purple curve is the median $t_{\rm cool}/t_{\rm ff}$ profile for the hot ($\rm T > 10^6$ K) gas; and the dashed and dash-dotted horizontal lines corresponds to the $t_{\rm cool}/t_{\rm ff} = 20$ and $t_{\rm cool}/t_{\rm ff} = 1$, respectively. Additionally, we have shaded some of the gas in the panels translucent orange. We discuss this component in detail in §2.0.1 below but first we examine the properties of the CGM gas (i.e. the gas in the radial range $0.1 \leq \rm R/R_{500} \leq 1$).

[5] While the gas is formally linearly thermally unstable for all $t_{\rm cool}/t_{\rm ff}$ (Choudhury & Sharma, 2016), nonlinearly, it becomes multiphase when the median ratio is lower than 10. In this work, we refer to the gas prone to condensation as "condensation-susceptible" gas.

Examining the distribution of $t_{\rm cool}/t_{\rm ff}$, we frequently find a large spread in the same radial shell. Specifically, $t_{\rm cool}/t_{\rm ff}$ extends to values as low as ~ 0.1, and in some instances down to 10^{-3} or even 10^{-5}, and as high as ~ 300. This again highlights the multiphase nature of the CGM. Esmerian et al. (2021) and Nelson et al. (2020) also find similarly large dynamic range in $t_{\rm cool}/t_{\rm ff}$ in their simulations.

Next, we consider the median ROMULUS $t_{\rm cool}/t_{\rm ff}$ profiles (purple curve in each panel) for the hot ($T > 10^6$ K) gas — see also, the left panel of Fig. 2.3, where all eight are juxtaposed for easy comparison. These profiles can be directly compared to the $t_{\rm cool}/t_{\rm ff}$ profiles in Fig. 11 of Nelson et al. (2020), which are for the hot gas in TNG50 groups of comparable masses to our ROMULUS groups. In terms of resolution, the TNG50 simulation is similar to ROMULUS: As described by Pillepich et al. (2019), TNG50 has gas and dark matter element mass of 8.5×10^4 $M_\odot$ and 4.5×10^5 $M_\odot$, respectively [versus gas and dark matter particle masses in ROMULUS of 2.12×10^5 $M_\odot$ and 3.39×10^5 $M_\odot$, respectively]; a Plummer equivalent gravitational force softening of 288 pc [versus 250 pc in ROMULUS]; and a minimum adaptive gas gravitational softening of 72 pc [versus a minimum SPH resolution of 70 pc].

Nevertheless, the results are strikingly different: All except two of our median profiles increase monotonically with radius, power-law-like, for $r \geq 10$ kpc ($r \geq 0.05 R_{500}$). Even the median profiles for halos 91655 and 77876, which feature a "bump"[6] within the central $\sim 0.1 - 0.2$ R/R_{500}, fall in with the rest and then rise towards larger radii. In contrast, the TNG50 profiles rise, have a maximum at $15 - 40$ kpc, and then decrease towards larger radii.

The shape of the ROMULUS profiles are in agreement with the observed $t_{\rm cool}/t_{\rm ff}$ profiles in galaxy groups (cf. O'Sullivan et al., 2017a), which also increase with radius for $r > 0.1 R_{500}$. This is illustrated in Fig. 2.3 by the solid black line, which corresponds to the observationally determined median $t_{\rm cool}/t_{\rm ff}$ profile for the subset of the CLoGS galaxy groups (O'Sullivan et al., 2017a) with available X-ray data, and the grey band, which illustrates the spread about the observed median. In the left panel, it is clear that the CLoGS profiles, like the ROMULUS profiles, increase with distance from the group center. However, the plot also gives the impression that the observed profiles have a slightly higher normalization. This offset is due to the fact that the ROMULUS halos span a larger range in $z_{\rm a}$ and halo mass than the CLoGS sample. In particular, the ROMULUS sample has more lower mass systems than CLoGS. We follow the scaling procedure described by Prasad et al. (2020a) to account

[6]The "bump" is due to ongoing AGN outbursts (see discussion and figure in §2.0.2 for further details). Similar central bump-like features are present in the observationally determined $t_{\rm cool}$ profiles of the CLoGS galaxy groups with jets (cf. Fig. 5 of O'Sullivan et al. 2017a.)

for these variations and the results are shown in the right panel of Fig. 2.3. The use of scaled $t_{\rm cool}/t_{\rm ff}$ leads to the narrowing of the scatter between the ROMULUS profiles, especially for R $>$ 0.1R$_{500}$, and an improved agreement with the normalization of the CLoGS curve. Rescaling the CLoGS median/band does not have much impact because the groups are all nearby ($z < 0.02$) and span a narrow range in mass and redshift.

Returning to the Nelson et al. (2020) results, we cannot discern whether the differences in the shape of their and our profiles are due to the baryon mass resolution of TNG50 being slightly better than that of ROMULUS; due to the differences in the hydrodynamic solvers used to run the two simulations; due to differences in the modeling and implementation of CGM heating and cooling (cf. §2.1 of Jung et al., 2022, for additional details); or some combination thereof. Whatever the reason, it also results in ROMULUS and TNG CGM group-scale gas entropy profiles having very different shapes (see Oppenheimer et al. 2021a for a detailed discussion); the shapes of the ROMULUS entropy profiles are in good agreement with the observations (Jung et al., 2022).

We also compare our results to Esmerian et al. (2021). The profiles in their Fig. 3 are not directly comparable to those in our Fig. 2.3 (left panel) because their halos are lower mass, Milky Way-like systems and their definition of the hot intragroup gas is based on an entropy cut (K $>$ 5 keVcm^2) as opposed to our temperature cut (T $>$ 10^{6}K). However, when we apply the Esmerian *et al.* entropy threshold and repeat the analysis, the resulting $t_{\rm cool}/t_{\rm ff}$ profiles, especially those of our lower mass systems, are in good agreement. Our collective results sit on the same continuum.

The condensation-susceptible CGM

Even a quick perusal of Fig. 2.2 shows that gas that is susceptible to condensation is *not restricted only to regions where the median curve falls below* $t_{\rm cool}/t_{\rm ff} = 20$. This is readily apparent in, for example, the ROMULUS C panel. Additionally, there are also radial zones, in halos 99966 and 38182 for example, where the median curve is below our threshold and yet, there is very little gas condensing out. Features like this in the observations have been use to argue that the $t_{\rm cool}$ may be a better indicator of thermal instability than $t_{\rm cool}/t_{\rm ff}$ (Hogan et al., 2017). Specifically, Hogan et al. (2017) argue that the nebular emission, a tracer of cold gas and star formation, mainly occurs in systems with median $t_{\rm cool} < 1$ Gyr at 10 kpc. We find that nearly all ROMULUS groups, both CCs and NCCs, have $t_{\rm cool} < 1$ Gyr at 10 kpc. However, not all halos' BGGs have ongoing star formation within the central 50 kpc sphere (see Table 2.2). Moreover, the recently published observed profiles of Martz et al. (2020) are

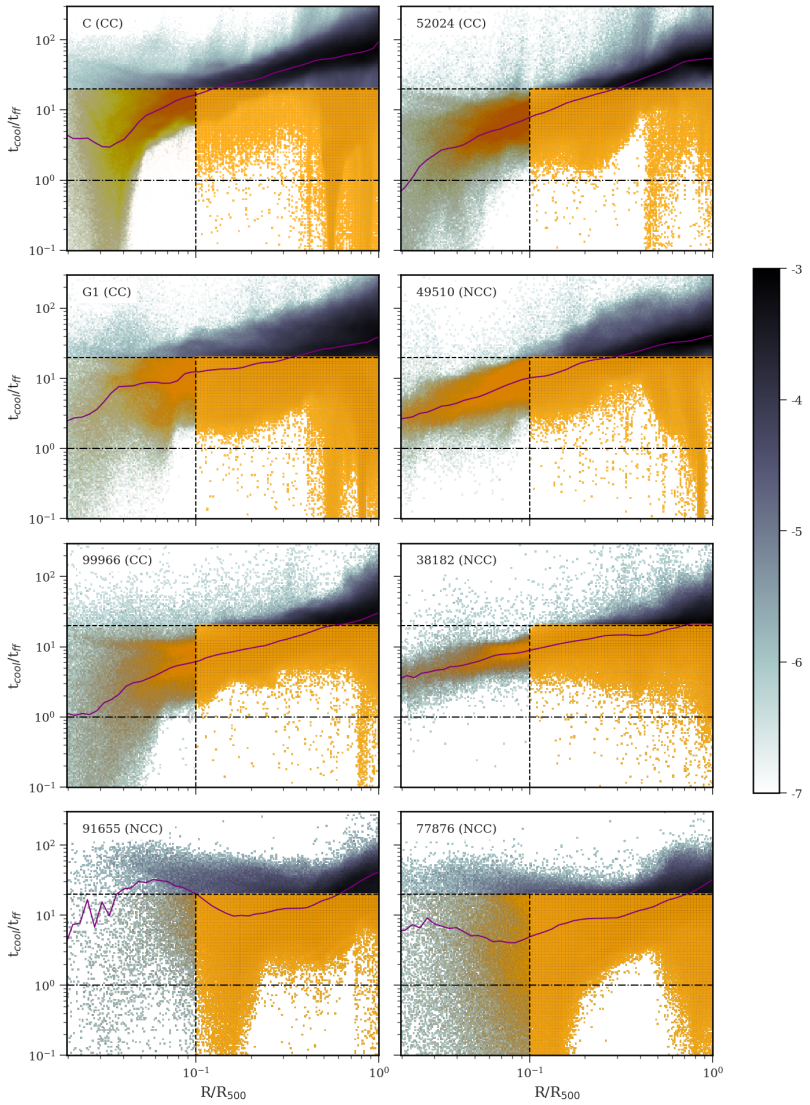

Figure 2.2: The distribution of $t_{\rm cool}/t_{\rm ff}$ for gas within R_{500} in ROMULUS groups under consideration at $z_{\rm a}$. The grey pixels show $t_{\rm cool}/t_{\rm ff}$ versus the radius of *all* gas. The radius is scaled by characteristic radius (R_{500}). The grey shading has the same meaning as Fig.2.1. The purple line is the median $t_{\rm cool}/t_{\rm ff}$ for the hot ($T > 10^6$ K) gas. The dashed black vertical line shows $r = 0.1$ R_{500}. As discussed in the text, we designate the gas at $0.1 \leq R/R_{500} \leq 1$ as the CGM. The dashed, black, horizontal line shows $t_{\rm cool}/t_{\rm ff} = 20$ and dash-dotted horizontal line shows $t_{\rm cool}/t_{\rm ff} = 1$. The significance of these thresholds is discussed in the text. The orange shading shows the distribution of "condensation-susceptible" CGM. We define this as gas between $0.1 \leq R/R_{500} \leq 1$ with $t_{\rm cool}/t_{\rm ff} < 20$ as well as gas between $0.02 < R/R_{500} < 0.1$ that has $t_{\rm cool}/t_{\rm ff} < 20$ at $z_{\rm a}$ *and* which entered this domain from beyond $0.1R_{500}$ in the 5 Gyrs prior to the time of analysis. We explicitly exclude ISM gas.

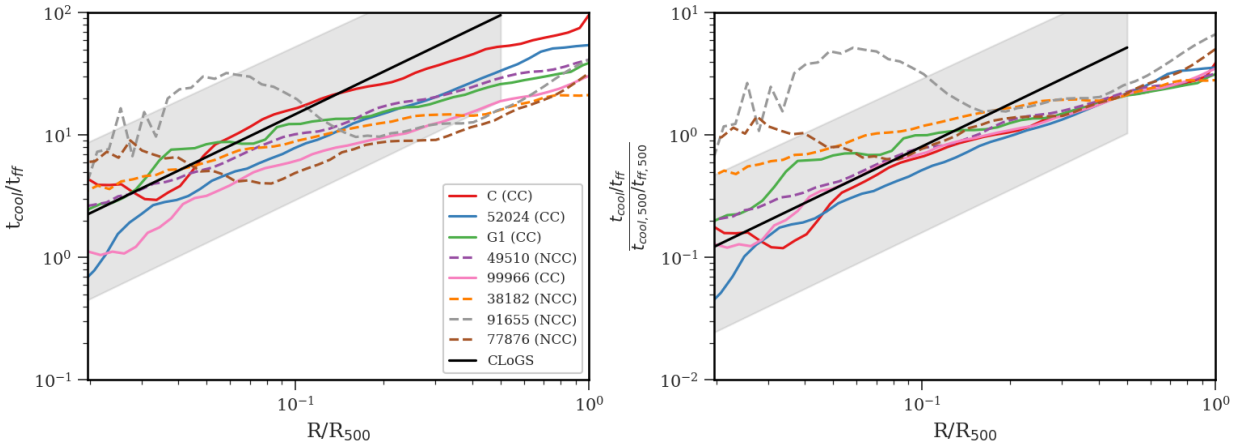

Figure 2.3: Median $t_{\rm cool}/t_{\rm ff}$ of hot ($T > 10^6$ K) gas for the eight ROMULUS halos vs radius. The left panel juxtaposes all median lines from Fig. 2.2. We show the median line for CC groups as solid lines, and NCC as dashed lines. The right panel shows the same $t_{\rm cool}/t_{\rm ff}$ profiles, scaled by $t_{\rm cool,500}/t_{\rm ff,500}$ following Prasad et al. (2020a). Black solid line is the median $t_{\rm cool}/t_{\rm ff}$ for observed CLoGS groups (O'Sullivan et al., 2017a) and the grey band shows the observed spread around the CLoGS median.

consistent with the ROMULUS results. They find a number of groups and clusters that have $t_{\rm cool} < 1$ Gyr in the central region but do not evidence star formation or molecular gas in and about their central galaxy. In light of this, we choose to stick with $t_{\rm cool}/t_{\rm ff}$.

Nonetheless, the existence of gas that is susceptible to condensation in radial zones where the median curve is above our threshold begs an explanation. We interpret such features as supporting the results of Choudhury et al. (2019), who investigated conditions under which both large and small density perturbations can become thermally unstable. They found that the crucial parameter signaling the medium's susceptibility to multiphase condensations is not whether the median $t_{\rm cool}/t_{\rm ff}$ is below some value but whether the perturbations' local $t_{\rm cool}/t_{\rm ff}$ falls below threshold, particularly if the perturbations are strong. And, as we will show in §2.0.2 and 2.0.3, gas in groups embedded in cosmologically realistic environments are regularly subject to strong perturbations.

As for the lack of condensing gas when the median curve is below our threshold, this can be due to lack of perturbations. However, a more likely explanation is that the picture sketched out here needs to be updated to account for transient heating episodes. During such episodes, even if a perturbation has short cooling time, it will not condense out if its radiative losses are offset by heating. A snapshot of $t_{\rm cool}$ or $t_{\rm cool}/t_{\rm ff}$ at a single moment will not reveal whether this is happening. However, as shown in Figs. 13 – 18 of Jung et al. (2022), all ROMULUS groups experience repeated episodic AGN outbursts.

Guided by these findings, we focus our analysis on *local* $t_{\rm cool}/t_{\rm ff}$ in CGM. In Fig. 2.2, we have shaded the CGM gas with local $t_{\rm cool}/t_{\rm ff}$ below 20 at the redshift of analysis, $z_{\rm a}$, translucent orange and will hereafter refer to this gas as "condensation-susceptible" CGM. The expectation is that the gas elements in this regime are susceptible to rapid cooling, or are actually in the process of doing so.

Note that although we are mainly interested in gas within the radial range $0.1 \leq {\rm R/R_{500}} \leq 1$, the translucent orange component in the panels extends inward to $0.02{\rm R_{500}}$. This is because we also want to capture cooling CGM gas that has fallen or flowed in past inner boundary but has not yet been incorporated into the BGG's ISM at $z_{\rm a}$. Specifically, we designate gas in the radial range $0.02 \leq {\rm R/R_{500}} < 0.1$ as "condensation-susceptible" CGM if it satisfies three conditions: (i) its $t_{\rm cool}/t_{\rm ff} \leq 20$ at $z_{\rm a}$; (ii) its temperature is greater than 5×10^4 K and its hydrogen number density is less than 0.1 cm^{-3} (i.e. it is not part of the BGG's ISM); and (iii) it was part of the CGM (i.e., in the region $0.1 \leq {\rm R/R_{500}} \leq 1$ at some point in the 5 Gyrs prior to the time of analysis).

Next, we mentioned above that some of the ROMULUS BGGs are star forming while others are not. We list the BGGs' star formation rates in Table 2.2, along with some of the

Halo ID	CC/NCC status	z_a	SFR [$M_\odot$/yr]	M_{500} [$M_\odot$]	M_{CGM} [$M_\odot$]	$f_{\text{condensation susceptible CGM}}$
C	CC	0.7	142.8	4.6e+13	5.3e+12	13.2%
52024	CC	0.29	73.9	1.0e+13	1.1e+12	32.0%
G1	CC	0.25	21.3	1.1e+13	1.2e+12	37.8%
49510	NCC	0.36	0.0	8.2e+12	8.7e+11	27.9%
99966	CC	0.31	22.3	3.9e+12	4.1e+11	66.7%
38182	NCC	0.44	0.0	2.8e+12	2.6e+11	74.0%
91655	NCC	0.26	0.64	1.7e+12	1.1e+11	66.9%
77876	NCC	0.25	8.6	1.8e+12	1.5e+11	88.0%

Table 2.2: Properties of the eight ROMULUS halos used in this study at z_a. CC/NCC status identifies the system as a cool core or non-cool group based on the classification criterion described in §2.0.1. SFR is the BGG's star formation rate at z_a measured within a 50 kpc sphere around the halo center. M_{500} is the total mass at z_a within R_{500}. M_{CGM} is total gas mass of CGM. $f_{\text{condensation}-\text{susceptible CGM}} = M_{\text{condensation}-\text{susceptible CGM}}/M_{CGM}$ is the fraction of CGM gas mass that meets the "condensation-susceptible" CGM criteria.

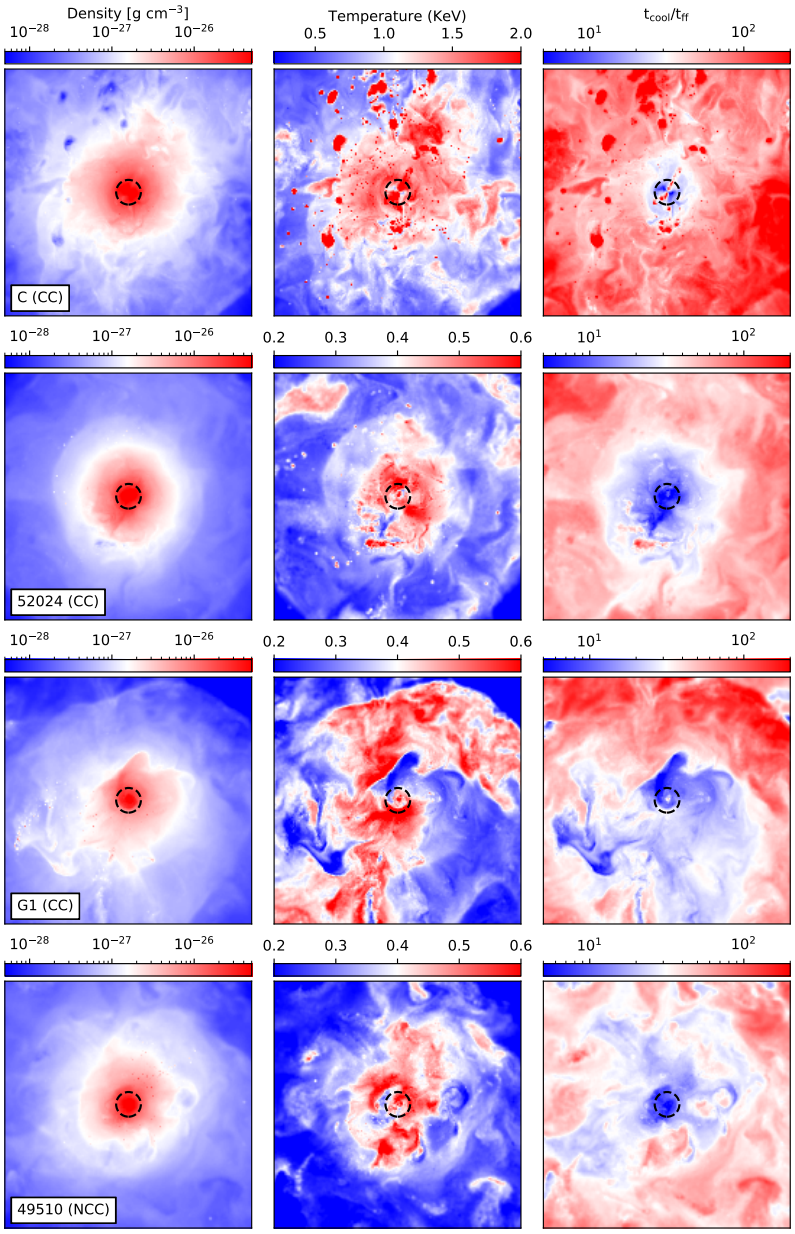

Figure 2.4: Each row shows maps of projected density, temperature and $t_{\rm cool}/t_{\rm ff}$ of the CGM in a 30 kpc slice through the halo center for the four halos in Fig.2.2, ROMULUS C (CC), 52024 (CC), G1 (CC), and 49510 (NCC) from top to bottom, at $z_{\rm a}$.Panels are $2R_{500}$ on each side. The dashed black circle shows r = $0.1R_{500}$. We only consider the gas beyond this distance as CGM. The other four halos are shown in Fig. 2.5.

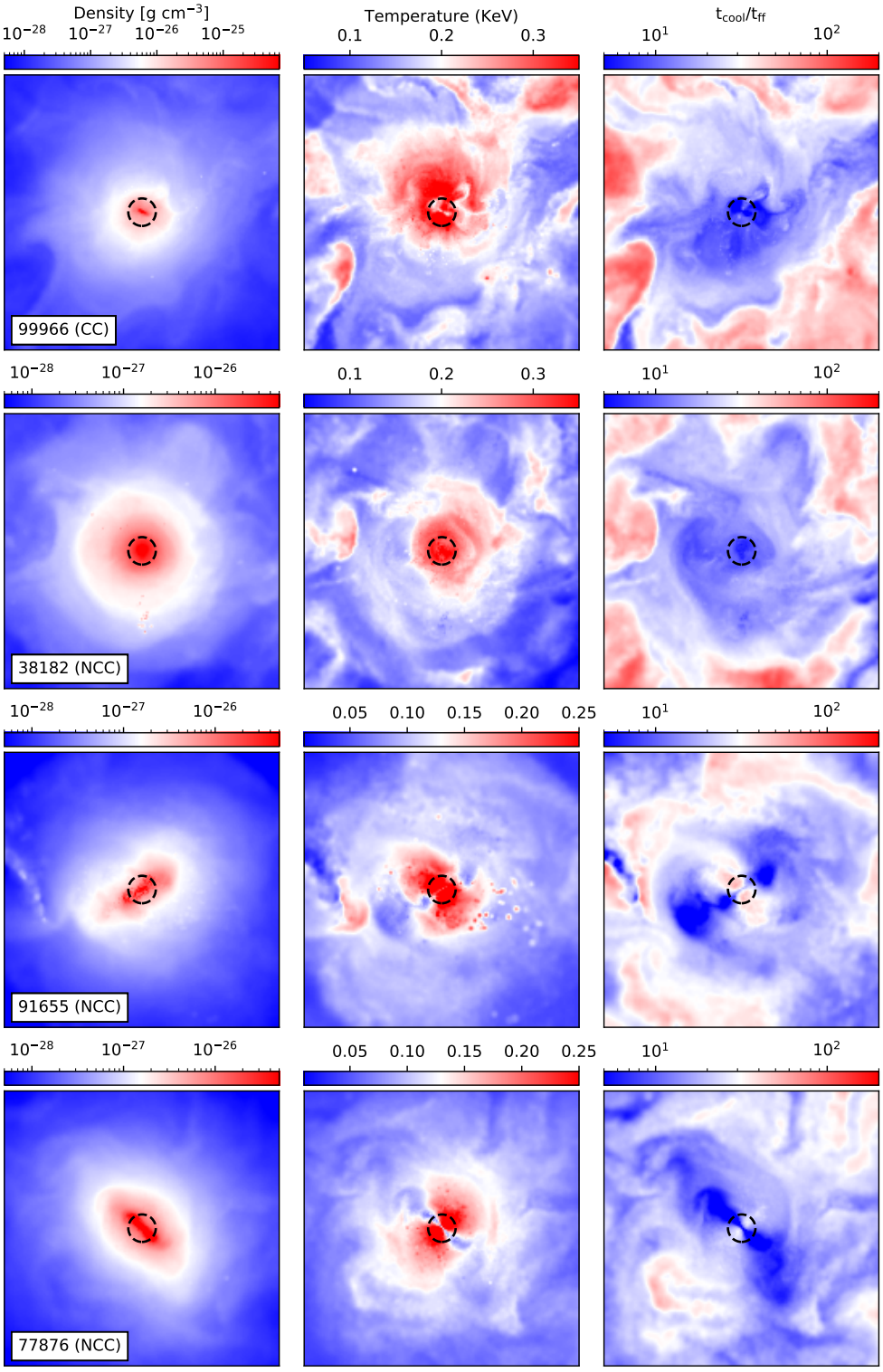

Figure 2.5: Same as Fig. 2.4 for halos 99966 (CC),38182 (NCC), 91655 (NCC), and 77876 (NCC) from top to bottom, at z_a.

other group/BGG properties including the groups' CC/NCC status. Of the eight halos we are studying in detail, four are CC and four are NCC groups. We note a strong correlation between the central group galaxy's star formation rate (SFR) and its CC/NCC status.

To understand this correlation, we focus first on $R > 0.1R_{500}$ gas in the groups. We find that the thermodynamic properties of the gas in both CC and NCC groups in this region are similar. This is demonstrated by the similarity of the median profiles for various quantities, such as $t_{\rm cool}/t_{\rm ff}$ (right panel of Fig. 2.3) as well as the scaled entropy (left panel of Fig 12 of Jung et al. 2022), in this region. These median profiles increase power-law-like towards larger radii, with nearly similar slopes in all halos, regardless of their CC/NCC status. We also looked at the fraction of the CGM that is identified as "condensation-susceptible" (last column in Table 2.2) and find that it too is not correlated with the CC/NCC status of the groups.

The main differences between CC and NCC groups are in the region $R < 0.1R_{500}$: CC groups have a greater amount of gas with $t_{\rm cool}/t_{\rm ff} < 20$ that has flowed into this region compared to NCC groups. This can be seen in the high contrast and the spread of the grey shading as well as the amount of orange-shaded gas in CC and NCC groups at $R < 0.1R_{500}$ in Fig.2.2. This deficit shows that the CGM gas in NCC groups is not cooling onto the BGGs, which would explain the BGGs' low/negligible star formation rates. In detail, the cooling and/or inflowing gas in NCC groups is heated by AGN feedback as it gets closer to the BGG. The impact of this heating is reflected, as already noted, in the groups' temperature profiles: CC groups' temperature profiles manifest a drop towards the centre while the NCC groups' temperature profiles are either flat or centrally peaked. Also, the median $t_{\rm cool}/t_{\rm ff}$ profiles of the CC groups are slightly steeper in the central region than those of NCC groups. For further discussion of CC and NCC groups see §2.0.4.

2.0.2 The nature and the origins of the CGM

To gain further insights about the CGM in our group halos, we highlight in Figs. 2.4 & 2.5 the spatial structure in the CGM of the systems shown in Fig. 2.2. From left to right, the columns show the distribution of mass-weighted average (along the line of sight) gas density, temperature, and $t_{\rm cool}/t_{\rm ff}$ ratio in slices with cross-sectional area, $2R_{500} \times 2R_{500}$, and 30 kpc thick, centered on the BGG. The black circle in each panel marks the central region of radius $0.1R_{500}$, the region we exclude when defining the CGM.

The inhomogeneous nature of the CGM in these halos is not obvious in the density panels due to projection effects. Mostly, the trends seen in the density panels are fairly typical of

the structure present in all ROMULUS groups: gas density is the highest at center and drops off with distance from the center. In all but the last row, the gas distribution is generally circularly symmetric. Nonetheless, there are indications of churning due to mergers and AGN outflows. For example, the ellipsoidal distribution in halos 91655 and 77876 in Fig. 2.5 is the result of ongoing AGN jets and ROMULUS C slice (first row of Fig. 2.4) contains numerous hot, low-density bubbles that are remnants of recent episodes of AGN feedback.

The inhomogeneities due to filamentary extensions as well as those due to AGN jets and jet-heated cavities show up prominently in the temperature (middle column) and $t_{\rm cool}/t_{\rm ff}$ (last column) panels. This includes the filament of cool gas extending to R_{500} in the first two rows of Fig. 2.5; the numerous hot, low-density AGN-inflated bubbles in the first row of Fig. 2.4; and the wide bipolar AGN outflow cones in the last two rows of Fig. 2.5[7]. We note that although half of the systems are labeled as cool core in Table 2.1, the declining gas temperature towards the group center is not evident in the panels because of the superposition of hotter gas along the line of sight.

The $t_{\rm cool}/t_{\rm ff}$ ratio in Figs. 2.4 & 2.5 ranges from a few to 200, with the blue colour corresponding to "condensation-susceptible" gas. This "condensation-susceptible" gas is ubiquitous within R_{500} of all halos in Romulus simulations and its distribution is amorphous and filamentary. Some of these filaments are due to cool inflowing gas in the plane perpendicular to the AGN outflows cones. See, for example, panels for halos 91655 and 77876, in Fig. 2.5. Such features highlight that hot outflows and cool inflows can co-exist in the same region.[8] As noted previously, we also see streams of unstable gas extending to R_{500} (see, for example, the first and second row of Fig. 2.5). These are either inflowing filaments of cold gas penetrating deep into the halos — such features are also present in the CGM of lower mass, Milky Way-like sytems as well (cf Figs. 11 and 13 of Sokołowska et al. 2018) — or tails of cool gas stripped from infalling or orbiting satellites. The latter are similar to features in Figs. 2-9 of Poole et al. (2006), who show that the tail of stripped gas initially has very different thermodynamic properties than the background medium.

We will discuss these various structures of "condensation-susceptible" gas in the group-scale halos in greater detail in section §2.0.3. We expect that some of this gas is condensing and contributing to the multiphase structure of the CGM. Additionally, orbiting and infalling

[7]See also Figs. 10 and 11 of Tremmel et al. 2017 and Figs. 2 and 3 of Chadayammuri et al. 2020 for different views highlighting the various accretion- and AGN-induced structures in ROMULUS C.

[8]These features also highlight the difficulty of heating the CGM isotropically via narrow bipolar outflows, leading to suggestions that a more effective implementation for AGN jets is to ensure that they change direction every so often (Babul et al., 2013a; Cielo et al., 2018). This is in fact how the jets behave in the ROMULUS simulations (cf. Fig. 11 of Tremmel et al., 2019).

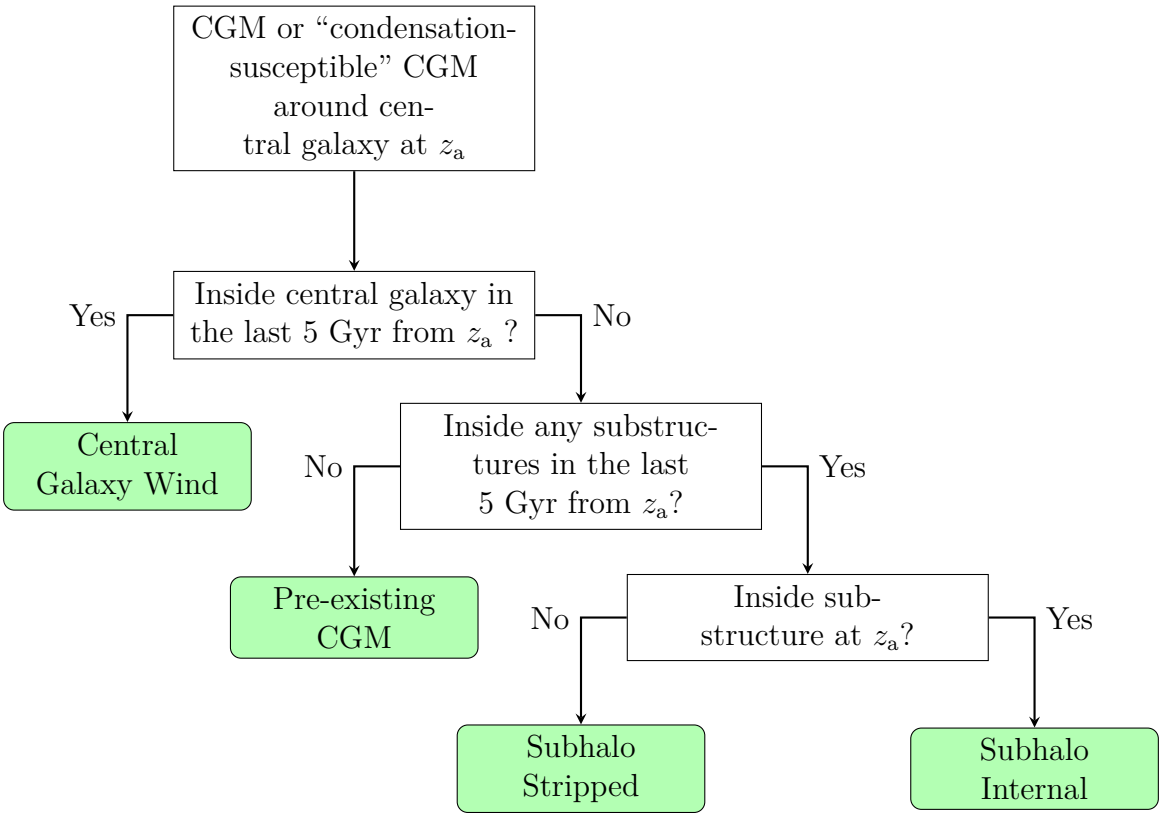

Figure 2.6: Flow chart summarising how we classify the CGM and the "condensation-susceptible" CGM (orange gas in Fig. 2.2). These are classified into 4 categories: *Central galaxy wind*, *subhalo internal*, *subhalo stripped*, and *pre-existing CGM*, based on its past history. See the text for a more detailed definition of each category.

substructures within halos engender wakes (see Kim 2007; Ghazvini Zadeh 2008; Ruszkowski & Oh 2011; Tamfal et al. 2021, and references therein) and again, it would not be a surprise if these induce strong perturbations in the background CGM, driving some of that gas to condense as well.

CGM tracking and classification

In the previous section, we inferred that the CGM gas has likely come from multiple sources. In this section, we investigate the origin of the CGM as well as the "condensation-susceptible" CGM at z_a by tracking the associated gas elements back in time. We consider four potential sources, which are as follows:

- *Central Galaxy Wind*: Gas in the region of interest that was part of the BGG's ISM (i.e. its halocentric distance was $< R_{gal}$, its temperature was $T < 5 \times 10^4$ K and

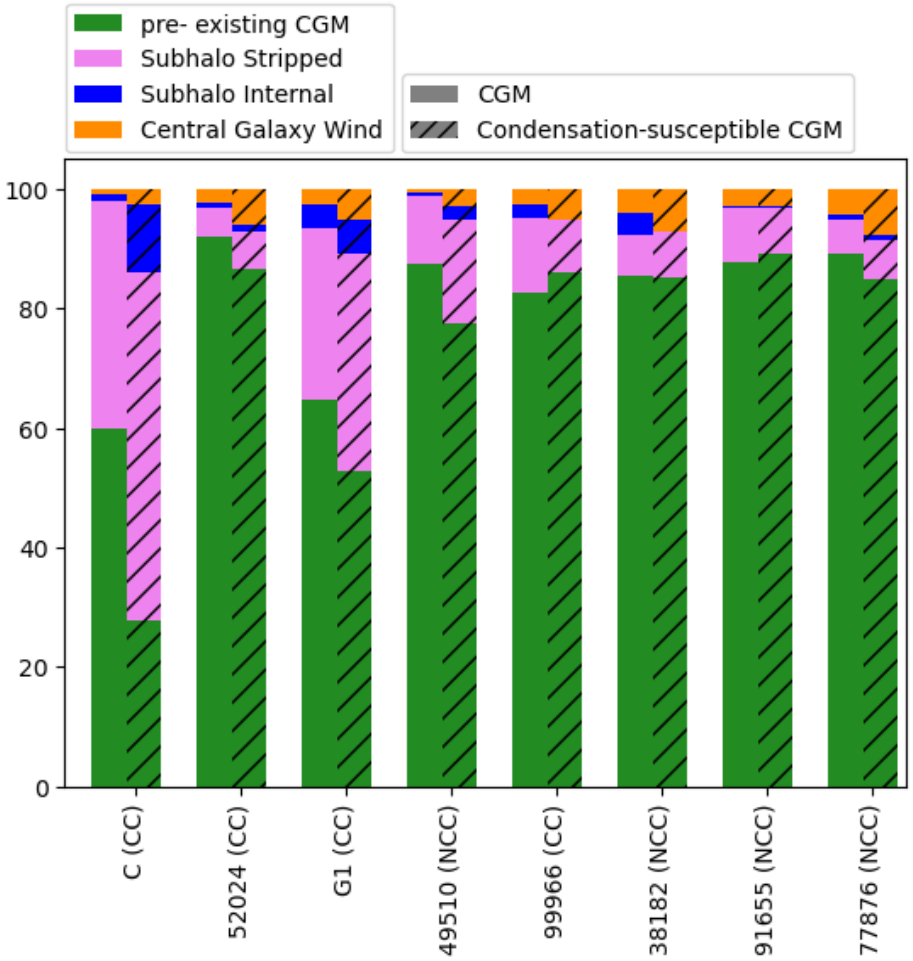

Figure 2.7: The CGM and the "condensation-susceptible" CGM at z_a are grouped into 4 categories based on their history over the preceding 5 Gyrs, as described in the text. This plot shows the fraction of CGM (solid bars) and the "condensation-susceptible" CGM (hatched bars) corresponding to the four categories.

its hydrogen number density was $n_H > 0.1\,\mathrm{cm}^{-3}$) at any point during the 5 Gyrs immediately preceding z_a. For an explanation for why we have adopted a 5 Gyrs timescale, we refer the reader to §2.0.3.

- *Subhalo Internal*: Gas in the region of interest that has been brought there by infalling subhalos and is identified by AHF as still bound to a subhalo at z_a.

- *Subhalo Stripped*: Gas in the region of interest that was bound to a subhalo at some point during the 5 Gyrs preceding z_a but is no longer bound to the subhalo at z_a. In this study, we do not concern ourselves with how the gas was removed from the subhalo. Possible mechanisms include expulsion from the subhalo via galactic winds, ram pressure stripping, and tails formed from debris of tidal interactions.

- *Pre-existing CGM*: Gas that was neither in the central galaxy nor bound to any subhalos in the 5 Gyrs preceding z_a. Gas in this category includes that which was always inside the sphere of radius $\mathrm{R}_{500}(z_\mathrm{a})$ over the 5 Gyrs window under consideration, as well as that which has accreted onto the region of interest from larger radii.

The flowchart in Fig. 2.6 summarizes our procedure for classifying the CGM and the "condensation-susceptible" CGM.

In Fig. 2.7 we use bar charts to show the fractions of the CGM and the "condensation-susceptible" CGM contributed by the four sources, for our eight ROMULUS groups. Each individual bar chart has a hatched and an unhatched side showing the results for the CGM and the "condensation-susceptible" CGM, respectively. The fractions vary from halo to halo but broadly, the halos can be grouped into two categories: those with quiescent merger histories over the 5 Gyrs period preceding the time of analysis, and those with active merger histories, including possibly major mergers prior to the start of the window. ROMULUS C and G1 halos belong to the latter category.

For both sets of halos, the dominant component of the CGM is *pre-existing CGM*. In the quiescent halos, it makes up $> 80\%$ of the CGM while in the active halos, the fraction is lower to $\sim 60\%$ while the *subhalo stripped* has grown to $30 - 40\%$ vs. $\leq 10\%$. Neither the *subhalo internal* nor the *central galaxy wind* fractions make up more than 4% generally. The low fraction of the latter component may seem surprising but we note that as per our definition of the CGM, we do not consider gas at $\mathrm{R} < 0.1\mathrm{R}_{500}$.

The low fraction of the *central galaxy wind* material in the CGM may seem at odds with the results of Hafen et al. (2019). They investigated the origins of the CGM in halos with smaller galaxies ($\mathrm{M}_* \simeq 10^6 - 10^{11}\ \mathrm{M}_\odot$) than ours and found that typically, the *central*

galaxy wind is the second most important component. However, they also note that in their low redshift sample, the *central galaxy wind* fraction decreases with increasing system mass, touching 10% in their highest mass systems. At the same time, their equivalent of our *subhalo stripped* grows to $\sim 30\%$. Our results are consistent with the extension of these trends to larger mass galaxies that we study.

Next, we consider the "condensation-susceptible" CGM. In the active halos, the two dominant fractions are still those associated with the *pre-existing CGM* and *subhalo stripped* components but which of the two dominates varies. In ROMULUS C, *subhalo stripped* makes up the largest fraction while in ROMULUS G1, *pre-existing CGM* dominates. In the quiescent systems, *pre-existing CGM* is still the dominant component and the corresponding fraction is similar to that in the CGM. The fraction of the second largest category, *subhalo stripped*, varies from being almost the same as in the CGM to slightly larger. In both sets of halos, the combined fraction of *subhalo internal* and *central galaxy wind* is generally larger for the "condensation-susceptible" CGM than the CGM, growing to as much 15%; however, as to which of the two is larger, there is no clear trend. In some halos, *central galaxy wind* is larger and in other halos, *subhalo internal* is larger.

2.0.3 Evolution of the condensation-susceptible CGM

To better understand the origin and the fate of the "condensation-susceptible" CGM at the time of analysis, we carry out a detailed particle tracking analysis. Specifically, we tracked the gas two Gyrs back and two Gyrs forward in time from z_a, allowing us to analyze its behavior over a four-Gyr period. Based on analyses in this time span, we find that the gas can be grouped into seven sub-components whose evolution is discernibly different.

In Figs. 2.8 and 2.9, we use ROMULUS G1 halo as an example to highlight these seven sub-components and illustrate how they each evolve in the period leading up to and following the time of analysis. Firstly, we direct attention to the last row in Fig. 2.8. This row corresponds to the time of analysis. This is the epoch around which our analysis pivots. In the left panel, we use the seven different colors to highlight a small subset of the gas belonging to each of the sub-components in the $t_{\rm cool}/t_{\rm ff}$ vs. radius plane. The main purpose of Figs. 2.8 and 2.9 is to clearly show the evolutionary trends. It is for this reason that we do not color all the gas because that results in a confusing plot with a hodgepodge of overlapping multi-coloured points. To further minimize the overlapping and enhance clarity, each subsamples were also extracted from targeted radial ranges. To that end, the distributions of the different colored points in the last row of Fig. 2.8 do not reflect either the mass fractions or the actual radial

distributions of the corresponding sub-components.

- The `cyan` points sample the sub-component of the *pre-existing CGM* that have a cooling flow-like behaviour.
- The `yellow` and `red` points sample sub-components of the *pre-existing CGM* that have been perturbed. We identify this gas by a sharp decrease in its $t_{\rm cool}/t_{\rm ff}$ within 0.5 Gyrs prior to z_a. We observe two distinct evolutionary patterns in this gas that correlate with the magnitude of the change in density. The yellow points correspond to gas with a significant increase in density, while the red points correspond to gas with a mild density change.
- The `lime-green` points sample gas that is moving outward at the time of analysis and has been doing so coherently for at least 0.5 Gyrs. Since this gas has never been part of the central galaxy, we treat it separately from the *central galaxy wind*.
- The `lavender` and `blue` points are a subset of *subhalo stripped* and *subhalo internal* gas, respectively.
- The `orange` points show a subset of the gas from the *central galaxy wind* category.

For completeness, we note that the grey shading and the purple curve shows, as before, all the gas in the halos and the median $t_{\rm cool}/t_{\rm ff}$ profile for the hot gas.

Although we do not show all the gas belonging to these categories, we have assessed all of the "condensation-susceptible" CGM gas in all eight halos listed in Table 2.1 and found the same evolutionary patterns across all the halos.

In the subsections below, we discuss the evolution of each of the sub-components in more detail but first, we briefly explain the organization of the rest of panels in Figs. 2.8 and 2.9. As noted, the bottom row in Fig. 2.8 corresponds to redshift of analysis, $z_{\rm a}$. The preceding three rows show the distribution of the sampled gas at three epochs prior to $z_{\rm a}$ while the four rows in Fig. 2.9 show the results at four epochs post-$z_{\rm a}$. The left panels show the changing gas distribution in the $t_{\rm cool}/t_{\rm ff}$ vs. radius plane and the right panels show the spatial distribution of the coloured points.

`Orange`: Central galaxy wind

We first consider the *central galaxy wind* sub-component of the "condensation-susceptible" CGM at $z_{\rm a}$. A sample of gas from this sub-category is colored `orange` in Figs. 2.8 & 2.9.

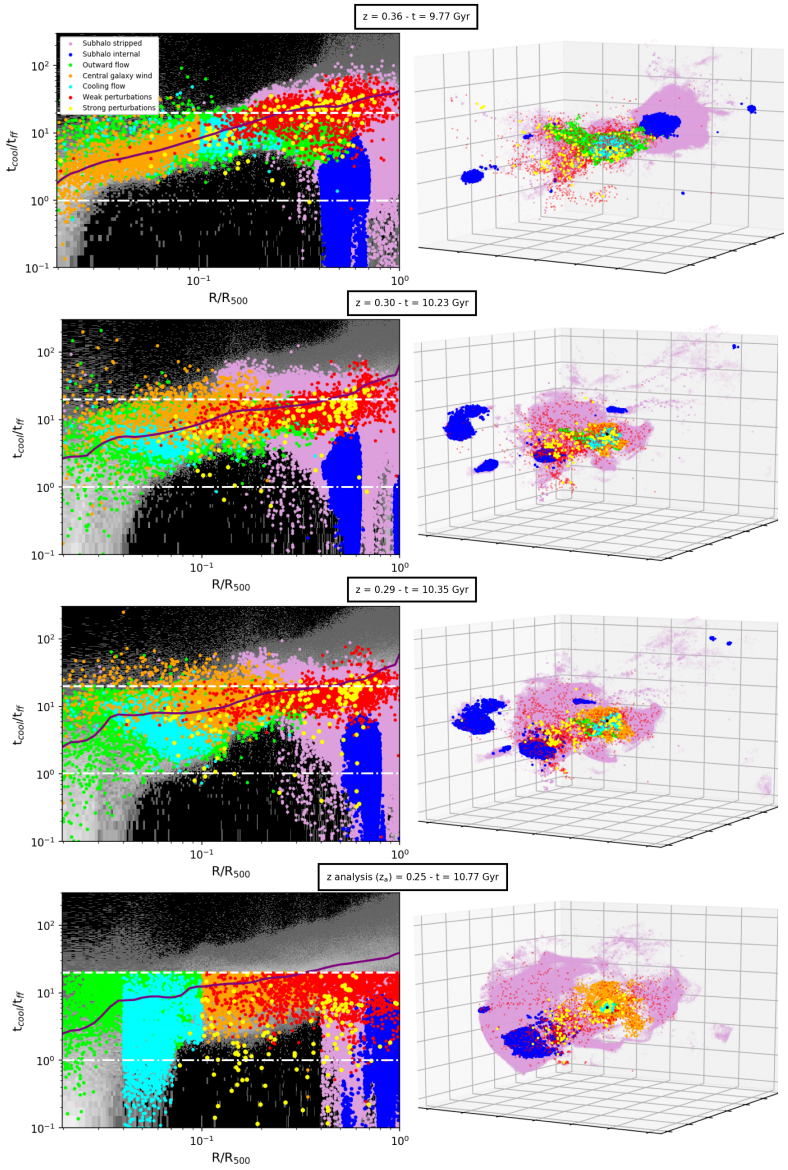

Figure 2.8: The "condensation-susceptible" at $z_{\rm a}$ (last row) comprises seven sub-components whose evolution is discernibly different (see text for details). Here, we use ROMULUS G1 group to illustrate how these sub-components evolve. At $z_{\rm a}$, we sub-sample gas associated with each sub-component; plot them in different colors (see legend) and follow this gas backward and forward in time. The first three rows show the state of the sub-components at three earlier epochs. The left column show the gas in the $t_{\rm cool}/t_{\rm ff}$ vs. radius plane; the right columns show its 3D spatial distribution.

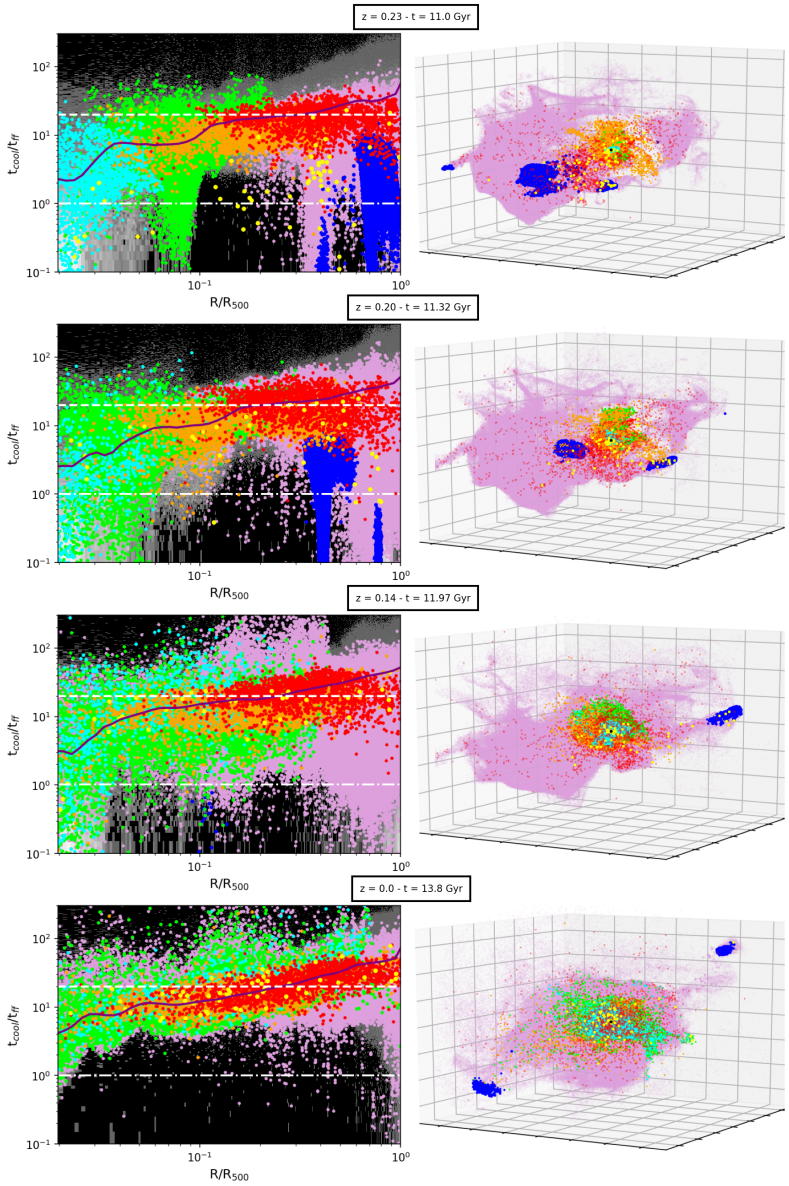

Figure 2.9: This figure is the same as Fig. 2.9 except that the plots correspond to four epochs following z_a. See caption for Figure 2.8 and the text for details.

This is gas that was part of the BGG's ISM and then expelled from the BGG after being heated by the AGN at some point during the preceding five Gyrs. The first row in Fig. 2.8 shows the state of this component roughly a gigayear before $z_{\rm a}$. The gas is concentrated within the central core. This is apparent in the left panel. In the right panel, the central concentration of `orange` points is obscured by the overlapping points associated with the other components. As the subsequent panels show, this component expands outward. The right panels show this gas breaking out of the central region. As it does so, it shocks, mixes, and about a gigayear after $z_{\rm a}$, essentially becomes part of the CGM. Thereafter, it evolves like the CGM. It is susceptible to perturbations and cooling but mostly it remains distributed about the median curve for hot CGM.

`Blue`: Subhalo internal and `Lavender`: Subhalo stripped

Next, we consider the sub-components identified as *subhalo internal* and *subhalo stripped*. The former is gas with $t_{\rm cool}/t_{\rm ff} < 20$ that, at $z_{\rm a}$, is bound to subhalos while the latter is gas that was removed from the subhalos in the 5 Gyrs preceeding $z_{\rm a}$. The `blue` and `lavender` points correspond to a subset of gas elements comprising these two categories.

Typically, subhalos and their gaseous tails (`blue` and `lavender` points) collectively enter the region of interest from the right in the left panels and move towards the center. However, the process is not unidirectional. Over the time period shown in Figs. 2.8 and 2.9, many subhalos reach their pericenters and travel outward in radius. A small number of satellites, typically the more massive ones, merge with central galaxy and contribute their cold gas to the BGGs. This is one way the BGGs acquire fresh cold gas and rejuvenate (e.g., Olivares et al. 2022; Lagos et al. 2022; Jung et al. 2022).

All orbiting subhalos eventually lose most of their gas. Visualizing this evolution in the left panels is not straightforward, which is why we also plot the 3D spatial distribution of the gas in the right panels. Consider, for example, the first three rows of Fig. 2.8. One can see a number of satellites (`blue` knots), make out their orbital paths, and observe gas loss in the form of `blue` elongations transitioning to `lavender` tails. The gas removed from the subhalos does not immediately detach from its source substructure nor does it immediate stop following the orbital trajectory it was on when stripped. It takes time for the gas to slow down and detach; in the meantime, the gas manifests as streams trailing the satellites.

After detaching, some of the gas cools, loses angular momentum due to drag and eventually falls to the center. This is more likely to happen when the satellite's initial pericenter is close to the BGG. And, this gas too contributes to the the re-emergence of gaseous and star

Halo ID	CC/NCC status	z_a	Cooling flow	Strongly perturbed	Weakly perturbed	Outward flow	Other
C	CC	0.7	70.55%	1.3%	5.60%	14.6%	8.70%
52024	CC	0.29	67.46%	1.4%	9.06%	14.2%	7.80%
G1	CC	0.25	29.78%	0.25%	30.26%	29.9%	9.97%
49510	NCC	0.36	33.80%	0.27%	25.88%	32.32%	8.70%
99966	CC	0.31	56.10%	0.89%	12.03%	23.08%	7.9%
38182	NCC	0.44	40.71%	0.11%	11.77%	36.77%	10.7%
91655	NCC	0.26	32.32%	0.1%	18.10%	35.02%	14.5%
77876	NCC	0.25	48.62%	0.02%	13.20%	31.30%	7.1%

Table 2.3: The table shows the fraction of *pre-existing CGM* that follows the four different evolutionary behaviours. In previous figures, the isothermal cooling flow, strongly and weakly perturbed gas, and outward flow are shown in `cyan`, `yellow` and `red`, and `lime-green`. Fractions of *pre-existing CGM* that are not following any of these behaviours are shown in the last column.

forming disks/rings in the BGGs (e.g., Olivares et al. 2022; Lagos et al. 2022; Jung et al. 2022). A larger fraction of the removed gas, however, shocks, heats up, mixes, and becomes part of the CGM.

We have determined the "mixing time" of gas from individual subhalos. The mixing time is defined as the time it takes for the entropy of 90% of the gas removed from subhalos, and which is at $R > 0.1R_{500}$, to reach an entropy level of more than 80% of the median entropy at all radii. This time is measured from the moment when the subhalo crosses R_{500}. In Fig. 2.10 we show this mixing time as a function of the free-fall time at R_{500} (i.e., t_{mix} / $t_{ff,500}$) against the ratio of the subhalo mass to its host halo mass M_{500}. Both subhalo and halo mass are computed at the time subhalo is at R_{500}. To make this plot, we selected at least two subhalos in each halo (three, in the case of more massive halos) in a manner that reflects the range of subhalo-to-halo mass ratios in our simulations. We find that on the whole t_{mix}/ $t_{ff,500}$ increases with $M_{subhalo}/M_{500}$, albeit with large scatter. Nevertheless, most of the subhalo gas tends to mix within 5 Gyr. For this reason, when categorising the CGM we consider gas removed from a subhalo > 5 Gyr prior to z_a as *pre-existing CGM*. For consistency we use the 5 Gyr look back window for all other categories as well.

Pre-existing CGM

The final category is *pre-existing CGM*. The gas in this category exhibits four broad evolutionary patterns. A subset of the gas from each of these four patterns are shown in Figs. 2.8 and 2.9 as `cyan`, `red`, `yellow`, and `lime-green` points. In describing their behaviour, we will refer to Figs. 2.8 and 2.9 as well as Fig. 2.11. Fig. 2.11 shows the radius, entropy, density,

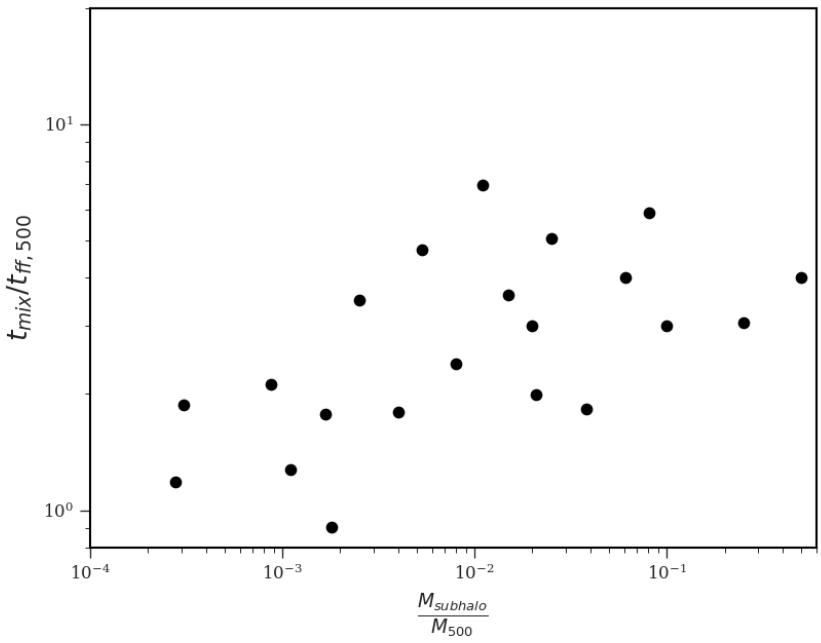

Figure 2.10: The amount of time that it takes for "stripped" gas from a substructure to mix with CGM. The y-axis shows mixing time over free-fall time at R_{500}. The x-axis shows the substructure mass relative to its host halo's mass, M_{500}. The scatter aside, the mixing time of the removed gas increases with mass fraction.

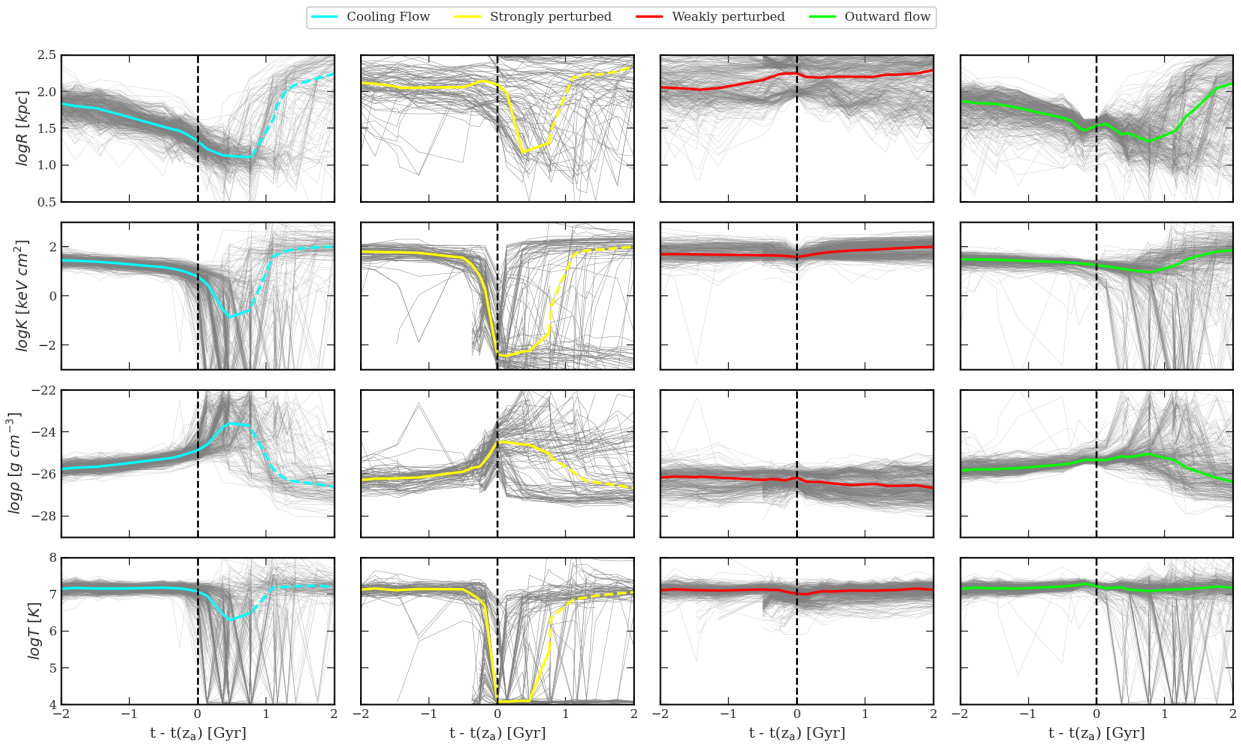

Figure 2.11: "condensation-susceptible" gas in *pre-existing CGM* category exhibits four different types of evolutionary behavior. This plot shows the thermodynamic history of the associated gas. Each column shows results for each evolutionary behavior. **First column:** gas that demarcates the isothermal cooling flow. **Second column:** gas that has been subjected to strong perturbations. **Thirds column:** gas that has been subjected to weak perturbations. **Fourth column:** initially inward flowing CGM that got turned around and at the time of analysis is moving outward. The rows show radius, entropy, density, and temperature, from top to bottom. We follow the gas for two Gyrs before and after the analysis time t($z_{\rm a}$), shown by a black dashed line. Solid coloured lines show the median, and individual tracers are shown in the faint grey line. The dashed coloured line shows the median of the gas that is returned to the CGM via galactic outflow.

and temperature of the sampled gas belonging to the four sub-components as a function of $\Delta t \equiv [t - t(z_a)]$. The coloured lines show the median time evolution of the quantities, and that of the individual tracer trajectories are shown as thin grey lines in the background. Each sub-component is represented by the same colour in Fig. 2.11 as in Figs. 2.8 and 2.9. And, while these plots are specific to ROMULUS G1, we observe similar trends in all the halos. The fraction of the *pre-existing CGM* in each of the four components, on a halo by halo basis, is given in Table 2.3.

`Cyan`: Cooling flow

Firstly, we describe the evolution of the gas characterized by the `cyan` points. The first row of Fig. 2.8 shows the state of the sampled gas ∼1 Gyr before z_a. The `cyan` points are distributed around the median t_{cool}/t_{ff} of hot CGM (purple line). Over time, this gas remains clustered about this median line as it flows inward.[9] This is clearly demonstrated by the cyan curve in the top left panel of Fig. 2.11. This is an example of an isothermal cooling flow (cf Nulsen, 1998) in that the temperature of this subcomponent does not change much leading up to z_a and even shortly thereafter (see bottom left panel in Fig. 2.11). The entropy of the gas is, however, dropping (see the second panel in the first column of Fig. 2.11) and the flow is radiatively losing energy. With respect to the temperature, compressional heating is largely balancing radiative losses.

During the above phase, the inward flow is subsonic, similar to that seen in the simulation discussed in Lewis et al. (2000). Also, as described in studies like those of Sokołowska et al. (2018); Stern et al. (2019, and references therein), it is mainly localized to filamentary structures threading the inner halo (as apparent in the third row of Fig. 2.4) and therefore, does not involve all of the gas at any radius. The fraction of gas in the cooling flow component in each of the eight halos is listed in Table 2.3. The most apt description of the flow is a revised version of that by Theuns (2003): a slowly-moving filamentary emulsion of gaseous blobs with slightly different densities and temperatures [than the median] that is cooling isothermally and slipping past the other components comprising the CGM.

Only after the gas enters the galaxy (i.e., $R < R_{gal}$) does its time evolution bifurcate. Most of the gas starts to cool rapidly — its density increases rapidly and both its entropy and temperature drop steeply — and it becomes part of the BGG's ISM. A small fraction, however, is halted and turned around by the outflowing galactic wind before rapid cooling happens (cf §2.0.3). The latter returns to the CGM.

[9] The behaviour in the entropy-radius plot (not shown) is similar. As the gas moves inwards, it remains clustered about the median entropy profile of the hot gas, which decreases towards the centre.

The gas that settles in the central galaxy has non-zero angular momentum and is the dominant source of the gas leading to the re-emergence of the gaseous disks seen in Jung et al. (2022). A fraction of this gas accretes onto the SMBH or fuels star formation, and a fraction is expelled as wind back into the CGM and eventually mixes with the ambient CGM. The `cyan` points in the last three panels of Fig. 2.9 correspond to both the pushed-back and the expelled gas; we preserve their colors to show that they were part of the cooling flow sub-component at $z_{\rm a}$. And in Fig. 2.11, the median properties of *this* gas is shown by dashed lines. The dispersal of this gas to large radii is clearly shown in the top left panel.

In Table 2.4, we show the fraction of the cooling flow that contributes to the star formation or accretes onto the SMBH. Not surprisingly, the fraction is correlated with the halo's CC/NCC status; also, a larger fraction at $z_{\rm a}$ corresponds to a larger SFR. We discuss these relationships further in Section 2.0.4.

`Yellow` and `Red`: Externally perturbed gas

Next, we examine the sub-components of the *pre-existing CGM* represented by the `yellow` and `red` points in Figs. 2.8 & 2.9. Both are examples of CGM gas that has been subjected to density perturbations. Various physical processes, including shocks, gravitational focusing and turbulence due to orbiting substructures, as well as shocks and turbulence caused by AGN- and SNe-powered galactic outflows, can (and do) induce density perturbations in the CGM. The forward evolution of these perturbations depend on whether locally they can cool efficiently, which in turn depends on their amplitudes (Choudhury et al., 2019; Das et al., 2021).[10] The `yellow` points sample the gas that experiences strong perturbations while the `red` points sample the gas that is only mildly perturbed. We characterize the perturbations as weak or strong on the basis of the increase in density (yellow and red curves in the third row of the second and third columns of Fig. 2.11) leading up to the time of analysis. The median of the `yellow` gas increases in density by a factor of $\sim$30 while the median of the `red` gas registers only a slight increase, and only for a very short time.

Before discussing the behaviour of the density perturbations in more detail, it is important to address a potential concern that the `yellow` and `red` particles are not the products of physical processes but of numerical noise, especially given the small fraction of mass involved (cf. columns 5 and 6 of Table 2.3). We check this in two ways: (i) Strictly speaking, a single tracer SPH particle is a non-independent resolution element in that although the particles carry physical properties, such as mass, density, volume, velocity, temperature, etc., the

[10] And in the case of simulations, also on whether their cooling lengthscale ($l_{\rm cool} = C_s t_{\rm cool}$) is resolved (Mandelker et al., 2021).

physical information about the fluid and the flow is actually carried by a cloud of particles comprising the particle and its nearest neighbours (Agertz et al., 2007a; Sigalotti et al., 2021). We therefore compare the cooling time of individual tracer particles to the average $t_{\rm cool}$ of a fluid element comprising all the particles within the tracer particle's SPH kernel. We find that for 70% of the tracer particles, their neighborhood's average $t_{\rm cool}$ is either statistically the same as the particle's cooling time or smaller (i.e. the neighbourhood is collectively cooling similarly or faster). This strongly suggests that majority of our yellow and red particles are not random, isolated points. They are part of a region that itself is prone to condensation. (ii) Additionally, we examine the spatial positions of the `red` and `yellow` particles in our halos. Fig. 2.12 shows that these tracers of perturbed *pre-existing CGM* are mainly found in and around streams of gas from the subhalos (shown as `lavendar` points), lending support to the idea that the main sources of the perturbations are the wakes and tails of orbiting subhalos. This was already suggested by the distributions of the `yellow` and `red` points in the right column of Figs. 2.8 and 2.9.

Focusing first on the strong perturbations, we note that in Figs. 2.8 & 2.9, the `yellow` points are sampling gas that starts at the median line. At $\Delta t \approx -0.3$ Gyr, the gas is perturbed mainly by the satellites and experiences a strong density enhancement with respect to its local background. In the second row of Fig. 2.8 a cluster of `yellow` points forms close to a satellite (`blue` points). This clustering can also be seen in the right panel (3D plots) overlapping the satellite and its gaseous tail. These perturbations cool rapidly; the temperature of the gas drops — from $\sim 10^7$ to $\sim 10^4$ K — and so does its entropy as well as its $t_{\rm cool}/t_{\rm ff}$ (see the panels in the second column of Fig. 2.11). By $z_{\rm a}$, $t_{\rm cool}/t_{\rm ff}$ of all the perturbations is below 20 (dashed line), and some are even below 1 (dash-dotted line). Eventually, all of these perturbations end up below $t_{\rm cool}/t_{\rm ff} = 1$.

Thereafter, some of the condensations fall in, some ride the satellites' wake for $\sim 1-2$ Gyrs before detaching and falling to the center, and some appear to be in stable orbits (see the first three 3D panels in Fig. 2.9 as well as the individual tracks in the first panel of the second column of Fig. 2.11).

Most of the infalling gas joins the BGG's ISM. We will refer to this cold infalling gas as "precipitation". Once in the BGG, some of precipitation contributes to star formation and fueling the SMBHs, like the cooling flow gas, and some is expelled back to the CGM, as illustrated by the yellow points in the last two panel of Fig. 2.9.

A more detailed analysis shows that while the substructures are the main source of large-amplitude density perturbations in the CGM of galaxies in cosmological simulations, the presence of the `yellow` points in the same region as the `orange` wind points in the left panel

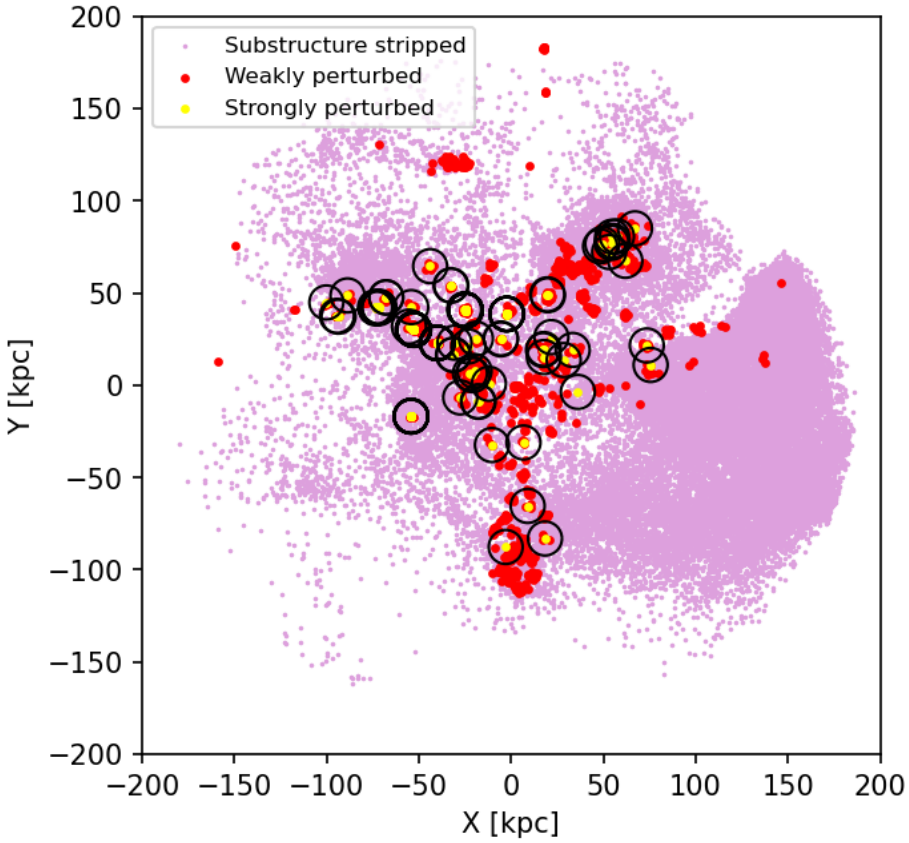

Figure 2.12: This 2D plot shows the position of the perturbed gas, shown as `yellow` and `red` points, and the subhalo stripped gas, shown in `lavender`. The black circles denote the location of the neighbouring particles within the SPH kernel of each `yellow` point. The plot demonstrates that strongly perturbed gas is consistently surrounded by gas that has been removed from subhalos and weakly perturbed CGM.

of third and fourth rows of Fig. 2.8 also suggests that outflows can perturb the gas, as seen previously in idealized simulations (cf. Prasad et al., 2015).

Next, we consider the `red` points. Like the strongly perturbed gas, this gas component is also initially distributed about the median purple line and it too is perturbed by the satellites. This can be seen in the last 3D plot in Fig. 2.8 and the first and second 3D plots of Fig. 2.9, where `red` points are in the tail of `blue` substructures. However, unlike the strongly perturbed gas, most of this gas is swept up and carried along in the satellite wakes. Additionally, while the $t_{\rm cool}/t_{\rm ff}$ of these perturbations initially drop and even fall below our threshold of 20 by $z_{\rm a}$, unlike the strongly perturbed gas, they do not enter a runaway cooling state. Instead, their ratios eventually bounce and return to the median value for the hot gas. This bounce is visible in going from the last row of Fig. 2.8 to the first row of Fig. 2.9.

Given the findings of Mandelker et al. (2021), one cannot help but wonder whether these perturbations are physically stable or whether they are stable due to numerical reasons? Mandelker et al. (2021) argue that under certain conditions, small-amplitude perturbations will not be able to cool and condense if their cooling lengths ($l_{\rm cool} = {\rm c_s t_{cool}}$) are not resolved. We tested whether this was the case and found that most of the weak perturbations' cooling lengths are in fact resolved.

Another possibility is that only perturbations whose local $t_{\rm cool}/t_{\rm ff}$ ratios drop below unity truly cool and condense (Voit, 2021). We have tracked the evolution of the weak perturbations and find that this does indeed appear to be the case. In fact, $\geq$ 95% of the perturbations bounce before reaching $t_{\rm cool}/t_{\rm ff} = 2$. And, while we find that $\sim$1% of perturbations drop below unity before bouncing, the $l_{\rm cool}$ of nearly all of these is not resolved.

To understand the "bouncing" perturbations better, we examine their properties more closely. The first panel of the third column of Fig. 2.11 shows that the gas is first swept up in satellite wakes roughly a Gyr prior to t($z_{\rm a}$). From this point on, the overall density of the gas (third row, third column of Fig. 2.11) decreases steadily but gently, except for a brief period of compression at t($z_{\rm a}$). In the second panel, we note that the gas entropy leading up to t($z_{\rm a}$) increases, albeit slightly. At t($z_{\rm a}$), we witness a slight dip, and then it continues to rise. Cooling time ($t_{\rm cool}$) too behaves similarly. Simply put, we do not see the perturbations' cooling times shortening. Then why does $t_{\rm cool}/t_{\rm ff}$ drop?

Most of the studies investigating $t_{\rm cool}/t_{\rm ff}$ of gas perturbations assume that the ratio varies due to decreasing $t_{\rm cool}$, but in our case, this is not what is happening. When weak perturbations are swept up in the wakes and carried to larger radii, their free fall times ($t_{\rm ff}$) increase. The downward trajectory of $t_{\rm cool}/t_{\rm ff}$ is due to the denominators becoming larger. The perturbations are not cooling and therefore, they do not condense. When the

gas detaches from the wake, it mixes with the ambient medium and reverts to the median line. We observe this as $t_{\rm cool}/t_{\rm ff}$ bouncing. This demonstrates that even looking only at the local $t_{\rm cool}/t_{\rm ff}$ of gas perturbations without tracking its history can result in an erroneous conclusion.

Finally, we note that while the high resolution of the Romulus simulations makes it possible to *begin* to see the effects of the perturbations in the CGM, what we observe is very likely only the tip of the iceberg. Much more improvement in resolution is needed to fully study the phenomena and the impact of complex interplay between processes like turbulence compression and turbulent diffusion (see, for example, Rennehan et al., 2019; Rennehan, 2021, and references therein); depositional growth via mass flow onto the cloud due to radiative cooling and mixing-induced cooling; and growth via coalescence (see Faucher-Giguere & Oh, 2023).

Outward flow

Lastly, we consider the fourth sub-component of the *pre-existing CGM*, shown in `lime-green` in Figs. 2.8 & 2.9. This is gas that has not been part of the BGG's ISM in the past 5 Gyrs and at $z_{\rm a}$ it is moving radially outward. This outward flowing gas is treated separately from the *central galaxy wind* because by our definition, the latter is essentially outflowing ISM.

As seen in the last column of Fig. 2.11, this gas was initially moving inward via either the cooling flow or the rapidly cooling, infalling precipitation prior to $z_{\rm a}$. However, before it becomes part of the BGG's ISM, it is pushed back outward into the CGM by AGN outflows. This reversal appears as a change of slope at $\Delta t = 0$ in the top right panel of Fig. 2.11. After $z_{\rm a}$, this component essentially behaves like the *pre-existing CGM*.

The total amount of gas involved and its outward velocity varies from halo to halo. It is generally more pronounced in lower mass halos but is also affected by the timing and the strength of the last AGN outburst.

2.0.4 Cool core vs. non-cool core groups

At the end of §2.0.1 we discussed the properties of CC and NCC groups and indicated that the $r > 0.1R_{500}$ gas properties of these groups are very similar. This similarity is also evident in the evolutionary behavior of the "condensation-susceptible" CGM analyzed in this section. The evolution of the seven patterns discussed above is largely the same regardless of whether the group is CC or NCC. The main differences are in the mass fraction of *pre-existing CGM* that is cooling via cooling flow and precipitation, and directly contributing to the fueling

Halo ID	CC/NCC status	$z_{\rm a}$	Cooling flow	Precipitation	SFR [$M_\odot$/yr]
C	CC	0.7	73.5%	28.2%	142.8
52024	CC	0.29	61.7%	17.1%	73.9
G1	CC	0.25	30.1%	25.0%	21.3
49510	NCC	0.36	2.1%	3.1%	0.0
99966	CC	0.31	71.5%	57.8%	22.3
38182	NCC	0.44	0.03%	0.0%	0.0
91655	NCC	0.26	1.2%	3.1%	0.64
77876	NCC	0.25	14.1%	4.1%	8.6

Table 2.4: Cooling flow and precipitation are the two main channels through which gas in the *pre-existing CGM* cools. The table shows what fraction of gas that cools via these processes contributes to the star formation of the central galaxy or accretes to the SMBHs. The last column is the SFR of the central galaxy in each halo. The NCC groups generally have much less contribution to SF from cooling gas and, also have, much smaller SFR compared to the CC groups.

star formation and the central SMBH when reaching the halo center. These are listed in Table 2.3 and 2.4.

In ROMULUS groups, 30-50% of the "condensation-susceptible" *pre-existing CGM* in NCC groups behaves like cooling flow. In CC groups, this fraction increases to 60-70%. G1, however, is an exception to this rule. A more detailed analysis shows that G1 experienced a merger just before the start of our two Gyr window. It is just settling into the CC state and this transition is affecting its properties.

The next most important subcomponent of the *pre-existing CGM* in the NCC group is the outward flow, comprising $\geq$ 35%. This subcomponent moves outward because of its interaction with winds and AGN outflow. One of the highest fractions of outward flow belongs to halo 91655, which is undergoing an AGN outburst at $z_{\rm a}$, as seen in last row of Fig. 2.4. The gas mass fraction for this subcomponent is lower in CC groups ($\sim$ 20%), likely because CC groups have lower AGN activity at $z_{\rm a}$ than NCC groups.

As for the strongly perturbed (condensing) component, CC groups have $\sim$ 10 times more (in mass fraction) compare to the NCC groups, with G1 again being an exception. We note, however, that the fraction of condensing gas is, in general, small compared to all other components; this is expected since it is a phenomenon that requires ultra-high resolution to be resolved (Hummels et al., 2019; Das et al., 2021; Mandelker et al., 2021). In these ROMULUS simulations, we are only just beginning to see the "tip of the iceberg" of this subcomponent.

All in all, an average of 65% of "condensation-susceptible" gas is flowing inwards in CC systems (again G1 is an exception), while in NCC it is $\sim$ 40%. Cooling flow and precipitation are the two main channels through which gas in the *pre-existing CGM* cools. Table 2.4 shows what fraction of gas that cools via these two cooling channels contributes to fueling star formation or SMBH when it reaches the halo center (we have not distinguished between fueling star formation or SMBH in this table). A much higher fraction of the gas that cools via the cooling flow and precipitation in CC groups ($\sim$65% and $\sim$30%) contributes to star formation than NCC ($\sim$3-4% and $\sim$3%). Correspondingly, the SFR in CC systems is much higher. In two NCC systems, halos 38182 and 49510, there is no detectable star formation activity.

However, not all of the cooling gas reaches the BGG. In cosmological simulations, AGN outflows and stellar winds play an essential role in preventing the overcooling of the gas and the formation of higher than observed stellar mass. This is readily apparent in Figure 9 of Tremmel et al. (2019). The star formation history in galaxy groups closely follow the ups and downs in SMBH activity. Every increase in the SMBH activity is correlated with a

decrease in the SFR, and conversely, when SMBH activity is quiescence, the SFR increases.

2.0.5 Summary and Discussion

Summary

We begin our discussion by summarizing our main findings. The aim of our study is to investigate the origin and the evolution of the CGM around massive central galaxies in group-scale halos. In the present study, we define the CGM as all gas in the radial zone $0.1 \leq \mathrm{R/R_{500}} \leq 1$, and focus our attention on a 5 Gyrs time segment during which the region under consideration is not disturbed by massive satellites. A summary of our main findings is as follows:

(a) The CGM of massive galaxies in the ROMULUS simulations is far from uniform. It is threaded by filaments of inflowing cooling gas and gaseous tails from satellites. It also has localized patches of rapidly cooling gas, regions of shocked gas, conical bipolar outflows linked to active AGN outbursts, and hot, low-density cavities inflated by recent AGN outflows. Not surprisingly, the gas at any given radius consists of a spectrum of coexisting gas phases whose cooling times and $t_{\rm cool}/t_{\rm ff}$ ratios typically vary by ~ 2 orders of magnitude.

(b) We investigate the origin of the CGM in the ROMULUS groups halos and identify four key "sources: *central galaxy wind*, *subhalo internal*, *subhalo stripped*, and *pre-existing CGM*. The fraction of gas from each of these categories varies from halo to halo. However, in all the halos, the first two make up only a minor fraction of the CGM while the largest contribution comes from the last category. In halos with quiet merger histories over the time period under consideration, $> 80\%$ of the gas is associated with *pre-existing CGM* and $\leq 10\%$ is associated with *subhalo stripped*. In halos with a high rate of minor mergers or major mergers before the start of the analysis window, the *subhalo stripped* fraction rises to $30 - 40\%$ while the *pre-existing CGM* drops to $\sim 60\%$.

(c) We find no significant difference in the CGM properties of the CC and NCC groups on scales $\mathrm{R/R_{500}} > 0.1$. For instance, their scaled gas temperature and entropy profiles are similar. The differences between the two are in the central region. CC groups have temperature profiles that drop towards the center. They also have a greater amount of gas flowing/falling onto the BGGs and a higher central star formation rate. We find that all ROMULUS groups cycle through the CC and NCC states, with the former typically occurring between AGN outbursts.

(d) We find that CGM is also very dynamic. Apart from undergoing repeated heating and cooling cycles, it is also subject to ongoing weak-to-strong density perturbations. However, unlike idealized simulations where the main sources of the perturbations are shocks and turbulence caused by AGN outflows, in *realistic* cosmological systems, the dominant sources of the perturbations are wakes, debris of tidal interactions, and stripped gas tails of orbiting satellites. We observe some of these perturbations forming cold condensations.

(e) With respect to the condensing gas, one of our key findings is that the formation of condensations is *not* restricted to regions in the halo where the median hot gas $t_{\rm cool}/t_{\rm ff}$ ratio falls below 10 or 20 or even 30. At the same time, we also observe regions where the median $t_{\rm cool}/t_{\rm ff}$ ratio is below a threshold with very little gas condensing out. This suggests that the median value of $t_{\rm cool}/t_{\rm ff}$ of the X-ray emitting gas is not the main measure of the CGM's susceptibility to condensation. In a realistic cosmological environment, the amplitude of the density perturbations is just as, if not more, important.

(f) We focus on local regions within the CGM with $t_{\rm cool}/t_{\rm ff} \leq 20$ and investigate their evolution. In choosing this criterion, we are guided by Choudhury et al. (2019) who suggest that local density perturbations with $t_{\rm cool}/t_{\rm ff} \leq 10$ in a stratified diffuse CGM are prone to condense. We have increased our bound to $t_{\rm cool}/t_{\rm ff} = 20$ because of factor ~ 2 uncertainties in theoretical assessments (Choudhury & Sharma, 2016). We find two distinct evolutionary behaviours:

- Case I: The density perturbations cool rapidly. The temperatures of the associated gas decrease to $\sim 10^4$ K; the densities increase by a factor of $\gtrsim 30$; their $t_{\rm cool}/t_{\rm ff}$ ratios drop to very low values; and they condense to form cool clouds. In due course, most of these cool clouds fall inward towards the central galaxy.
- Case II: Neither the density, temperature, entropy nor $t_{\rm cool}$ change much. However, their $t_{\rm cool}/t_{\rm ff}$ ratios drop for a time, even dropping below our threshold, and then bounce back, eventually settling around the median value for the hot gas. Examining these perturbations more closely, we find that these are weak perturbations that are dragged along in the wakes of orbiting satellites and swept to larger radii. The reason their $t_{\rm cool}/t_{\rm ff}$ drops temporarily is not because these perturbations are cooling rapidly but because their free-fall timescale is increasing. In due course, this gas detaches and mixes with the ambient CGM. The latter is the reason for the bounce in $t_{\rm cool}/t_{\rm ff}$. The evolution of these weak perturbations show that *the local value* $t_{\rm cool}/t_{\rm ff}$ *falling below threshold* does not*, by itself, unambiguously signal runaway cooling of a perturbation.*

(g) We find that in cosmological simulations, the perturbations in the CGM beyond the very central region (i.e. $R/R_{500} > 0.1$) are primarily caused by infalling/orbiting substructure.

(h) Finally, we find that the flow of the CGM onto the BGG occurs via three key channels: Firstly, a fraction of the gas removed from the satellites cools and settles in the central galaxy. Secondly, regions subject to strong density perturbations cool and fall in. And, thirdly, we identify a radiatively cooling component that flows subsonically into the central galaxy. We find that the latter is not a spherically symmetric feature. Rather, the cooling gas flows inward via filaments. Most of these inflows have non-zero angular momentum and are responsible for the re-emergence of the gaseous disks in rejuvenating BGGs (cf. Jung et al., 2022; Lagos et al., 2022).

Lastly, it is important to note that we are able to *begin to* observe multiphase structure of CGM and especially, the effects of density perturbations on this gas reservoir, because the ROMULUS suite of simulations are among the highest resolution cosmological simulations available. However, we acknowledge that we are only scratching the surface. To fully capture these varied phenomena and their impact on both the group central galaxies and the groups as a whole, considerable improvement in resolution is still needed.

Comparison with previous studies

Recently, a number of studies have investigated the CGM around central galaxies in halos of different masses (van de Voort et al., 2019; Suresh et al., 2019; Hafen et al., 2019; Peeples et al., 2019; Nelson et al., 2020; Esmerian et al., 2021; Stern et al., 2021). Most of these investigations have been carried out using either the FIRE-2 galaxy formation model (Hopkins et al., 2018) layered onto the GIZMO hydrodynamics code (Hopkins, 2015); FOGGIE galaxy formation model (Peeples et al., 2019) layered onto Enzo (Bryan et al., 2014); or TNG50 (Pillepich et al., 2019) and Auriga (Grand et al., 2017) layered onto the AREPO code (Springel, 2010). All except Nelson et al. (2020) have limited their efforts to the CGM of Milky Way mass galaxies ($M_{vir} \sim 10^{12}$ $M_{\odot}$) or lower. Additionally, most of the studies focus mainly on the origin of CGM. Only Suresh et al. (2019), Nelson et al. (2020) and Esmerian et al. (2021) investigate the dynamics of the CGM. In our study, we use ROMULUS galaxy formation model, which is different in detail from the FIRE-2 and the TNG models, to probe the origin and dynamics of the CGM around BGGs. ROMULUS simulations are run using Tree+SPH code CHANGA (Menon et al., 2015), which itself is different from the AREPO and GIZMO hydrodynamic codes. Comparing the results from various simulations

is challenging due to the differences in the galaxy formation models used and the hydrodynamical codes leveraged to solve fluid equations, not to mention details like the mass of the halos under study and even the criteria used to tease out the details. Nonetheless, we attempt a brief comparison to the relevant results from previous studies.

We find that the CGM of BGGs in ROMULUS simulations is multiphase and dynamic, characterized by a large range of densities, entropies, $t_{\rm cool}$ and $t_{\rm cool}/t_{\rm ff}$. As discussed in §2.0.1, both Esmerian et al. (2021) and Nelson et al. (2020) find the same. The multiphase nature of the CGM in the ROMULUS C halo (the highest mass halo in our analysis) has been discussed previously by Butsky et al. (2019). They find gas with a range of temperatures ($10^4 < \rm T < 10^6$ K) at all radii. Upon examining this gas further, Butsky et al. (2019) find that some of it is highly enriched gas, which they interpret as evidence that it is gas from satellite galaxies. We explicitly show that this gas is an important contributor to the multiphase structure of the CGM — and can make up as much as 30–40% of the cool gas — in not only ROMULUS C but also other group halos.

Examining the origin of the CGM in more detail, we find that the *pre-existing CGM* makes up the largest proportion ($> 60\%$) of the CGM, followed by gas removed from subhalos. The other categories, gas inside subhalos, and gas from the *central galaxy winds*, make up only a small fraction ($\lesssim 4\%$) of the total. Both Hafen et al. (2019) and Nelson et al. (2020) also explored the origin of the CGM. A detailed comparison with Nelson et al. (2020) is not straightforward due to differences in our classification criteria. Hafen et al. (2019) use similar criteria as us but they study the CGM around galaxies with masses $\rm M_* \simeq 10^6 - 10^{11}\ M_\odot$ and find that the relative contribution of the different sources varies with galaxy mass. However, their highest mass systems at low redshift appear to be similar to our groups: the *pre-existing CGM* contributes the highest fraction ($> 60\%$) to the CGM, followed by gas from satellite galaxies and then the *central galaxy wind*[11]. This is consistent with our results.

Our analysis shows that the CGM cools via two main channels: a filamentary isothermal cooling flow and strong perturbations that cool, condense and then rain onto the central galaxy. Unlike idealized simulations, we find that the dominant source of strong perturbations in cosmological systems are satellite wakes and tails. We were initially concerned whether this feature in the ROMULUS simulations were real, as opposed to numerical artefacts. However, the fact that Nelson et al. (2020) and Esmerian et al. (2021) find similar behaviour gives us some confidence. Additionally, we also examined the neighbourhood of the rapidly cooling gas and confirmed that they are spatially correlated with the satellite tails.

[11] Hafen et al. (2019) refer to these categories as *smooth IGM accretion*, *satellite wind*, and *wind*, respectively.

We do not have sufficient resolution to distinguish the extent to which the cooling is radiative, mixing-induced or both in near-equal measure. Like us, Esmerian et al. (2021) find that over 70% of the cold phase in the CGM around their simulated Milky Way-like galaxies are also the products of non-linear density perturbations caused by cosmological accretion, feedback-driven winds, and the debris of tidal interactions from the central and satellite galaxies. Nelson et al. (2020) also conclude the same, that the cold CGM is formed via large-density perturbations whose initial seeds are either fragments of tidal debris, ram-pressure stripped tails of satellites or non-linear perturbations in the CGM induced by satellite galaxies. We note that in the present study, we have not considered local perturbations in, for example, gas removed from the subhalos, only the induced perturbations in the *pre-existing CGM*. The former too will be subject to condense to form clouds.

Turning to the *central galaxy wind* component, our analysis shows that it does not play an important role in contributing to cold gas. Some of the gas in *central galaxy wind* cools, but most of it mixes with the CGM. This finding is different from that of Suresh et al. (2019) who note that $\sim$ 70% of the cold CGM in their simulations has been processed by the central galaxy and forms due to the rapid cooling of wind material interacting with the hot halo. This difference could be due to any number of details, including differences in (i) the mass of the systems: Suresh et al. (2019) study the CGM of a $M_{halo} \sim 10^{12}$ at z $\sim$ 2. (ii) hydrodynamics solvers used to run the two simulations; (iii) the simulations' resolution: Suresh et al. (2019) run has enhanced resolution in CGM, achieving gas mass and spatial resolutions of 2200 $M_\odot$ and 95 pc, respectively. (iv) differences in the treatment of sub-grid physical processes, like mixing: moving mesh schemes have been shown to be more effective than SPH in capturing small-scale mixing and in tracking perturbations at mixing interfaces (Rennehan et al., 2019; Rennehan, 2021); (v) how the two galaxy formation models handle galactic winds or other related physics: Suresh et al. (2019) specifically discuss that their results are sensitive to details of galactic winds treatments and changes in this treatment can result in little to no wind particles cooling and condensing.

Variations and Caveats

Exploring the impact of varying $t_{\rm cool}/t_{\rm ff}$ threshold

In §2.0.1, we noted that various theoretical analyses suggest that when a local perturbations $t_{\rm cool}/t_{\rm ff}$ falls below $\sim$ 10, there is a high likelihood that non-linear damping mechanisms will not be able to prevent the non-linear growth of thermal instability. This value is not a "threshold' in the strict sense because the competition between damping vs. growth

also depends on various environmental properties, including the shape of the gravitational potential, the entropy profile, the efficacy of thermal conduction, and whether AGN feedback is on or off (Voit, 2021; Choudhury & Sharma, 2016; Binney et al., 2009). For example, Choudhury & Sharma (2016) argue that the value can be a factor of ~ 2 higher. For these reasons, we adopted a value of $(t_{\rm cool}/t_{\rm ff})_{\rm threshold} = 20$; however, we have also repeated the analysis for $(t_{\rm cool}/t_{\rm ff})_{\rm threshold} = 10$ and 30. Specifically, we have assessed the impact of varying the threshold on (i) the sources of the CGM and the "condensation-susceptible" CGM and (ii) the dynamics of the "condensation-susceptible" CGM by computing the corresponding mass fractions.

Simply put, we find that changing the threshold does not alter the source categories — *pre-existing CGM*, *subhalo stripped*, *subhalo internal*, and *central galaxy wind*. However, we find that the mass fractions associated with these source categories do change. Specifically, the mass fractions of *subhalo internal, subhalo stripped, and central galaxy wind* increase. More precisely, the mass in the *subhalo internal* category does not change because of its very low $t_{\rm cool}/t_{\rm ff}$; the fraction increases because of the total mass of the gas with $t_{\rm cool}/t_{\rm ff}$ below threshold *does* decrease as the latter is lowered from 30 to 10. As for *subhalo stripped* and *central galaxy wind*, the associated masses decrease with the threshold but not as quickly as the mass of the gas below our threshold. Only the mass fraction of *pre-existing CGM* decreases. In spite of this, *pre-existing CGM* and *subhalo stripped* remain the top two categories, and the ratio of these two mass fractions depends on whether the group under consideration is active or quiescent, as we had found previously.

As for the dynamics, we find that all seven behavioural patterns — *central galaxy wind*, *subhalo internal*, *subhalo stripped*, *cooling flow*, *strongly perturbed* gas, *weakly perturbed* gas and *outward flow* — are present regardless of the value of $(t_{\rm cool}/t_{\rm ff})_{\rm threshold}$ but again, the gas mass fraction associated with each of these varies. We find that lowering the threshold from 30 to 10, leads to an increase in the mass fraction of the cooling flow and strongly perturbed CGM, while the mass fraction of weakly perturbed gas decreases. All of these variations are straightforward to understand. The $t_{\rm cool}/t_{\rm ff}$ of the strongly perturbed gas drops to fairly low values and therefore, changing the threshold does not significantly alter the total mass in this component. However, lowering the threshold does, as noted, decrease the total mass of the gas below threshold. This drives the mass fraction up. The mass of cooling flow gas decreases as the threshold is lowered but not as fast as the total and therefore, the mass fraction also increases. On the other hand, $t_{\rm cool}/t_{\rm ff}$ of the weakly perturbed gas has a lower bound and consequently, associated mass with $(t_{\rm cool}/t_{\rm ff})_{\rm bounce} < (t_{\rm cool}/t_{\rm ff})_{\rm threshold}$ decreases as $(t_{\rm cool}/t_{\rm ff})_{\rm threshold}$ is lowered.

In addition to varying the $t_{\rm cool}/t_{\rm ff}$, we also examine the impact of defining "condensation-susceptible" CGM using the criterion $t_{\rm cool} < 1$ Gyr. From Figs. 2.1, it is apparent that condensing gas is not limited to regions where the median $t_{\rm cool}$ of hot gas is below this threshold, and there are also regions where the median $t_{\rm cool}$ is below the threshold, yet only a small amount of gas is condensing out. This once again highlights the critical role of strong local perturbations in the formation of cold, condensed gas.

A more detailed analysis shows that even with the $t_{\rm cool} < 1$ Gyr criterion, the sources and behavior patterns are the same as before, only details, like the corresponding mass fractions, change. The *pre-existing CGM* and *subhalo stripped* categories are still the top two categories and their respective mass fraction depends on whether a halo is active or quiescent, as discussed before. However, in one of our larger active halos, the *subhalo internal* mass fraction is larger than that of the *subhalo-stripped* mass fraction at the time of analysis. This is a transient state. As the orbiting substructures are stripped, this will change. As for the behavioral patterns, the fraction of cooling flow and strongly perturbed gas increases, compared to the $(t_{\rm cool}/t_{\rm ff})_{\rm threshold} = 10$ case, because their masses decreases at a slower rate than the total mass of the CGM with $t_{\rm cool} < 1$ Gyr. On the other hand, the fraction of weakly perturbed gas decreases because the cooling time of 90% of the perturbations is always longer than 1 Gyr and these are excluded by the $t_{\rm cool} < 1$ Gyr criterion.

The most important outcome of these exercises is that our results regarding the origin of the CGM, the manner in which it evolves, and even our results concerning the cooling channels, are robust, independent of the specific choice of the threshold criterion adopted.

Metal line cooling in ROMULUS simulations

Pushing to high resolution often requires making compromises. In the case of ROMULUS, a deliberate choice was made to treat only low-temperature ($T \leq 10^4$ K) metal-line cooling. This is explained in detail in Tremmel et al. (2019); Butsky et al. (2019) and Jung et al. (2022). Here, we consider the potential implications for our study.

Metal lines collectively comprise the dominant radiative cooling channel for $T \sim 10^{5-7}$ K gas. All things being equal, had full metal-line cooling been included in ROMULUS, one would expect the CGM cooling time to shorten, which then would lead to (i) more gas with $t_{\rm cool}/t_{\rm ff}$ ratio below the threshold, (ii) more massive cooling flow, and (iii) more gas condensing out. In other words, the phenomena we have described in this paper ought be even more prominent.

However, this line of reasoning does not account for the fact that in real systems, stellar

and AGN feedback, act to offset cooling. While this will undoubtedly alter exactly how much mass is associated with any one phenomenon, or how much gas is associated with cooling flows versus condensations, we assert that the general dynamics and the categories we have identified in this study are robust.

As for the details, although the precise fractions of cool and cold gas that forms in the CGM of massive galaxies are important for making observational predictions, these will have to await more realistic group simulations that are able to reproduce both the observed galaxy and the gas properties of groups. As discussed in detail in §2 of Jung et al. (2022), in current generation of cosmological simulations, SMBH accretion and feedback sub-grid models are rather basic: They are tuned to offset cooling mainly to produce reasonably realistic distribution of galaxies. In simulations that include full metal-line cooling, a higher degree of cooling leads to more frequent and/or more energetic SMBH feedback episodes. And while the CGM in these simulations is thermally balanced in a global, time-averaged sense, in detail the entropy profiles of the simulated groups typically have large, flat, high entropy cores (Oppenheimer et al., 2021a). Since observed groups have power-law entropy profiles (O'Sullivan et al., 2017a, and references therein), we do not expect the detailed cooling/condensing profiles of these simulations to reflect that of real groups.

Impact of Numerics: Resolution and Hydrodynamic Solvers

We have already noted previously that investigations with enhanced CGM resolution show that as the resolution becomes increasingly finer, the CGM's warm/hot gas content decreases and its cool/cold gas content grows; this cool/cold gas fragments to progressively smaller sizes; and these clouds survive for a longer time (Hummels et al., 2019; Suresh et al., 2019; van de Voort et al., 2019; Peeples et al., 2019). At the same time, it is not clear how improving resolution will impact the modeling of, and the interplay between, processes like turbulent compression, turbulent mixing, and turbulent diffusion. Some processes, like turbulent diffusion, can limit fragmentation (see, for example, Rennehan et al., 2019; Rennehan, 2021, and references therein) while others will exacerbate it. These details will undoubtedly affect the precise amount of gas associated with different categories and dynamical behaviours.

Finally, we also consider the possibility that the mass fractions may be sensitive to the numerical method used to solve the hydrodynamic equations, as suggested by the recent study by Braspenning et al. (2022). This study investigated the unfolding of cloud-wind interactions in simulations employing a variety of hydrodynamics solvers used in cosmological simulations. To isolate the influence of the hydrodynamic solvers, all simulations used the

same initial conditions, were non-radiative, and did not include physical conduction.

In summary, they found a range of outcomes. At one end of the spectrum, the trail of stripped gas from the primary cloud fragments into a swarm of dense, long-lived, cloudlets. At the other end of the spectrum, the gas forms a diffuse, swirling tail that rapidly mixes with the ambient medium. This mixing, or lack thereof, is entirely numerical but we would expect that such differences will also impact the fractions of gas in the different components and states. Moreover, we note that the inclusion of additional physical processes — turbulent mixing, turbulent diffusion, physical conduction, radiative cooling, etc. — will all also impact the outcome.

Separately from the above issue, one can even question whether the condensing gas in our simulations is a numerical artefact. Throughout this paper, we have been concerned about this. However, we are assured that it is not, that at least it is not a product of CHaNGa's hydrodynamic solver. After all, both Nelson et al. (2020) and Esmerian et al. (2021), who use simulations that employ very different hydrodynamic solvers, also report condensing gas.

2.0.6 Conclusions

Our results highlight the complex and dynamic nature of CGM around massive galaxies in the Romulus suite of high-resolution hydrodynamic cosmological simulations. The high resolution of Romulus allows us to begin to see the evolving multiphase structure of CGM. The key outcomes of our study are our results about the origin of the CGM and the manner in which the different components of the CGM evolve, including the two main cooling channels. With respect to the latter, the CGMs flows onto the central BGG via a filamentary cooling flow as well as infalling cold gas. We find that the latter are condensations that form from large density, "condensation-susceptible" perturbations induced mainly by orbiting satellites. In general, we find that these satellites trigger both strong and weak perturbations and the high resolution Romulus simulations allow us to witness the evolution of both classes of perturbations. The $t_{\rm cool}/t_{\rm ff}$ ratios of both initially drop, and may even fall below threshold but in the case of the strong perturbations, this is due to a drop in $t_{\rm cool}$ and the perturbations rapidly cool. In the case of weak perturbations, the drop is due to increasing $t_{\rm ff}$ and these perturbations do not condense. We also see the settling of gas stripped from orbiting satellites; on the average, however, this is sub-dominant.

The patterns that we have described above are robust. We also compute the fractions of mass associated with the different components. Knowing these fractions are essential for making observational predictions. However, as discussed, there are too many uncertain-

ties that have yet to be resolved, not to mention genuine large halo-to-halo variations that correlate with the merger history of the halos and with the cycle of AGN outbursts.

Acknowledgements

We thank M. Lehnert, B. Oppenheimer, C. Hayward, D. Fielding, M. Ruszkowski, G.M. Voit, M. Donahue, I. Butsky, A. Man, U. Steinwandel, I.A. Asensio, and B. Keller for insightful discussions and suggestions. VS, AB, and DR acknowledge support from the Natural Sciences and Engineering Research Council of Canada (NSERC) through its Discovery Grant program. DR also acknowledges support from NSERC through a Canada Graduate Scholarship (funding reference number: 534263). AB acknowledges support from the Infosys Foundation via an endowed Infosys Visiting Chair Professorship at the Indian Institute of Science. AB, TQ, and MT were partially supported by NSF award AST-1514868. SLJ is supported by the Australian National University Research Scholarship. MT is supported by an NSF Astronomy and Astrophysics Postdoctoral Fellowship under award AST-2001810. SIL is supported in part by the National Research Foundation of South Africa (NRF Grant Number: 146053). EOS acknowledges support from NASA through XMM-Newton award 80NSSC19K1056. And, PS acknowledges a Swarnajayanti Fellowship (DST/SJF/PSA-03/2016-17) and a National Supercomputing Mission grant from the Dept. of Science and Technology, India.

The ROMULUS simulation suite is part of the Blue Waters sustained-petascale computing project, which is supported by the National Science Foundation (via awards OCI-0725070, ACI-1238993, and OAC-1613674) and the state of Illinois. Blue Waters is a joint effort of the University of Illinois at Urbana-Champaign and its National Center for Supercomputing Applications. Resources supporting this work were also provided by the (a) NASA High-End Computing (HEC) Program through the NASA Advanced Supercomputing (NAS) Division at Ames Research Center; and (b) Extreme Science and Engineering Discovery Environment (XSEDE), supported by National Science Foundation grant number ACI-1548562. Analysis reported in this paper was enabled in part by WestGrid and Digital Research Alliance of Canada (alliancecan.ca). Our analysis was performed using the Python programming language (Python Software Foundation, https://www.python.org). The following packages were used throughout the analysis: numpy (Harris et al. 2020), SciPy (Virtanen et al. 2020), and matplotlib (Hunter 2007). This research also made use of the publicly available tools Pynbody (Pontzen et al. 2013a) and TANGOS (Pontzen & Tremmel 2018).

Finally, VS and AB acknowledge the lək̓ʷəŋən peoples on whose traditional territory the University of Victoria stands, and the Songhees, Equimalt and W̱SÁNEĆ peoples whose

historical relationships with the land continue to this day. Similarly, SLJ acknowledges the Ngunnawal and Ngambri people as the traditional owners and ongoing custodians of the land on which the Research School of Astronomy & Astrophysics is sited at Mt Stromlo.

Data Availability

The data directly related to this article will be shared on reasonable request to the corresponding author. Galaxy database and particle data for ROMULUS is available upon request from Michael Tremmel.

Personal contribution clarification:

This chapter contributes to the first part of my dissertation, which focuses on enhancing our understanding of the gaseous halo that cocoons galaxies. It specifically investigates the origin and dynamics of the circumgalactic medium around massive galaxies. I did all aspects of the analysis for this study, from reviewing current literature and planning the different stages of the analysis, to implementing innovative methods for analyzing the Romulus simulation data. Arif Babul provided scientific guidance during the early stages, challenged me to formulate a physical understanding of the results, and offered suggestions on how to present the results clearly by commenting on my drafts of the document. S. Lyla Jung and Douglas Rennehan provided insights through discussions during the analysis phase, as well as feedback on the final draft. Michael Tremmel, Thomas R. Quinn, Zhiwei Shao, Prateek Sharma, Lucio Mayer, E. OSullivan, and S. Ilani Loubser helped to sharpen the interpretation by drawing on their expertise and suggesting different features to examine in order to gain an understanding of how the main results I found arise.

Chapter 3

Modeling the Circumgalactic Medium with a super-Lagrangian Refinement Scheme

As discussed in Chapter 1 and demonstrated by the results of Chapter 2, resolving the cold gas in the CGM of galaxies requires extremely high resolution($\sim$ 1 pc, Hummels et al., 2019). Current high-resolution cosmological simulations, such as the ROMULUS simulation used in the previous Chapter, offer a valuable opportunity to begin exploring the multiphase structure of the CGM. However, even with such high resolution, we are merely scratching the surface of understanding this phenomenon. For a deeper understanding, a much higher resolution within the CGM is needed.

The resolution in state-of-the-art simulations is generally adaptive, following a (quasi-) Lagrangian approach in which mass resolution is kept constant. Consequently, these simulations achieve spatial resolutions in the low-density regions of galactic halos that are orders of magnitude lower than those attained in the high-density disks of galaxies. This problem cannot be addressed by simply increasing the resolution everywhere in the simulation as it would be prohibitively expensive to do.

A potential solution to achieve high resolution in the CGM without incurring excessive computational costs is to selectively enforce high resolution in the CGM region surrounding a galaxy, without increasing the resolution within the galaxies themselves. The aim of this targeted approach is to avoid having to evolve galaxies in the simulations at very high resolution while enabling more accurate and much more realistic modeling of the spatial and dynamic structures in the CGM.

Over the past few years, efforts have been made to achieve higher resolution in the CGM (Hummels et al., 2019; Peeples et al., 2019; Suresh et al., 2019; van de Voort et al., 2019). Studies by Suresh et al. (2019) and van de Voort et al. (2019) have used the Illustris TNG100 (Nelson et al., 2019b) and Auriga (Grand et al., 2017) galaxy formation models,

layered onto the AREPO code (Springel, 2010). Peeples et al. (2019) conducted the FOGGIE (Figuring Out Gas & Galaxies In Enzo) simulations, and Hummels et al. (2019) employed the TEMPEST simulation, both using Enzo code (Bryan et al., 2014).

The code bases used in the simulations of the aforementioned studies are based on Eulerian mesh-based hydrodynamics (e.g. Stone & Norman, 1992). This method employs a grid of fixed sample points in space. Each cell on this grid represents a specific volume in space, with fluid properties such as density, temperature, and velocity being calculated at these cells. In simpler terms, the Eulerian approach treats the frame of reference as stationary, allowing for the transport of mass, energy, and momentum between sample points on the grid.

Significant enhancements to the Eulerian method include the Adaptive Mesh Refinement (AMR; Berger & Colella, 1989) and Moving Mesh (MM; Gnedin, 1995; Springel, 2010) techniques. The AMR technique adaptively adds and modifies additional, finer grids over regions requiring higher resolution, a method employed by Enzo. On the other hand, the MM approach, as implemented in codes like AREPO, allows the grid to move and deform along with the fluid. This adaptability can lead to more accurate simulations of complex flows, particularly in cosmological and astrophysical contexts.

Another common approach in cosmological simulations is the gridless, Lagrangian method. The most widely used Lagrangian method is Smoothed Particle Hydrodynamics (SPH; Lucy, 1977; Gingold & Monaghan, 1977). In Lagrangian hydrodynamical simulations, matter fields are decomposed into finite mass particles. This method tracks individual elements or particles in the fluid, with the properties of each particle calculated based on its position and interactions with neighbouring particles. The particles follow the fluid's motion through the simulated volume, in contrast to the fixed, stationary observer perspective of the Eulerian approach.

Both the Eulerian and Lagrangian methods have their own advantages and disadvantages. The Eulerian approach accurately captures shock waves and handles fluid instabilities. However, this method faces several challenges. A notable issue is its problem with conserving angular momentum, a critical factor in simulations of galaxy formation where rotation is ubiquitous. The fixed grid system of the Eulerian method also leads to inaccuracies in modeling complex flow trajectories and fine-scale structures in mixing processes, often resulting in overestimated mixing due to numerical diffusion. Furthermore, this method struggles with accurately capturing turbulent mixing, tracking interfaces in multiphase flows, and representing advection, particularly in high-speed or turbulent flows, leading to issues like artificial smearing of advected properties.

On the other hand, Lagrangian methods like SPH naturally conserve angular momentum. SPH effectively tracks individual fluid elements, allowing for accurate mass movement tracking across simulation volumes. However, SPH has its own limitations, such as poor shock resolution and low-order accuracy in handling contact discontinuities. It also tends to suppress fluid instabilities under certain conditions (Agertz et al., 2007b) and does not inherently produce entropy through mixing (Springel & Hernquist, 2002).

To bridge these gaps, the GIZMO N-body+hydrodynamics code (Hopkins, 2015), in its "meshless finite mass" (MFM) mode, offers an innovative solution. MFM is a mesh-free Lagrangian finite-volume Godunov method that combines the benefits of both Eulerian and Lagrangian approaches. It provides adaptive resolution, minimizes advection errors, and improves angular momentum conservation relative to Eulerian codes. MFM also exhibits superior performance in shock-capturing and fluid-mixing problems, while avoiding the low-order errors inherent to SPH. In this section, I employ the GIZMO MFM to develop a model that enhances resolution specifically in the CGM around galaxies. As shown in Hopkins (2015), MFM performs well with different particle masses, unlike many SPH methods where the errors increase when having unequal-mass particles interacting, which is crucial for my hyper-renement simulations.

3.0.1 Cosmological Galaxy Formation Model

To implement and apply my model I need a galaxy formation model to base my model on. For the galaxy formation model, I use Simba (Davé et al., 2019). Simba is a natural option since it is written in GIZMO for the MFM method; also, Simba includes models of star formation, gas cooling, stellar feedback, SMBH formation and evolution, and AGN feedback. Simba simulations are calibrated to reproduce observed galaxy properties across cosmic time and include runs with high resolution (i.e., $2.85 \times 10^5 \mathrm{M}_\odot$ and $1.5 \times 10^6 M_\odot$ for gas and dark matter resolution, respectively). Therefore this simulation is a proper starting point for enhancing resolution in CGM. In addition, recently, a state-of-the-art chemical enrichment model for Simba has been developed which resolves many earlier models deficits (Hough et al., 2023a) and makes it especially suitable for tracing metals in CGM. I point the interested reader to Davé et al. (2019) for the details of the galaxy formation model. Here I focus on the numerical model used to enhance resolution in the CGM.

3.0.2 CGM Refinement Scheme

As the name suggests, in the GIZMO "meshless finite mass" approach, particles are kept in a finite mass. These particles undergo a binary split or merge based on their mass variations compared to the initial particle mass. If a particle's mass drops below half of the initial mass of all particles (mass $\leq 0.5\mathrm{m_{init}}(\mathrm{t_0})$) and it is the least massive particle among its neighbour list, it merges with the neighbouring particle with the next lowest mass. This merging process is straightforward: the less massive particle is removed, and conservation requires that the more massive particle inherits the summed mass, momentum, and energy (and their time rates of change). After the merger, the particle's position is updated to the center of mass of the original pair.

Similarly, when a particle's mass exceeds three times of particles' initial mass (mass $\geq 3\mathrm{m_{init}}(\mathrm{t_0})$), and it is the most massive among its neighbours, it undergoes a binary split. The resulting particles each obtain half of the original mass and inherit the specific (per-unit-mass) properties of the parent particle. The challenge in this splitting process lies in determining the spatial positioning of the newly created particles. They cannot placed at the same location as the parent particle and must be slightly separated. To achieve this without introducing significant fluctuations in volumetric quantities, GIZMO uses a simple but effective method: the two new particles are positioned apart by $dr = \min\,(h_i/8, |r_{\mathrm{near}}|/3)$; where h_i is the smoothing length and $|r_{\mathrm{near}}|$ is the distance to the nearest neighbour. This separation is done in opposite directions along an axis perpendicular to the particle number density gradient, to minimize the perturbation to volumetric quantities.

I build my model on the GIZMO split/merge model. First I outline the setup of my simulation. I focus on zoom-in simulations of a Milky Way mass halo. A zoom-in simulation is a technique where a specific, smaller region of a larger, coarser resolution simulation is re-simulated at a higher resolution. This method primarily targets a selected host halo, or a pair of halos, re-creating the region encompassing all particles that will eventually be part of that halo with enhanced detail. Such zoom-in simulations are particularly useful to achieve high-resolution cosmological simulation of halos of specific mass and history. They provide an excellent foundation for refining CGM resolution and conducting preliminary tests before scaling up to a full cosmological volume.

In my study, I run four zoom-in simulations of a Milky Way mass halo ($M_{halo} \sim 10^{12} M_{\odot}$). Starting from a coarser resolution simulation in a box with side length L = 100 cMpc $\mathrm{h^{-1}}$

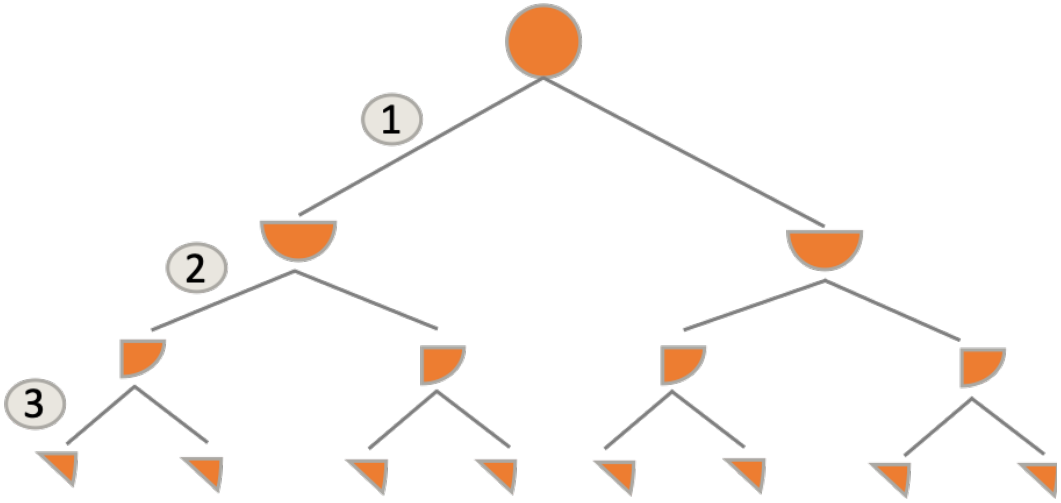

Figure 3.1: Schematic illustration of particle splitting in my model to enhance the resolution in the CGM. When a particle meets the criteria for splitting, it splits into two particles. If the target is to enhance the resolution by, for example, 8 times, this splitting continues until the target particle mass is met. The numbers indicate how many times a particle has been split. The shapes are only for illustration of mass fractions and do not reflect the actual shapes of the particles.

(150 cMpc [1]), I run the zoom-in simulation for $3R_{vir}$ of a $10^{12} M_{\odot}$ halo at z = 0 ($\sim$ 778 ckpc). The sets of runs comprise one fiducial simulation and three simulations with enhanced CGM resolution. The simulations begin from initial conditions generated with MUSIC (Hahn & Abel, 2011) at a redshift of z = 249, with a standard ΛCDM cosmology: $\Omega_m = 0.3$, $\Omega_\Lambda = 0.7$, $\Omega_b = 0.048$, $h = 0.68$, $\sigma_8 = 0.82$. The mass resolution of gas and dark matter, which all the simulations start with, are $2.85 \times 10^5\,M_{\odot}$ and $1.5 \times 10^6\,M_{\odot}$, respectively. The adaptive gravitational softening (Hopkins, 2015; Hopkins et al., 2018) is used to compute the softening lengths of all of the particles and enforce a minimum softening length of 0.5 kpc h^{-1}. All simulations follow the same sub-grid model for star formation, stellar feedback, and gas cooling from Simba. Note that feedback from supermassive black holes is not included in any of these simulations. This exclusion of the Simba BH feedback model is an intentional decision for simplification. Based on the halo mass scale of my simulations, the impact of BH feedback is anticipated to be negligible, since such feedback becomes significant mainly for halos with $M_{halo} > 10^{12} M_{\odot}$ (Vogelsberger et al., 2013).

In each simulation, dark matter halos are identified using a Friends-of-Friends (FoF)

[1] ckpc and cMpc denote comoving kiloparsecs and comoving megaparsecs, respectively. Comoving distances remain constant over time as they adjust for the expansion of the universe, thus allowing for consistent comparisons of distances across different cosmological epochs.

algorithm (Davis et al., 1985). Upon identifying each halo, its center is determined using the shrinking sphere method (Power et al., 2003). Then the R_{200} of each halo is calculated which is defined as the radius within which the mean overdensity is 200 times the cosmic mean density at the given redshift. Building upon GIZMO's split/merge model, I further developed my approach to enhance the resolution specifically in the CGM. In my model, when a "gas" particle meets the following criteria it splits:

- It is in the CGM: $\alpha R_{200} < r < \beta R_{200}$, where $\alpha = 0.1$ and $\beta = 1$
- Its hydrogen number density is $n_h < 0.2\,\mathrm{cm}^{-3}$

The density criteria are chosen to avoid splitting high-resolution elements inside satellite galaxies ISM entering the CGM of the central galaxy in groups. The splitting continues until it reaches the target mass resolution. Conversely, when a particle exits the CGM, it merges with neighbouring particles to maintain a lower resolution in other regions (e.g. within galaxies). This process of splitting and merging is executed at every timestep, with each split resulting in the creation of two new particles. Consequently, for example, to achieve an 8 times higher mass resolution, a particle must undergo splitting across three consecutive timesteps. A schematic illustrating this splitting process is shown in Fig. 3.1.

I start my fiducial zoom-in simulation with a resolution of $M_{gas} \sim 2.85 \times 10^5 M_\odot$ and split the particles in the CGM to get to 8, 32, and 128 times better resolution. This results in a suite of simulations with increasing resolution of $M_{gas} \sim 3.56 \times 10^4 M_\odot, 8.9 \times 10^3 M_\odot$, and $2.23 \times 10^3 M_\odot$, respectively. In total, this suite comprises four simulations: one fiducial and three with enhanced CGM resolutions.

In my simulation with an 8× resolution enhancement, particle splitting begins as soon as the FoF algorithm is first called ($z \sim 12$). From there all particles in the CGM split to achieve an 8× better resolution in this region. Fig. 3.2 shows the mass resolution in fiducial and 8× enhanced CGM simulations at $z = 0$. The black dashed line shows the minimum mass of particles (mass resolution) in the fiducial run. The mass resolution is correctly enhanced 8 times and the minimum mass is $M_{gas} \sim 3.56 \times 10^4 M_\odot$ in the right panel.

To achieve 32 and 128 times higher CGM resolution while further saving computational costs, I implement a novel approach that incrementally increases CGM resolution throughout the simulation running time. For instance, to achieve a 128× enhancement by $z = 0$, the simulation is structured to gradually increase resolution at specific redshift milestones. Starting from $z = 8$, particles split once, doubling the resolution. This continues until the simulation reaches $z = 5$, at which point CGM particles split two times, achieving a 4×

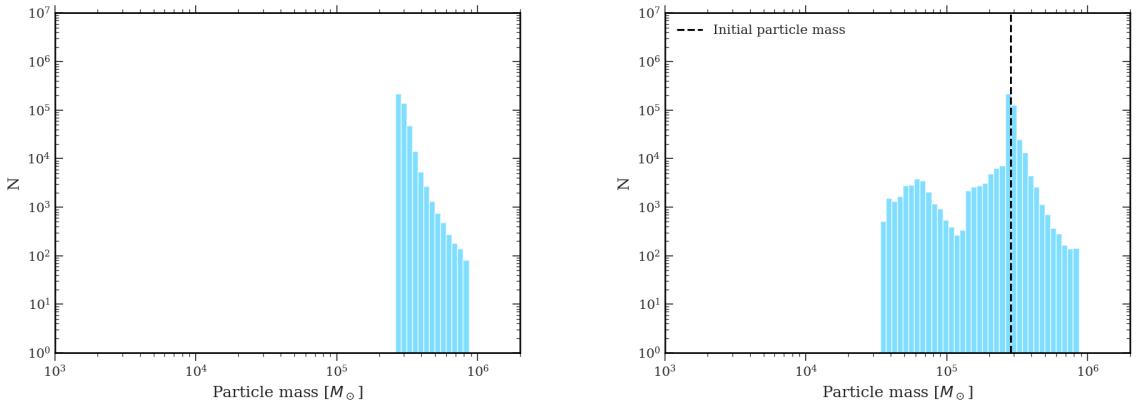

Figure 3.2: *Left*: mass distribution of gas particles in the fiducial simulation, *right*: mass distribution of gas particles in the simulation with 8× enhanced resolution in CGM. The dashed black line represents the minimum particle mass with which both runs began.

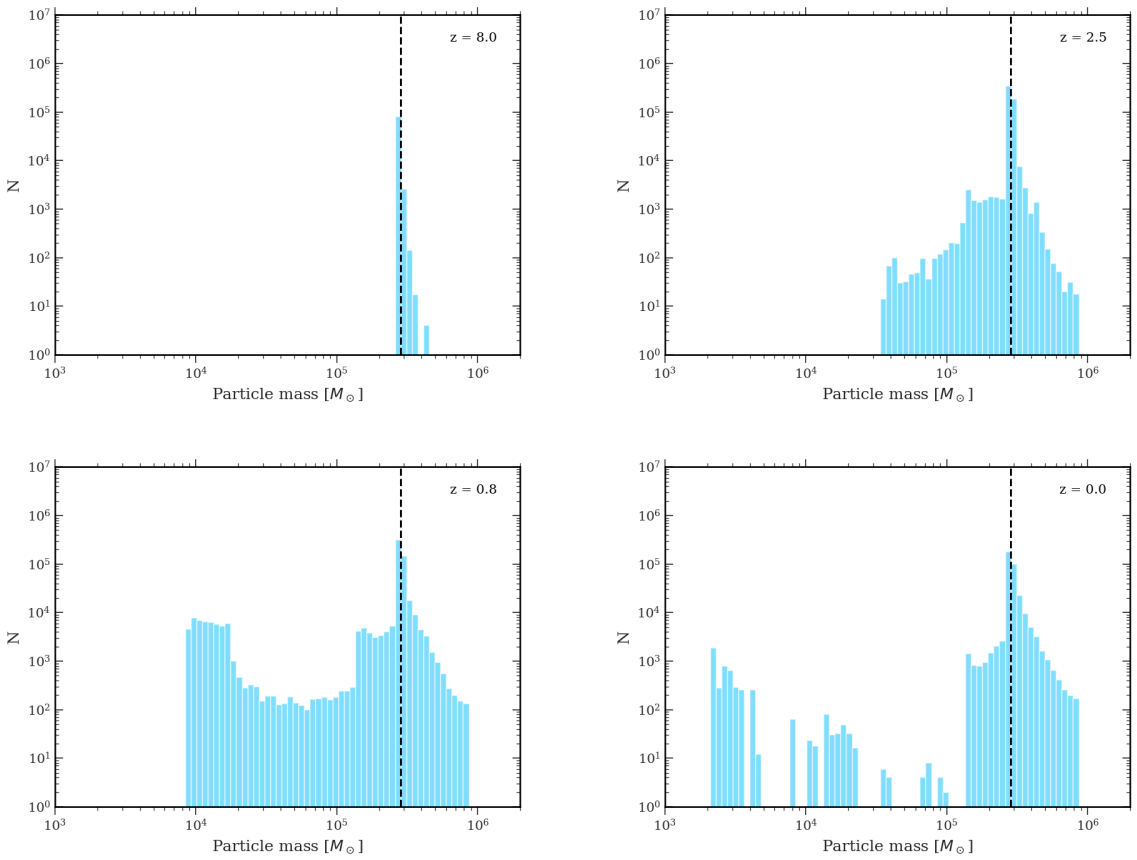

Figure 3.3: Mass distribution of gas particles in the run with a gradual enhancement of resolution in CGM. *Top left:* The starting point of splitting at z = 8. *Top right:* Illustrates a sample redshift when splitting reaches 3×, indicating an 8× enhancement in CGM resolution. *Bottom left:* A sample when the simulation reaches 5 times splitting, equivalent to a 32× enhancement in resolution. *Bottom right:* simulation reaching 128× enhancement in resolution at z = 0.

enhancement in resolution compared to the fiducial simulation. This enhancement progresses at key redshifts: from $z = 3$ to $z = 2$, particles split three times; from $z = 2$ to $z = 1$, they split four times; from $z = 1$ to $z = 0.5$, they split five times, enhancing the resolution 32×; and from $z = 0.5$ to $z = 0.25$, they split six times. Finally, from $z = 0.25$ to $z = 0$, all CGM particles split seven times, achieving a resolution 128× better than the fiducial simulation.

Fig. 3.3 illustrates the particle mass in the simulation that gradually achieves a 128 times enhancement in CGM resolution. The panels display the mass distribution in the CGM at four key stages: z = 8 (starting point of splitting), z = 2.5, z = 0.8 and z = 0, demonstrating the progressive enhancement of resolution. This effectively confirms that the codes and models are functioning as intended, thereby laying a solid foundation for future analyses.

3.0.3 Summary and Future Outlook

In this section, I have described a novel model that I implemented using the GIZMO code to specifically enhance resolution in the CGM around galaxies. Employing GIZMO for hyper-refinement in the CGM represents an entirely novel approach and marks a significant contribution to the field. My model successfully increases the resolution in the CGM up to 128 times compared to the fiducial resolution.

Currently, my suite of simulations consists of one fiducial and three enhanced CGM resolution simulations. This setup enables two distinct analytical approaches. First, it allows for the analysis of each simulation individually, leveraging their high resolution to study the multiphase structure of the CGM. Second, it provides a comprehensive platform for comparing varying resolutions and their implications on the physical processes and evolution of the CGM.

Looking ahead, the inclusion of Active Galactic Nucleus (AGN) feedback in these simulations is a promising next step. AGN feedback plays a crucial role in the heating and cooling cycles of more massive halos ($M_{halo} > 10^{12} M_{\odot}$). Incorporating it into this advanced CGM resolution model would be a pioneering advancement in the realm of high-resolution simulations.

Furthermore, applying this model in a full cosmological box simulation presents a next level opportunity. It would enable the generation of a more extensive dataset for robust statistical analysis and facilitate direct comparisons with observational properties of the CGM, thus broadening the scope and applicability of this innovative approach.

PART II: Dual and Binary SMBHs Steering Galactic Fates

Chapter 4

Dual AGNs: Precursors of Binary Supermassive Black Hole Formation and Mergers

Accepted for publication at the Astrophysical Journal.

Authors: Vida Saeedzadeh[1], Arif Babul[1,2], Suvodip Mukherjee[3], Michael Tremmel[4], Thomas R. Quinn[5], Lucio Mayer[6]

Abstract: The presence of dual active galactic nuclei (AGN) on scales of a few tens of kpc can be used to study merger-induced accretion on supermassive black holes (SMBHs) and offer insights about SMBH mergers, using dual AGNs as merger precursors. In this study, we use the ROMULUS25 cosmological simulation to investigate the properties and evolution of dual AGNs. We first analyze the properties of AGNs ($L_{bol} > 10^{43}$erg/s) and their neighboring SMBHs (any SMBHs closer than 30 pkpc to an AGN) at $z \leq 2$. This is our underlying population. Subsequently, we applied the luminosity threshold of $L_{bol} > 10^{43} erg/s$ to the neighboring SMBHs thereby identifying dual and multiple AGNs in our simulation. We examined the properties and statistics of dual AGNs in comparison to single AGNs. Our findings indicate an increase in the number of both single and dual AGNs from lower to higher redshifts. All dual AGNs in our sample resulted from major mergers. Compared

[1]Department of Physics and Astronomy, University of Victoria, 3800 Finnerty Road, Victoria, BC, V8P 1A1, Canada
[2]Infosys Visiting Chair Professor, Indian Institute of Science, Bangalore 560012, India [3]Department of Astronomy & Astrophysics, Tata Institute of Fundamental Research, 1, Homi Bhabha Road, Colaba, Mumbai 400005, India
[4]School of Physics, University College Cork, College Road, Cork T12 K8AF, Ireland
[5]Astronomy Department, University of Washington, Box 351580, Seattle, WA, 98195-1580, USA
[6]Institute for Computational Science, University of Zürich, Winterthurerstrasse 190, 8057 Zürich, Switzerland

with the single AGN population, duals are characterized by a lower black hole to halo mass ratio. We found that the properties of dual AGN host halos, including halo mass, stellar mass, star formation rate (SFR), and gas mass, are generally consistent with those of single AGN halos, albeit tending towards the higher end of their respective property ranges. Our analysis uncovered a diverse array of evolutionary patterns among dual AGNs, including rapidly evolving systems, slower ones, and instances where SMBH mergers are ineffective.

4.1 Introduction

The currently favored hierarchical structure formation paradigm, wherein the cosmic structure is built up via successive mergers of systems of increasingly larger size, essentially means that SMBH-SMBH mergers will be ubiquitous over cosmic time, especially since most galaxies are thought to host SMBHs (e.g. Kormendy & Ho, 2013). The path from galaxy-galaxy mergers to the eventual SMBH-SMBH mergers involves a sequence of processes spanning a large dynamic range of spatial scales. In some cases, two SMBHs will pass through a phase where both are accreting and radiating efficiently (e.g. Di Matteo et al., 2005; Hopkins et al., 2008), thereby appearing as close pairs of luminous AGNs (e.g. Gerke et al., 2007; Comerford et al., 2009). Dual AGN events can be used to study accretion on SMBHs and as precursors of SMBH-SMBH mergers (e.g. Saeedzadeh et al., 2023c). They have also been proposed to be indicators of galaxy mergers (Comerford et al., 2009).

Over the past decade, significant attention has been devoted to the detection and study of dual AGNs. Observationally, many dual AGNs have been detected serendipitously. However, recent systematic searches are beginning to address the statistical properties of these systems (De Rosa et al., 2019), focusing on both their occurrence and properties. These detections primarily cover low redshifts, but recent efforts by several groups are extending these detections to high-redshift close pairs using novel observational techniques (Shen et al., 2019, 2021; Hwang et al., 2020; Silverman et al., 2020; Chen et al., 2022b; Mannucci et al., 2022). A small number of multiple [2] AGN systems have also been reported in the literature (e.g. Djorgovski et al., 2007; De Rosa et al., 2015; Hennawi et al., 2015; Liu et al., 2019; Pfeifle et al., 2019), with separations ranging from a few tens to hundreds of kpc.

Given the recent observations and the increasing detection of dual AGNs, there is a growing need for a sample of simulated counterparts to understand the observed sample and its astrophysical implications. Within the realm of idealized galaxy-merger simulations, several studies have focused on AGNs turning on at various pair separations. They also

[2]Three or more

investigate the impact of galaxy merger parameters, including host galaxy mass ratio and morphology on turning on an AGN (e.g. Van Wassenhove et al., 2012a; Blecha et al., 2013; Capelo et al., 2017) and black hole merger timescales (e.g. Mayer, 2017). Idealized merger simulations can resolve sub-kpc scales, which are essential for tracking the dynamics of SMBHs. Nonetheless, these simulations cannot provide predictions about the fraction of AGN pairs in comparison to the total number of AGNs in the universe.

On the other hand, cosmological simulations, which have lower resolution than idealized simulations, can in principle, identify the incidence of dual AGN and shed light on their origins. For example, Steinborn et al. (2016) and Chen et al. (2022b) analyzed the differences between dual and offset AGN. Volonteri et al. (2016) and Ricarte et al. (2021a) examined dual AGN in the context of wandering SMBHs, which are the population of SMBHs that do not settle in the galaxy center and, therefore, are not merging with the central SMBH. Rosas-Guevara et al. (2019a) investigated the abundance of dual AGN as a function of redshift and confirmed that non-simultaneous accretion on SMBHs decreases the detection probability. Volonteri et al. (2022a) investigated the connection between dual AGNs, galaxy mergers, and SMBH mergers. Their study was also expanded to include multiple AGNs.

Among the cosmological simulations mentioned above, very few have been able to produce sub-kpc dual AGNs. This is primarily because achieving sub-kpc spatial resolution, necessary to resolve such close pairs, is computationally expensive in a cosmological context. Additionally, in many simulations, SMBHs are pinned to the gravitational potential minimum to avoid artificial scattering of the SMBH (e.g. Crain et al., 2009; Sijacki et al., 2015; Davé et al., 2019). This results in the rapid merging of two central SMBHs during a galaxy merger, precluding their capture at $\sim$ kpc separations.

ROMULUS is a cosmological simulation that offers the advantages of large-scale simulations for studying the statistics of dual versus single AGN, while also providing high resolution capable of resolving sub-kpc scales. Additionally, the dynamical-friction modeling in ROMULUS allows for one of the first studies of the evolution of AGN pairs and their activation in the context of cosmological simulations. In this paper, we are using ROMULUS25 which is a (25 Mpc)^3 volume simulation with gas and dark matter mass resolution of $2.12 \times 10^5 M_\odot$ and $3.39 \times 10^5 M_\odot$, respectively, and plummer equivalent spatial resolution of 0.25 kpc, which allows AGN pairs to be resolved at separations of few hundred parsecs, a few hundred Myrs after their host galaxies have merged.

In this paper, we investigate the properties of dual AGNs and their host galaxies in comparison with single AGNs. The paper is organized as follows: Section 1.3 provides a summary of the Romulus simulations and explains the detection and definition criteria

used to select AGNs and dual/multiple AGNs. In Section 4.3, we present the results of our analysis, starting from the analysis of AGNs and all their neighboring SMBHs to the properties of dual AGNs and their host halos in comparison with those of single AGNs, highlighting differences and patterns. We also explore the evolution of dual AGNs over time. Finally, in Section 4.4, we summarize our findings.

4.2 Methods

4.2.1 Romulus Simulation

In this study, we present results from analyzing the ROMULUS25 simulation. ROMULUS25 is a $(25; \mathrm{cMpc})^3$ cosmological volume simulation from the Romulus suite (Tremmel et al., 2017, 2019; Butsky et al., 2019; Jung et al., 2022; Saeedzadeh et al., 2023b).

The simulation was run using the Tree+Smoothed Particle Hydrodynamics (Tree+SPH) code CHaNGa (Menon et al., 2015; Wadsley et al., 2017), with the Plummer equivalent gravitational force softening of 250 pc (or 350 pc spline kernel), a maximum SPH resolution of 70 pc, and gas and dark matter particle masses of $2.12 \times 10^5 M_\odot$ and $3.39 \times 10^5 M_\odot$, respectively. The background cosmology is a ΛCDM universe with cosmological parameters consistent with the Planck 2016 results (Ade et al., 2016): $\Omega_\mathrm{m} = 0.309$, $\Omega_\Lambda = 0.691$, $\Omega_\mathrm{b} = 0.0486$, $\mathrm{H}_0 = 67.8\,\mathrm{km\,s^{-1}Mpc^{-1}}$, and $\sigma_8 = 0.82$.

The full details about the ROMULUS25 simulation, including a thorough discussion of the hydrodynamics code and the specifics of the ROMULUS galaxy formation model, the subgrid physics incorporated therein, the various modeling choices made, and the simulation's many unique features, have been described in a number of published papers. In the interest of brevity, we do not repeat this information here and instead refer interested readers to Tremmel et al. (2015, 2017, 2019, 2020); Sanchez et al. (2019); Butsky et al. (2019); Chadayammuri et al. (2020); and Jung et al. (2022). The latter especially offers a concise yet complete summary.

There are, however, a few aspects of the ROMULUS25 simulation that are important to highlight as these are relevant to the present discussion. These pertain to the treatment of SMBH seeding, growth, and dynamical evolution in the ROMULUS25 (Tremmel et al., 2017).

However, it is important to highlight the aspects of the ROMULUS25 simulation that are relevant to this study. Specifically, these involve the treatment of SMBH seeding, growth, and dynamical evolution in the ROMULUS25 (Tremmel et al., 2017).

SMBH Seeding

The ROMULUS25 simulation adopts a unique approach to SMBH seeding that diverges from the methodologies employed in many other cosmological simulations (e.g., Schaye et al., 2015; Weinberger et al., 2017; Pillepich et al., 2018; Davé et al., 2019). In contrast to models that require a host halo or galaxy to exceed a specific mass threshold for the formation of a SMBH, in ROMULUS25 seeding of SMBHs depends only on the local gas properties (Tremmel et al., 2017). As a result, the SMBHs in ROMULUS25 can form in low mass halos and tend to form much earlier (z > 5, Tremmel et al., 2017). Additionally, multiple SMBHs can arise in the same halo.

A gas particle converts into a SMBH seed if it meets the following criteria: (i) it is eligible and selected to form a star following a probabilistic process. (ii) it has very low metallicity ($Z < 3 \times 10^{-4}$); (iii) its density is 15 times the threshold for star formation ($\geq 3\ m_p/\mathrm{cm}^3$), and (iv) its temperature is within the range of $9,500$ - $10,000$ K. This seeding mechanism resembles the direct collapse black hole scenario, where high temperatures and low metallicities inhibit fragmentation, enabling large gas clouds to directly collapse into an SMBH seed (Lodato & Natarajan, 2007; Alexander & Natarajan, 2014; Natarajan, 2021). In ROMULUS25, the SMBHs are seeded with an initial mass of 10^6 $\mathrm{M}_\odot$ to ensure that they are always more massive than dark matter and star particles to mitigate spurious scattering events (Tremmel et al., 2015).

The resulting SMBH occupation fraction at z=0 is consistent with current observations (Ricarte et al., 2019a). Furthermore, the correlation between SMBH masses and their host galaxies' stellar masses follows the observed SMBH mass-stellar mass relation (Tremmel et al., 2017; Ricarte et al., 2019b).

SMBH Dynamics and Mergers

Another aspect where the ROMULUS25 SMBH model differs from other cosmological simulations lies in the treatment of SMBH dynamics. In contrast to several simulations that pin SMBHs at the centers of their host galaxies artificially (e.g. Crain et al., 2009; Sijacki et al., 2015; Davé et al., 2019), ROMULUS25 accurately tracks the dynamical evolution of SMBHs down to sub-kpc scales, which is highly advantageous for this study. To accomplish this, the simulation implements a sub-grid model to represent the unresolved dynamical friction from stars and dark matter, which affects the SMBHs (Tremmel et al., 2015). This effect is calculated for each SMBH by assuming a local isotropic velocity distribution and applying Chandrasekhar's formula, integrating from the 90-degree deflection radius (r_{90}) up to the

gravitational softening length (ϵ_g) of the SMBH. The resulting acceleration is

$$\mathbf{a}_{DF} = -4\pi G^2 \, M_\bullet \, \rho(v < v_{BH}) \, \ln\Lambda \, \frac{\mathbf{v}_{BH}}{v_{BH}^3}, \tag{4.1}$$

Where $\ln\Lambda$ is defined as $\frac{\epsilon_g}{r_{90}}$, with $\mathbf{v}_{BH}$ denoting the SMBH's velocity relative to the local center of mass velocity of the closest 64 star and dark matter particles. Moreover, ρ signifies the mass density, and G is the gravitational constant.

For two SMBHs to merge, they need to be closer than two gravitational softening lengths (0.7 kpc) and have a low enough relative velocity that allows them to be gravitationally bound; that is, $\frac{1}{2} \, \Delta\mathbf{v}^2 < \Delta\mathbf{a} \cdot \Delta\mathbf{r}$, where $\Delta\mathbf{v}$ represents the velocity difference, $\Delta\mathbf{a}$ the acceleration difference between the black holes, and $\Delta\mathbf{r}$ the separation distance (Bellovary et al., 2011; Tremmel et al., 2017)[3]. The criterion of two gravitational softening lengths is used because the simulation's precision in tracking the dynamics of the SMBH pair becomes less reliable below this threshold.

Upon merging, the resulting SMBH is assigned a velocity that conserves momentum, and its mass is the sum of its progenitors' masses. Mergers are one of the two processes through which SMBHs grow.

SMBH Growth and Feedback

Another mechanism for SMBH growth is through the accretion of gas. In the Romulus25 simulation, the rate of gas accretion is determined using a modified Bondi-Hoyle formula (Bondi 1952, for modifications see Tremmel et al. 2017) applied to the smoothed properties of the 32 closest gas particles:

$$\dot{M}_\bullet = \alpha \times \begin{cases} \frac{\pi (G M_\bullet)^2 \rho_{\rm gas}}{(v_{bulk}^2 + c_s^2)^{3/2}} & \text{if } v_{bulk} > v_\theta \\ \\ \frac{\pi (G M_\bullet)^2 \rho_{\rm gas} c_s}{(v_\theta^2 + c^2)^2} & \text{if } v_{bulk} < v_\theta \end{cases}, \tag{4.2}$$

where $\rho_{\rm gas}$ is the ambient gas density, c_s is the ambient sound speed, v_θ is the local rotational velocity of surrounding gas, and v_{bulk} is the bulk velocity relative to the SMBH. These ambient quantities are calculated based on the 32 gas particles closest to the SMBH. The inclusion of v_θ and v_{bulk} in this formulation is designed to address the original Bondi-Hoyle-Lyttleton approach's oversight of the gas's bulk movement and angular momentum. To correct for the suppression of the black hole accretion rate due to resolution effects, the

[3]Note that there is a typographical error in the criterion for boundedness in Tremmel et al. (2017).

coefficient α is employed, which is defined as

$$\alpha = \begin{cases} (\frac{n}{n_{th,*}})^2 & \text{if } n \geq n_{th,*} \\ \\ 1 & \text{if } n \leq n_{th,*} \end{cases}, \tag{4.3}$$

where $n_{th,*}$ is the star formation number density threshold ($0.2\ m_p/cc$).

The process of gas accretion onto a SMBH generates energy that is released into the black hole's surrounding area. In the ROMULUS25 simulation, this released energy is assumed to be electromagnetic, with a portion of it coupled to the nearby gas and contributing to its internal energy. The rate at which thermal energy is deposited is described by $\dot{E}_{\bullet,th} = \epsilon_r \epsilon_f \dot{M}_\bullet c^2$, where ϵ_r represents the radiative efficiency (set at 10%) and ϵ_f denotes the efficiency of coupling to the gas (set to 2%). This thermal energy is isotropically distributed to the closest 32 gas particles based on the smoothing kernel. We refer readers to Tremmel et al. (2017) for further details.

4.2.2 Halo catalogue and substructure definition

In the Romulus simulations, halos are identified and processed using the Amiga Halo Finder (AHF, Knebe et al., 2008; Knollmann & Knebe, 2009). Their evolution over time is tracked with TANGOS (Pontzen & Tremmel, 2018).

Halos and subhalos form a hierarchical arrangement in which halos serve as the primary structures and the subhalos are nested within them. AHF employs an adaptive smoothing method to detect density peaks for identifying these structures. It identifies all gravitationally bound particles (including dark matter, gas, stars, and SMBHs) associated with each density peak and then moves to higher levels in the hierarchy to locate larger structures. After halos are identified, their centers are determined using the shrinking sphere method (Power et al., 2003), which relies on the distribution of bound particles linked to each halo.

The masses of the halos (M_Δ) are calculated by enclosing each halo center within a sphere of radius R_Δ. This sphere is constructed so that the average density within it, $\langle \rho_{\mathrm{m},\Delta}(z) \rangle$, matches Δ times the critical cosmological density, $\rho_{\mathrm{crit}}(z)$. Here, ρ_{crit} is critical density of the universe and Δ is a constant (see, for example, Babul et al., 2002). In this study, we refer to (M_{200}, R_{200}) which correspond to $\Delta = 200$.

The above prescription is only specifically for the halos. For subhaloes, AHF tracks the local density profile relative to the distance from the peak's center. At some point, the external gravitational field becomes dominant, and correspondingly, the behavior of the

density profile changes. The distance from the peak where this happens marks the size of the subhalo, and the mass enclosed is recorded as the subhalo's mass.

4.2.3 Selection of dual/multiple AGNs

We perform our analysis at nine different outputs from z = 0.05 to z = 2 in increments of $\Delta z \sim 0.25$. At each redshift, a detected AGN is defined as a SMBH with a bolometric luminosity $L_{bol} > 10^{43}$erg/s. This threshold allows us to focus on AGNs that are sufficiently powerful to be identified observationally.

As mentioned in section 1.3 in the ROMULUS black hole model, during the accretion process, thermal energy is injected isotropically into the surrounding gas particles, assuming a radiative eciency of 10% and a feedback coupling eciency of 2%. To determine the bolometric luminosities, we adopt the same radiative efficiency. Therefore, $L_{bol} = 0.1\dot{M}_\bullet c^2$, where $\dot{M}_\bullet$ is mass accretion rate into the SMBH and c is speed of light.

We begin by identifying SMBHs within a 30 pkpc from a detected AGN, labeling these as neighbor SMBHs. This 30 pkpc threshold is theoretically motivated by focusing on systems likely to interact or that are currently interacting. It also aligns with the typical separations used in observational searches for dual AGNs (e.g. Comerford et al., 2013; Silverman et al., 2020). In this stage, the selection of neighbor SMBHs is not subject to specific mass or luminosity thresholds (note that our seed SMBH mass is $10^6\,M_\odot$; therefore all SMBHs necessarily have $M_\bullet > 10^6\,M_\odot$). These neighboring SMBHs may reside within the same halo as the AGN or in a separate halo. The combined set of AGNs and their neighbor SMBHs form the underlying population for our study.

To categorize AGNs as single, dual, or multiple, we investigate each detected AGN for neighboring SMBHs that are "active" defined as having $L_{bol} > 10^{43}$erg/s. An AGN is classified as "single AGN" if none of its neighboring SMBHs meet this luminosity criterion. Conversely, if one neighboring SMBH is active, we classify the AGN and its active neighbor as a "dual AGN". In scenarios where more than one neighboring SMBH is active, they are classified as "multiple AGNs", leading to the identification of triple and quadruple AGN configurations in our study.

According to the procedure just described, two non-central SMBHs may be classified as a dual AGN, and systems with multiple AGNs may be counted as more than one dual. For example, in a scenario where three AGNs within a 30 kpc radius region meet the criteria, they would be counted as three separate dual AGNs. To prevent overcounting, we adopt a hierarchical approach, starting with the highest order of multiplets and working down

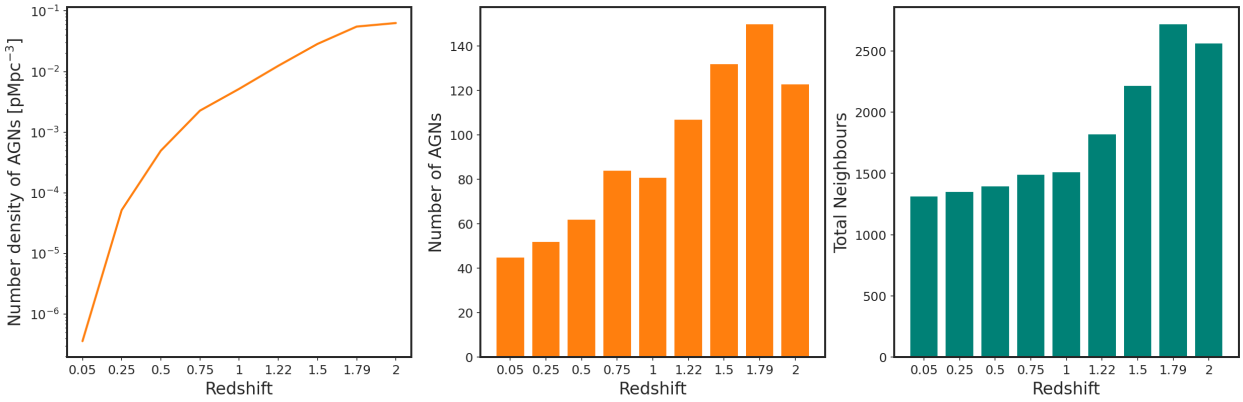

Figure 4.1: AGN number density, AGN counts and total number of neighboring SMBHs across redshifts. The first panel illustrates the number density of AGNs detected at redshifts under consideration. The middle and right panel presents the absolute number of AGNs and the total number of SMBH neighbors within a 30 pkpc radius of the AGNs, respectively.

to duals. We first identify clusters of four AGNs the highest multiple for our reference luminosity and distance cuts and remove them from the list. Then we proceed similarly with triplets, ultimately leaving us with 'pure dual AGNs.

In dual AGNs, the brighter AGN in the pair is referred to as the "primary" and the fainter one is called the "secondary". Primary and secondary AGNs are selected at the same output, i.e. at the same redshift. We identify the host galaxies of the SMBHs with AHF. However, it should be noted that during the close encounters of galaxies, AHF is not always able to separate the merging systems well. This is especially the case for hosts that have undergone strong gas and stellar disruption. Finally, when tracing SMBH host galaxy properties back in time, we always follow the more massive progenitor if the SMBH of interest has gone through prior mergers.

4.3 Results

In §4.3.1, we delve into the statistics and properties of our underlying population of AGNs and their neighboring SMBHs, establishing a baseline for our study. Following this, §4.3.2 is dedicated to examining the occurrence rate of dual and multiple AGNs in our simulation. Then, in §4.3.3, we focus on dual AGNs and conduct a detailed analysis of the characteristics of these AGNs and their host halos in comparison with those of single AGNs, highlighting differences and patterns. Finally, in §4.3.4, we trace the evolution of dual AGNs over time, exploring their developmental trajectories.

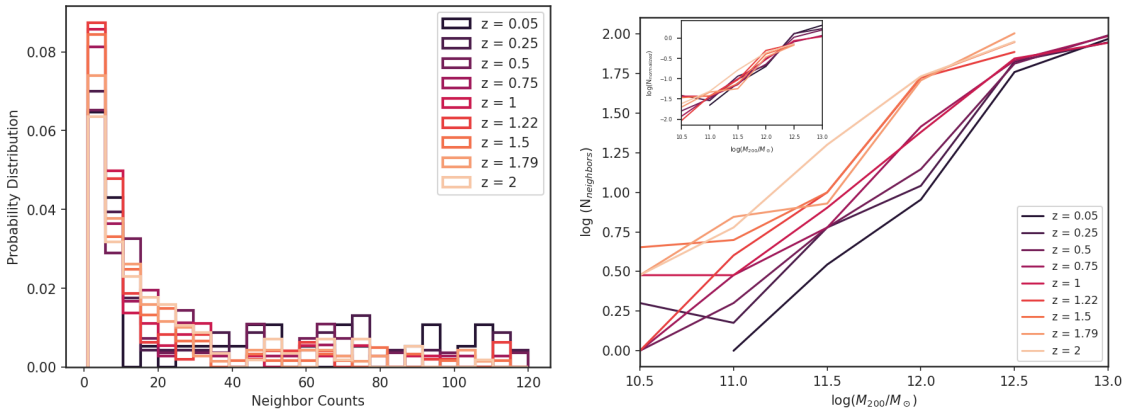

Figure 4.2: The *top panel* displays the probability distribution of neighbor counts around AGNs at varying redshifts normalized to integrate to unity. Lighter colors represent higher redshifts and darker colors indicate lower redshifts. The *bottom panel* shows the logarithm of the number of neighbors as a function of the host AGN halo M_{200}, with each line representing the median of neighbors counts at each mass bin. This demonstrates a near-linear relationship between halo mass and neighbor counts, with higher mass halos having more neighboring SMBHs.

4.3.1 Characteristics of the Underlying AGN Population

We begin our analysis by examining the statistics of AGNs within the Romulus25 simulation across the redshifts under consideration. This analysis also includes their neighboring SMBHs that are situated within 30 pkpc of each AGN. As mentioned above, at this stage, no mass or luminosity thresholds are applied to these neighboring SMBHs.

The left panel of Fig. 4.1 displays the number density of AGNs at each redshift, while the middle and right panels show the absolute numbers of AGNs and neighboring SMBHs, respectively. The AGN number density increases from z = 0.05 to z = 2, aligning with observational results of AGN number density (Hewitt & Burbidge, 1993; Steffen et al., 2003; Wolf et al., 2003; Brusa et al., 2010; Ceraj et al., 2018). The AGN count rises from 40 at z = 0.05 to over 140 at z = 1.79, then slightly declines to 120 at z = 2 in the simulation volume (25 cMpc^3). The total number of neighboring SMBHs reflects a similar pattern, increasing from 1000 to more than 2600 from lower to higher redshifts.

The probability distribution of neighboring SMBH counts around an AGN at each redshift is shown in the top panel of Fig. 4.2. Each distribution is normalized to integrate to unity, which facilitates comparison across different epochs. Dark-to-light colors in the figure correspond to lower to higher redshifts. At all epochs, each AGN has at least one neighbor. While most ($\sim$ 83%) of neighbor counts are below 40, they can reach up to 120, with a

higher probability of encountering more than 40 neighbors at lower redshifts.

The bottom panel of Fig. 4.2 demonstrates that the number of neighbors increases with halo mass. Each line represents the median number of neighbors versus AGN host halo mass. The number of neighboring SMBHs scales roughly linearly with the halo mass, a trend stretching from dwarf galaxy halos to massive galaxy groups. These findings align with the results of previous studies on SMBH distribution in ROMULUS halos. Ricarte et al. (2021b), who investigated all wandering SMBHs in Romulus halos, also identified a linear relationship between the number of SMBHs in a halo and their host halo mass. They showed that the majority of these wandering SMBHs originate from the centers of destroyed infalling satellite galaxies. Therefore, as higher mass halos are expected to have undergone more mergers in hierarchical assembly, having a higher number of neighbor SMBHs is not surprising.

Exploring the redshift dependency: for redshifts $z > 1$, the halo mass range is $10.5 < \log(M_{200}/M_\odot) < 12.5$, while for $z < 1$, it extends to massive groups with $\log(M_{200}/M_\odot) \leq 13$. This expansion of the range at lower redshifts explains the observed increase in the probability of larger neighbor counts around AGNs at these redshifts. There are more massive halos at these redshifts, and massive halos have a higher number of neighbors; thus, there is a higher count of neighbors at low redshifts. Another notable feature is that in low-mass halos, the number of neighbors decreases with decreasing redshift, reflecting the evolution of the SMBH occupation fraction towards the present. The inset subplot in the top left normalizes the median in each mass bin at each redshift by the total number of neighboring SMBHs at that redshift. This effectively removes the redshift effect, resulting in all lines converging.

Another insightful aspect is neighbours' spatial distribution. Fig. 4.3 shows the median distance of neighbor SMBHs to their corresponding AGN as a function of AGN's host halo mass. Across all redshifts, we observe that the median distance ranges from less than 5 kpc to greater than or equal to 15 kpc. A notable trend emerges: higher halo masses correspond to larger median distances between AGNs and their neighboring SMBHs. This trend can be attributed to the higher velocity dispersion in massive halos, which extends the orbital decay time (Binney & Tremaine, 2008), causing SMBHs to be more widely dispersed. Moreover, these massive halos are more likely to experience frequent mergers, further introducing SMBHs and increasing the velocity dispersion. Consequently, larger halos not only contain a greater number of SMBHs but also their SMBHs are more dispersed.

Furthermore, we highlight that most SMBH concentrations are found within 20 kpc of the AGN. When we scale these distances by the R_{200} of the AGN's host halo, we find that the majority of neighboring SMBHs reside within $0.2R_{200}$. Those outside this boundary

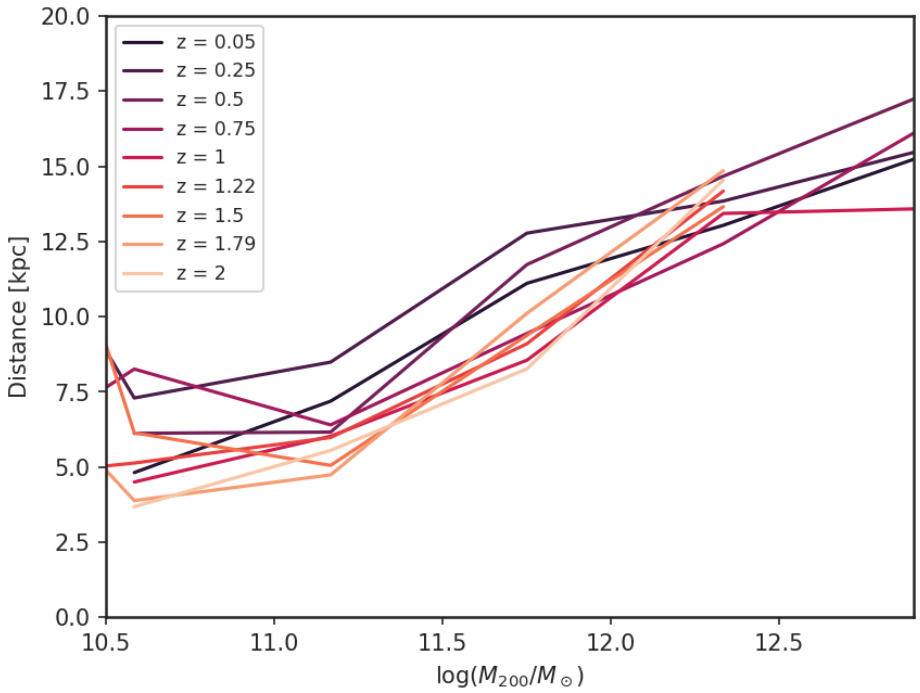

Figure 4.3: Relationship between halo mass and distance of neighboring SMBHs from their corresponding AGN across redshifts. Each line represents the median distance at a specific redshift. The increasing trend illustrates that higher halo masses correlate with a greater spread of neighboring SMBHs.

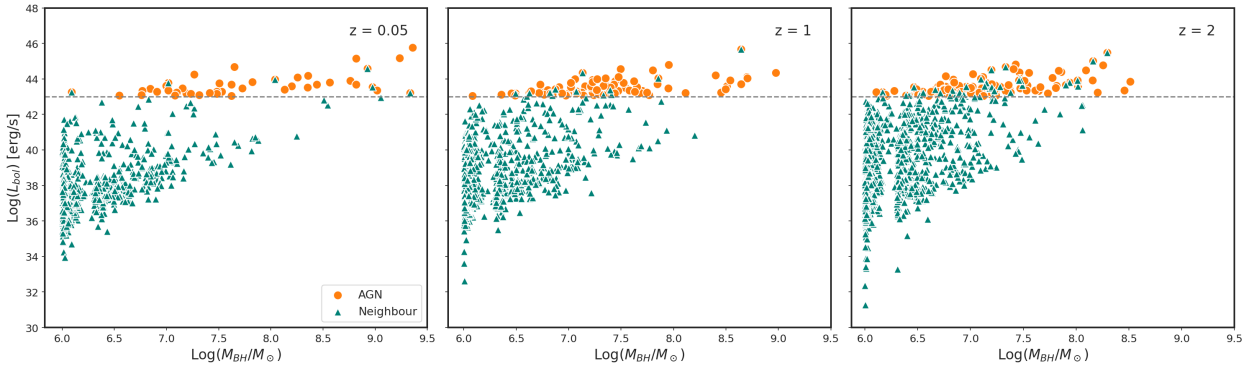

Figure 4.4: Bolometric luminosity as a function of SMBH mass for AGNs and their neighboring SMBH at three different redshifts (z = 0.05, 1, and 2). AGNs are represented by orange circles, while the neighboring SMBHs are depicted as teal triangles. The dashed line indicates the luminosity cut for defining AGNs.

are typically associated with subhalos, accounting for less than 2% of the total counts of neighboring SMBHs at each redshift.

Lastly, we turn our attention to the mass and luminosity of AGNs and their neighboring SMBHs. A variety of models predicts that neighboring SMBHs can manifest as off-nuclear X-ray or radio sources (Fujita, 2008; Bellovary et al., 2010; Sijacki et al., 2011; Steinborn et al., 2016; Barrows et al., 2019; Zivancev et al., 2020; Guo et al., 2020; Bartlett et al., 2021). In Fig. 4.4, we plot the bolometric luminosities of AGNs (as orange circles) and neighboring SMBHs (as teal triangles) against their mass. The grey dashed line shows the luminosity cut used to define AGNs. We present illustrative results at z = 0.05, 1, and 2 for brevity, but we confirm that the observed trend remains consistent across all redshifts under consideration.

At higher redshifts, we see that the SMBH mass range is generally limited to $M_\bullet < 10^8 M_\odot$. Interestingly, even SMBHs with masses close to the seed mass ($M_\bullet \geq 10^6 M_\odot$) contribute to high luminosity ($L_{bol} > 10^{43} erg/s$). We also note that the luminosity range for neighboring black holes can be as low as $L_{bol} \sim 10^{31} erg/s$. As redshift decreases, the general count of AGNs with luminosity above the threshold (and also the number of neighbor SMBHs) diminishes. Their mass range expands to $M_\bullet > 10^9 M_\odot$, and SMBHs with mass $M_\bullet < 10^7 M_\odot$ are less likely to contribute to high luminosities. On the other hand, the minimum luminosity of neighbors increases, with their minimum be $L_{bol} \sim 10^{34} erg/s$. These findings suggest that with more sensitive instruments, a significantly larger number of AGNs with luminous companions could be detected.

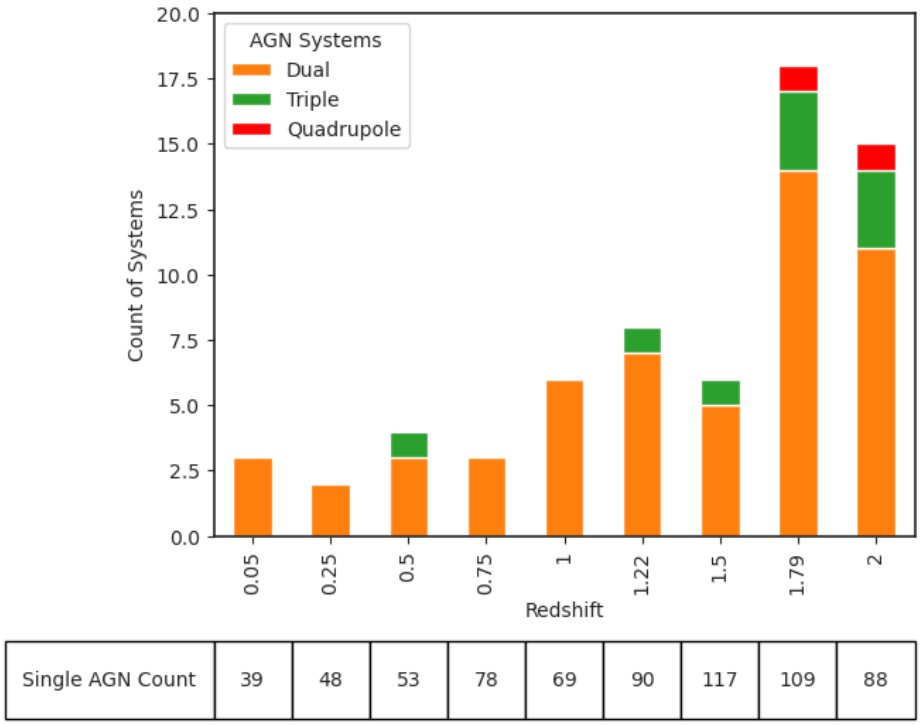

Single AGN Count	39	48	53	78	69	90	117	109	88

Figure 4.5: Count of AGN systems at different redshifts in the Romulus25 simulation, categorized by dual (orange), triple (green), and quadruple (red) AGNs. The number of single AGNs for each redshift is displayed in the table cells located below the corresponding bars in the chart.

4.3.2 Occurrence Rates of Dual/Multiple AGNs

In the Romulus25 simulations, not only dual AGNs are present but also there are instances where more than two luminous AGNs are in close proximity to each other. The occurrence of dual and multiple AGN systems, in comparison to the population of single AGNs, could serve as an indicator of the frequency of massive galaxy mergers and flag the potential binary SMBH that are nano-Hertz gravitational wave sources (Saeedzadeh et al., 2023c).

Fig. 4.5 presents the distribution of systems with single, dual, triple, and quadruple AGNs. It is evident that multiple (i.e. triple, and quadruple) AGNs predominantly occur at higher redshifts, with quadruple systems exclusively identified at z = 1.79 and 2. Additionally, the data shows a rise in the counts of dual AGNs with increasing redshift. This trend is consistent with an increase in overall AGN number densities with redshift, as shown in Fig. 4.1, which correlates with higher frequency of galaxy interactions in the higher redshifts (Patton et al., 2002; Hopkins et al., 2007).

We calculated the probability of an AGN having another AGN counterpart at each red-

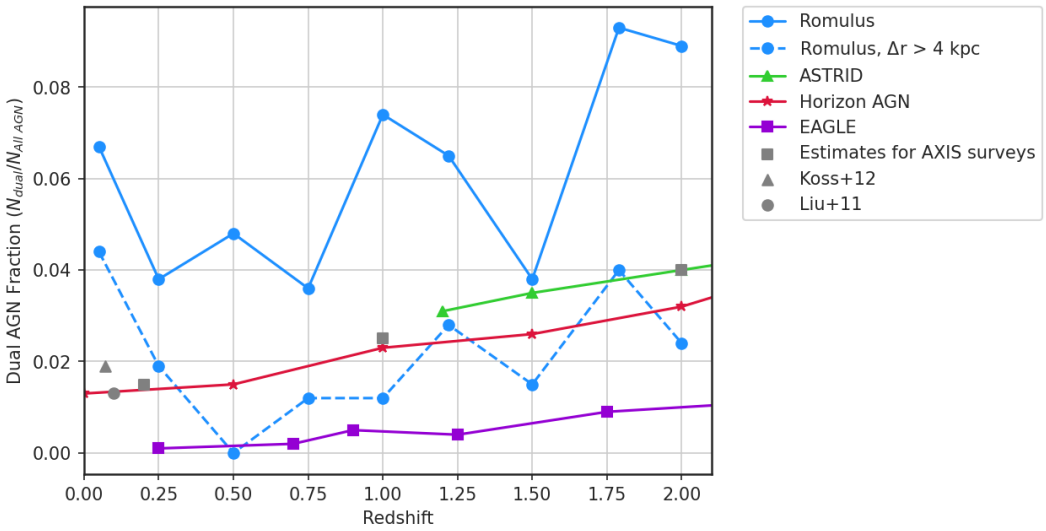

Figure 4.6: Predictions of the dual AGN fraction as a function of redshift from our sample in ROMULUS (blue solid line) compared to other cosmological simulations: ASTRID (Chen et al., 2023), HORIZON-AGN (Volonteri et al., 2022a), EAGLE (Rosas-Guevara et al., 2019b) with green, red and purple lines respectively. We also show the dual fraction in ROMULUS with a separation criterion of 4 kpc $< \Delta r <$ 30 kpc with a dashed blue line. Observational estimates and predictions are presented with grey square (predictions for upcoming AXIS surveys, Foord et al., 2023), grey triangle (Koss et al., 2012) and grey circle (Liu et al., 2011).

shift. To do so we divided the number of AGNs within dual or multiple systems by the total AGN population. Results show that the likelihood of an AGN having *at least* one AGN counterpart increases markedly from lower to higher redshifts, starting from a range of 7 to 14% between z = 0.05 and z = 1.5, and jumping to 27% at z = 1.79 and z = 2.

Furthermore, in Fig. 4.6, we focus exclusively on the fraction of dual AGNs relative to all AGNs in ROMULUS compared with other simulations and observational results up to z = 2. ROMULUS exhibits a higher fraction than all other simulations. This can be attributed to ROMULUS having a higher spatial resolution than the simulations mentioned, allowing it to resolve dual AGNs with separations of less than 1 kpc, as well as the fact that it has a sophisticated dynamical friction model that tracks SMBH dynamics and does not force them to merge when galaxies merge. Among other simulations, EAGLE (Rosas-Guevara et al., 2019b) does not implement a dynamical friction model for SMBHs and reports dual AGNs with a minimum separation of 5 kpc. HORIZON AGN includes a dynamical friction model, but its merging criteria merge SMBHs with separations of less than 4 kpc (Volonteri et al., 2022a), thus not allowing for the resolution of duals below that separation. ASTRID includes a dynamical friction model and also has a higher resolution than both EAGLE and HORIZON AGN, with a spatial resolution of $\sim$ 1.4 kpc, and exhibits a higher fraction than the others (Chen et al., 2023) as well. The observational results also suffer from the inability to resolve closely separated dual AGNs. All mentioned observational estimates (Liu et al., 2011; Koss et al., 2012) as well as the theoretical estimates for upcomming AXIS surveys (Foord et al., 2023) report separations of greater than 5 kpc . It's worth noting that if we limit our sample to duals with separations greater than 4 kpc, our dual AGN fraction (shown by a dashed blue line) decreases and aligns with other simulations and observational estimates. These results predict a substantial likelihood of dual AGNs motivating deep surveys and sensitive instruments capable of testing this prediction.

4.3.3 Properties of Dual AGNs

Having explored the occurrence rates of dual and multiple AGNs, we now narrow our focus to dual AGNs for a more detailed analysis. We only concentrate on dual AGNs because of the relatively low statistical representation of multiple AGNs in our simulations, which limits the robustness of any analysis we could conduct on them. Here we explore dual AGNs properties, such as their separation, luminosity, mass, and the characteristics of their host halos.

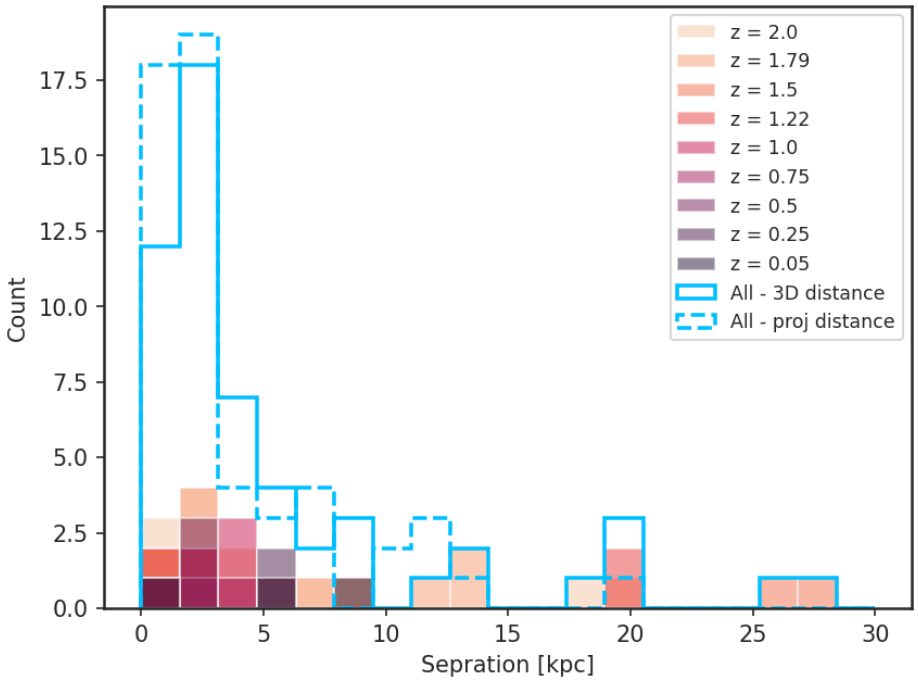

Figure 4.7: Distribution of separations between SMBHs in dual AGNs at redshifts under consideration. Each redshift is represented by a distinct color, with filled histograms indicating the count of dual AGNs at that specific redshift. The solid blue line outlines the combined count for all redshifts, illustrating the 3D physical separation between dual AGNs, while the dashed blue line represents the projected 2D separations on the x-y plane. The plot highlight a higher frequency of dual AGNs with separations less than 10 kpc, peaking around 2 kpc.

Separation

Fig. 4.7 illustrates the distribution of separations between the two SMBHs in dual AGNs across the redshifts under consideration. The distribution at each redshift is represented by filled histograms, while the combined data for all redshifts is shown in an unfilled blue histogram. The solid blue line indicates the 3D physical separation. The projected physical separation is also shown by a dashed blue line to mimic the selection function of observations. Here, we take the projected separation to be the projection of the 3D separation onto the x − y plane.

The blue solid histogram indicates that the majority of dual AGNs in our sample have separations below 10 kpc, with a notable increase within 5 kpc and a peak around 2 kpc. In our sample, the probability of observing a dual AGN with a separation of less than 2 kpc is seven times higher than at larger separations. The 2D projected separation histogram shows

closer separations between the duals, resulting in an increase in duals with separation < 1 kpc and a maximum separation of 20 kpc (compared to 27 kpc in 3D). The overall trend is consistent with the 3D data, showing a higher concentration of duals within 10 kpc and a peak at 2 kpc. Since our simulation adopts a sub-grid dynamical friction model and it has a high resolution, it allows for the identification of dual AGNs at separation ~ 0.7 kpc. In previous works, Rosas-Guevara et al. (2019b) observed a peak in dual separations near $20 - 25$ kpc, but their study excluded pairs below 5 kpc. Other simulations using different sub-grid dynamical friction models which allow black holes to approach closer than 5 kpc before merging, have similarly found a higher probability density of duals at separations less than 5 kpc, aligning with our findings (Steinborn et al., 2016; Volonteri et al., 2022b; Chen et al., 2023).

In our comparative analysis of the dual AGN population across various redshifts, we find interesting dierences. Specifically, we find that at $z < 1$, all dual AGN in our sample shows a separation of less than 10 kpc. At higher redshifts ($z > 1$), the number of dual AGN systems with separations higher than 10 kpc increases, such that 23% of dual AGNs at these redshifts have separations exceeding 10 kpc. This variance suggests an evolution in the spatial dynamics of dual AGNs over cosmic time. All duals are detected to be in the same halo at the time of observation, where the host halos are identified with the subhalo catalog generated by AHF. The only exception is the SMBHs in a dual AGN with a 27 kpc separation at $z = 1.5$, which are located in two different halos.

Mass and Luminosity

Fig. 4.8 displays the relationship between luminosity and mass for the two SMBHs involved in the dual AGN systems at all redshifts under consideration, alongside the population of single AGNs for comparison. A single AGN is an AGN when none of its neighboring SMBH has luminosity above the threshold of $10^{43} erg/s$. The central panel shows the scatter plot of luminosity against SMBH mass, while the upper and right panels present the 1D distributions of SMBH masses and luminosities, respectively. In this figure, the primary (brighter) SMBHs of the dual AGNs are represented in orange, while the secondary (fainter) SMBHs are indicated in blue. The single AGNs are plotted in grey. Each histogram is normalized to the total population of SMBHs within the respective category they represent and dashed lines show the median of the properties for each category.

The luminosity of the AGNs ranges from our threshold of 10^{43} to $10^{46} erg/s$ and masses range from the simulation SMBH seed mass of 10^6 to $3 \times 10^9\,\mathrm{M}_\odot$. From the scatter plot

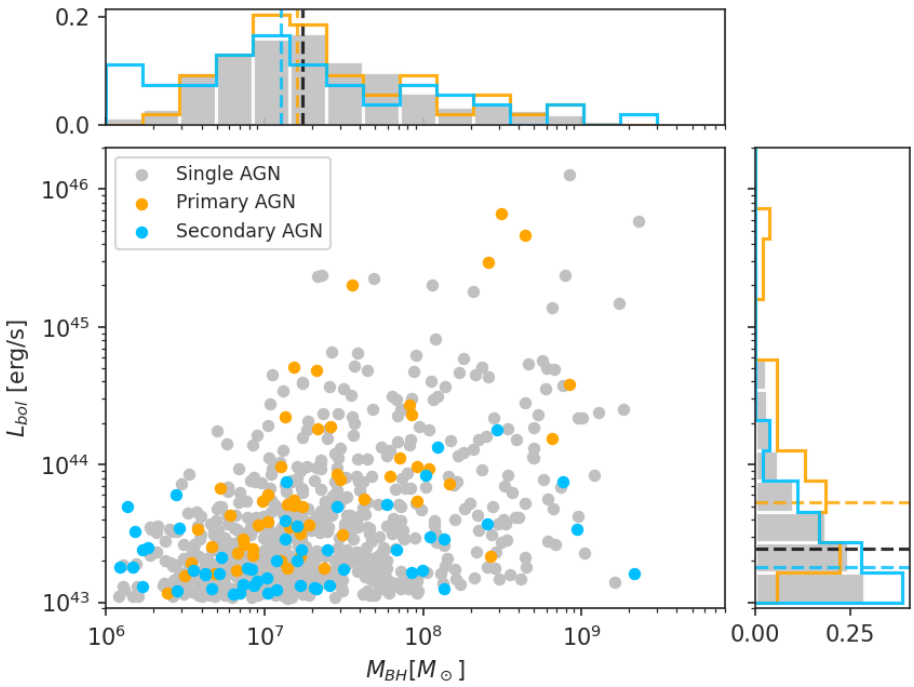

Figure 4.8: The relationship between the bolometric luminosity and mass of SMBHs in single and dual AGN systems. Single AGNs are represented by grey dots, primary AGNs in dual systems by orange dots, and secondary AGNs by blue dots. The top panel shows the normalized distribution of SMBH mass for the different populations, while the right panel displays the normalized distribution of bolometric luminosity. Dashed lines showing the medians.

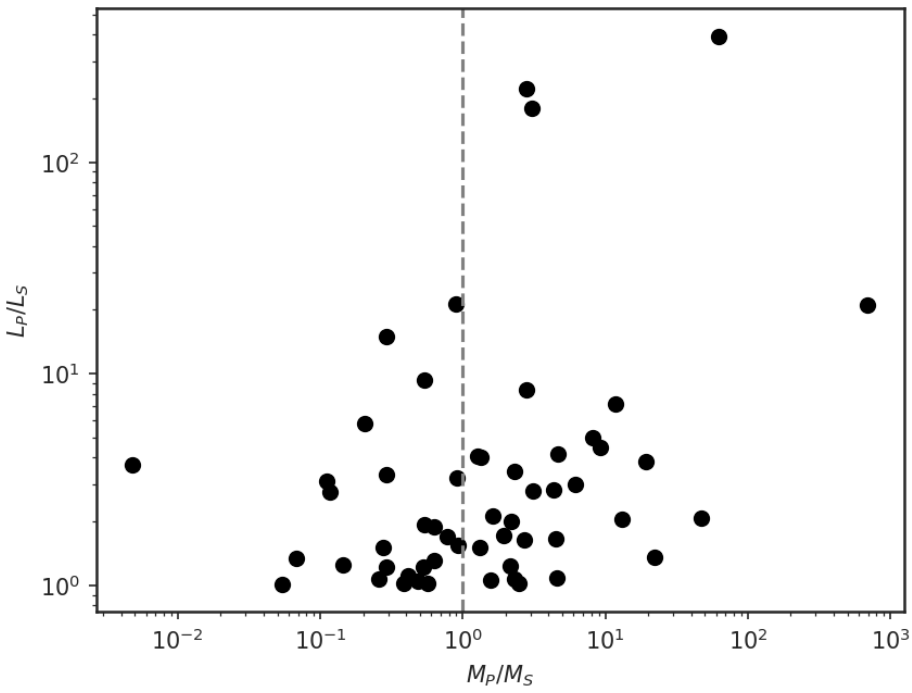

Figure 4.9: Scatter plot illustrating the ratio of bolometric luminosities to the mass ratio of primary to secondary supermassive black holes (SMBHs) in dual AGN systems. Each point represents a dual AGN, plotted with respect to the mass ratio on the x-axis and luminosity ratio on the y-axis. The dashed vertical line at $M_p/M_s = 1$ demarcates equal mass pairs.

and histograms, we find that the ranges of luminosity and mass for dual AGNs are not significantly different from those of single AGNs. This finding is in agreement with the observational results reported by Tang et al. (2021).

Examining the top panel of Fig. 4.8, we see that the shape of the mass histograms for the primary and secondary SMBHs in dual AGNs, as well as for single AGNs, are generally similar, each peaking at approximately $M_{BH} \sim 10^7 M_\odot$. The main differences compared to single AGNs are: (i) a higher proportion of primary SMBHs in dual AGNs have a mass of $10^7 M_\odot$ and (ii) secondary SMBHs in dual systems more frequently exhibit masses lower than $10^7 M_\odot$. This suggests that a low-mass black hole with a bolometric luminosity greater than $L_{bol} > 10^{43} erg/s$ is more likely to be part of a dual system than to be a single AGN.

In terms of luminosity distribution (right panel, Fig. 4.8), the secondary SMBHs exhibit a pattern similar to that of single AGNs, with a large proportion clustered around the threshold $L_{bol} \sim 10^{43} erg/s$. Conversely, the luminosity distribution of primary SMBHs in dual systems skews towards higher values, a trend that arises from our definition of the primary SMBH as the more luminous of the pair. Notably, a greater fraction of primary SMBHs display luminosities exceeding $10^{44} erg/s$ compared to single AGNs. Among all AGNs in our sample with luminosities above $10^{45} erg/s$, $\sim$30% are part of a dual AGN system.

We explore the primary to secondary SMBHs luminosity and mass ratio in Fig. 4.9. The luminosity ratio can exceed values of 10, though only about 10% of duals present such a high luminosity contrast, with the primary AGN being more than ten times brighter than the secondary. This high contrast has been reported in observational works such as Koss et al. (2012) and has been seen in various simulations (e.g. Callegari et al., 2009; Steinborn et al., 2016; Capelo et al., 2017; Chen et al., 2023) as well. The majority of duals in our sample display a more moderate average luminosity contrast of 3 to 1.

Notably, there are 45% of duals with mass ratio $M_p/M_s < 1$ and luminosity ratio $L_p/L_s > 1$, indicating that the lower mass SMBH in the dual AGN system is outshining the more massive one. We investigate the environment resulting in such cases in the next section (§4.3.4). Our findings suggest that the local gas density within the vicinity (less than 1 kpc) of SMBHs plays a crucial role in instances when the less massive SMBH becomes more luminous than its more massive counterpart. Specifically, a higher gas density surrounding the less massive black hole leads to increased accretion rates, thereby boosting its luminosity. This is predominantly observed when the less massive SMBH is near pericenter and gas fueling and the loss of angular momentum are enhanced. This result is in agreement with idealized high-resolution binary black hole merger simulations (e.g. Capelo et al., 2017)

Host halos

In this section, we shift our focus to the host halos of dual AGNs, comparing their properties with those of single AGN hosts. Fig. 4.10 central panel illustrates the $M_{BH}-M_{200}$ relationship for dual and single AGNs and their respective host halos, while the top panel presents the one-dimensional distribution of the halo masses with histograms and their median with dashed lines. The mass distributions of all single AGNs are shown in grey. The red dashed curve represents the median M_{BH} for these AGNs within each halo mass bin and the shaded region encloses the scatter of the 16 - 84% of the M_{BH} in that halo mass bin. The masses of the primary and secondary AGNs are represented in orange and blue, respectively, plotted against the mass of their host halo. Our sample included only one dual AGN system in separate halos, which is excluded from this analysis to maintain consistency, as all other dual systems are in the same halo.

From the 1D distribution of halo mass, we see that dual AGNs, shown with cyan histogram, favor the more massive halos. For single AGNs, the halo masses peak at $2\times10^{11}M_{\odot}$. The host halo mass distribution for dual AGNs exhibits a bimodal pattern, with the first peak being only marginally higher than that for single AGNs, at $3\times10^{11}M_{\odot}$. The second peak occurs at $3\times10^{12}M_{\odot}$. Notably, the occurrence of dual AGNs significantly decreases in less massive halos. Furthermore, a larger proportion of dual AGNs' host halos exhibit $M_{200}>10^{12}M_{\odot}$. Part of the reason for the skewed halo mass distribution of duals is that the dual AGN mostly selects out primaries that are on the massive end of the single AGN population (see Fig. 4.8). Comparing the $M_{BH}-M_{200}$ relation of duals with that of single AGNs in the central panel, we see that more than 80% of pairs have halo masses above the median relation in the same SMBH mass bin of single AGNs, meaning that SMBHs in duals are under-massive relative to their host halos. This finding aligns with results from a previous study by Steinborn et al. (2016) on z = 2 AGN pairs, which noted that the M_{BH} in these pairs was systematically under-massive compared to their host masses. One possible explanation is that the host halos of SMBHs that are now involved in a dual AGN system merge but it takes a longer time for the SMBHs themselves to merge and meet the median $M_{BH}-M_{200}$ relation of single AGNs. We tested this hypothesis by comparing the sum of the SMBH masses in each dual system against halo mass; the combined SMBH masses fall within the grey shaded area that matches the single AGN mass-halo mass relationship.

Fig. 4.11 compares the stellar mass, specific star formation rate (sSFR) and gas mass within a 30 kpc radius from the centers of host halos for dual AGNs with those of single AGN hosts. In our analysis, we normalize the histogram counts for each property by the

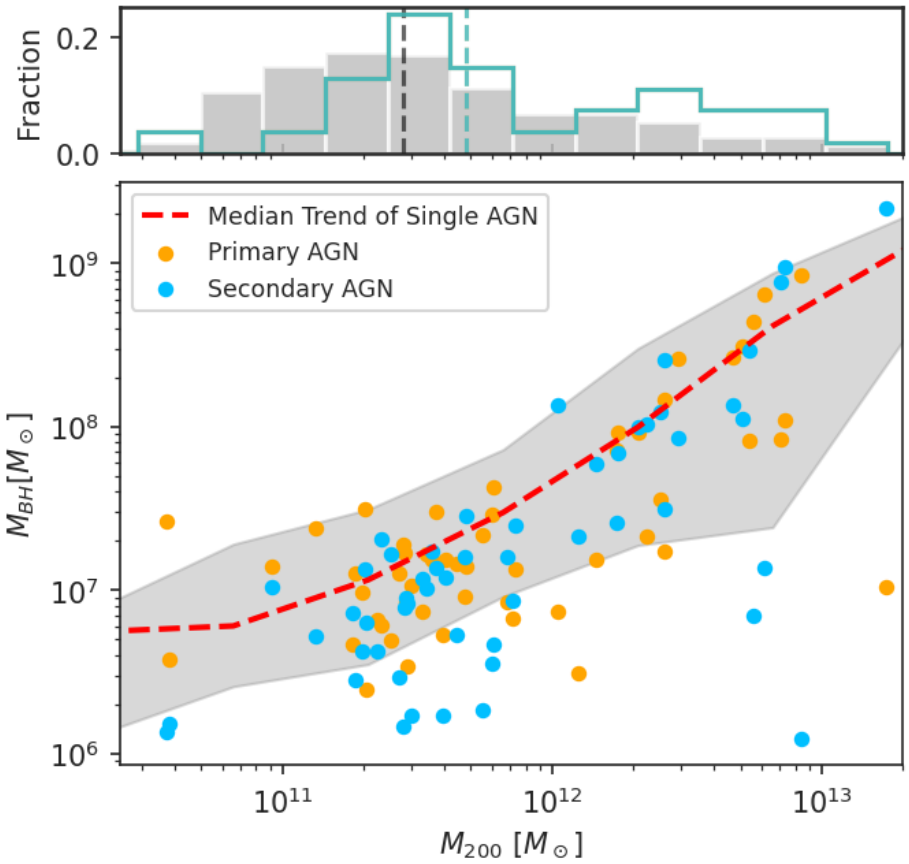

Figure 4.10: Relationship between Black Hole Mass and Halo Mass for dual AGNs. This scatter plot illustrates the primary AGN masses in orange and the secondary AGN masses in blue, plotted against their host halo mass. The dashed red line indicates the median trend of single AGNs for comparison. The shaded region encloses the scatter of the 16 to 84% of the MBH in the halo mass bin. The histogram at the top displays the normalized count of the halo mass distribution for single AGN hosts in grey and for dual AGN host halos in cyan. Dashed lines show medians.

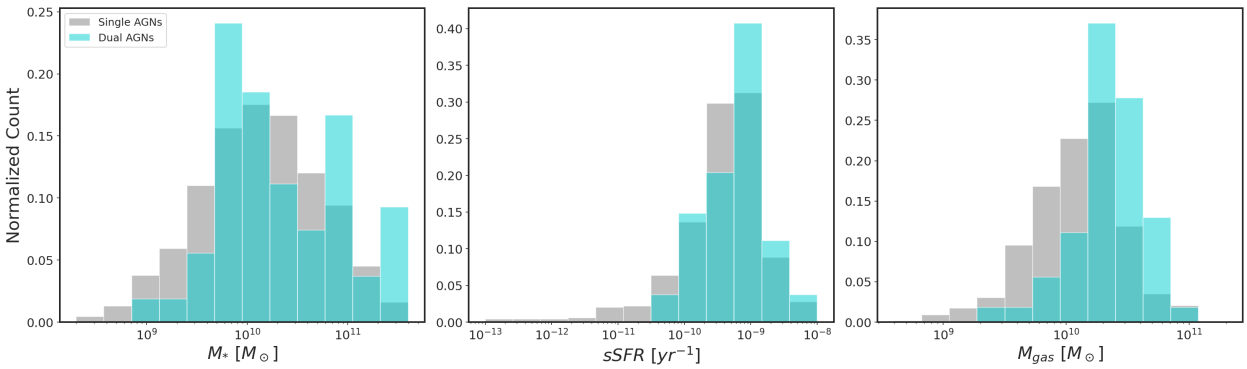

Figure 4.11: Comparative Distribution of AGN Host Properties. The left panel displays the stellar mass distribution, the center panel shows the specific star formation rate gas mass distribution and the right panel illustrates the gas mass distribution for single (grey) and dual (cyan) AGNs inside a 30 kpc sphere around their host halo center.

total counts of single and dual AGNs, respectively. The first panel, which focuses on stellar mass, reveals similar distributions for both dual and single AGN host galaxies. This finding aligns with the observation of Stemo et al. (2021), who reported no significant differences in the galaxy mass distributions between AGN pairs and single AGN samples. Our results, however, appear to contrast with those of Chen et al. (2023), who found dual AGNs residing in significantly larger mass galaxies compared to single AGNs, the discrepancy primarily stems from the differences in how dual and single AGNs are defined in our study versus that of Chen et al. (2023). Chen et al. (2023) define SMBHs with mass greater than $10^7 M_\odot$ as single AGNs, whereas we classify SMBHs with a $L_{bol>}10^{43} erg/s$ as single AGNs. When applying a luminosity threshold to define single AGNs, Chen et al. (2023) also find results indicating no significant differences between hosts of the dual and single AGN populations.

Furthermore the first panel of Fig. 4.11 shows that dual AGNs are less commonly found in lower-mass galaxies, specifically those with a stellar mass less than $5 \times 10^9 M_\odot$. This suggests that hosting two sufficiently luminous AGNs typically requires a galaxy to have undergone at least one relatively major merger, and that massive galaxies experience, overall, more mergers than their lighter counterpart (e.g. Rodriguez-Gomez et al., 2015; Dubois et al., 2016). Additionally, a dichotomy is seen in the dual AGN distribution, with peaks at $10^{10} M_\odot$ and $7 \times 10^{10} M_\odot$.

In the second panel of Fig. 4.11, we show the sSFR distribution. To calculate sSFR, we sum the SFR within a 30 kpc radius from the host halo center and then divide this by the total stellar mass within the same radius. Both dual and single AGNs show similar sSFR distribution shapes, with a central value around $10^{-9} yr^{-1}$. However, dual AGNs are shifting more towards slightly higher sSFR values and are not represented as much in the low sSFR tail, which is noticeable in single AGN host halos. This trend aligns with findings from previous studies using idealized galaxy merger simulations (e.g. Van Wassenhove et al., 2012b), which found peaks in the host galaxies SFR after several pericentric passages when the duals are separated by only a few kpc.

Lastly, the distribution of the gas mass for dual AGNs exhibits a peak similar to that of single AGNs, yet it is characterized by significantly higher fractions at higher M_{gas} values. This pattern suggests that dual AGNs are more likely to be found in halos with higher gas mass compared to the average single AGN host halos.

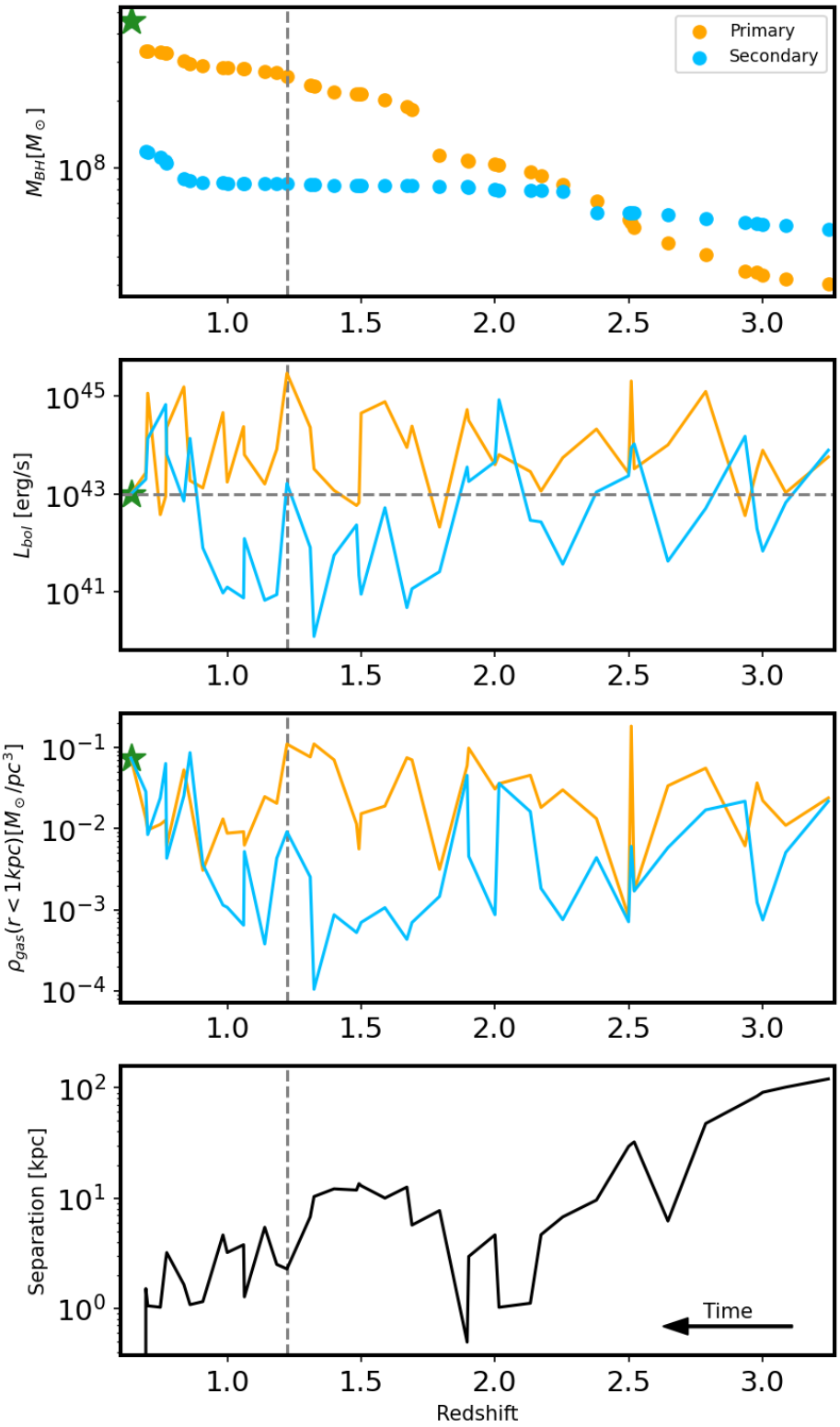

Figure 4.12: Evolution of dual AGNs that merge. The figure shows the evolutionary properties of a dual AGN system from the time that they were in two distinct halos until they merged (shown by a green star). We trace their masses (first panel), luminosity (second panel), surrounding gas density (third panel), and pair separation (fourth panel). The dashed vertical line shows the redshift that duals have been detected. We remind the reader that, in our study, detection is confined to selected epochs at z $\leq$ 2 (see Section 4.2.3). The dashed horizontal line is the luminosity threshold for AGN definition in our study.

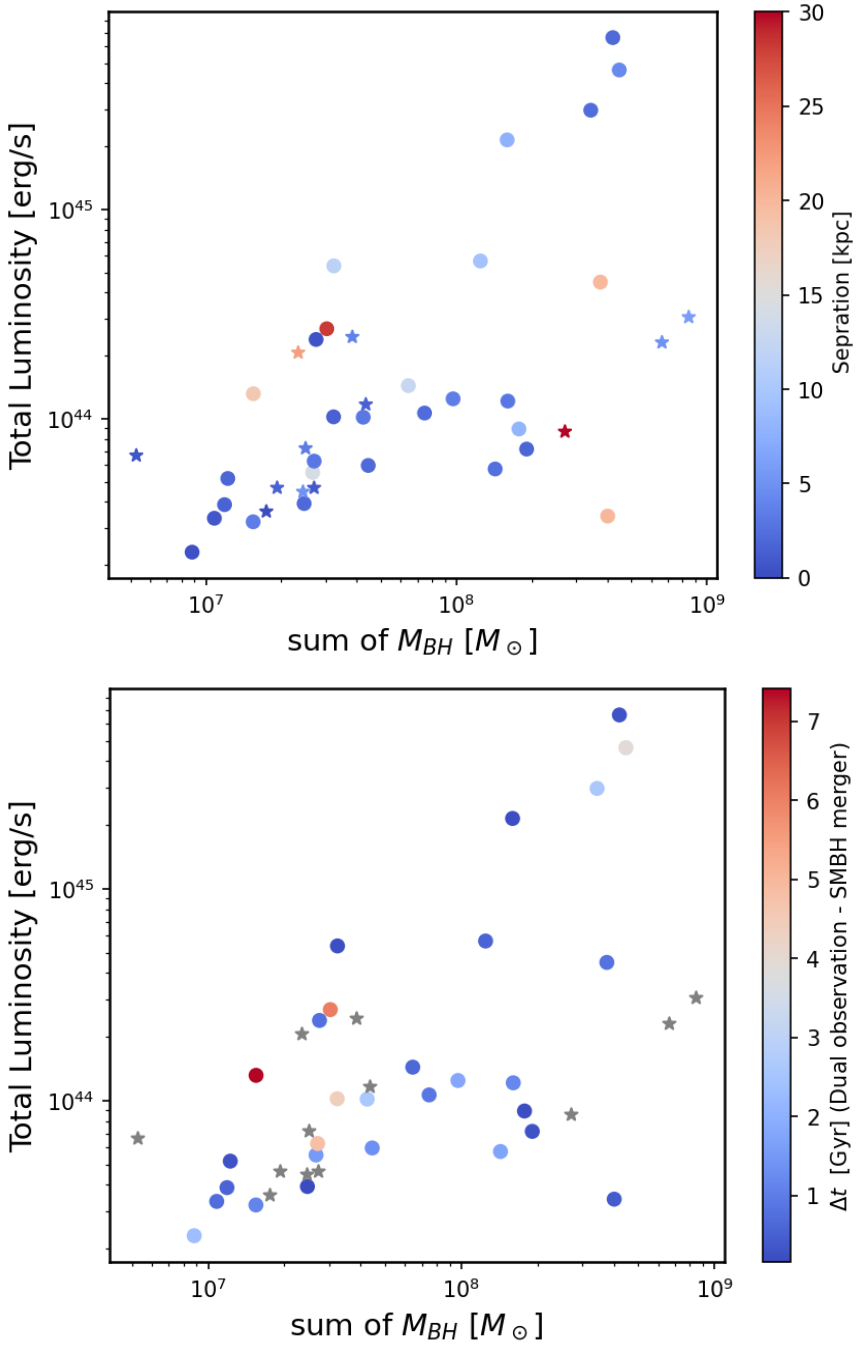

Figure 4.13: The total luminosity of two SMBHs in a dual AGN system versus their combined mass. SMBHs within a dual system that eventually merge are represented with circles, while those that do not merge by z = 0 are represented by stars. In the *top panel*, the data points are color-coded based on the separation between the two SMBHs when they are detected as a dual AGN. The data points in the *bottom panel* are color-coded according to the time elapsed between the detection of the dual AGN and the merger of the two SMBH. The stars are shown in grey because the merging time is not applicable to them.

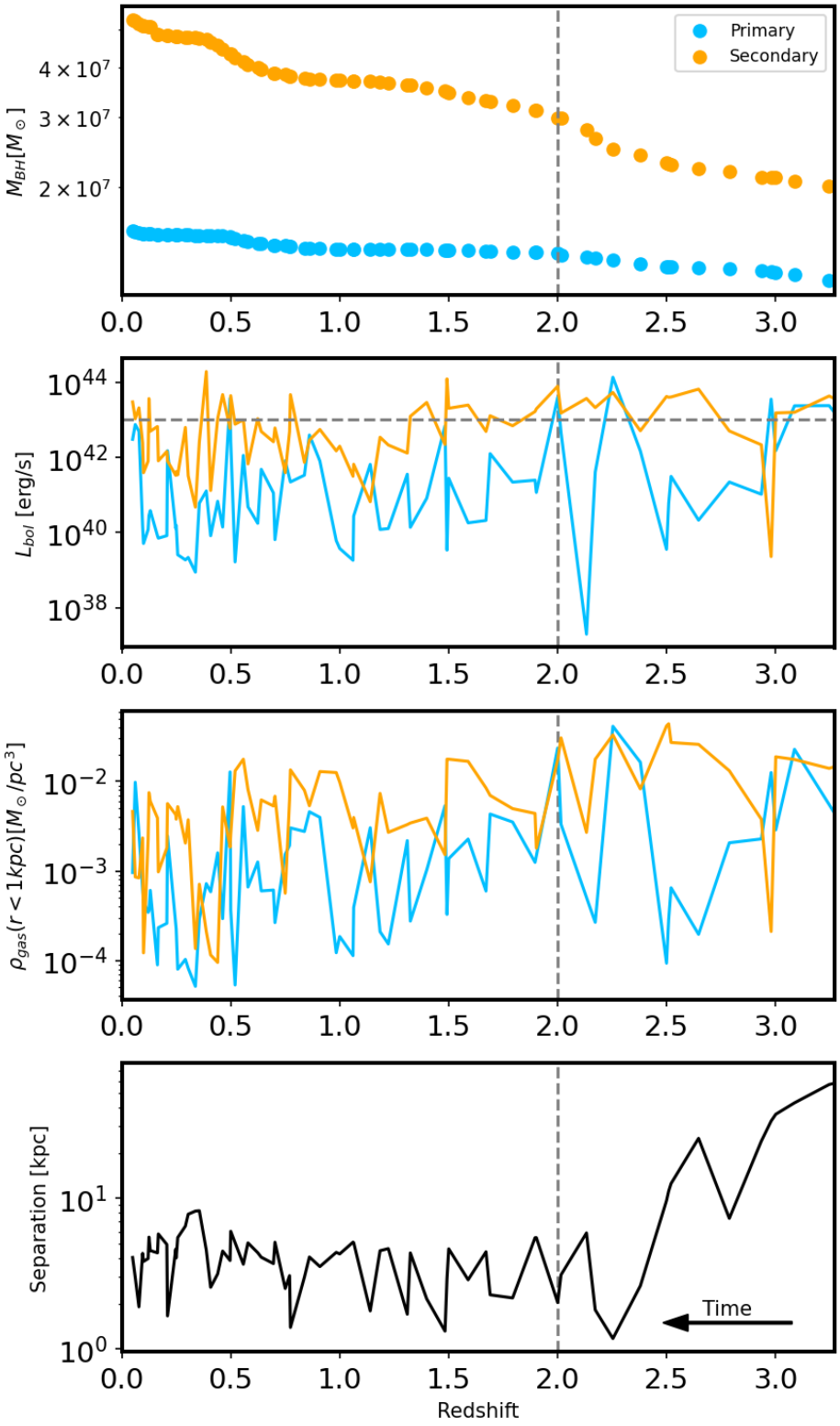

Figure 4.14: Evolution of dual AGNs that do not merge. The figure shows the evolutionary properties of a dual AGN system from the time that they were in two distinct halos until z = 0. The colors and properties of each panel are the same as Fig.4.12.

4.3.4 Evolution of Dual AGN

To deepen our understanding of the evolution of dual AGNs and their relation to galaxy and SMBH mergers, we leverage the simulation's capacity to trace the evolution of these pairs across time. Specifically, we follow the SMBHs within dual AGN systems forward in time until they either merge or reach z = 0. For this analysis, we consider the SMBHs to be merged when they are numerically merged in the simulation (see §4.2.1 for SMBH merging criteria). Additionally, we trace their history back to the point where they resided in separate halos, with their host halos completely distinct (i.e., the host halos are outside of each other's R_{200}). Note that all [4] dual AGNs we are analyzing here are in the same halo at the time of analysis. Based on our analyses, we find that our dual AGN sample includes rapidly evolving systems, slower ones, and even ineffective SMBH mergers. We show illustrative case studies in Figs. 4.12 & 4.14.

Fig. 4.12 presents the evolutionary trajectory of dual AGNs that are detected at z = 1 (marked by a vertical dashed grey line). The chosen dual AGN is typical among our sample, although there is a large variance among the population. From top to bottom, the panels display the SMBH mass, bolometric luminosity, gas density, and AGN separation as a function of redshift. The gas density is computed within a 1 kpc sphere around each SMBH. The primary and secondary SMBH, defined as the brighter and fainter AGN *at the time of analysis*, are represented in orange and blue, respectively.

In this system, the initially less massive SMBH is situated in an environment characterized by high gas density. During the halo mergers, this SMBH undergoes rapid growth via accretion and, by the time of analysis, becomes the more massive and brighter AGN. Its luminosity, though varying over time, mainly remains above $10^{43} erg/s$.

The secondary SMBH experiences more gradual growth in mass. Its luminosity is on average below $10^{43} erg/s$ with occasional peaks above it. The peaks correlate with changes in the surrounding gas density. As the gas density increases, so does the AGN's luminosity. This pattern results in multiple epochs where the dual AGN is detectable, although these periods are typically short-lived.

After its second pericentric, the gas surrounding the secondary SMBH becomes disrupted, leading to a decrease in its luminosity. This trend continues until the secondary SMBH approaches its next pericentric passage, orbiting very close around the primary black hole, where both become highly active. Eventually, the two SMBHs become very close and merge, forming a final SMBH with a mass of $5 \times 10^8 M_\odot$.

[4] There is only one dual AGN in our sample that the SMBHs are in two different halos at the time of analysis.

Table 4.1: Merger and Non-Merger Rates of dual AGNs at Different Separations

Separation	Merger Rate	Non-Merger Rate
< 5 kpc	73%	27%
> 5 kpc	66%	34%
< 10 kpc	68%	32%
> 10 kpc	78%	22%
< 15 kpc	71.5%	28.5%
> 15 kpc	66%	33%

The case study above provides an illustrative example of a dual AGN in which the SMBHs eventually merge. However, as mentioned at the beginning of this section, not all SMBHs in a dual AGN system end up merging. This is not surprising. Galaxy mergers do not invariably lead to SMBH mergers, as SMBH dynamics can be inefficient on both large (Dosopoulou & Antonini, 2017; Tremmel et al., 2018a; Pfister et al., 2019; Li et al., 2020; Bortolas et al., 2020, 2021) and small scales (Begelman et al., 1980; Milosavljević & Merritt, 2001; Muñoz et al., 2019).

Among SMBHs in dual AGNs systems in our sample, 70% will end up merging [5] , 25% stay in close orbit as stalled pairs and the remaining 5% involve cases where one of the black holes in the duals is ejected from the system due to another galaxy merger. The fraction of successful mergers reaches 87% for duals powered by SMBHs both with mass $> 3 \times 10^7 M_\odot$. This fraction also increases, for duals surrounded by stellar density higher than 0.24 $M_\odot/pc^3$. This is because the simulation includes star dynamical friction

In Fig. 4.13, we present the total luminosity of dual AGNs versus the sum of the masses of SMBHs in these dual systems. Circles represent duals whose SMBHs merge, while stars indicate non-merging ones. In the top panel, the data points are color-coded by separation. In the bottom panel, points are color-coded by the time span between the detection of dual AGNs (i.e., when both AGNs have luminosities above our threshold of 10^{43}, erg/s within the considered redshifts) and the subsequent SMBH mergers, for cases where a merger occurs. Stars are shown in grey because the merging time difference is not applicable to them. Note that in our study, the detection redshift range is restricted to $z \leq 2$.

As previously mentioned, 70% of the black holes in dual AGNs are projected to merge. If we limit the sample exclusively to dual AGNs with a separation of less than 5 kpc, the fraction expected to merge slightly increases to 73%, with 27% not merging. Conversely, for AGNs with a separation greater than 5 kpc, 66% are expected to merge, and 34% are not expected to merge. Table 4.1 shows the fractions with 10 and 25 kpc separation cutoffs. The results show that the merging fraction is only marginally sensitive to the separation cut-off, implying that both merging and non-merging duals are found across all separations at similar rates.

The top panel of Fig. 4.13 displays a wide range of timescales between the detection of dual AGN and SMBH mergers, spanning from a few hundred Myr to 7 Gyr. Most duals merge in less than 5 Gyr. It is only for those with a separation greater than 15 kpc that

[5] In this analysis of linking dual AGN to SMBH mergers we do not include dual AGN at z = 0.05, since this is the last redshift we have SMBH information in the simulation, and by denition they cannot give rise to an SMBH merger by the same redshift.

the timescale exceeds 5 Gyr. However, this is not an absolute rule; there are also duals with separations up to 20 kpc that merge within a timescale of less than 2 Gyr. The total luminosity of these duals ranges between 2×10^{43} and 8×10^{45} erg/s, and their total mass is $M_{BH} > 5 \times 10^7 M_\odot$. Fig. 4.13 highlights that all duals with a total bolometric luminosity $L_{bol} > 3 \times 10^{44}$ erg/s will merge, regardless of their separation, which can be as large as 15 kpc. These duals will merge within a timeframe of less than 4 Gyrs.

We note that what we refer to as a 'merger' is a 'numerical merger in the simulation'. In Romulus, two SMBHs are considered to merge when they are closer than 0.7 kpc and gravitationally bound to each other. Therefore, what we actually observe can be described as a 'successful pairing'. This is because, at scales below tens of parsecs, numerous bottlenecks can slow down or suppress SMBH binary formation and further decay (De Rosa et al., 2019; Amaro-Seoane et al., 2023). For the most massive and luminous SMBH systems, specifically those above $10^8 M_\odot$, our simulation's resolution is sufficiently close to the separation at which binary formation occurs. This proximity makes the extrapolation to actual mergers relatively reliable. This assertion is supported by the findings of **?**, in preparation, which indicate that massive SMBHs are the most likely candidates for actual mergers.

Figure 4.14 presents an illustrative example of a dual AGN system, where the SMBH pair persists without merging until z = 0. Initially, both black holes have masses within an order of magnitude of the seed mass ($10^6 M_\odot$). As the system evolves, both SMBHs experience slow growth primarily through accretion, with intermittent AGN activity. The higher-mass SMBH consistently maintains a luminosity above our defined AGN threshold until z = 1.5, whereas the lower-mass SMBH only occasionally exceeds this threshold. These luminosity peaks are aligned with its pericentric passages, coinciding with times when it encounters regions of higher gas density.

At the redshift of analysis, the secondary SMBH is in its third pericentric passage, causing its luminosity to surge above $10^{43} erg/s$. Following this, it settles into a steady orbit around the primary SMBH at separation < 5 kpc until z = 0, during which its surrounding gas density, and consequently its luminosity, gradually decreases. Sometimes, the luminosity of the secondary drops to as low as $L_{bol} < 10^{40} erg/s$. Meanwhile, The primary SMBH's luminosity stays high for ~ 1 Gyr after the time of analysis and then decreases as its surrounding gas density decreases as well. These observations indicate that when two high-accreting SMBHs maintain close orbits over an extended period, they eventually deplete the gas in their vicinity, affecting the AGN activity of both.

This analysis underscores the importance of local environmental properties, particularly gas density, in influencing AGN activity. A notable manifestation of this is when a less mas-

sive black hole outshines its larger counterpart. A more detailed analysis reveals that when the less massive SMBH goes through a region with higher gas density than that surrounding the more massive SMBH, its luminosity tends to increase, potentially surpassing that of the larger black hole. This result is in agreement with idealized high-resolution binary black hole merger simulations (e.g. Capelo et al., 2017)

So far in this section, our focus has been on the evolution of dual AGNs and their potential connection to SMBH mergers. However, dual AGNs are also suggested to be indicators of galaxy mergers (Comerford et al., 2009). As mentioned earlier, we tracked dual AGNs until they resided in two distinct halos. Consistently, we found that all dual AGNs in our sample could be traced back to a previous major galaxy/halo merger. This finding aligns with earlier analyses of cosmological simulations (Steinborn et al., 2016; Rosas-Guevara et al., 2019b; Volonteri et al., 2022b; Chen et al., 2023) which suggest that dual AGNs are typically associated with mergers involving substantial mass ratios. Our analysis indicates that these mass ratios typically range from 10:1 to 1:1, with an average of $\sim$ 2.2:1. This fraction is slightly larger than the $\sim$ 3:1 ratio found by Volonteri et al. (2022b) for dual AGNs in the same galaxies. The discrepancy likely arises from the different time points at which we calculate the mass ratio. We assess the mass ratio of host galaxies of dual AGNs when they are completely outside each others host halos R_{200}, whereas Volonteri et al. (2022b) computed it when only the galaxies were separate. During a halo encounter, the smaller galaxy tends to lose mass through stripping, while the larger one gains mass which results in a smaller mass ratio.

Furthermore, linking all dual AGNs in our sample to halo/galaxy mergers, coupled with the finding that 95% of SMBHs in these systems ultimately form binary SMBHswith 70% merging and 25% remaining in binary systemsdemonstrates that dual AGN systems are a more reliable indicator of binary SMBH formation and subsequent mergers compared to an average galaxy merger (Tremmel et al., 2018a). This phenomenon is likely due to the fact that galaxy mergers resulting in dual AGNs are typically massive, major mergers.

4.4 Summary and Conclusion

In this paper, we first analyzed the properties of AGNs and their neighboring SMBHs. AGNs were identified using the canonical luminosity threshold of $L_{bol} > 10^{43} erg/s$ while neighboring SMBHs were identified based on their distance being less than 30 kpc from an AGN, without applying any luminosity or mass thresholds. Subsequently, we applied the luminosity threshold of $L_{bol} > 10^{43} erg/s$ to the neighboring SMBHs, which led to the identification

of dual and multiple AGNs. We then characterized the properties and evolution of these dual AGNs. All analyses are conducted at redshifts z = 0.05, 0.25, 0.5, 0.75, 1, 1.22, 1.5, 1.79 and 2 using the high-resolution ROMULUS25 cosmological simulation. ROMULUS25 simulation carefully corrects the dynamical friction force onto SMBHs and produces occupation fractions consistent with observations using only local seeding conditions. The main findings are summarized as follows:

- The number of AGNs in ROMULUS increases from lower to higher redshifts, which is consistent with observational studies. Consequently, the total number of neighboring SMBHs also increases. Every AGN has at least one neighbor SMBH. The number of these neighbors scales linearly with halo mass and can be as high as 120 neighbor SMBHs in a $10^{13} M_{\odot}$ halo. The spatial distribution of these neighboring SMBHs also correlates linearly with their number. Thus, in higher mass halos, there are not only more neighboring SMBHs but also a more extended spatial distribution. Ricarte et al. (2021b) find that the majority of these neighboring SMBHs originate from the centers of destroyed infalling satellite galaxies. This finding supports the expectation that higher mass halos, having undergone more mergers and also having a higher orbital decay timescale, would naturally harbor a greater number of neighboring SMBHs.

- Investigating the mass and luminosity range of neighboring SMBHs, We find SMBHs with luminosities exceeding $L_{bol} > 10^{43} erg/s$ around primary AGNs, indicating the presence of dual and multiple AGN systems in the ROMULUS25 simulation. The number of dual AGNs increases with redshift, while multiple AGNs (triple and quadruple) are predominantly found at z > 1. Our analysis shows that the fraction of dual AGN rises from 4% to 9% moving from lower to higher redshifts.

- Dual AGNs in this study are predominantly found within a separation closer than 5 kpc from each other, with a peak distance of 2 kpc. The resolution and dynamical friction model in the ROMULUS25 simulation allows for the resolving of duals with separations of $\sim$ kpc scale.

- In dual AGN systems, the SMBHs exhibit luminosity and mass ranges similar to those of single AGNs, although the differences are statistically insignificant. A notable trend is that secondary SMBHs in dual systems more frequently have masses lower than $10^{7} M_{\odot}$. This suggests that a low-mass black hole with a bolometric luminosity exceeding $L_{bol} > 10^{43} erg/s$ is more likely to be in a dual system than to exist as a single

AGN. Additionally, a larger proportion of primary SMBHs in dual systems display luminosities higher than $10^{44} erg/s$ compared to their single AGN counterparts.

- The properties of host halos for dual AGNs, including halo mass, stellar mass, SFR, and gas mass, are largely consistent with those of the single AGN population, albeit marginally skewed towards the higher end. The SMBHs in dual systems tend to be undermassive relative to their host halos, exhibiting an SMBH mass to halo mass ratio below the median value found in similarly massive SMBHs. A possible explanation for this is that during halo mergers, black holes become associated with a higher mass remnant halo well before they themselves merge, thereby not keeping pace with the halo's growth mass.

- The analyses of dual AGN systems in the sample in this study reveal a diverse range of evolutionary patterns, including rapidly evolving systems, slower ones, and even cases where SMBH mergers are ineffective. Approximately 70% of dual AGNs are associated with an ensuing SMBH merger, 25% orbit in a stalled pair, and last 5% experience ejecting from the system. The time span for mergers varies significantly, ranging from a few hundred Myr years to over 7 Gyrs. We found that duals with total bolometric luminosity $L_{bol} > 3 \times 10^{44}$ erg/s will merge in a timeframe of less than 4 Gyrs regardless of their separation.

- An investigation into the mass and luminosity ratios of SMBHs in dual AGN systems reveals instances where a lower mass SMBH exhibits a higher luminosity than its more massive counterpart. A more detailed analysis indicates that this occurs when the less massive SMBH passes through an area with higher gas density compared to the environment of the more massive SMBH, leading to an increase in its luminosity, sometimes even surpassing that of the larger black hole. This finding underscores the significance of local environmental properties in influencing the evolution of SMBHs.

- All dual AGN in the sample of this study are linked to a halo merger, typically characterized by a mass ratio of $\sim$ 2.2:1.

In conclusion, the findings of this paper indicate the existence of a substantial population of neighboring SMBHs and the prevalence of dual/multiple AGNs. The discovery of numerous neighboring SMBHs with luminosities slightly below the common threshold of $10^{43} erg/s$ calls for more sensitive instruments. With improved sensitivity, a significantly larger number of AGNs with luminous companions could be detected. Additionally, the finding of dual

AGNs with sub-kpc separations underscores the need for both higher sensitivity instruments and higher resolution cosmological simulations. This dual approach is essential for the deeper study of these systems, both observationally and theoretically.

Acknowledgements

We thank Pedro R. Capelo for insightful discussions and suggestions. VS and AB acknowledge support from the Natural Sciences and Engineering Research Council of Canada (NSERC) through its Discovery Grant program. AB acknowledges support from the Infosys Foundation via an endowed Infosys Visiting Chair Professorship at the Indian Institute of Science. The work of SM is a part of the ⟨data|theory⟩ Universe-Lab which is supported by the TIFR and the Department of Atomic Energy, Government of India. MT was supported by an NSF Astronomy and Astrophysics Postdoctoral Fellowship under award AST-2001810. AB, TQ, and MT were partially supported by NSF award AST-1514868.

The ROMULUS simulation suite is part of the Blue Waters sustained-petascale computing project, which is supported by the National Science Foundation (via awards OCI-0725070, ACI-1238993, and OAC-1613674) and the state of Illinois. Blue Waters is a joint effort of the University of Illinois at Urbana-Champaign and its National Center for Supercomputing Applications. Resources supporting this work were also provided by the (a) NASA High-End Computing (HEC) Program through the NASA Advanced Supercomputing (NAS) Division at Ames Research Center; and (b) Extreme Science and Engineering Discovery Environment (XSEDE), supported by National Science Foundation grant number ACI-1548562. The analysis reported in this paper was enabled in part by WestGrid and Digital Research Alliance of Canada (alliancecan.ca) and on the cluster of ⟨data|theory⟩ Universe-Lab supported by DAE. Our analysis was performed using the Python programming language (Python Software Foundation, https://www.python.org). The following packages were used throughout the analysis: numpy (Harris et al. 2020), matplotlib (Hunter 2007), Pynbody (Pontzen et al. 2013b), SciPy (Virtanen et al. 2020), and TANGOS (Pontzen & Tremmel 2018).

Finally, VS and AB acknowledge the lək̓ʷəŋən peoples on whose traditional territory the University of Victoria stands, and the Songhees, Equimalt and W̱SÁNEĆ peoples whose historical relationships with the land continue to this day.

Data Availability

The data directly related to this article will be shared on reasonable request to the corresponding author. Galaxy database and particle data for ROMULUS is available upon request

from Michael Tremmel.

Personal contribution clarification:

This chapter contributes to the second part of my dissertation, which focuses on the properties of host galaxies of merging SMBHs. It specifically examines the statistics and characteristics of host galaxies of rapidly accreting SMBHs that are in close separation, appearing as dual AGNs. I designed and executed the entire analysis, formulated the research questions, and conducted all analyses for this study. Arif Babul provided essential scientific guidance and recommendations throughout the process and gave feedback on the manuscript draft. Suvodip Mukherjee, Michael Tremmel, Thomas R. Quinn, and Lucio Mayer are members of the collaboration. Michael Tremmel and Thomas R. Quinn designed the subgrid model that allows Romulus simulation to track SMBHs dynamics, an innovation that provides the foundation for this study. Suvodip Mukherjee and Lucio Mayer are experts in BH-BH mergers. We had many discussions that provided me with insights into what results the BH-BH merger community would find interesting. One outcome of these discussions is the next chapter that builds on the analysis done for this project to look at implications for Pulsar Timing Array (PTA) searches for merging SMBHs.

Chapter 5

Shining Light on the Hosts of the nano-Hertz Gravitational Wave Sources: A Theoretical Perspective

Originally published in Monthly Notices of the Royal Astronomical Society, Volume 529, Issue 4, April 2024, Pages 42954310. Reproduced by permission of Oxford University Press. https://doi.org/10.1093/mnras/stae513

Authors: Vida Saeedzadeh[1], Suvodip Mukherjee[2], Arif Babul[1,3], Michael Tremmel[4], Thomas R. Quinn[5]

Abstract: The formation of supermassive black holes (SMBHs) in the Universe and its role in the properties of the galaxies is one of the open questions in astrophysics and cosmology. Though, traditionally, electromagnetic waves have been instrumental in direct measurements of SMBHs, significantly influencing our comprehension of galaxy formation, gravitational waves (GW) bring an independent avenue to detect numerous binary SMBHs in the observable Universe in the nano-Hertz range using the pulsar timing array observation. This brings a new way to understand the connection between the formation of binary SMBHs and galaxy formation if we can connect theoretical models with multi-messenger observations namely GW data and galaxy surveys. Along these lines, we present here the first paper

[1]Department of Physics and Astronomy, University of Victoria, 3800 Finnerty Road, Victoria, BC, V8P 1A1, Canada
[2]Department of Astronomy & Astrophysics, Tata Institute of Fundamental Research, 1, Homi Bhabha Road, Colaba, Mumbai 400005, India
[3]Infosys Visiting Chair Professor, Indian Institute of Science, Bangalore 560012, India [4]School of Physics, University College Cork, College Road, Cork T12 K8AF, Ireland
[5]Astronomy Department, University of Washington, Box 351580, Seattle, WA, 98195-1580, USA

on this series based on ROMULUS25 cosmological simulation on the properties of the host galaxies of SMBHs and propose on how this can be used to connect with observations of nano-Hertz GW signal and galaxy surveys. We show that the most dominant contribution to the background will arise from sources with high chirp masses which are likely to reside in low redshift early-type galaxies with high stellar mass, largely old stellar population, and low star formation rate, and that reside at centers of galaxy groups and manifest evidence of recent mergers. The masses of the sources show a correlation with the halo mass and stellar mass of the host galaxies. This theoretical study will help in understanding the host properties of the GW sources and can help in establishing a connection with observations.

5.1 Introduction

The discovery of Gravitational Waves (GWs) by the LIGO-Virgo-KAGRA (LVK) Collaboration from coalescing compact object binaries of a few tens of solar masses inaugurated the era of gravitational-wave astronomy, enabling the observations of previously inaccessible astrophysical phenomena (Aasi et al., 2015; Abbott et al., 2016a; Acernese et al., 2014, 2019; Abbott et al., 2018; Akutsu et al., 2019, 2020). Following this initial discovery, several more binary objects have been detected, one of which (GW170817) also had an electromagnetic (EM) counterpart and stands as the first multi-messenger measurement involving GW signal (Abbott et al., 2016b, 2017, 2021b,a; Abbott et al., 2023a; The LIGO Scientific Collaboration et al., 2021; Abbott et al., 2023b). With the aid of ongoing and upcoming networks of GW detectors, several more detections of coalescing black hole binaries are likely over the frequency range of 10 Hz and above.

Along with the high-frequency GW signal, coalescing supermassive black holes (SMBHs) can also produce GW signals detectable at low-frequency bands, ranging from a few nano-Hertz to milli-Hertz range. In the milli-Hertz frequency range, upcoming GW detectors – such as Laser Interferometer Space Antenna (LISA; Amaro-Seoane et al., 2017; Baker et al., 2019) – can probe signal from the SMBHs of masses in the range approximately 10^4- 10^7 $M_\odot$. The nano-Hertz GW signal from sources with masses above 10^8 $M_\odot$ can be detected and characterized using the timing data from several extremely well-studied millisecond pulsars (Sesana et al., 2008b; Foster & Backer, 1990). These signals are the target of the International Pulsar Timing Array (IPTA) collaboration (Antoniadis et al., 2022), comprising the European Pulsar Timing Array (EPTA; Desvignes et al., 2016), the North American Nanohertz Observatory for Gravitational Waves (NANOGrav; McLaughlin, 2013), the Indian Pulsar Timing Array Project (InPTA; Joshi et al., 2018) and the Parkes

Pulsar Timing Array (PPTA; Manchester et al., 2013). Along with the IPTA Collaboration, the Chinese Pulsar Timing Array (CPTA; Xu et al., 2023a) are also making measurements in this band. In the future with the operation of the Square Kilometer Array (SKA) (Sesana et al., 2008b; Terzian & Lazio, 2006; Janssen et al., 2014) more accurate measurement of this signal will be possible (Burke-Spolaor et al., 2019). The recent evidence of the stochastic GW background (SGWB) in the nano-Hertz range by CPTA (Xu et al., 2023b), EPTA+InPTA (Antoniadis et al., 2023a), NANOGrav (Agazie et al., 2023) and PPTA (Reardon et al., 2023) promises to open an exciting new window onto the evolving population of binary supermassive black holes (SMBBHs) in the Universe.

The presence of nano-Hertz GW signal leads to several interesting questions such as: What are the astrophysical properties of the host galaxies of the source SMBBHs, and can one use conventional galaxy surveys to identify (if not uniquely detect) these host galaxies? Since SMBHs reside in the centers of galaxies, SMBBHs are expected to be byproducts of galaxy mergers. Consequently, SMBBHs-host galaxy identifications can potentially shed light on the pathways leading to the formation of the SMBBHs, including their dynamical evolution from the time of first encounter, and more generally on the astrophysics of galaxy mergers. They can also potentially provide insights into the growth of SMBHs and the implications of SMBH-SMBH mergers on galaxy formation (Cattaneo et al., 2009), including conditions leading to the transition between radiative versus kinetic feedback modes (eg Narayan & Quataert, 2005; Merloni & Heinz, 2008; Benson & Babul, 2009; Babul et al., 2013b). (See also O'Sullivan et al. 2012, Reynolds et al. 2014, Prasad et al. 2020b and O'Sullivan et al. 2021 for rare examples of observed SMBHs in unexpected state.) This would be an important step towards a new paradigm of multi-messenger science capable of addressing a broad spectrum of questions related to astrophysics and cosmology.

However, typical PTA localizations in the near term are expected to encompass several thousand (if not more) galaxies. Theoretical and computational modeling offers an opportunity to not only explore environments where SMBH - SMBH mergers take place but also a way to narrow the field of candidate host galaxies for more detailed observational scrutiny (Rosado & Sesana, 2014; Goldstein et al., 2019; Volonteri et al., 2003, 2020; Muhamed Kozhikkal et al., 2023). In this study, we use results from a high-resolution Romulus cosmological simulation (Tremmel et al., 2017, 2019) to explore this possibility. As we discuss in §5.3, Romulus suite of simulations is especially suited for investigating SMBH/SMBBH-galaxy connections because of its unique approach to seeding, accretion, and especially the dynamics of supermassive black holes. Consequently, the simulations have previously been used to explore a variety of related topics, including the timescale for the formation of close

SMBH pairs following galaxy mergers (Tremmel et al., 2018b), the galaxy-SMBH coevolution (Ricarte et al., 2019c), the origin and demographics of wandering black holes (Ricarte et al., 2021a), and the demographics of dual active galactic nuclei (Saeedzadeh et al., 2023a).

The paper is organized as follows: In §5.2, we briefly discuss the motivation behind the present study and in §5.3, we discuss the ROMULUS simulation. The expected SGWB based on the simulation and the astrophysical properties of the galaxies hosting SGWB sources are discussed in §5.4 and §5.5. Among the properties we consider are: gas density ($\rho_{\rm gas}$), star formation rate ($\dot{M}_*$ or SFR), stellar mass ($\rm M_*$), galaxy morphology, galaxy color, specific star formation rate (sSFR $\equiv \dot{M}_*/M_*$) and halo mass ($\rm M_h$, which we take to be $\rm M_{500}$; see §5.3.4 for the definition of $\rm M_{500}$). Then, we discuss possible techniques to validate the connection between the SMBBHs and their host galaxies that we find in §5.6. Finally, we summarise our findings and discuss the future outlook in §5.7.

5.2 Motivation

On one hand, we have the recently detected SGWB in the nano-Hertz range from coalescing SMBHs of mass $\rm M > 10^7\ M_\odot$. On the other hand, we have spectroscopic/photometric galaxy surveys that are capable of detecting faint galaxies up to high redshifts, some of which will be hosts of the SMBBHs that are contributing to the nano-Hertz SGWB. The combination of these two opens up the prospect of a new multi-messenger science that can shed light on several key questions in astrophysics and cosmology. A limited list of these key questions are: (i) How do the SMBHs grows with time? (ii) How do SMBBHs form and is there a relationship between their formation and one or more properties of the host galaxies? (iii) Do the astrophysical properties of the host galaxies play a role in coalescing of the SMBBHs? (iv) What is the occupation number of the SMBHs in galaxies (or halos) of different masses?

We are interested in understanding the theoretical dimensions of these questions and in identifying whether the key astrophysical properties of the host galaxies can be predicted based on our current understanding of galaxy formation. In this paper, we explore the astrophysical "tells" of galaxies that host SMBBHs in the ROMULUS simulation volume. We also investigate the properties of the halos of these galaxies. Although the ROMULUS simulations can track black holes across nearly three orders of magnitude in mass (10^6- 10^9 $\rm M_\odot$), in the present paper we focus primarily on coalescing binaries black holes that can contribute to the stochastic gravitational wave background in the frequency band accessible to PTA. We perform a simulation-based study of the correlations between the SMBBHs and their host galaxies. The specific galaxy properties we focus on include their morphology,

star formation rate, galaxy color, stellar mass, gas density, and halo mass. Uncovering a theoretical connection between the properties of the host galaxy and its SMBBH will help motivate observational and data analysis strategies aimed at identifying the host galaxies of the GW sources from the photometric/spectroscopic galaxy catalogs. This, in turn, can contribute to building a data-driven understanding of the evolution of SMBBHs in galaxies.

In future papers in this series, we will consider black holes accessible to LISA, examine possible connections between these and SMBBHs detectable with PTA, and its implementation on the latest nano-Hertz observations (Xu et al., 2023b; Antoniadis et al., 2023b; Agazie et al., 2023; Zic et al., 2023) to identity the possible host candidates. For completeness, we note that there are several analytical and numerical simulation-based studies estimating SGWB signal in the PTA frequency range (Rajagopal & Romani, 1995; Jaffe & Backer, 2003; Kocsis & Sesana, 2011; Chen et al., 2017; DeGraf et al., 2021; Izquierdo-Villalba et al., 2022, 2023). Additional studies are referenced throughout the text.

5.3 The Romulus Simulations

In this work, we present results from the analysis of the Romulus25 simulation, which is a $(25\ \mathrm{cMpc})^3$ cosmological volume simulation from the Romulus suite (Tremmel et al., 2017, 2019; Butsky et al., 2019; Jung et al., 2022; Saeedzadeh et al., 2023b).

The simulation was run using the Tree+Smoothed Particle Hydrodynamics (Tree+SPH) code CHaNGa (Menon et al., 2015; Wadsley et al., 2017). CHaNGa incorporates the standard physics models previously employed in the simulation codes GASOLINE/GASOLINE2 and has been extensively tested (Stinson et al., 2006). Including modules for star formation, stellar feedback, turbulent diffusion (Shen et al., 2010b), the UV background, low-temperature metal cooling, and an improved treatment of both weak and strong shocks. However, the models for SMBH formation, dynamics, growth, and feedback are novel (Tremmel et al., 2015, 2017). We will discuss them in more detail in the following subsections.

The Romulus25 simulation was run assuming a flat ΛCDM universe with cosmological parameters consistent with the Planck 2016 results (Ade et al., 2016): $\Omega_\mathrm{m} = 0.309$, $\Omega_\Lambda = 0.691$, $\Omega_\mathrm{b} = 0.0486$, $\mathrm{H}_0 = 67.8\,\mathrm{km\,s^{-1}Mpc^{-1}}$, and $\sigma_8 = 0.82$. The simulation has a Plummer equivalent gravitational force softening of 250 pc (or 350 pc spline kernel) and a maximum SPH resolution of 70 pc. Differing from many similar cosmological runs, the dark matter distribution in Romulus25 is oversampled with 3.375 times more dark matter particles than gas particles. This results in a dark matter particle mass of $3.39 \times 10^5 M_\odot$ and a gas particle mass of $2.12 \times 10^5 M_\odot$. This deviation from the standard approach of simulating

equal numbers of gas and dark matter particles minimizes numerical noise and allows for more precise black hole dynamics (Tremmel et al., 2015).

More details about the ROMULUS25 simulation have been described in a number of published papers. We refer interested readers to Tremmel et al. (2015, 2017, 2019, 2020); Sanchez et al. (2019); Butsky et al. (2019); Chadayammuri et al. (2020); Jung et al. (2022); and Saeedzadeh et al. (2023b). The latter two especially offer a concise yet complete summary. Additionally, for comparisons with galaxy formation models employed in other cosmological simulations, interested readers are referred to Somerville & Davé (2015); Vogelsberger et al. (2020); Oppenheimer et al. (2021b)

There are, however, a few aspects of the ROMULUS25 simulation that are important to highlight as these are relevant to the present discussion. These pertain to the treatment of SMBH seeding, growth, and dynamical evolution in the ROMULUS25 (Tremmel et al., 2017).

5.3.1 SMBH Seeding

Unlike many other cosmological simulations (e.g., Schaye et al., 2015; Weinberger et al., 2017; Pillepich et al., 2018; Nelson et al., 2019b; Davé et al., 2019), the ROMULUS25 SMBH seed model does not depend on a halo or a galaxy to exceed a certain mass threshold for a SMBH to form. Rather, the seeding depends only on the local gas properties (Tremmel et al., 2017). As a result, the SMBHs in ROMULUS25 can form in low mass halos and tend to form much earlier ($z > 5$, Tremmel et al., 2017). Additionally, one can also have multiple SMBHs arising in the same halo.

The criteria for converting gas particle into a SMBH seed in ROMULUS25 are as follows: (i) The gas particle must be *both* eligible and selected to form a star. The latter is a probabilistic process. (ii) The gas particle must have very low metallicity ($Z < 3 \times 10^{-4}$); (iii) its density must be very high; i.e. at least 3 m_p/cc or greater. And, (iv) its temperature is within the range of 9500 - 10000 K. This seeding prescription resembles the direct collapse black hole scenario, where high temperatures and low metallicities suppress fragmentation and allow sizeable gas clouds to collapse directly into an SMBH seed (Lodato & Natarajan, 2007; Alexander & Natarajan, 2014; Natarajan, 2021).

In the ROMULUS25 simulation, SMBHs are seeded with a mass of 10^6 $M_\odot$. This seeding mass differs slightly from other simulations like TNG50/100/300, EAGLE, Horizon AGN, and SIMBA-C where the initial SMBH seed masses are set at $\sim 8 \times 10^5 M_\odot$, $10^8 M_\odot$, $10^5 M_\odot$ and $10^4 M_\odot$respectively (Nelson et al., 2019b; Kaviraj et al., 2017; Crain et al., 2015; Hough et al., 2023b). The choice of the SMBH seed mass in ROMULUS25 is constrained primarily

by two factors: (i) the resolution of the simulation, with the dark matter and gas mass resolutions in ROMULUS25 being $3.39 \times 10^5 M_\odot$ and $2.12 \times 10^5 M_\odot$ respectively, and (ii) the necessity to keep SMBHs more massive than dark matter and star particles. This latter requirement is crucial for reducing the occurrence of spurious scattering events (Tremmel et al., 2015).

The resulting SMBH occupation fraction at z=0 is consistent with current observations even on the scale of dwarf galaxies (Ricarte et al., 2019a). Additionally, the SMBH masses correlate with the stellar masses of their host galaxies, following the observed SMBH mass - stellar mass relation (Tremmel et al., 2017; Ricarte et al., 2019b).

5.3.2 SMBH Dynamics and Mergers

The other difference in the SMBH model between ROMULUS25 and other cosmological simulations is SMBH dynamics. Unlike many other cosmological simulations, where the SMBHs are artificially placed at the gravitational potential minimum of their host galaxies (e.g. Crain et al., 2009; Sijacki et al., 2015; Davé et al., 2019), the ROMULUS25 simulation accurately tracks the dynamical evolution of SMBHs down to sub-kpc scales, which is highly advantageous for the present study. To achieve this, a sub-grid correction is employed that accounts for the unresolved dynamical friction from stars and dark matter that the SMBHs ought to be experiencing(Tremmel et al., 2015). For each SMBH in the simulation, this force is estimated by assuming a locally isotropic velocity distribution and integrating Chandrasekhar's equation (Chandrasekhar, 1943b) from the 90-degree deflection radius (r_{90}) to the SMBH's gravitational softening length (ϵ_g). The resulting acceleration is

$$\mathbf{a}_{DF} = -4\pi G^2 \, M_\bullet \, \rho(v < v_{BH}) \, \ln\Lambda \, \frac{\mathbf{v}_{BH}}{v_{BH}^3}, \tag{5.1}$$

In order for two SMBHs to merge, they must be within a distance of two gravitational softening lengths (0.7 kpc) and possess a low enough relative velocity to be mutually bound; i.e. $\frac{1}{2}\,\Delta\mathbf{v}^2 < \Delta\mathbf{a}\cdot\Delta\mathbf{r}$, where $\Delta\mathbf{v}$ and $\Delta\mathbf{a}$ are the differences in velocity and acceleration of the two black holes, and $\Delta\mathbf{r}$ is the distance between them (Bellovary et al., 2011; Tremmel et al., 2017)[2]. The separation limit of two gravitational softening lengths is deemed appropriate because once the separation drops below this limit, the simulation's ability to accurately track the SMBH pair's dynamics becomes less reliable.

When a merger takes place, the resulting SMBH is assigned a velocity that conserves momentum, and its mass is the sum of the masses of its progenitors. Mergers are one of the

[2]Note that there is a typographical error in the criterion for boundedness in Tremmel et al. (2017).

two processes driving the growth of SMBHs.

5.3.3 SMBH Growth and Feedback

The other process by which SMBHs grow is via the accretion of gas. In ROMULUS25, this accretion rate is estimated via a modified Bondi-Hoyle (Bondi 1952, for modifications see Tremmel et al. 2017) prescription applied to the smoothed properties of the 32 nearest gas particles:

$$\dot{M}_\bullet = \alpha \times \begin{cases} \frac{\pi (G M_\bullet)^2 \rho_{\rm gas}}{(v_{bulk}^2 + c_s^2)^{3/2}} & \text{if } v_{bulk} > v_\theta \\ \\ \frac{\pi (G M_\bullet)^2 \rho_{\rm gas} c_s}{(v_\theta^2 + c_s^2)^2} & \text{if } v_{bulk} < v_\theta \end{cases}, \tag{5.2}$$

where $\rho_{\rm gas}$ is the ambient gas density, c_s is the ambient sound speed, v_θ is the local rotational velocity of surrounding gas, and v_{bulk} is the bulk velocity relative to the SMBH. All ambient quantities are calculated using the 32 nearest gas particles. The introduction of v_θ and v_{bulk} terms in the above aims to remedy the neglect of gas bulk motion and angular momentum in the original Bondi-Hoyle formulation. Finally, the coefficient α is introduced to correct for the suppression of the black hole accretion rate due to resolution effects. It is defined as

$$\alpha = \begin{cases} (\frac{n}{n_{th,*}})^2 & \text{if } \; n \geq n_{th,*} \\ \\ 1 & \text{if } \; n \leq n_{th,*} \end{cases}, \tag{5.3}$$

where $n_{th,*}$ is the star formation number density threshold ($0.2 \; m_p/cc$).

Gas accretion onto a SMBH results in energy release into the environment around the black hole. In ROMULUS25, it is assumed that this energy is electromagnetic and that a fraction of it will couple to the ambient gas and contribute to its internal energy. The thermal energy deposition rate is given by $\dot{E}_{\bullet,th} = \epsilon_r \epsilon_f \dot{M}_\bullet c^2$, where ϵ_r is the radiative efficiency (assumed to be 10%) and ϵ_f is gas coupling efficiency (set to 2%). The thermal energy is imparted isotropically to the 32 nearest gas particles, with the energy being distributed among these gas particles according to the smoothing kernel. We refer readers to Tremmel et al. (2017) for further details.

5.3.4 Selection of Halos and Binary SMBHs

The halos in ROMULUS simulations are extracted and processed using the Amiga Halo Finder (hereafter, AHF; Knebe et al., 2008; Knollmann & Knebe, 2009), and tracked across time with TANGOS (Pontzen & Tremmel, 2018).

The halos and subhalos exist in a nested hierarchy, where the halos are the primary structures and the subhalos are incorporated within them. To identify these structures, AHF first locates density peaks in an adaptively smoothed density field and identifies all the particles (dark matter, gas, stars, and black holes) that are gravitationally bound to these peak. This process is repeated on successively larger scales until all the structures in the hierarchy have been found. Once the halos are identified, their centers are found by applying the shrinking sphere approach (Power et al., 2003) to the distribution of bound particles associated with each of the halos.

The masses of the halos (M_Δ) are determined by creating a sphere with a radius of R_Δ around each halo center. This sphere is constructed so that the average density within it, $\langle \rho_{\mathrm{m},\Delta}(z) \rangle$, is equal to Δ times the critical cosmological density, $\rho_{\mathrm{crit}}(z) = 3\mathrm{H}^2(\mathrm{z})/8\pi\mathrm{G}$ (see, for example, Babul et al., 2002). In this study, we reference (M_{200}, R_{200}) and (M_{500}, R_{500}), which correspond to $\Delta = 200$ and $\Delta = 500$, respectively. For our assumed cosmology, $M_{500}/M_{200} \approx 0.7$ and $R_{500}/R_{200} \approx 0.68$.

In the case of subhaloes, AHF tracks the local density profile from the peak center outward. At some point, the external gravitational field starts to dominate, altering the shape of the density profile. The distance from the peak to where this happens is taken to be the size of the subhalo, and the mass enclosed is recorded as the subhalo's mass.

We also track all the SMBHs in the ROMULUS25 simulation volume. We use the resulting information to construct merger trees for all the black holes. At each redshift, we then identify black holes that have experienced a merger during the immediately preceeding output and flag the about-to-merge SMBH pairs as candidate sources of nano-Hertz SGWB. The time resolution (Δt) and redshift resolutions (Δz) for the saved output files within our redshifts of interest (see §5.5.1) vary in the ranges of 10 Myr $< \Delta$t $<$ 400 Myr and 0.002 $<$ Δz < 0.1, getting to smaller values as approaching z = 0. The typical separation of merging SMBH pairs is $\sim$ 1 kpc and their maximum separation is 2.8 kpc. For completeness, we also identify all black hole pairs separated by $\leq$ 1.4 kpc and which are not flagged as merging in the next output. We will refer to these as proximate pairs.

We emphasize that the SGWB from flagged SMBBHs with separation scale of $\sim$ 1 kpc cannot contribute to the nano-Hertz frequency band unless they coalescence down to sub-

parsec (10^{-5} pc) scale. This journey of the SMBBHs from the scale of $\sim$ 1 kpc to $\leq$ 10^{-5} pc is governed not only by GW emission but also by environmental effects such as dynamical friction, stellar loss cone and viscous gas drag. These processes are not resolvable in ROMULUS25 or, for that matter, in any other cosmological simulation. We therefore need to model this coalescence separately.

5.4 Estimation of SGWB in the nano-Hertz

5.4.1 Modeling SGWB signal from coalescing SMBBHs

In order to calculate the contribution to the SGWB signal from the coalescing SMBBHs, we start with the expression for the characteristic strain of the GW signal h_c at frequency f for a source emitting at a rest-frame frequency $f_r = (1+z)f$ (Rajagopal & Romani, 1995; Phinney, 2001; Sesana et al., 2008a):

$$h_c^2(f) = \frac{4G}{c^2\pi f^2} \iiint dz\, dm_1\, dm_2\, \frac{d^3n_{GW}(m_1, m_2, z)}{dm_1 dm_2 dz} \times \frac{1}{1+z} \frac{dE_{\rm GW}(m_1, m_2, z)}{d\ln f_r}, \tag{5.4}$$

where the distribution function, $\frac{d^3n_{\rm GW}(m_1,m_2,z)}{dm_1 dm_2 dz}$, is the number density of SMBBH GW sources with black hole masses in the range $[m_1,\ m_1 + dm_1]$ and $[m_2,\ m_2 + dm_2]$ at redshift $[z,\ z + dz]$ and determines the amplitude and spectral shape of the SGWB signal. The second term, $\frac{dE_{\rm GW}(m_1,m_2,z)}{d\ln f_r}$, quantifies the amount of GW energy released per logarithmic rest-frame frequency by a binary of source masses m_1 and m_2 at redshift z. The latter is the product of the GW energy emission rate ($\frac{dE_{\rm GW}(m_1,m_2,z)}{dt_r}$), and the residence time (i.e. the amount of time a source spends at a frequency: $\frac{dt_r}{d\ln f_r}$). Following Kelley et al. (2017a,b), we write the energy released as

$$\frac{dE_{\rm GW}(m_1, m_2, z)}{d\ln f_r} = \frac{dE_{\rm GW}(m_1, m_2, z)}{d\ln f_r}\bigg|_{\rm GW} \frac{\tau_h}{\tau_{\rm GW}}(f), \tag{5.5}$$

$$= f_r \frac{dE_{\rm GW}(m_1, m_2, z)}{df_r}\bigg|_{\rm GW} \frac{\tau_h}{\tau_{\rm GW}}(f),$$

where

$$\left.\frac{dE_{\rm GW}(m_1,m_2,z)}{df_r}\right|_{\rm GW} = \frac{(\pi G)^{2/3}M_c^{5/3}}{3(1+z)f_r^{1/3}}, \tag{5.6}$$

for circular orbits emitting signals up to the innermost circular stable orbit (ISCO). Here, $M_c = (m_1 m_2)^{3/5}/(m_1+m_2)^{1/5}$ is the binary's chirp mass, and f is the frequency, which at ISCO is given by $f_{r,\rm ISCO} = c^3/(6^{3/2}\pi G M_{\rm tot})$ in terms of total mass of the binary $M_{\rm tot} = m_1 + m_2$. In the presence of higher harmonics, this equation modifies to a sum over the higher harmonics (Enoki & Nagashima, 2007).

As for the second term in Eq. (5.5), the ratio $\frac{\tau_h}{\tau_{\rm GW}}(f)$ captures the residence time of the GW signal at a particular frequency. The numerator ($\tau_h \equiv \frac{a}{da/dt_t}$) is the binary hardening time expressed in terms of the semi-major axis of the binary a. Initially, this timescale depends on the environmental effects arising due to the interaction between the binaries and their local environment. These effects include (i) dynamical friction, (ii) stellar loss-cone scattering, and (iii) viscous drag. The impact of these environmental effects is among the major sources of uncertainty in the spectral shape of the signal but typically these environmental effects reduce the residence time of the GW signal at a particular frequency and the ratio will be less than one.

As we have noted, the above environmental effects cannot be directly computed from the Romulus25 simulation. Moreover, from an EM observations point of view, resolving galaxies on sub-parsec scales at a cosmological distance is not possible with currently ongoing and upcoming surveys. However, we can determine the average astrophysical properties of a galaxy — like gas density, stellar mass, halo mass, and other properties — on kpc scales from cosmological simulations as well as observations. We therefore model the ratio, $\frac{\tau_h}{\tau_{\rm GW}}$, in terms of the average astrophysical properties of host SMBBH galaxies:

$$\frac{\tau_h}{\tau_{\rm GW}}(f) = \mathcal{E}(f, \dot{M}_*, M_*, M_h, \rho_{\rm gas}, z). \tag{5.7}$$

In effect, we want to construct a framework that can relate the nano-Hertz (nHz) GW signal detectable from PTA with the observable quantities of galaxies.

5.4.2 Modelling the environmental effect

In this subsection, we discuss the model for $\mathcal{E}(f, \dot{M}_*, M_*, M_h, \rho_{\rm gas}, z)$ in greater detail. But first we note that the impact of the environmental effects is greatest when the binaries are further away from each other and are radiating at lower frequencies of GW (Volonteri et al., 2003, 2020; Kocsis & Sesana, 2011; Sampson et al., 2015; Chen et al., 2017; Kelley et al.,

2017a,b). As the SMBBHs inspiral and their separation decreases, they emits GW signals at increasingly higher frequencies. At frequencies of around 1 yr^{-1} (or about a few $\times 10^{-8}$ Hz), the environmental effects are no longer dominant. The SMBBHs' evolution is dominantly through GW emission, and the frequency-dependent part of the ratio $\frac{\tau_h}{\tau_{\rm GW}}(f)$ approaches unity. Impact of these effects on the GW strain are often modelled using parametric forms (Sampson et al., 2015; Chen et al., 2017).

In the present case, ROMULUS25 allows us to track the evolution of the black holes down to a few hundred parsecs but none of the current generation of cosmological simulations have the resolution to follow their evolution due to the above processes to smaller scales. Moreover, one also needs very high-resolution observations to determine the density profile of stars and gas at these scales. We therefore use a parametric equation to capture the environmental effect $\mathcal{E}$. In effect, $\mathcal{E}$ can be thought of as a subgrid model that uses accessible galaxy properties to estimate the overall number of SMBBH sources that will contribute to the nHz signal as well as the amount of their orbital energy that goes into GWs.

As noted in the last section, one of the key aspects of the problem where the astrophysical properties of the galaxies play an important role is in determining the fraction of SMBBHs that can reach the orbital separation of about 10^{-5} pc (i.e. the GW emission-dominated regime) from $\sim$ kpc scales within the age of the Universe *as well as* contribute to the SGWB in the nHz range. We model this via a dimensionless parameter α, which quantifies how efficiently the SMBBHs identified in the simulations on a $\sim$ kpc scale will overcome the last parsec problem. We expect that α will depend on the various astrophysical properties of the host galaxy and given the specific nature of the processes involved, we make an ansatz that α will primarily depend on the galaxys gas density ($\rho_{\rm gas}$), stellar mass (M_*), and star formation rate ($\dot{M}_*$), and can be written as

$$\begin{aligned}\alpha = &\alpha_\rho \left(\frac{\log(\rho_{\rm gas} = 10^7 M_\odot/\mathrm{kpc}^3)}{\log(\rho_{\rm gas})}\right) \\ &+ \alpha_{M_*}\left(\frac{\log(M_* = 10^{10} M_\odot)}{\log(M_*)}\right) \\ &+ \alpha_{\dot{M}_*}\left(\frac{\log(\dot{M}_* = 10^8 M_\odot/\mathrm{Gyr})}{\log(\dot{M}_*)}\right),\end{aligned} \tag{5.8}$$

where α_ρ, α_{M_*}, and $\alpha_{\dot{M}_*}$ govern how gas density, stellar mass and star formation rate, respectively, are in driving the hardening of the black hole binaries.

The other aspect, which plays a crucial role in controlling the shape of the stochastic GW power spectrum, is the amount of orbital energy that is lost via environmental processes.

This energy loss is modeled by the factor $(1+\beta(\frac{f}{f_t})^{-\kappa})^{-\gamma}$. Here the dimensionless factor β captures the frequency-dependent loss of GW signal due to processes like dynamical friction, stellar hardening, and viscous drag, relative to the case where these environmental effects are absent and the hardening of the binary is driven only by GW emission. We model this as

$$\beta = \beta_\rho \left(\frac{\log(\rho_{\rm gas} = 10^7 M_\odot/{\rm kpc}^3)}{\log(\rho_{\rm gas})} \right) + \beta_{M_*} \left(\frac{\log(M_* = 10^{10} M_\odot)}{\log(M_*)} \right). \tag{5.9}$$

The term κ controls the spectral behavior of the environmental effects (Sampson et al., 2015). The value for some of the effects such as stellar scattering is 10/3. However, the combination of various effects can lead to a different spectral index. Finally, the parameter γ controls the overall tilt of the environmental effects. For a fiducial case with a GW-emission-only scenario, the value of $\gamma = 1$ can be considered as a fiducial. However, there can be deviations due to astrophysical effects. For the spectral shape of the signal, we use three parameters, namely γ, κ, and f_t where f_t is the transition frequency at which the GW dominant effects become important over the environmental effects. The transition frequency can be expressed in terms of the stellar density ρ_* (in units of $\rm M_\odot$ $\rm pc^{-3}$) and velocity dispersion σ_* (in units of km/s), eccentricity e, and chirp mass M_c (in units of solar mass) as

$$f_t = f_0 \left(\frac{\rho_*}{F(e)\sigma_*} \right)^{3/10} M_c^{-2/5}, \tag{5.10}$$

where $F(e) = (1+(72/24)e^2+(37/96)e^4)/((1-e^2)^{7/2})$. f_0 is a correction factor incorporating any effect that may not be captured by this simplistic approximate formula (such as mass ratio). For $\rho_* = 100 M_\odot$ $\rm pc^{-3}$, $\sigma_* = 200$ km/s, $M_c = 10^9$ $\rm M_\odot$, $f_0 = 1$, the value of f_t is around 0.4 nHz (Chen et al., 2017). Combining all the together, we can write the total contribution from the host galaxy properties as

$$\mathcal{E}(f, \dot{M}_*, M_*, \rho_{\rm gas}, z) = \alpha \left[1 + \beta \left(\frac{f}{f_t} \right)^{-\kappa} \right]^{-\gamma}, \tag{5.11}$$

where α, β are defined above in Eq. (5.8) and Eq. (5.9).

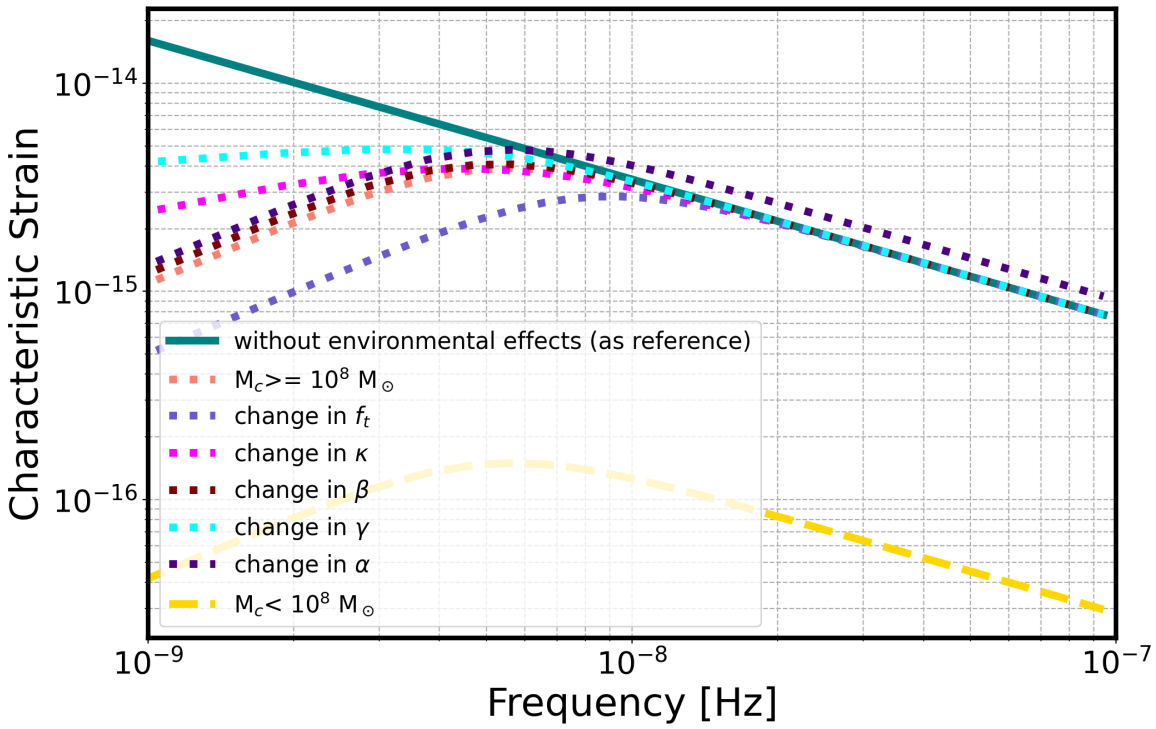

Figure 5.1: We show the SGWB strain as a function of the frequency with change in the fiducial values of the parameters $\alpha = 0.2$, $f_t = 5$ nano-Hertz, $\beta = 1$, $\kappa = 10/3$, and $\gamma = 1$, and also for SMBBHs with chirp mass $M_c < 10^8 M_\odot$ and $M_c >= 10^8 M_\odot$.

5.4.3 SGWB estimation from SMBBHs in Romulus simulation

Having put in place the above elements, we can use Eq. (5.4), Eq. (5.5), and Eq. (5.7) to estimate the SGWB signal from discrete sources in a cosmological simulation as follows

$$h_c^2(f) = \frac{4G}{c^2 \pi f^2 V_c} \sum_i \frac{1}{(1+z^i)} \left[\frac{dE_{\rm GW}(m_1^i, m_2^i, z^i)}{d\ln f_r} \bigg|_{GW} \frac{\tau_h}{\tau_{\rm GW}}(f) \right]_i , \tag{5.12}$$

where the sum runs over all the source SMBHHs (or equivalently, host galaxies in which coalescing SMBHs are present) in a simulation box of comoving volume $V_c = (25\text{Mpc})^3$ that contributes to GW background.

We use the GW sources identified in the ROMULUS25 simulation (see §5.5.1 for details about how these sources are identified) and the above relationships to model the SGWB. As described in §5.4.2, the environmental effects — the $\frac{\tau_h}{\tau_{\rm GW}}(f)$ part of Eq.5.12 — are modelled by $\mathcal{E}$ via the α and β parameters defined in Eq. (5.8) and Eq. (5.9). For ρ_{gas}, M_*, and $\dot{M}_*$ values that enter into these equations, we use the median values of these properties from the central 1 kpc region of the host galaxies of the ROMULUS 25 sources. For additional details, see §5.5.1. As for our procedure, after inputting the median values of ρ_{gas}, M_*, and $\dot{M}_*$ into Eq. (5.8) and Eq. (5.9), the free parameters of α_ρ, αM_*, $\alpha_{\dot{M}*}$, β_ρ, and β_{M_*} are chosen such that that the amplitude of the signal matches with the observed nHz signal at frequency $f = 1yr^{-1}$ (Xu et al., 2023b; Antoniadis et al., 2023a; Agazie et al., 2023; Zic et al., 2023). This results in $\alpha = 0.2$ and $\beta = 1$.

The results of modeling the SGWB are shown in Fig. 5.1. For SMBHs with chirp mass $M_c \geq 10^8$ $M_\odot$, the results for the case where environmental effects are *not considered* is shown as solid teal line and denoted as "reference". The dotted and dashed lines show the results for SMBBHs with chirp mass $M_c \geq 10^8$ $M_\odot$ and $M_c \leq 10^8$ $M_\odot$, respectively, when environmental effects are taken into account. The salmon dotted line corresponds to $M_c \geq 10^8$ $M_\odot$ and parameters $\alpha = 0.2$, $\beta = 1$, $f_t = 5$ nHz, $\kappa = 10/3$ and $\gamma = 1$. The values of α and β are computed as described above and the values of f_t, κ and γ, which control the shape of the signal, are fiducial values from physical models discussed in the previous subsection (cf §5.4.2). For the same parameters, the result for SMBBHs with $M_c \leq 10^8$ $M_\odot$ is shown by a yellow dashed line. An important point to note is that the contribution to the total signal from SMBBHs with chirp mass $M_c < 10^8$ $M_\odot$ is not significant; they only contribute about 10% of the signal arising from sources with $M_c \geq 10^8$ $M_\odot$.

To illustrate the impact of variations in environmental properties, we present results for

SMBBHs with $M_c \geq 10^8$ $M_\odot$ where we vary the values of α, β, f_t, κ and γ. Specifically, we examine the effects of changing f_t from 5 to 8 nHz (shown in purple), κ from 10/3 to 7/3 (in magenta), β from 1.0 to 0.8 (in brown), γ from 1. to 0.5 (in cyan), and α from 0.2 to 0.3 (in indigo). As each parameter value is changed, the spectral shape of the signal exhibits only moderate changes. We will explore the parameter estimation using the galaxy catalog in future work (in preparation). If the properties of the underlying host galaxy can be inferred, then the values of the parameters that control the environmental effects can be measured.

5.4.4 Connecting SGWB signal with galaxy properties

In the case of ROMULUS25 simulation, we have firsthand knowledge of $\frac{d^3 n_{\rm GW}(m_1,m_2,z)}{dm_1 dm_2 dz}$, the number density of GW sources. However, we aim to find a map between the GW sources and the EM observations – specifically, the galaxies in a complete galaxy catalog.

To connect the EM and GW observational sectors, we assert that the total number of GW sources should equal the total number of GW source host galaxies

$$\int dz \, \frac{dV}{dz} \iint dm_1 \, dm_2 \frac{d^3 n_{\rm GW}(m_1, m_2, z)}{dm_1 dm_2 dz} = \int dz \, \frac{dV}{dz} \iiint d(\dot{M}_*) \, dM_* \, dM_h \, d\rho_{\rm gas} \times \frac{d^4 n_{\rm EM}(\dot{M}_*, M_*, M_h, \rho_{\rm gas}, z)}{d\dot{M}_* dM_* dM_h d\rho_{\rm gas}}, \tag{5.13}$$

where $\frac{d^3 n_{\rm GW}(m_1,m_2,z)}{dm_1 dm_2 dz}$ is as described previously and $\frac{d^4 n_{\rm EM}(\dot{M}_*,M_*,M_h,\rho_{\rm gas},z)}{d\dot{M}_* dM_* dM_h d\rho_{\rm gas}}$ is the number density of EM sources (that are hosts of a GW source) in a bin of star formation rate ($\dot{\rm M}_*$), stellar mass ($\rm M_*$), halo mass ($\rm M_h$), and gas density ($\rho_{\rm gas}$). This is just the conservation of numbers; we are, however, implicitly assuming that there is only one SMBBH per host galaxy which can emit in the PTA frequency range.

Given a complete galaxy catalog, we can relate the GW source host galaxies to the galaxies in the catalog via $\eta(z, m_1, m_2, \dot{M}_*, M_*, M_h, \rho_{\rm gas})$, the occupancy fraction of PTA sources of masses m_1 and m_2 in galaxies at redshift z with star formation rate ($\dot{\rm M}_*$), stellar mass ($\rm M_*$), halo mass ($\rm M_h$), and gas density ($\rho_{\rm gas}$). Incorporating this and the number conservation (Eq. 5.13), we can connect the SGWB signal to the distribution of galaxies in a catalog:

$$h_c^2(f) = \frac{4G}{c^2\pi f^2} \iint \iiint dz\, d\dot{M}_*\, dM_*\, dM_h\, d\rho_{\rm gas} \eta(z, m_1, m_2, \dot{M}_*, M_*, M_h, \rho_{\rm gas}) \\ \times \frac{d^4 n_{\rm gal}(\dot{M}_*, M_*, M_h, \rho_{\rm gas}, z)}{d\dot{M}_* dM_* dM_h d\rho_{\rm gas}} \\ \times \frac{1}{1+z} \frac{dE_{\rm GW}(m_1, m_2, z)}{d\ln f_r}\bigg|_{\rm GW} \frac{\tau_h}{\tau_{\rm GW}}(f). \tag{5.14}$$

The term α, coming from $\frac{\tau_h}{\tau_{\rm GW}}(f)$ (cf Eq. 5.11), and the occupation fraction η appear in the above as a multiplicative factor ($\alpha \times \eta$), which now takes care of the overall occupation of the number of the SMBBHs contributing to the SGWB in terms of both black hole masses and also the astrophysical properties of the galaxies. One can compare this with the observations and make an inference of this quantity.

Finally, we can also write the GW source distribution function, $\frac{d^3 n_{\rm GW}(m_1,m_2,z)}{dm_1 dm_2 dz}$, in terms of the halo mass function

$$\frac{d^3 n_{\rm GW}(m_1, m_2, z)}{dm_1 dm_2 dz} = \int \frac{d^4 n_{\rm GW}(m_1, m_2, z)}{dm_1 dm_2 dz dn_{\rm halo}(M_h, z)} \frac{dn_{\rm halo}(M_h, z)}{dM_h} dM_h, \tag{5.15}$$

where $\frac{d^4 n_{\rm GW}(m_1,m_2,z)}{dm_1 dm_2 dz dn_{\rm halo}(M_h,z)}$ is the SMBBHs occupation number density in a halo of mass $\rm M_h$ and $\frac{dn_{\rm halo}(M_h,z)}{dM_h}$ is the halo mass function, i.e. the number density of halos in halo mass bin $\rm M_h$ (We remind the reader that in the present study, we identify $\rm M_h$ with $\rm M_{500}$.).

From a simulation, we can estimate the population of SMBBHs which can contribute to the SGWB in the PTA frequency range, and also identify the mass and redshift of the host halo. This gives us a connection between the SMBHs and halo mass M_h written in Eq. (5.15). Similarly we can identify the astrophysical properties of the host galaxies of the coalescing binaries from simulations. These would also be accessible from EM observations. This gives us an avenue to connect the astrophysical properties of the host galaxies with the SMBH properties.

5.5 Properties of the host galaxies of the nano-Hertz GW sources

The dynamics of the SMBBHs and their contribution to the nHz frequency depends on the local astrophysical properties as discussed in the previous section. However, to identify the key astrophysical properties of the host galaxies that can be identified from observations, we

need to explore the large-scale properties of the host galaxy. In this section, we explore both local astrophysical properties in the vicinity of SMBBHs and their host galaxy properties. The properties we consider include gas density, stellar mass, and star formation rate. While discussing the host galaxies, we also comment on the properties of the halos in which these galaxies reside.

5.5.1 Local galactic properties

In this section, we focus on the characteristics of the gas and stars in the vicinity of the SMBBHs, and specifically, within a 1 kpc radius around the more massive black hole in SMBBHs, as the most massive BH drives the chirp mass and hence the strength of the signal. We also restrict ourselves to SMBBHs with a chirp mass $M_c \geq 10^8$ $M_\odot$[3] and $z \leq 2$. These SMBBHs account for $\sim 90\%$ of the total SGWB power spectrum (see Fig. 5.1). Our analysis of the ROMULUS25 simulation reveals six nHz GW sources. Considering the redshift range in which these sources are detected and our simulation volume, we calculate the number density of nHz GW sources to be 7.7×10^{-6}cMpc^{-3}. This value closely aligns with the number densities estimated in Mingarelli et al. (2017) and Casey-Clyde et al. (2022) and that derived by Antoniadis et al. (2023c) from PTA data release, which are 1.6×10^{-6}cMpc^{-3}, 6.6×10^{-6}cMpc^{-3} and 1.5×10^{-5}cMpc^{-3} respectively.

In Fig. 5.1 we have shown the GW background for various different cases based on the median value of the gas density, star formation rate and stellar mass within a 1 kpc radius around the more massive black hole in nHz GW SMBBH sources in the ROMULUS25 simulation. Fig. 5.2 shows, from top to bottom, the gas density ($\rho_{\rm gas}$), star formation rate (SFR), and stellar mass (M_*), vs redshift, of the individual host galaxies of the nHz GW SMBBH sources. No significant evolution with redshift is found for the local SFR and the local stellar mass. However, the top panel shows an increasing trend of $\rho_{\rm gas}$ with redshift. Nonetheless, examining the properties around black holes solely in nHz GW sources doesn't provide a comprehensive view. Therefore, we compare these to the same properties surrounding the most massive of the two black holes in our full set of proximate and merging (cf §5.3.4) pairs of black holes in the ROMULUS25 simulation. The resulting distributions for gas density, SFR, and stellar mass are shown as salmon histograms in Fig. 5.3. The corresponding quantities for nHz GW sources are denoted by a vertical line. We find that the local $\rho_{\rm gas}$ and SFR around our nHz GW sources are typical. Specifically, the increasing gas density with redshift around the nHz GW sources simply reflects the fact that all systems

[3] $M_c \geq 10^8$ $M_\odot$ implies that the most massive SMBH in the pair is *at least* 8.7×10^7 $M_\odot$ if both SMBHs are equal mass, or more realistically $> 2.5 \times 10^8$ $M_\odot$ since the BH mass ratios are typically < 0.2.

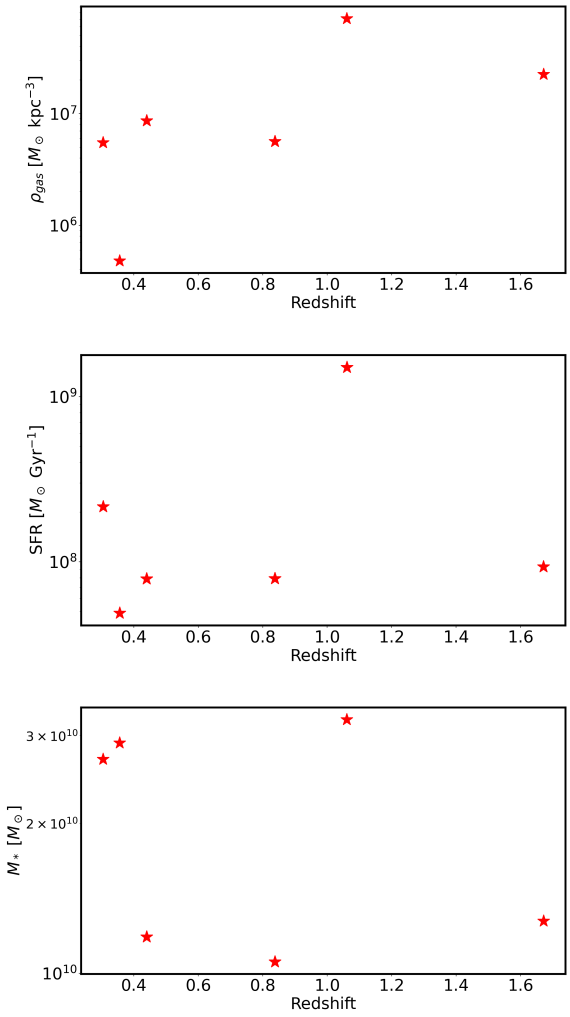

Figure 5.2: The local astrophysical properties of the galaxies: gas density (top), SFR (middle), and stellar mass (bottom) within 1 kpc of the more massive SMBH in merging SMBBHs detected in ROMULUS25 and contributing most of the SGWB signal (i.e. with chirp masses $M_c \geq 10^8$ M$_\odot$), shown as a function of the host redshift.

Figure 5.3: The vertical line in each panel shows the gas density (first and second row), star formation rate (third and fourth row) stellar mass (fifth and sixth row) within 1 kpc of the more massive SMBH in the merging SMBBH pairs identified as nano-Hertz GW source (i.e. with chirp masses $M_c \geq 10^8$ $M_\odot$) at the host galaxy's redshift. The histogram shows the corresponding quantities around the more massive black holes in all SMBH pairs (merging and proximate) in the ROMULUS25 simulation at the same redshift.

have more gas at earlier epochs. However, the stellar mass in the vicinity of our nHz GW sources falls in the high mass tail of the corresponding distribution, as illustrated in Fig. 5.3. This indicates that nHz GW sources are more likely to be found in environments with high local stellar mass or equivalently, stellar density. Though it is important to note that this conclusion is based on only 6 events detectable in a simulation box of $(25\ \mathrm{cMpc})^3$. A study from a bigger box simulation will help in better understanding the statistical properties.

5.5.2 Global galactic and host halo properties

In this section, we consider the global galactic characteristics of the hosts of nHz GW sources, delving into the observable properties of these host galaxies. We also examine the properties of the halos of these host galaxies.

Figure 5.4 illustrates the relation between galaxies' gas density (ρ_{gas}), stellar mass (M_*), star formation rate (SFR), and specific star formation rate (sSFR) vs redshift. Each of these quantities is calculated inside a 25 kpc sphere around the galaxy center. The first panel shows the galaxy gas density. No significant evolution with redshift is observed. On the other hand, the second and third panels clearly show a decrease in the stellar mass and an increase in SFR with redshift, respectively. Not surprisingly, this results in a rising sSFR with redshift, as shown in the lower right panel. Additionally, the stellar mass of the host galaxies suggests that at the redshifts of interest, these galaxies are among the most massive systems in the ROMULUS volume. Based on analyses of Jung et al. (2022) and Saeedzadeh et al. (2023b), we guess that these are the massive central galaxies in group-scale halos. We will discuss this elaborately at a later part in this section. The specific star formation rate (sSFR) is frequently used to classify galaxies as star forming or quenched. We show the evolution of the sSFR with redshift for the host of the SMBBHs with $M_c \geq 10^8\ \mathrm{M}_\odot$ in the last panel in Fig. 5.4.

In this paper, we adopt the criteria from Genel et al. (2018), where they label a galaxy as "main sequence" if its sSFR is within ± 0.5 dex of the main sequence ridge and as "quenched" if its sSFR is 1 dex below the ridge. Genel et al. (2018) give a relationship between sSFR and M_* at few redshifts. We linearly interpolate across these to determine the main sequence ridge sSFR at redshifts and stellar masses of our host galaxies. In Fig. 5.5, we show $\Delta\log(\mathrm{sSFR}) \equiv \log(\mathrm{sSFR}_{\mathrm{galaxy}}) - \log(\mathrm{sSFR}_{\mathrm{ridge}})$ for our host galaxies. The shaded region shows the main sequence band and the dashed line corresponds to the threshold below which galaxies are classified as quenched. Five of our six hosts either lie in the quenched territory or are on the border. One galaxy, however, the $z = 1.061$ host, falls within the

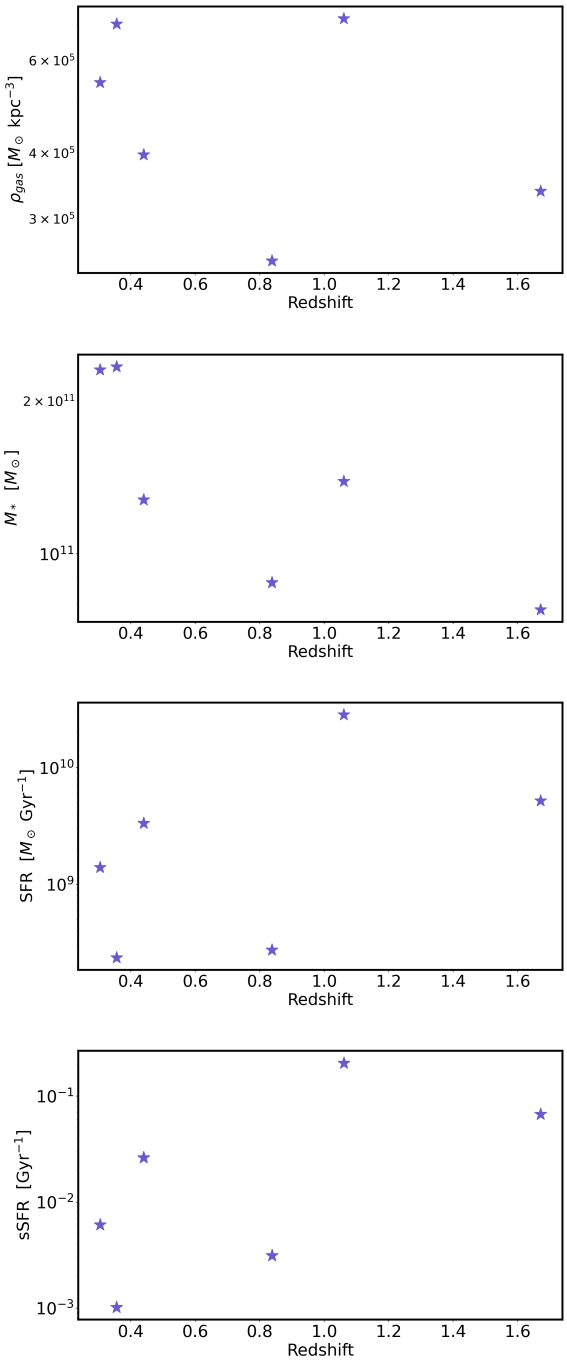

Figure 5.4: The global galactic properties of the galaxies hosting the merging SMBBH pairs identified as nano-Hertz GW sources (i.e. with chirp masses $M_c \geq 10^8$ $M_\odot$). The panels show gas density (first panel), stellar mass (second panel), SFR (third panel), and sSFR (fourth panel) as a function of redshift. All quantities are calculated inside a sphere with a 25 kpc radius around the galaxy center.

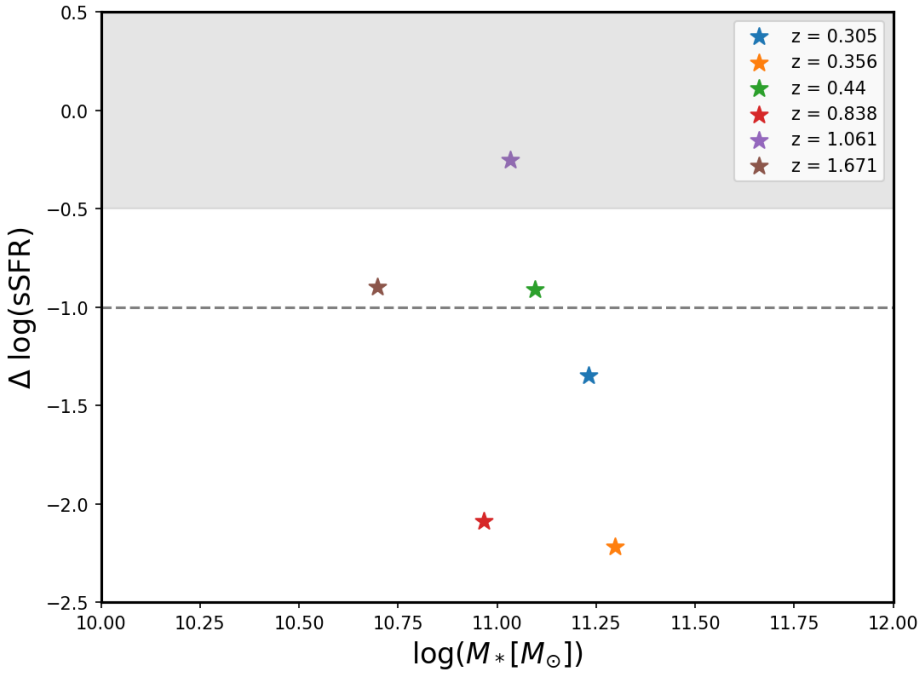

Figure 5.5: Categorising host galaxies of SMBBHs with $M_c > 10^8 M_\odot$ as star-forming or quenched following definition of Genel et al. (2018). Here we show $\Delta\log(\mathrm{sSFR}) = \log(\mathrm{sSFR}_{\mathrm{galaxy}}) - \log(\mathrm{sSFR}_{\mathrm{ridge}})$ for these host galaxies. The dashed line, which marks 1 dex below the ridge for each redshift, serves as the quenched threshold. The shaded region indicates the "main sequence". See text for detailed definitions.

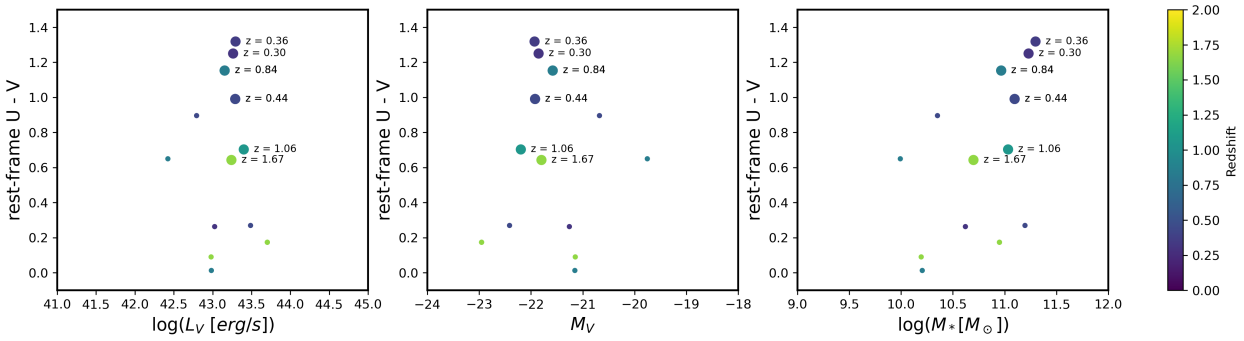

Figure 5.6: The rest-frame U-V vs rest-frame V-band luminosity (L_V) (first panel), vs rest-frame absolute magnitude (M_V) (second panel), and vs stellar mass M_* (last panel) of the host galaxies of the SMBHs for chirp mass $M_c \geq 10^8$ $\mathrm{M}_\odot$ (represented by big circles) and 10^7 $\mathrm{M}_\odot \leq M_c \leq 10^8$ $\mathrm{M}_\odot$ (represented by small circles). The data points are color-coded as a function of redshift, and the annotations show the exact redshift they are detected.

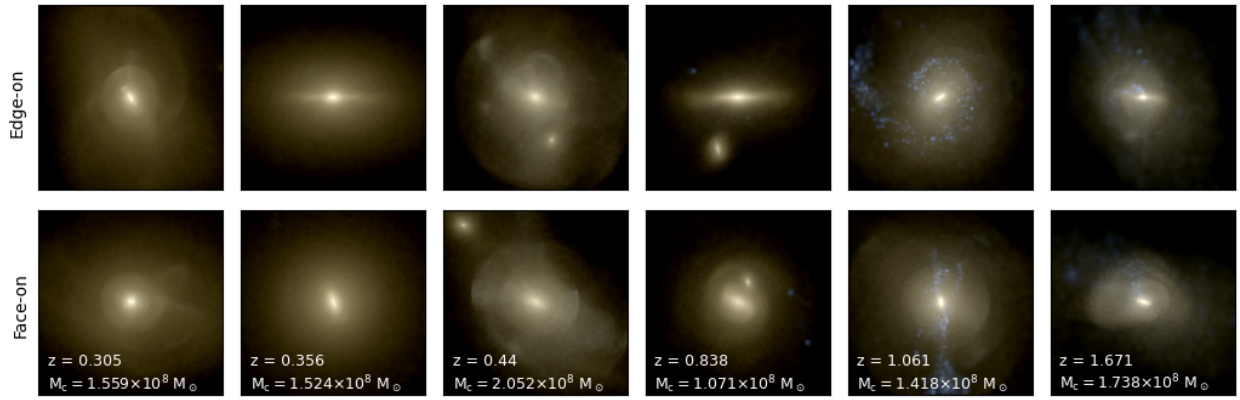

Figure 5.7: Multi-band composite image of the host galaxies for SMBBHs with chirp mass $M_c \geq 10^8$ $M_\odot$ is shown with edge-on (top) and face-on (bottom) views at redshifts they are detected at.

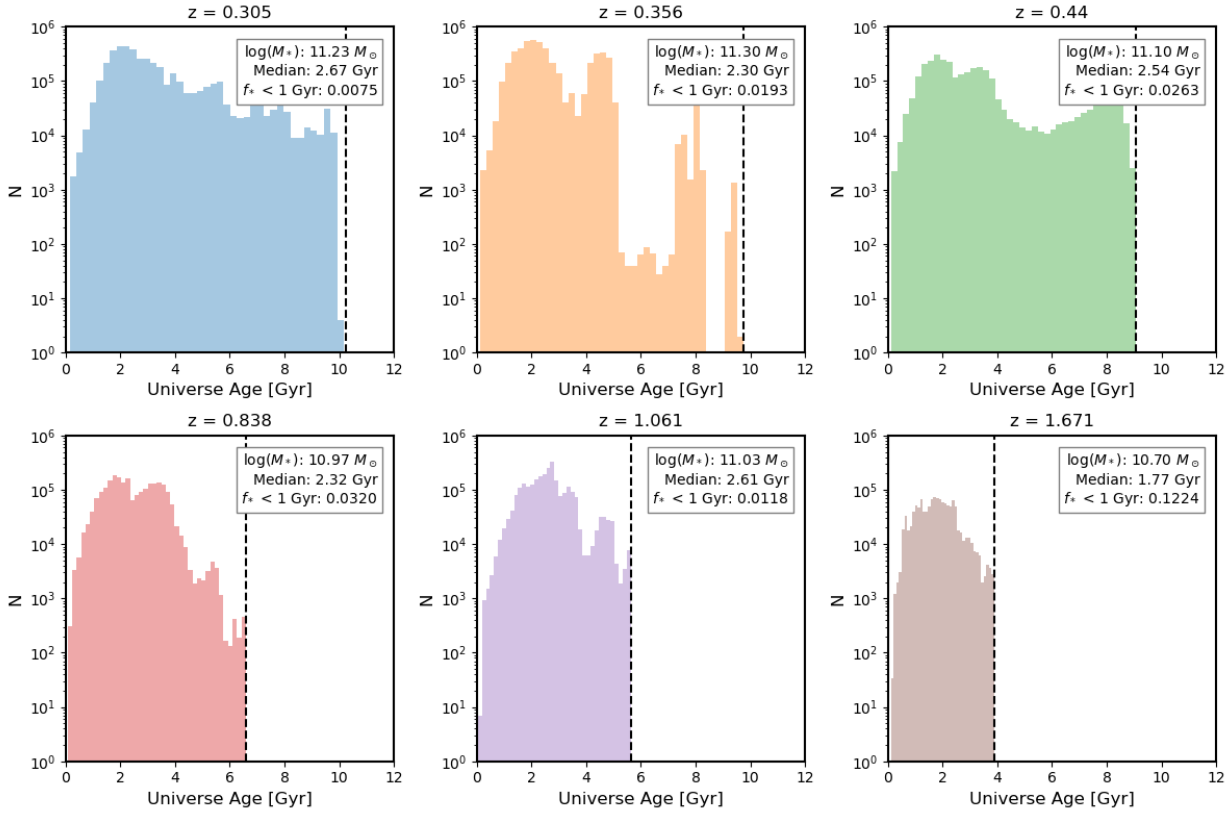

Figure 5.8: The age of the Universe when stars in the host galaxies of SMBBHs with a chirp mass $M_c \geq 10^8$ $M_\odot$ formed. The dashed line represents the age of the Universe at the time the SMBBHs are detected. The values in the top right box, from top to bottom, indicate the stellar mass within 25 kpc from the galaxy center, the median age of the stars, and the fraction of the stellar mass observed that is aged ≤ 1 Gyr.

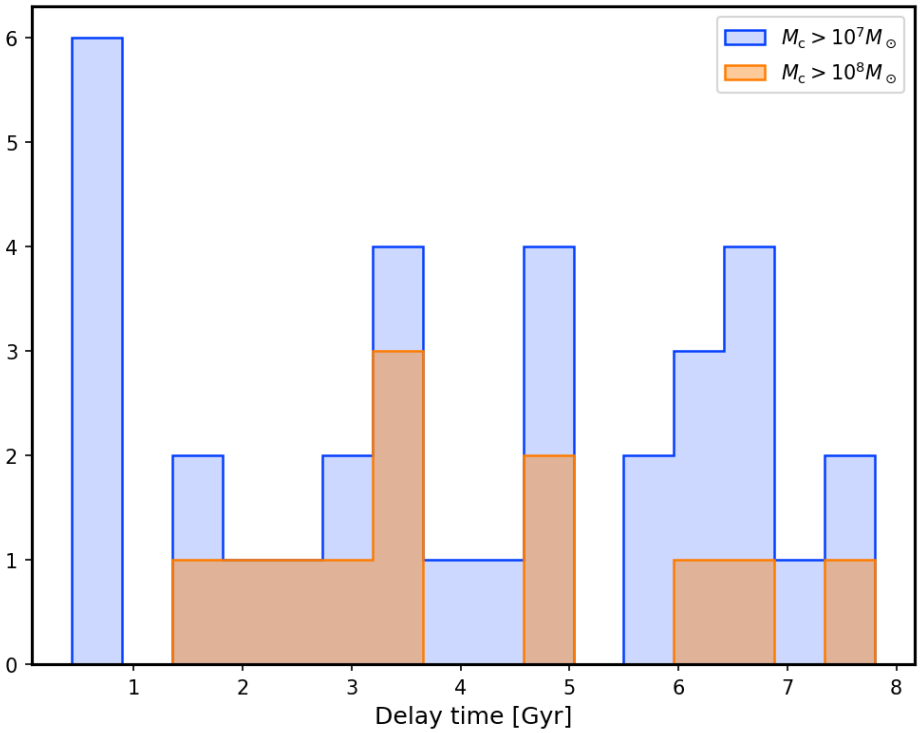

Figure 5.9: The amount of time taken by the SMBHs to grow the last 50% of its mass it possesses at the time of the merger is shown for sources with chirp mass $M_c \geq 10^7$ $M_\odot$ (in blue) and $M_c \geq 10^8$ $M_\odot$ (in orange). The distribution indicates that the SMBHs with chirp mass $M_c \geq 10^8$ $M_\odot$ need at least 10% of the age of the Universe to grow, indicating these objects are likely to be host in old galaxies.

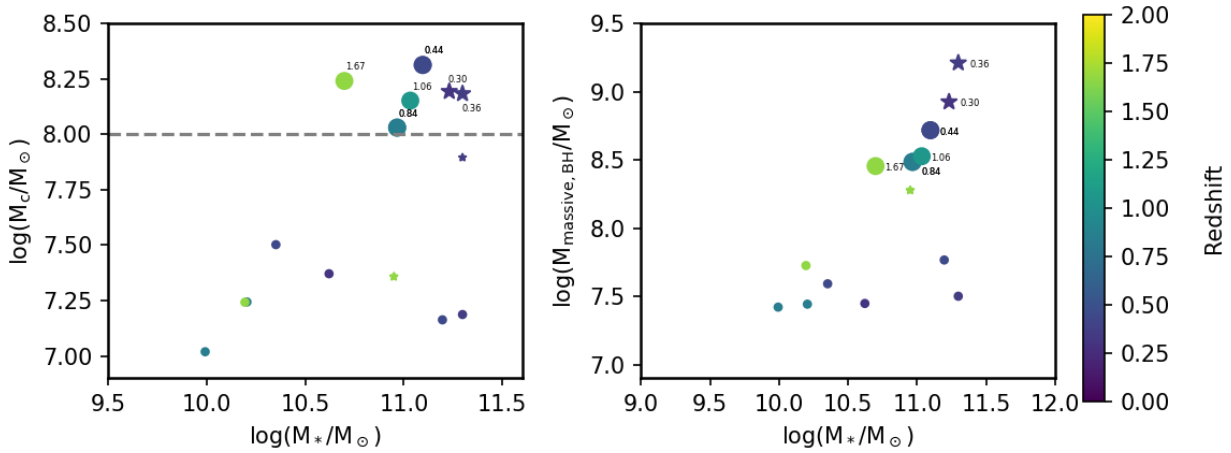

Figure 5.10: Left panel: The chirp mass of SMBBHs plotted against the stellar mass of their host galaxy. Right panel: Mass of the more massive black hole in SMBBHs versus the stellar mass of their host galaxy. SMBBHs with a mass ratio $q < 0.1$ are represented by stars, while those with $q > 0.1$ are represented by circles. Large symbols correspond to SMBBHs with chirp mass $M_c \geq 10^8$ M$_\odot$ and small symbols denote those with 10^7 M$_\odot$ $\leq M_c \leq 10^8$ M$_\odot$. The data points are colored according to redshift, and the annotations show the exact redshift they are detected at.

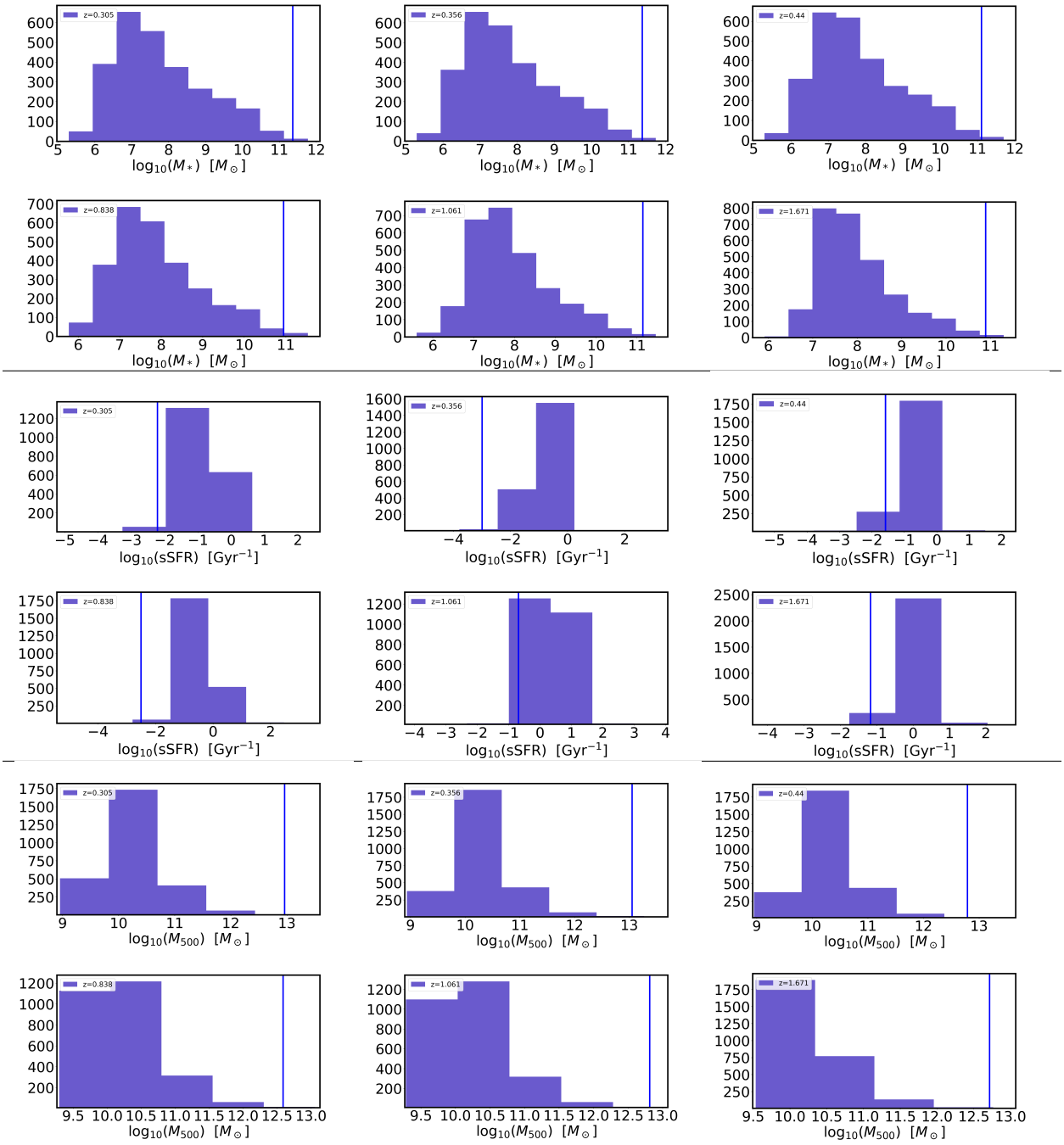

Figure 5.11: Vertical line in each panel shows properties of host galaxies and host halo of the merging SMBBH pairs identified as nano-Hertz GW sources (i.e. with chirp masses $M_c \geq 10^8$ $M_\odot$) at the corresponding redshift. The corresponding distribution for all galaxies or halos with $M_{200} > 4.5\times10^9 M_\odot$ in the Romulus25 simulation at the same redshift with a background histogram. **First and second row:** display the stellar mass. **Third and fourth row:** present the sSFR. **Fifth and six row:** show M_{500} of the host halos. All properties are measured at the host galaxy's redshift. The stellar mass and sSFR are calculated within a 25 kpc sphere around the galaxy center.

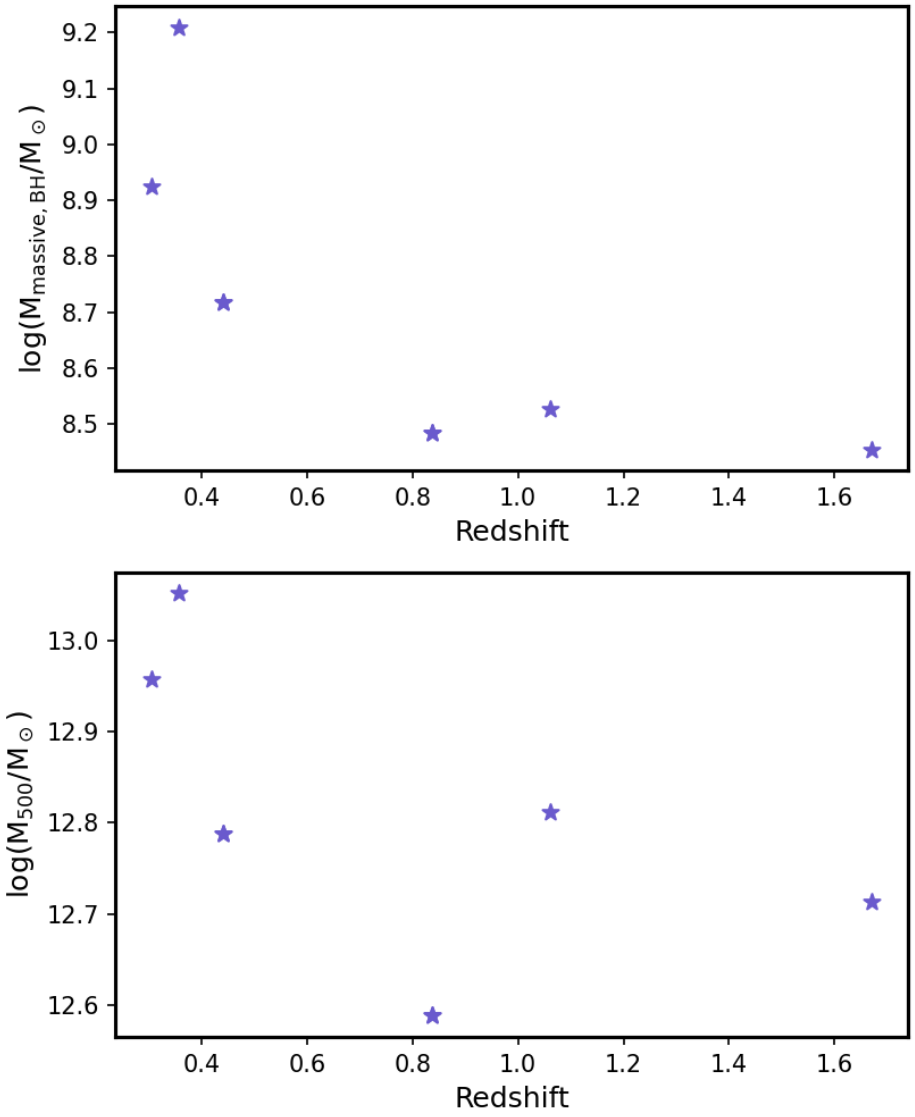

Figure 5.12: Top panel: Mass of most massive halo in SMBBH pairs identified as nano-Hertz GW sources as a function of redshift. Bottom panel: The M_{500} of host halos of nano-Hertz GW sources vs. redshift.

star-forming main sequence band.

Next, we examine the rest-frame U-V colors of the host galaxies. For completeness, we show $(\mathrm{U\text{-}V})_{\mathrm{rest-frame}}$ versus rest-frame V-band luminosity ($\mathrm{L_V}$), rest-frame absolute magnitude ($\mathrm{M_V}$), and stellar mass ($\mathrm{M_*}$). In these plots, large circles represent the host galaxies of nHz GW sources with $M_c \geq 10^8 \mathrm{M}_\odot$, while small circles delineate hosts of nHz GW sources with chirp masses ranging between $10^7 M_\odot < M_c < 10^8 M_\odot$. Generally, the latter tend to be bluer and less massive than the hosts of our nHz GW sources. The four $z < 1$ host galaxies are consistent with the quenched, early-type galaxies in Coma and Virgo clusters (Renzini, 2006) as well as the SDSS and the CANDELS Multi-Cycle Treasury Survey (Bell et al., 2012). This aligns with the trends identified by Izquierdo-Villalba et al. (2023), who shows that elliptical galaxies are significant hosts of massive binary black holes at $z < 1$. The two $z > 1$ hosts, one of which is star-forming and the other quenched according to the Genel et al. (2018) criterion, are both just slightly bluer than the population of quenched early-types at comparable redshifts in the CANDELS Multi-Cycle Treasury Survey (Bell et al., 2012). The comparison to galaxies at the same redshifts is important since the stellar population in higher redshift galaxies is inherently younger and therefore bluer.

To gain better insight into why the two higher redshift exhibit bluer colors and to further clarify the nature of the host galaxies generally, we examine the images of the host galaxies. These are shown in Fig. 5.7. The top row shows the edge-on view of the galaxies and the bottom row shows the face-on view. The stars are colored based on their magnitudes, determined by their age and metallicity. The magnitudes from the 'i' band influence the red component of the image, 'v' the green, and 'u' the blue. These channels are then combined to produce a multiband composite image of the galaxy.[4] Visually, *all* of the galaxies appear to be early types, and the majority of the stars in these galaxies are old in the sense that 50% had formed within the first 2.5-2.6 Gyrs after the Big Bang. This is illustrated by the histograms in Fig. 5.8, which show the cosmic age (i.e. the age of the Universe) when the stars in the galaxies formed. Turning back to Fig. 5.7, we see that nearly all of the galaxies appear to have experienced recent merger(s). They all manifest features like stellar streams and shells (eg Fardal et al., 2007, and references therein). Some of the mergers are gas rich, as in the case of the host galaxy at $z = 1.06$ where one can clearly see an extended stream with ongoing star formation against a background of older stars. A less prominent stellar stream can also be seen in the host galaxy at z = 1.671. A detailed analysis of the morphology of host galaxy of merging binary black holes by Bardati et al. (2023) shows that the dominant morphological signature of SMBH mergers is the presence of a classical bulge

[4]The galaxy images are generated using PYNBODY package (Pontzen et al., 2013b).

that is also a sign of major mergers of these host galaxies. The panels in Fig. 5.8 provide additional information, including the fraction of stellar mass at the time of observation that has an age ≤ 1 Gyr. The latter varies from $< 1\%$ to as much as 12% in the highest redshift system. This small fraction of very young stars is the likely explanation for the two $z > 1$ galaxies' bluer colors. As shown by Pipino et al. (2009), even a small fraction ($\sim 1\%$) of young stars (~ 0.1 Gyr) can have a dramatic impact on UV-optical colors.

For the SMBBHs, we show the time taken by these sources to grow to masses above $M_c = 10^7$ $M_\odot$ from their progenitor mass of 50% of the source masses in Fig. 5.9 for both the SMBHs in a SMBBH. The distribution of the delay time for the black holes with $M_c \geq 10^7$ $M_\odot$ and $M_c \geq 10^8$ $M_\odot$ is shown in blue and orange respectively in Figure 5.9. The shortest delay time observed for these black holes is 1.4 billion years, roughly 10% of the age of the Universe for sources with $M_c \geq 10^8$ $M_\odot$, which contribute significantly to the SGWB. This indicates that the number of mergers of the PTA sources is likely to be more towards low redshift than high redshift, and the corresponding properties of the host galaxies will be towards older galaxies.

In Fig. 5.10, left panel, we show the correlation between the chirp mass of SMBBHs with the stellar mass of their host galaxy. The right panel shows the mass of more massive black holes in the SMBBHs vs. the host galaxies' stellar mass. Sources with black holes mass ratio $q < 0.1$[5] are shown by stars and ones with $q > 0.1$ are shown by circles. Large symbols correspond to SMBBHs with chirp mass $M_c \geq 10^8$ $M_\odot$ and small symbols denote those with 10^7 $M_\odot \leq M_c \leq 10^8$ $M_\odot$. The plot indicates that sources with the highest chirp mass are primarily present at low redshift and are hosted in galaxies with stellar mass greater than 10^{11} $M_\odot$. Furthermore, the heaviest black holes are found in pairs with chirp masses $M_c \geq 10^8$ $M_\odot$, which are hosted by massive galaxies. These observations support the hypothesis we presented at the beginning of this section: that nHz GW sources predominantly inhabit massive, group-central galaxies. We will explore this further below.

In Fig. 5.11, we compare the global properties (i.e. global stellar mass and sSFR) and the environment (i.e. the halo mass and location therein) of the host galaxies of nHz GW sources with $M_c > 10^8 M_\odot$ (vertical lines) against the properties of all galaxies in the simulations within halos with $M_{200} > 4.5 \times 10^9 M_\odot$[6] (histograms). The plot supports the discussion we have presented above in the context of the colors and quenched/star-forming status of the host galaxies, that the sSFR of these galaxies places them in the low sSFR tail of the sSFR

[5]The mass ratio is defined as $q \equiv m_1/m_2$ with $m_2 > m_1$.

[6]This threshold is applied solely during the calculation of background histograms to save computational time, as we are not interested in very small halos.

distribution of the galaxies in the ROMULUS25 simulation volume. From Fig. 5.11 we deduce that our host galaxies are among the most massive galaxies in the ROMULUS25 simulation volume. That the host galaxies of the nHz GW sources reside in galaxies with high stellar mass and low sSFR making them a unique class of objects.

This is further confirmed by comparing the host halo M_{500} to all[7] halos M_{500} in the ROMULUS simulation which is shown in the histogram, we note that the host halo masses are in the high-mass tail of the distribution (see the last two panels in Fig. 5.11). The halos in which the host galaxies reside are group scale systems and based on the results of Jung et al. (2022) and Saeedzadeh et al. (2023b), we expected – and have subsequently confirmed – that these galaxies are massive central group galaxies. Collectively these findings strongly suggest that the nHz GW sources are hosted by massive early-type galaxies at the centers of groups and clusters. *However, we assert that the typical hosts of the nHz GW sources will be group-central galaxies.* For one, there are many more groups than clusters. Moreover, the lower velocity dispersion of group satellites makes dynamical friction in group halos more efficient, and consequently, group environments are much more conducive to mergers, especially between the satellite and the central galaxies (O'Sullivan et al., 2017b; Oppenheimer et al., 2021b, and references therein).

For completeness, in Fig. 5.12, we present the mass of the more massive black hole in nHz GW sources and the host halo mass of these sources in the top and bottom panels, respectively. As expected, these plots indicate that as redshifts increase, the halo mass decreases, and the black hole mass in the pair also reduces.

In this section, we have elucidated the unique astrophysical properties of the host galaxies of the SMBBHs which contribute to the SGWB signal in comparison to all galaxies in the simulation. Our findings highlight that GW source hosts (with chirp mass $M_c \geq 10^8$ $M_\odot$) predominantly reside in galaxies characterized by lower star formation, higher stellar mass, and higher halo masses compared to most counterparts at a given redshift. Specifically, these hosts are located within group-scale halo systems, identifying as massive central group galaxies. These host galaxies are early-type galaxies, displaying a distinct trend in the color-magnitude diagram across redshifts. These astrophysical properties inferred theoretically about the SMBBHs make it possible to correlate electromagnetic observations of the galaxies with the GW sources. Exploring such connections, coupled with comparisons to theoretical models, offers insights into the interplay between galaxy formation and black hole formation.

[7] All halos with $M_{200} > 4.5 \times 10^9$

5.6 Possible techniques to connect observations with theoretical models

In the last two sections, we have discussed a scheme to connect the global astrophysical properties of the galaxies with the spectrum of the SGWB signal in the PTA band and have applied that to the ROMULUS simulation to understand the underlying theoretical correlation. The next interesting step forward is to connect this with the observations available from currently ongoing/upcoming surveys (see Burke-Spolaor et al. (2019) for review article). The observation of the GW signal from PTA observations in the nHz range can happen as (i) SGWB and (ii) GW signal from individual events. Both of these kind of observations can bring complementary information.

SGWB: The measurement using PTA observations provides a measurement of the spectrum of the SGWB signal. However, it is still unclear what are the properties of the host galaxies of the SMBBHs that contribute to the signal. As we have shown in the previous section, the simulations show that the binaries are likely to form in galaxies with high stellar mass, high halo mass, and low SFR, and mostly early-type galaxies, that show signs of mergers in not too distant a past. We also showed that the host galaxies are central group galaxies. The host of the GW sources also shows a trend in the color-magnitude diagram as a function of redshifts.

Based on these understandings, we can classify galaxies from electromagnetic observations based on their color, stellar mass, halo-mass, SFR, and galaxy type and can explore spatial cross-correlation of the galaxy distribution with the anisotropic SGWB signal (Mingarelli et al., 2013; Hotinli et al., 2019; Sato-Polito & Kamionkowski, 2023) and explore cross-correlation between the two quantities (Mukherjee & Silk, 2020; Yang et al., 2020; Mukherjee & Silk, 2021; Yang et al., 2023). A detailed paper on this formalism will be followed up in a companion paper. The cross-correlation of the SGWB signal with the galaxies of different types will be maximum for types of galaxies that are host of the GW sources. The exploration of the cross-correlation signal will give us an understanding of the population of the GW sources contributing to the background and we can estimate the occupation number of SMBHs. This will be useful in understanding the SGWB measurement in terms of the astrophysical properties of galaxies given in Eq. (5.14) based on observations. In future work, we will explore this aspect from the measurement of the SGWB signal and galaxies detected from optical and infrared surveys.

Signal from individual events: The measurement of the nHz GW signal from individual sources is likely to be possible from the future array of radio antennae such as Square Kilometer Array (SKA) (Ellis, 2013; Burke-Spolaor, 2013; Kharb et al., 2017). With such

observations of individual GW signals, we can fit the astrophysical properties of the galaxies with the frequency dependence of the GW signal and fit the parameters on the occupation number and the signature of the environmental effects on the GW strain by directly comparing the properties of the host galaxy such as the gas density, stellar mass, halo mass, SFR, galaxy morphology, and color. Furthermore, an interesting avenue will be to perform a dedicated study of the hosts of the GW sources with high-resolution spectroscopic surveys to better understand its astrophysical properties.

5.7 Conclusion and Future Outlook

In this work, we explore the astrophysical properties of the host galaxies of the SMBBHs which can produce nano-Hertz SGWB using the ROMULUS25 cosmological simulation. ROMULUS25 is capable of modeling the astrophysical properties of galaxies and its unique approach to seeding, accretion, and particularly the dynamics of SMBHs makes it especially well-suited for investigating SMBH/SMBBH-galaxy connections. Using this simulation, we have calculated the SGWB signal from the SMBBHs by modeling the environmental effects around the SMBHs.

We found that SMBBHs with chirp mass $M_c > 10^8 \mathrm{M}_\odot$ are primary source of the SGWB signal. In our simulation up to $z = 2$, we found six such sources resulting in a number density of $7.7 \times 10^{-6} \mathrm{cMpc}^{-3}$ consistent with the results from PTA studies (Mingarelli et al., 2017; Casey-Clyde et al., 2022; Antoniadis et al., 2023c). Although the ROMULUS25 is a cosmological simulation and not an idealized simulation specifically designed for SMBH-SMBH physics, it still successfully produces a correct number density. This highlights its potential for further studies in this domain.

We then continue by studying the redshift evolution of the astrophysical properties of the host galaxies such as gas density, SFR, stellar mass, and halo mass, across redshifts. These host galaxies are early-type galaxies, characterized predominantly by older star populations. They exhibit a distinct trend in the color-magnitude diagram across redshifts, which could be of particular interest to compare with observations.

Our analysis further reveals that, compared to their counterparts at similar redshifts, the host galaxies of nHz GW sources exhibit lower SFRs, greater stellar masses, and more substantial halo masses. Our findings collectively suggest that nHz GW sources are predominantly hosted by massive early-type galaxies at the centers of groups and clusters. However, we assert that the typical hosts for these GW sources are expected to be group-central galaxies. This is supported by two main factors: (i) groups are more common than clusters,

and (ii) the lower velocity dispersion in groups leads to more effective dynamical friction, thereby increasing the likelihood of mergers, especially between satellite galaxies and the central galaxy of the group (O'Sullivan et al., 2017b; Oppenheimer et al., 2021b).

It is important to note that our conclusions remain robust even if the seed mass in ROMULUS25 were set lower than $10^6 M_\odot$. As discussed in Section 5.5.1, the SGWB power spectrum signal in the nHz regime is predominantly due to SMBBHs with chirp masses greater than $10^8 M_\odot$. These systems are composed of individual SMBHs, each with a mass exceeding $8 \times 10^7 M_\odot$, which is significantly above our minimum SMBH mass. Thus, our findings regarding the properties of host galaxies of nHz GW sources remain valid.

The theoretical connection of the host galaxy properties of the GW sources and the black hole masses indicates which kind of galaxies and their evolution are linked with the black hole merger. This theoretical connection shown in this work will be a guideline for us to explore the connections from GW observations in the nHz band and optical and infrared galaxy observations. By measuring the spatial cross-correlation between the anisotropic SGWB with galaxies as well as a targeted search of individual galaxies for the nHz GW events in the SKA era.

The multi-messenger technique by exploring the connection between the astrophysical properties of host galaxies with the SMBHs and the strain of the GW signal from the coalescing SMBHs will make it possible to establish from observations how the SMBBHs evolution depends on the astrophysical properties of the galaxies. The occupation number of SMBHs in galaxies of different types will make it possible to test theoretical models using observations. In the future with the data from the ongoing International Pulsar Timing Array and upcoming Square Kilometer Array (SKA) (Janssen et al., 2015), we will be able to make high-precision measurements of the nHz GW signal. In synergy with the galaxy surveys up to high redshifts such as Dark Energy Spectroscopic Instrument (DESI Collaboration et al., 2016), Euclid (Laureijs et al., 2011), Vera Rubin Observatory (LSST Dark Energy Science Collaboration, 2012), and Roman Telescope (Akeson et al., 2019) we will make joint estimation of GW and galaxies to unveil the open question of formation of SMBHs and its connection with the galaxy evolution.

Acknowledgement

The work of SM is a part of the ⟨data|theory⟩ Universe-Lab which is supported by the TIFR and the Department of Atomic Energy, Government of India. VS and AB acknowledge support from the Natural Sciences and Engineering Research Council of Canada (NSERC)

through its Discovery Grant program. AB acknowledges support from the Infosys Foundation via an endowed Infosys Visiting Chair Professorship at the Indian Institute of Science. MT was supported by an NSF Astronomy and Astrophysics Postdoctoral Fellowship under award AST-2001810. AB, TQ, and MT were partially supported by NSF award AST-1514868.

The ROMULUS simulation suite is part of the Blue Waters sustained-petascale computing project, which is supported by the National Science Foundation (via awards OCI-0725070, ACI-1238993, and OAC-1613674) and the state of Illinois. Blue Waters is a joint effort of the University of Illinois at Urbana-Champaign and its National Center for Supercomputing Applications. Resources supporting this work were also provided by the (a) NASA High-End Computing (HEC) Program through the NASA Advanced Supercomputing (NAS) Division at Ames Research Center; and (b) Extreme Science and Engineering Discovery Environment (XSEDE), supported by National Science Foundation grant number ACI-1548562. The analysis reported in this paper was enabled in part by WestGrid and Digital Research Alliance of Canada (alliancecan.ca) and on the cluster of ⟨`data|theory`⟩ `Universe-Lab` supported by DAE. Our analysis was performed using the Python programming language (Python Software Foundation, https://www.python.org). The following packages were used throughout the analysis: numpy (Harris et al. 2020), matplotlib (Hunter 2007), Pynbody (Pontzen et al. 2013b), SciPy (Virtanen et al. 2020), and TANGOS (Pontzen & Tremmel 2018).

Finally, VS and AB acknowledge the lək̓ʷəŋən peoples on whose traditional territory the University of Victoria stands, and the Songhees, Equimalt and W̱SÁNEĆ peoples whose historical relationships with the land continue to this day.

Data Availability

The data directly related to this article will be shared on reasonable request to the corresponding author. Galaxy database and particle data for ROMULUS is available upon request from Michael Tremmel.

Personal contribution clarification:

This chapter also contributes to the second part of my dissertation, focusing on the properties of host galaxies of merging SMBHs. This project was an extension of my Dual AGN study, and I conducted 90% of the analysis for this project and I was the project lead. My efforts involved following the trajectories of SMBHs, identifying which SMBHs are likely to form binaries, and which are potential nanoHz gravitational wave (GW) sources. At this

stage, I quantified the properties of their host galaxies. Once the binary SMBHs separation reaches the minimum separation that can be resolved in Romulus simulation, a subgrid model was used to determine their nanoHz GW signal. This subgrid model, designed by Suvodip Mukherjee, requires the internal properties of the host galaxies as input, which I was able to provide. I wrote 80% of the paper. The description of the subgrid model was written by Suvodip Mukherjee, but I substantially edited it to ensure clarity for the cosmic structure formation community. Arif Babul provided essential scientific guidance and recommendations throughout the process and gave feedback on the paper draft. Michael Tremmel and Thomas R. Quinn designed the novel SMBH model in the Romulus simulation that tracks SMBH dynamics and is the foundation upon which this study was built. They also provided feedback on the final draft.

Chapter 6

Conclusions

This dissertation delves into the intricate dynamics of galaxy groups, where conditions and processes within those environments play a crucial role in galaxy evolution. The increased density of galaxies and the relatively low velocity dispersion within these groups (cf. O'Sullivan et al. 2017a; Werner & Mernier 2020; Lovisari & Ettori 2021) make galaxies, both central and satellites, susceptible to mergers, tidal interactions, and ram pressure stripping (McCarthy et al., 2008). Moreover, these galaxies are affected by cooling flows, as they are enveloped in a sea of hot X-ray emitting plasma. Given that over 50% of galaxies in the Universe reside in groups (Eke et al., 2006), and some of the most massive galaxies are formed within such systems (cf. Rennehan et al. 2020; Jung et al. 2022), understanding the interplay within galaxy groups becomes crucial to get a comprehensive view of galaxy evolution. The main goal of my dissertation has been twofold (i) to investigate the multiphase structure of circumgalactic medium (CGM) surrounding the brightest group galaxies (BGGs) and (ii) to use dual and binary supermassive black holes (SMBHs) as markers of galaxy mergers to examine how their host galaxies evolve during times of SMBHs active accretion and the SMBH - SMBH mergers. This chapter provides an overview of the main conclusions presented in this dissertation.

6.0.1 Circumgalactic Medium

Since the multiphase structure of the CGM arises from complex physics, numerical simulations play a crucial role in understanding this phenomenon. However, capturing this multiphase structure, specifically its cold phase, requires very high resolution ($\sim$ 1 pc Hummels et al., 2019). Such high resolution has so far remained in the domain of idealized simulations because cosmological simulations cannot achieve the requisite resolution due to computational costs. Idealized simulations allow for controlled experiments and very high

resolutions, but they lack important features of realistic cosmological simulations. In cosmological environments, bulk and turbulent gas motions, which can seed density perturbations, arise from mergers, motions of substructures, as well as AGN outbursts and winds. In contrast, idealized simulations only seed density perturbations through turbulence triggered by AGN jet outbursts (Prasad et al., 2017). Additionally, in cosmological simulations, infalling substructures can introduce thermally unstable gas into the CGM via ram pressure stripping and tidal disruption, aspects that idealized simulations miss due to not considering a realistic growth history of galaxy groups. Therefore, to gain a comprehensive understanding of the multiphase structure of the CGM, high-resolution cosmological simulations are needed.

Recent improvements in the resolution of cosmological simulations (e.g., Tremmel et al., 2017; Pillepich et al., 2019; Hopkins et al., 2018) have offered a unique environment to investigate the phenomenology of the multiphase circumgalactic medium. Such high-resolution simulations open a new era of studying properties of the CGM. One such set of simulations is the state-of-the-art high-resolution ROMULUS cosmological hydrodynamic simulations (Tremmel et al., 2017, 2019), comprising one uniform cosmological volume (25 Mpc per side) and three group/cluster-scale zoom simulations.

In Chapter 2, I used the ROMULUS simulations to conduct a thorough and novel analysis of the origin and dynamics of the CGM around massive galaxies ($M_{halo} > 10^{12} M_{\odot}$). This analysis revealed that the CGM in these simulations is indeed multiphase, allowing us to begin investigating its complex structure. My investigation into the origin and evolution of the CGM demonstrated that gas in this medium cools through two main channels: (1) filamentary cooling inflows and (2) condensations forming from rapidly cooling density perturbations. My findings suggest that in cosmological simulations, the perturbations are mainly seeded by infalling or orbiting satellite galaxies, unlike idealized simulations where their perturbations are seeded only by turbulence triggered by AGN jet outbursts.

My results also show that the mass fraction of gas cooling in the CGM due to perturbations is relatively small. Additionally, a portion of the gas failed to continue cooling after being perturbed, as their cooling length was not resolved. These findings highlight that even with such high resolutions, we are merely scratching the surface of understanding the multiphase structure of the CGM. To gain a comprehensive understanding of CGM much higher resolution is needed.

Addressing this challenge, however, is not straightforward. Traditional simulations attain spatial resolutions in low-density galactic halos that are significantly lower compared to those achieved in high-density disks of galaxies. Simply increasing resolution across the board in simulations is not a viable solution due to the prohibitive computational costs. One solution

is to selectively enhance resolution in the CGM region surrounding a galaxy while maintaining lower resolutions within the galaxies themselves. This targeted strategy aims to bypass the need for extremely high-resolution evolution of galaxies within the simulations. By doing so, it allows for a more accurate and realistic modeling of the spatial and dynamic structures in the CGM, facilitating deeper insights into these critical areas of galactic evolution.

In Chapter 3 I implemented a novel approach to enhance the resolution in CGM of galaxies. For implementing this model, I used the GIZMO, a publicly available N-body+hydrodynamics simulation code (Hopkins, 2015) in its meshless finite-mass (MFM) mode. MFM is a mesh-free, Lagrangian finite-volume Godunov method that combines the advantages of particle-based and grid-based methods. Employing GIZMO for hyper-refinement in the CGM is an entirely novel approach, marking a significant contribution to the field. My model successfully enhances the resolution in CGM up to 128 times the fiducial resolution.

6.0.2 Dual and Binary Super Massive Black Holes

The satellite galaxies in galaxy groups not only perturb the CGM around the central galaxy but also bring with them SMBHs that reside in their centers. The merging of these galaxies with BGGs eventually results in SMBH-SMBH mergers. The path from galaxy-galaxy mergers to the eventual SMBH-SMBH mergers involves a sequence of processes spanning a large dynamic range of spatial scales. In some cases, two BHs will pass through a phase where both are accreting and radiating efficiently (e.g. Di Matteo et al., 2005; Hopkins et al., 2008), thereby appearing as close pairs of luminous AGNs (e.g. Gerke et al., 2007; Comerford et al., 2009). These dual AGN systems, observable through electromagnetic waves, can be used to study accretion on SMBHs and SMBH-SMBH mergers. Traditionally, electromagnetic observations have been the primary means to study SMBHs. However, in recent years, the detection of gravitational waves (GW) presents a novel and independent method for detecting binary SMBHs in the Universe. Specifically, GWs in the nano-Hertz range can be detected using pulsar timing array (PTA) observations, providing a fresh perspective on the relationship between binary SMBH formation and galaxy evolution. I used Romulus cosmological simulations to study luminous dual AGNs in Chapter 4 and binary SMBHs detectable by PTA in Chapter 5.

In Chapter 4 I demonstrated how the increasing detection of dual AGNs in recent observations underscores the necessity for a simulated counterpart sample to comprehend the observed sample and its astrophysical implications. However, not all simulations can produce dual AGNs with close (sub-kpc) separation. This limitation arises primarily from two fac-

tors: (1) the resolution limit of the simulations and (2) the modeling of black hole dynamics in most cosmological simulations. Typically, these simulations do not track the dynamics of SMBHs to the resolution limit. Instead, they pin them to the minimum potential of their host halos. As a result, when galaxies merge, the two SMBHs are repositioned to the center of the newly formed remnant galaxy and are forced to merge prematurely.

In Chapter 4, I used the ROMULUS simulation, leveraging its innovative SMBH model that follows the dynamics of SMBHs to sub-kpc scales, to study dual AGNs. I examined the properties and statistics of dual AGNs in contrast to single AGNs, explored the conditions leading to dual luminous AGNs, and investigated the properties of host galaxies of dual AGNs compared to those hosting single AGNs. My findings indicate that the number of both AGNs and dual AGNs increases from lower to higher redshifts. The dual AGNs in my sample all result from major mergers with a typical mass ratio of ~ 0.45. I find that the dual AGN host halo properties including halo mass, stellar mass, star formation rate (SFR), and gas mass, mainly align with the range of single AGN halos, although they are skewed towards higher ends of their respective property ranges. My analyses reveal a diverse range of evolutionary patterns in dual AGNs, encompassing rapidly evolving systems, slower ones, and cases where SMBH mergers are ineffective. Approximately 70% of dual AGNs eventually lead to mergers, while the remainder either remain in orbit around each other or one is ejected from the system due to another galaxy merger. This variety is made visible through the application of Romulus's more realistic SMBH model.

Moving from electromagnetic wave-based studies to GW observations, in Chapter 5 I used the ROMULUS25 simulation to create catalogs of merging SMBHs that emit low-frequency GW radiation and investigate the properties of their host galaxies. My findings show that the most dominant contribution to the stochastic GW background (SGWB) arises from sources with high chirp masses ($M_c > 10^8\,\mathrm{M}_\odot$). These sources are likely to reside in low-redshift early-type galaxies with high stellar mass, largely old stellar populations, and low star formation rates, and are located at the centers of galaxy groups, manifesting evidence of recent mergers.

This kind of study is particularly important since typical PTA localizations in the near term are expected to encompass several thousand galaxies. Thus, theoretical and computational modeling provides a unique opportunity not only to investigate the environments where SMBH mergers occur but also to refine the search for potential host galaxies for closer observational follow-up. The connections shown in my work can serve as a guideline to explore the links between GW observations in the nano-Hertz band and currently ongoing/upcoming galaxy surveys.

6.0.3 Final remarks

The work presented in this dissertation provides a stepping stone towards a better understanding of galaxy evolution. To better comprehend the evolution of a galaxy, it is essential to delve into the intricate interplay of various physical processes both within and surrounding galaxies. This includes the study of their gaseous environments and the evolution of their central supermassive black holes. These processes are interlinked, and a thorough understanding of each is crucial to forming a holistic view of galaxy evolution.

As computational power and capacity continue to advance, along with the refinement of numerical models, simulations are becoming more sophisticated, offering a more detailed representation of galaxy formation and evolution. Concurrently, observational technology is breaking new ground, yielding richer and more comprehensive data sets. The synergy between these cutting-edge simulations and observations is key to painting a complete picture of how galaxies evolve and holds the potential to revolutionize our understanding of this field. Indeed, it is an exciting time to be an astronomer! (And for those reading this in the far future – don't laugh; we are doing our best, OK?!)

Bibliography

Aasi J., et al., 2015, Class. Quant. Grav., 32, 074001

Abbott B. P., et al., 2016a, Phys. Rev. D, 93, 112004

Abbott B. P., et al., 2016b, Phys. Rev. Lett., 116, 061102

Abbott B. P., et al., 2017, Phys. Rev. Lett., 119, 161101

Abbott B. P., et al., 2018, Living Rev. Rel., 21, 3

Abbott R., et al., 2021a, Physical Review X, 11

Abbott R., et al., 2021b, Astrophys. J. Lett., 913, L7

Abbott R., et al., 2023a, Physical Review X, 13, 011048

Abbott R., et al., 2023b, ApJ, 949, 76

Acernese F., et al., 2014, Classical and Quantum Gravity, 32, 024001

Acernese F., et al., 2019, Phys. Rev. Lett., 123, 231108

Ade P., et al., 2016, Astron. Astrophys., 594, A13

Agazie G., et al., 2023, Astrophys. J. Lett., 951

Agertz O., Kravtsov A. V., 2016, The Astrophysical Journal, 824, 79

Agertz O., et al., 2007a, Monthly Notices of the Royal Astronomical Society, 380, 963

Agertz O., et al., 2007b, MNRAS, 380, 963

Akeson R., et al., 2019, arXiv e-prints, p. arXiv:1902.05569

Akutsu T., et al., 2019, Nat. Astron., 3, 35

Akutsu T., et al., 2020, arXiv:2005.05574

Alexander T., Natarajan P., 2014, Science, 345, 1330

Amaro-Seoane P., et al., 2017, arXiv e-prints, p. arXiv:1702.00786

Amaro-Seoane P., et al., 2023, Living Reviews in Relativity, 26, 2

Anglés-Alcázar D., Faucher-Giguère C.-A., Kereš D., Hopkins P. F., Quataert E., Murray N., 2017, Monthly Notices of the Royal Astronomical Society, 470, 4698

Antoniadis J., et al., 2022, Mon. Not. Roy. Astron. Soc., 510, 4873

Antoniadis J., et al., 2023a, arXiv e-prints, p. arXiv:2306.16214

Antoniadis J., et al., 2023b, arXiv e-prints, p. arXiv:2306.16227

Antoniadis J., et al., 2023c, arXiv e-prints, p. arXiv:2306.16227

Armillotta L., Fraternali F., Werk J. K., Prochaska J. X., Marinacci F., 2017, MNRAS, 470, 114

Babul A., Balogh M. L., Lewis G. F., Poole G. B., 2002, Monthly Notices of the Royal Astronomical Society, 330, 329

Babul A., Sharma P., Reynolds C. S., 2013a, The Astrophysical Journal, 768, 11

Babul A., Sharma P., Reynolds C. S., 2013b, ApJ, 768, 11

Babyk I. V., McNamara B., Nulsen P., Russell H., Vantyghem A., Hogan M., Pulido F., 2018, The Astrophysical Journal, 862, 39

Bahcall J. N., Spitzer Lyman J., 1969, ApJ, 156, L63

Baker J., et al., 2019, Bull. Am. Astron. Soc., 51, 243

Bardati J., Ruan J. J., Haggard D., Tremmel M., 2023, arXiv e-prints, p. arXiv:2308.03828

Barrows R. S., Mezcua M., Comerford J. M., 2019, ApJ, 882, 181

Bartlett D. J., Desmond H., Devriendt J., Ferreira P. G., Slyz A., 2021, MNRAS, 500, 4639

Begelman M. C., Blandford R. D., Rees M. J., 1980, Nature, 287, 307

Beifiori A., Courteau S., Corsini E. M., Zhu Y., 2012, MNRAS, 419, 2497

Bell E. F., et al., 2012, ApJ, 753, 167

Bellovary J. M., Governato F., Quinn T. R., Wadsley J., Shen S., Volonteri M., 2010, ApJ, 721, L148

Bellovary J., Volonteri M., Governato F., Shen S., Quinn T., Wadsley J., 2011, ApJ, 742, 13

Benson A. J., Babul A., 2009, MNRAS, 397, 1302

Berg T. A. M., Ellison S. L., Tumlinson J., Oppenheimer B. D., Horton R., Bordoloi R., Schaye J., 2018, MNRAS, 478, 3890

Berger M. J., Colella P., 1989, Journal of Computational Physics, 82, 64

Bergeron J., 1986, A&A, 155, L8

Bianchi S., Chiaberge M., Piconcelli E., Guainazzi M., Matt G., 2008, MNRAS, 386, 105

Binney J., Tremaine S., 2008, Galactic Dynamics: Second Edition

Binney J., Nipoti C., Fraternali F., 2009, Monthly Notices of the Royal Astronomical Society, 397, 1804

Blecha L., Loeb A., Narayan R., 2013, MNRAS, 429, 2594

Bondi H., 1952, Monthly Notices of the Royal Astronomical Society, 112, 195

Bonetti M., Haardt F., Sesana A., Barausse E., 2018, MNRAS, 477, 3910

Booth C. M., Schaye J., 2009, MNRAS, 398, 53

Bordoloi R., et al., 2014, ApJ, 796, 136

Bordoloi R., Wagner A. Y., Heckman T. M., Norman C. A., 2017, ApJ, 848, 122

Borthakur S., Heckman T., Strickland D., Wild V., Schiminovich D., 2013, ApJ, 768, 18

Bortolas E., Capelo P. R., Zana T., Mayer L., Bonetti M., Dotti M., Davies M. B., Madau P., 2020, MNRAS, 498, 3601

Bortolas E., Franchini A., Bonetti M., Sesana A., 2021, ApJ, 918, L15

Bower R. G., Schaye J., Frenk C. S., Theuns T., Schaller M., Crain R. A., McAlpine S., 2017, MNRAS, 465, 32

Braspenning J., Schaye J., Borrow J., Schaller M., 2022, arXiv preprint arXiv:2203.13915

Brusa M., et al., 2010, ApJ, 716, 348

Bryan G. L., et al., 2014, The Astrophysical Journal Supplement Series, 211, 19

Buff J., McCray R., 1974, ApJ, 189, 147

Burchett J. N., Tripp T. M., Wang Q. D., Willmer C. N. A., Bowen D. V., Jenkins E. B., 2018, MNRAS, 475, 2067

Burke-Spolaor S., 2013, Class. Quant. Grav., 30, 224013

Burke-Spolaor S., et al., 2019, Astron. Astrophys. Rev., 27, 5

Butsky I. S., Burchett J. N., Nagai D., Tremmel M., Quinn T. R., Werk J. K., 2019, Monthly Notices of the Royal Astronomical Society, 490, 4292

Callegari S., Mayer L., Kazantzidis S., Colpi M., Governato F., Quinn T., Wadsley J., 2009, ApJ, 696, L89

Campitiello M. G., et al., 2021, ApJ, 911, 144

Capelo P. R., Volonteri M., Dotti M., Bellovary J. M., Mayer L., Governato F., 2015, MNRAS, 447, 2123

Capelo P. R., Dotti M., Volonteri M., Mayer L., Bellovary J. M., Shen S., 2017, MNRAS, 469, 4437

Casey-Clyde J. A., Mingarelli C. M. F., Greene J. E., Pardo K., Nañez M., Goulding A. D., 2022, ApJ, 924, 93

Cattaneo A., et al., 2009, Nature, 460, 213

Ceraj L., et al., 2018, A&A, 620, A192

Chadayammuri U., Tremmel M., Nagai D., Babul A., Quinn T., 2020, arXiv preprint arXiv:2001.06532

Chandrasekhar S., 1943a, ApJ, 97, 255

Chandrasekhar S., 1943b, Astrophysical Journal, 97, 255

Chen H.-W., Lanzetta K. M., Webb J. K., 2001, ApJ, 556, 158

Chen S., Sesana A., Del Pozzo W., 2017, Mon. Not. Roy. Astron. Soc., 470, 1738

Chen N., et al., 2022a, MNRAS, 514, 2220

Chen Y.-C., Hwang H.-C., Shen Y., Liu X., Zakamska N. L., Yang Q., Li J. I., 2022b, ApJ, 925, 162

Chen N., et al., 2023, MNRAS, 522, 1895

Choudhury P. P., Sharma P., 2016, Monthly Notices of the Royal Astronomical Society, 457, 2554

Choudhury P., Sharma P., Quataert E., 2019, Monthly Notices of the Royal Astronomical Society, 488, 3195

Christensen C., Governato F., Quinn T., Brooks A. M., Shen S., McCleary J., Fisher D., Wadsley J., 2014, Monthly Notices of the Royal Astronomical Society, 440, 2843

Cielo S., Babul A., Antonuccio-Delogu V., Silk J., Volonteri M., 2018, Astronomy & Astrophysics, 617, A58

Ciotti L., Ostriker J. P., 1997, ApJ, 487, L105

Cisternas M., et al., 2011, ApJ, 726, 57

Comerford J. M., et al., 2009, ApJ, 698, 956

Comerford J. M., Gerke B. F., Stern D., Cooper M. C., Weiner B. J., Newman J. A., Madsen K., Barrows R. S., 2012, ApJ, 753, 42

Comerford J. M., Schluns K., Greene J. E., Cool R. J., 2013, ApJ, 777, 64

Conselice C. J., 2006, The Astrophysical Journal, 638, 686

Cooksey K. L., Thom C., Prochaska J. X., Chen H.-W., 2010, ApJ, 708, 868

Cox T. J., Jonsson P., Primack J. R., Somerville R. S., 2006, MNRAS, 373, 1013

Crain R. A., et al., 2009, MNRAS, 399, 1773

Crain R. A., et al., 2015, Monthly Notices of the Royal Astronomical Society, 450, 1937

DESI Collaboration et al., 2016, arXiv e-prints, p. arXiv:1611.00036

Das H. K., Choudhury P. P., Sharma P., 2021, Monthly Notices of the Royal Astronomical Society, 502, 4935

Davé R., Anglés-Alcázar D., Narayanan D., Li Q., Rafieferantsoa M. H., Appleby S., 2019, Monthly Notices of the Royal Astronomical Society, 486, 2827

Davis M., Efstathiou G., Frenk C. S., White S. D. M., 1985, ApJ, 292, 371

De Rosa A., et al., 2015, MNRAS, 453, 214

De Rosa A., et al., 2019, New Astron. Rev., 86, 101525

DeGraf C., Sijacki D., Di Matteo T., Holley-Bockelmann K., Snyder G., Springel V., 2021, Mon. Not. Roy. Astron. Soc., 503, 3629

Desvignes G., et al., 2016, MNRAS, 458, 3341

Di Matteo T., Springel V., Hernquist L., 2005, Nature, 433, 604

Djorgovski S. G., Courbin F., Meylan G., Sluse D., Thompson D., Mahabal A., Glikman E., 2007, ApJ, 662, L1

Donahue M., Voit G. M., 2022, Physics Reports, 973, 1

Dosopoulou F., Antonini F., 2017, ApJ, 840, 31

Duarte M., Mamon G. A., 2015, Monthly Notices of the Royal Astronomical Society, 453, 3848

Dubois Y., Gavazzi R., Peirani S., Silk J., 2013, MNRAS, 433, 3297

Dubois Y., Peirani S., Pichon C., Devriendt J., Gavazzi R., Welker C., Volonteri M., 2016, MNRAS, 463, 3948

Edwards D., Heath D., 1976, Ap&SS, 41, 183

Eke V. R., Baugh C. M., Cole S., Frenk C. S., Navarro J. F., 2006, Monthly Notices of the Royal Astronomical Society, 370, 1147

Ellis J. A., 2013, Class. Quant. Grav., 30, 224004

Ellison S. L., Patton D. R., Mendel J. T., Scudder J. M., 2011, MNRAS, 418, 2043

Ellison S. L., Mendel J. T., Scudder J. M., Patton D. R., Palmer M. J. D., 2013, MNRAS, 430, 3128

Enoki M., Nagashima M., 2007, Prog. Theor. Phys., 117, 241

Esmerian C. J., Kravtsov A. V., Hafen Z., Faucher-Giguère C.-A., Quataert E., Stern J., Kereš D., Wetzel A., 2021, Monthly Notices of the Royal Astronomical Society, 505, 1841

Fabian A. C., 2012, ARA&A, 50, 455

Fardal M. A., Guhathakurta P., Babul A., McConnachie A. W., 2007, MNRAS, 380, 15

Faucher-Giguere C.-A., Oh S. P., 2023, arXiv preprint arXiv:2301.10253

Ferrarese L., Merritt D., 2000, ApJ, 539, L9

Fiacconi D., Mayer L., Madau P., Lupi A., Dotti M., Haardt F., 2017, Monthly Notices of the Royal Astronomical Society, 467, 4080

Fielding D. B., et al., 2020, The Astrophysical Journal, 903, 32

Foord A., Gültekin K., Nevin R., Comerford J. M., Hodges-Kluck E., Barrows R. S., Goulding A. D., Greene J. E., 2020, ApJ, 892, 29

Foord A., et al., 2023, arXiv preprint arXiv:2311.07664

Foster R. S., Backer D. C., 1990, ApJ, 361, 300

Franchetto A., et al., 2021, The Astrophysical Journal Letters, 922, L6

Fujita Y., 2008, ApJ, 685, L59

Gaspari M., Ruszkowski M., Sharma P., 2012, The Astrophysical Journal, 746, 94

Gebhardt K., et al., 2000, ApJ, 543, L5

Genel S., et al., 2018, MNRAS, 474, 3976

Gerke B. F., et al., 2007, ApJ, 660, L23

Ghazvini Zadeh A., 2008, PhD thesis

Gingold R. A., Monaghan J. J., 1977, MNRAS, 181, 375

Gnedin N. Y., 1995, ApJS, 97, 231

Goldstein J. M., Sesana A., Holgado A. M., Veitch J., 2019, MNRAS, 485, 248

Goulding A. D., et al., 2018, PASJ, 70, S37

Governato F., Colpi M., Maraschi L., 1994, MNRAS, 271, 317

Governato F., et al., 2015, MNRAS, 448, 792

Grand R. J., et al., 2017, Monthly Notices of the Royal Astronomical Society, 467, 179

Green P. J., Myers A. D., Barkhouse W. A., Mulchaey J. S., Bennert V. N., Cox T. J., Aldcroft T. L., 2010, ApJ, 710, 1578

Guedes J., Callegari S., Madau P., Mayer L., 2011, ApJ, 742, 76

Gunn J. E., Gott J. Richard I., 1972, ApJ, 176, 1

Guo M., Inayoshi K., Michiyama T., Ho L. C., 2020, ApJ, 901, 39

Hafen Z., et al., 2019, Monthly Notices of the Royal Astronomical Society, 488, 1248

Hahn O., Abel T., 2011, MNRAS, 415, 2101

Haiman Z., Kocsis B., Menou K., 2009, ApJ, 700, 1952

Hani M. H., Sparre M., Ellison S. L., Torrey P., Vogelsberger M., 2018, MNRAS, 475, 1160

Häring N., Rix H.-W., 2004, ApJ, 604, L89

Harris C. R., et al., 2020, Nature, 585, 357

Heckman T., Borthakur S., Wild V., Schiminovich D., Bordoloi R., 2017, ApJ, 846, 151

Heitsch F., Putman M. E., 2009, ApJ, 698, 1485

Hennawi J. F., Prochaska J. X., Cantalupo S., Arrigoni-Battaia F., 2015, Science, 348, 779

Hewitt A., Burbidge G., 1993, ApJS, 87, 451

Hirschmann M., Dolag K., Saro A., Bachmann L., Borgani S., Burkert A., 2014, MNRAS, 442, 2304

Hogan M., et al., 2017, The Astrophysical Journal, 851, 66

Hopkins P. F., 2015, Monthly Notices of the Royal Astronomical Society, 450, 53

Hopkins P. F., Hernquist L., Cox T. J., Di Matteo T., Robertson B., Springel V., 2006, ApJS, 163, 1

Hopkins P. F., Bundy K., Hernquist L., Ellis R. S., 2007, ApJ, 659, 976

Hopkins P. F., Hernquist L., Cox T. J., Kereš D., 2008, ApJS, 175, 356

Hopkins P. F., et al., 2018, Monthly Notices of the Royal Astronomical Society, 480, 800

Hosokawa T., Yorke H. W., Inayoshi K., Omukai K., Yoshida N., 2013, ApJ, 778, 178

Hotinli S. C., Kamionkowski M., Jaffe A. H., 2019, Open J. Astrophys., 2, 8

Hough R. T., Rennehan D., Kobayashi C., Loubser S. I., Davé R., Babul A., Cui W., 2023a, MNRAS, 525, 1061

Hough R. T., Rennehan D., Kobayashi C., Loubser S. I., Davé R., Babul A., Cui W., 2023b, MNRAS, 525, 1061

Huang Y., et al., 2014, MNRAS, 439, 2927

Huang S., Katz N., Scannapieco E., Cottle J., Davé R., Weinberg D. H., Peeples M. S., Brüggen M., 2020a, Monthly Notices of the Royal Astronomical Society, 497, 2586

Huang S., Katz N., Scannapieco E., Cottle J., Davé R., Weinberg D. H., Peeples M. S., Brüggen M., 2020b, Monthly Notices of the Royal Astronomical Society, 497, 2586

Hubble E., 1929, Proceedings of the National Academy of Science, 15, 168

Hummels C. B., et al., 2019, The Astrophysical Journal, 882, 156

Hunter J. D., 2007, Computing in science & engineering, 9, 90

Hwang H.-C., Shen Y., Zakamska N., Liu X., 2020, ApJ, 888, 73

Ibrahem R. T., Tino P., Pearson R. J., Ponman T. J., Babul A., 2015, in Neural Information Processing Volume 9491. pp 323–331

Izquierdo-Villalba D., Sesana A., Bonoli S., Colpi M., 2022, MNRAS, 509, 3488

Izquierdo-Villalba D., Sesana A., Colpi M., 2023, MNRAS, 519, 2083

Jackson R., Kaviraj S., Martin G., Devriendt J., Noakes-Kettel E., Silk J., Ogle P., Dubois Y., 2022, Monthly Notices of the Royal Astronomical Society, 511, 607

Jaffe A. H., Backer D. C., 2003, ApJ, 583, 616

Janssen G. H., et al., 2014, Gravitational wave astronomy with the SKA (arXiv:1501.00127)

Janssen G., et al., 2015, PoS, AASKA14, 037

Johnson J. L., Whalen D. J., Fryer C. L., Li H., 2012, ApJ, 750, 66

Joshi B. C., et al., 2018, Journal of Astrophysics and Astronomy, 39, 51

Jung S. L., et al., 2022, Monthly Notices of the Royal Astronomical Society, 515, 22

Kaviraj S., et al., 2017, MNRAS, 467, 4739

Kazantzidis S., et al., 2005, ApJ, 623, L67

Kelley L. Z., Blecha L., Hernquist L., 2017a, Mon. Not. Roy. Astron. Soc., 464, 3131

Kelley L. Z., Blecha L., Hernquist L., Sesana A., Taylor S. R., 2017b, Mon. Not. Roy. Astron. Soc., 471, 4508

Kereš D., Katz N., Weinberg D. H., Davé R., 2005, Monthly Notices of the Royal Astronomical Society, 363, 2

Kharb P., Lal D. V., Merritt D., 2017, Nature Astronomy, 1, 727

Kim W.-T., 2007, The Astrophysical Journal, 667, L5

Kim D. C., Yoon I., Evans A. S., Kim M., Momjian E., Kim J. H., 2020, ApJ, 904, 23

Knebe A., Draganova N., Power C., Yepes G., Hoffman Y., Gottlöber S., Gibson B. K., 2008, Monthly Notices of the Royal Astronomical Society: Letters, 386, L52

Knollmann S. R., Knebe A., 2009, The Astrophysical Journal Supplement Series, 182, 608

Kocevski D. D., et al., 2015, ApJ, 814, 104

Kocsis B., Sesana A., 2011, MNRAS, 411, 1467

Kolokythas K., OSullivan E., Intema H., Raychaudhury S., Babul A., Giacintucci S., Gitti M., 2019, Monthly Notices of the Royal Astronomical Society, 489, 2488

Kolokythas K., Vaddi S., OSullivan E., Loubser I., Babul A., Raychaudhury S., Lagos P., Jarrett T. H., 2022, Monthly Notices of the Royal Astronomical Society, 510, 4191

Kormendy J., Gebhardt K., 2001, in Wheeler J. C., Martel H., eds, American Institute of Physics Conference Series Vol. 586, 20th Texas Symposium on relativistic astrophysics. pp 363–381 (arXiv:astro-ph/0105230), doi:10.1063/1.1419581

Kormendy J., Ho L. C., 2013, ARA&A, 51, 511

Kormendy J., Richstone D., 1995, ARA&A, 33, 581

Koss M., Mushotzky R., Treister E., Veilleux S., Vasudevan R., Trippe M., 2012, ApJ, 746, L22

Koss M. J., et al., 2018, Nature, 563, 214

Kroupa P., 2001, MNRAS, 322, 231

LSST Dark Energy Science Collaboration 2012, arXiv e-prints, p. arXiv:1211.0310

Lagos P., et al., 2022, Submitted to Monthly Notices of the Royal Astronomical Society

Lakhchaura K., et al., 2018, Monthly Notices of the Royal Astronomical Society, 481, 4472

Lambert T. S., Kraan-Korteweg R., Jarrett T., Macri L., 2020, Monthly Notices of the Royal Astronomical Society, 497, 2954

Lanzetta K. M., Bowen D. V., Tytler D., Webb J. K., 1995, ApJ, 442, 538

Laureijs R., et al., 2011, arXiv e-prints, p. arXiv:1110.3193

Lehner N., Howk J. C., Wakker B. P., 2015, ApJ, 804, 79

Leroy A. K., et al., 2015, ApJ, 814, 83

Lewis G. F., Babul A., Katz N., Quinn T., Hernquist L., Weinberg D. H., 2000, The Astrophysical Journal, 536, 623

Li Y., Bryan G. L., Ruszkowski M., Voit G. M., OShea B. W., Donahue M., 2015, The Astrophysical Journal, 811, 73

Li K., Bogdanović T., Ballantyne D. R., 2020, ApJ, 896, 113

Liang C. J., Chen H.-W., 2014, MNRAS, 445, 2061

Liang L., Durier F., Babul A., Davé R., Oppenheimer B. D., Katz N., Fardal M., Quinn T., 2016, Monthly Notices of the Royal Astronomical Society, 456, 4266

Liu X., Shen Y., Strauss M. A., Hao L., 2011, ApJ, 737, 101

Liu X., Shen Y., Strauss M. A., 2012, ApJ, 745, 94

Liu X., et al., 2019, ApJ, 887, 90

Liu A., et al., 2022, Astronomy & Astrophysics, 661, A2

Lodato G., Natarajan P., 2007, Monthly Notices of the Royal Astronomical Society: Letters, 377, L64

Loubser S., Lagos P., Babul A., OSullivan E., Jung S., Olivares V., Kolokythas K., 2022, Submitted to Monthly Notices of the Royal Astronomical Society

Lovisari L., Ettori S., 2021, The Physical Properties of the Groups of Galaxies

Lucy L. B., 1977, AJ, 82, 1013

Magorrian J., et al., 1998, AJ, 115, 2285

Maller A. H., Bullock J. S., 2004, Monthly Notices of the Royal Astronomical Society, 355, 694

Manchester R. N., et al., 2013, PASA, 30, e017

Mandelker N., van den Bosch F. C., Springel V., van de Voort F., Burchett J. N., Butsky I. S., Nagai D., Oh S. P., 2021, The Astrophysical Journal, 923, 115

Mannucci F., et al., 2022, Nature Astronomy, 6, 1185

Martini P., Leroy A. K., Mangum J. G., Bolatto A., Keating K. M., Sandstrom K., Walter F., 2018, ApJ, 856, 61

Martz C., et al., 2020, The Astrophysical Journal, 897, 57

Mayer L., 2017, in Journal of Physics Conference Series. p. 012025 (arXiv:1703.00661), doi:10.1088/1742-6596/840/1/012025

McCarthy I. G., Frenk C. S., Font A. S., Lacey C. G., Bower R. G., Mitchell N. L., Balogh M. L., Theuns T., 2008, Monthly Notices of the Royal Astronomical Society, 383, 593

McCourt M., Sharma P., Quataert E., Parrish I. J., 2012, Monthly Notices of the Royal Astronomical Society, 419, 3319

McKeith C. D., Greve A., Downes D., Prada F., 1995, A&A, 293, 703

McLaughlin M. A., 2013, Classical and Quantum Gravity, 30, 224008

McNamara B. R., Nulsen P. E. J., 2007, ARA&A, 45, 117

Mechtley M., et al., 2016a, ApJ, 830, 156

Mechtley M., et al., 2016b, ApJ, 830, 156

Meece G. R., OShea B. W., Voit G. M., 2015, The Astrophysical Journal, 808, 43

Menon H., Wesolowski L., Zheng G., Jetley P., Kale L., Quinn T., Governato F., 2015, Computational Astrophysics and Cosmology, 2, 1

Merloni A., Heinz S., 2008, MNRAS, 388, 1011

Milosavljević M., Merritt D., 2001, ApJ, 563, 34

Mingarelli C. M. F., Sidery T., Mandel I., Vecchio A., 2013, Phys. Rev. D, 88, 062005

Mingarelli C. M. F., et al., 2017, Nature Astronomy, 1, 886

Moreno J., Torrey P., Ellison S. L., Patton D. R., Bluck A. F. L., Bansal G., Hernquist L., 2015, MNRAS, 448, 1107

Muñoz D. J., Miranda R., Lai D., 2019, ApJ, 871, 84

Muhamed Kozhikkal M., Chen S., Theureau G., Habouzit M., Sesana A., 2023, arXiv e-prints, p. arXiv:2305.18293

Mukherjee S., Silk J., 2020, Mon. Not. Roy. Astron. Soc., 491, 4690

Mukherjee S., Silk J., 2021, Phys. Rev. D, 104, 063518

Murakami I., Babul A., 1999, Monthly Notices of the Royal Astronomical Society, 309, 161

Murray N., Quataert E., Thompson T. A., 2005, ApJ, 618, 569

Narayan R., Quataert E., 2005, Science, 307, 77

Narayan R., Yi I., 1994, ApJ, 428, L13

Natarajan P., 2021, Monthly Notices of the Royal Astronomical Society, 501, 1413

Nelson D., et al., 2019a, in High Performance Computing in Science and Engineering'18: Transactions of the High Performance Computing Center, Stuttgart (HLRS) 2018. pp 5–20

Nelson D., et al., 2019b, Computational Astrophysics and Cosmology, 6, 2

Nelson D., et al., 2020, Monthly Notices of the Royal Astronomical Society, 498, 2391

Nielsen N. M., Kacprzak G. G., Pointon S. K., Churchill C. W., Murphy M. T., 2018, ApJ, 869, 153

Nulsen P., 1998, Monthly Notices of the Royal Astronomical Society, 297, 1109

O'Sullivan E., et al., 2012, MNRAS, 424, 2971

O'Sullivan E., et al., 2017a, Monthly Notices of the Royal Astronomical Society, 472, 1482

O'Sullivan E., et al., 2017b, MNRAS, 472, 1482

O'Sullivan E., et al., 2018, Astronomy & Astrophysics, 618, A126

O'Sullivan E., Combes F., Babul A., Chapman S., Phadke K. A., Schellenberger G., Salomé P., 2021, MNRAS, 508, 3796

Ogle P. M., Lanz L., Nader C., Helou G., 2016, The Astrophysical Journal, 817, 109

Ogle P. M., Jarrett T., Lanz L., Cluver M., Alatalo K., Appleton P. N., Mazzarella J. M., 2019, The Astrophysical Journal Letters, 884, L11

Olivares V., et al., 2022, accepted by Astronomy & Astrophysics journal

Oppenheimer B. D., Davé R., 2006, MNRAS, 373, 1265

Oppenheimer B. D., Davé R., Kereš D., Fardal M., Katz N., Kollmeier J. A., Weinberg D. H., 2010, Monthly Notices of the Royal Astronomical Society, 406, 2325

Oppenheimer B. D., Babul A., Bahé Y., Butsky I. S., McCarthy I. G., 2021a, Universe, 7, 209

Oppenheimer B. D., Babul A., Bahé Y., Butsky I. S., McCarthy I. G., 2021b, Universe, 7, 209

Ostriker E. C., 1999, ApJ, 513, 252

Patton D. R., et al., 2002, ApJ, 565, 208

Pearson R. J., et al., 2017, Monthly Notices of the Royal Astronomical Society, 469, 3489

Peeples M. S., et al., 2019, The Astrophysical Journal, 873, 129

Pfeifle R. W., et al., 2019, ApJ, 883, 167

Pfister H., Volonteri M., Dubois Y., Dotti M., Colpi M., 2019, MNRAS, 486, 101

Phinney E. S., 2001, arXiv e-prints, pp astro–ph/0108028

Pillepich A., et al., 2018, MNRAS, 473, 4077

Pillepich A., et al., 2019, Monthly Notices of the Royal Astronomical Society, 490, 3196

Pipino A., Kaviraj S., Bildfell C., Babul A., Hoekstra H., Silk J., 2009, MNRAS, 395, 462

Pointon S. K., Nielsen N. M., Kacprzak G. G., Muzahid S., Churchill C. W., Charlton J. C., 2017, ApJ, 844, 23

Pontzen A., Tremmel M., 2018, The Astrophysical Journal Supplement Series, 237, 23

Pontzen A., Roškar R., Stinson G. S., Woods R., Reed D. M., Coles J., Quinn T. R., 2013a, pynbody: Astrophysics Simulation Analysis for Python

Pontzen A., Roškar R., Stinson G., Woods R., 2013b, pynbody: N-Body/SPH analysis for python, Astrophysics Source Code Library, record ascl:1305.002 (ascl:1305.002)

Poole G. B., Fardal M. A., Babul A., McCarthy I. G., Quinn T., Wadsley J., 2006, Monthly Notices of the Royal Astronomical Society, 373, 881

Pope E. C., Babul A., Pavlovski G., Bower R. G., Dotter A., 2010, Monthly Notices of the Royal Astronomical Society, 406, 2023

Power C., Navarro J., Jenkins A., Frenk C., White S. D., Springel V., Stadel J., Quinn T., 2003, Monthly Notices of the Royal Astronomical Society, 338, 14

Prasad D., Sharma P., Babul A., 2015, The Astrophysical Journal, 811, 108

Prasad D., Sharma P., Babul A., 2017, Monthly Notices of the Royal Astronomical Society, 471, 1531

Prasad D., Sharma P., Babul A., 2018, The Astrophysical Journal, 863, 62

Prasad D., Sharma P., Babul A., Voit G. M., OShea B. W., 2020a, Monthly Notices of the Royal Astronomical Society, 495, 594

Prasad D., Sharma P., Babul A., Voit G. M., O'Shea B. W., 2020b, MNRAS, 495, 594

Prochaska J. X., Weiner B., Chen H.-W., Mulchaey J., Cooksey K., 2011b, The Astrophysical Journal, 740, 91

Prochaska J. X., Weiner B., Chen H. W., Mulchaey J., Cooksey K., 2011a, ApJ, 740, 91

Prochaska J. X., et al., 2017, ApJ, 837, 169

Pulido F., et al., 2018, The Astrophysical Journal, 853, 177

Putman M. E., Peek J. E. G., Joung M. R., 2012, ARA&A, 50, 491

Qiu Y., Bogdanović T., Li Y., McDonald M., McNamara B. R., 2020, Nature Astronomy, 4, 900

Quinlan G. D., 1996, New Astron., 1, 35

Rajagopal M., Romani R. W., 1995, ApJ, 446, 543

Reardon D. J., et al., 2023, ApJ, 951, L6

Rennehan D., 2021, Monthly Notices of the Royal Astronomical Society, 506, 2836

Rennehan D., Babul A., Hopkins P. F., Davé R., Moa B., 2019, Monthly Notices of the Royal Astronomical Society, 483, 3810

Rennehan D., Babul A., Hayward C. C., Bottrell C., Hani M. H., Chapman S. C., 2020, Monthly Notices of the Royal Astronomical Society, 493, 4607

Renzini A., 2006, ARA&A, 44, 141

Revaz Y., Combes F., Salomé P., 2008, Astronomy & Astrophysics, 477, L33

Reynolds C. S., Lohfink A. M., Babul A., Fabian A. C., Hlavacek-Larrondo J., Russell H. R., Walker S. A., 2014, ApJ, 792, L41

Ricarte A., Tremmel M., Natarajan P., Quinn T., 2019a, Monthly Notices of the Royal Astronomical Society, 489, 802

Ricarte A., Tremmel M., Natarajan P., Quinn T., 2019b, MNRAS, 489, 802

Ricarte A., Tremmel M., Natarajan P., Quinn T., 2019c, Monthly Notices of the Royal Astronomical Society, 489, 802

Ricarte A., Tremmel M., Natarajan P., Zimmer C., Quinn T., 2021a, Monthly Notices of the Royal Astronomical Society, 503, 6098

Ricarte A., Tremmel M., Natarajan P., Zimmer C., Quinn T., 2021b, MNRAS, 503, 6098

Rodriguez-Gomez V., et al., 2015, MNRAS, 449, 49

Rosado P. A., Sesana A., 2014, MNRAS, 439, 3986

Rosario D. J., McGurk R. C., Max C. E., Shields G. A., Smith K. L., Ammons S. M., 2011, ApJ, 739, 44

Rosas-Guevara Y. M., Bower R. G., McAlpine S., Bonoli S., Tissera P. B., 2019a, MNRAS, 483, 2712

Rosas-Guevara Y. M., Bower R. G., McAlpine S., Bonoli S., Tissera P. B., 2019b, MNRAS, 483, 2712

Rubinur K., Das M., Kharb P., 2019, MNRAS, 484, 4933

Ruszkowski M., Oh S. P., 2011, Monthly Notices of the Royal Astronomical Society, 414, 1493

Saeedzadeh et al. 2023a, Dual AGNs in Romulus Simulations, *in prep.*

Saeedzadeh V., et al., 2023b, arXiv e-prints, p. arXiv:2304.03798

Saeedzadeh V., Mukherjee S., Babul A., Tremmel M., Quinn T. R., 2023c, arXiv e-prints, p. arXiv:2309.08683

Sampson L., Cornish N. J., McWilliams S. T., 2015, Phys. Rev. D, 91, 084055

Sanchez N. N., Werk J. K., Tremmel M., Pontzen A., Christensen C., Quinn T., Cruz A., 2019, The Astrophysical Journal, 882, 8

Sarron F., Conselice C. J., 2021, Monthly Notices of the Royal Astronomical Society, 506, 2136

Sato-Polito G., Kamionkowski M., 2023, arXiv e-prints, p. arXiv:2305.05690

Satyapal S., Secrest N. J., McAlpine W., Ellison S. L., Fischer J., Rosenberg J. L., 2014, ApJ, 784, 113

Scannapieco E., 2017, ApJ, 837, 28

Scannapieco E., Brüggen M., 2015, The Astrophysical Journal, 805, 158

Schaye J., et al., 2015, Monthly Notices of the Royal Astronomical Society, 446, 521

Schleicher D. R. G., Palla F., Ferrara A., Galli D., Latif M., 2013, A&A, 558, A59

Schneider E. E., Robertson B. E., 2017, The Astrophysical Journal, 834, 144

Schneider E. E., Ostriker E. C., Robertson B. E., Thompson T. A., 2020, The Astrophysical Journal, 895, 43

Sesana A., 2013, Classical and Quantum Gravity, 30, 244009

Sesana A., Haardt F., Madau P., 2007, ApJ, 660, 546

Sesana A., Vecchio A., Colacino C. N., 2008a, Mon. Not. Roy. Astron. Soc., 390, 192

Sesana A., Vecchio A., Colacino C. N., 2008b, Monthly Notices of the Royal Astronomical Society, 390, 192

Sharma P., Parrish I. J., Quataert E., 2010, The Astrophysical Journal, 720, 652

Sharma P., McCourt M., Quataert E., Parrish I. J., 2012a, Monthly Notices of the Royal Astronomical Society, 420, 3174

Sharma P., McCourt M., Parrish I. J., Quataert E., 2012b, Monthly Notices of the Royal Astronomical Society, 427, 1219

Shen S., Wadsley J., Stinson G., 2010a, Monthly Notices of the Royal Astronomical Society, 407, 1581

Shen S., Wadsley J., Stinson G., 2010b, MNRAS, 407, 1581

Shen Y., Hwang H.-C., Zakamska N., Liu X., 2019, ApJ, 885, L4

Shen Y., et al., 2021, Nature Astronomy, 5, 569

Sigalotti L. D. G., Klapp J., Gesteira M. G., 2021, Frontiers in Applied Mathematics and Statistics, 7, 797455

Sijacki D., Springel V., Haehnelt M. G., 2011, MNRAS, 414, 3656

Sijacki D., Vogelsberger M., Genel S., Springel V., Torrey P., Snyder G. F., Nelson D., Hernquist L., 2015, MNRAS, 452, 575

Silverman J. D., et al., 2011, ApJ, 743, 2

Silverman J. D., et al., 2020, ApJ, 899, 154

Sokołowska A., Mayer L., Babul A., Madau P., Shen S., 2016, The Astrophysical Journal, 819, 21

Sokołowska A., Babul A., Mayer L., Shen S., Madau P., 2018, The Astrophysical Journal, 867, 73

Somerville R. S., Davé R., 2015, ARA&A, 53, 51

Spitzer Lyman J., 1956, ApJ, 124, 20

Springel V., 2005, MNRAS, 364, 1105

Springel V., 2010, MNRAS, 401, 791

Springel V., Hernquist L., 2002, MNRAS, 333, 649

Steffen A. T., Barger A. J., Cowie L. L., Mushotzky R. F., Yang Y., 2003, ApJ, 596, L23

Steinborn L. K., Dolag K., Comerford J. M., Hirschmann M., Remus R.-S., Teklu A. F., 2016, MNRAS, 458, 1013

Stemo A., Comerford J. M., Barrows R. S., Stern D., Assef R. J., Griffith R. L., Schechter A., 2021, ApJ, 923, 36

Stern J., Fielding D., Faucher-Giguère C.-A., Quataert E., 2019, Monthly Notices of the Royal Astronomical Society, 488, 2549

Stern J., et al., 2021, The Astrophysical Journal, 911, 88

Stinson G., Seth A., Katz N., Wadsley J., Governato F., Quinn T., 2006, MNRAS, 373, 1074

Stocke J. T., Keeney B. A., Danforth C. W., Oppenheimer B. D., Pratt C. T., Berlind A. A., Impey C., Jannuzi B., 2019, ApJS, 240, 15

Stone J. M., Norman M. L., 1992, ApJS, 80, 753

Strickland D. K., Heckman T. M., Colbert E. J. M., Hoopes C. G., Weaver K. A., 2004, ApJS, 151, 193

Sun M., Donahue M., Roediger E., Nulsen P., Voit G., Sarazin C., Forman W., Jones C., 2009, The Astrophysical Journal, 708, 946

Suresh J., Nelson D., Genel S., Rubin K. H., Hernquist L., 2019, Monthly Notices of the Royal Astronomical Society, 483, 4040

Tamfal T., Mayer L., Quinn T. R., Capelo P. R., Kazantzidis S., Babul A., Potter D., 2021, The Astrophysical Journal, 916, 55

Tamfal T., Mayer L., Quinn T. R., Babul A., Madau P., Capelo P. R., Shen S., Staub M., 2022, The Astrophysical Journal, 928, 106

Tang S., et al., 2021, ApJ, 922, 83

Terzian Y., Lazio J., 2006, Proc. SPIE Int. Soc. Opt. Eng., 6267, 62672D

The LIGO Scientific Collaboration et al., 2021, arXiv e-prints, p. arXiv:2111.03606

Theuns T., 2003, Cooling flows in clusters of galaxies, http://www.icc.dur.ac.uk/~tt/Lectures/Galaxies/Clusters/Xrays/clusters_cflows.html

Thom C., et al., 2012, ApJ, 758, L41

Tonnesen S., Bryan G. L., Chen R., 2011, ApJ, 731, 98

Torrey P., Cox T. J., Kewley L., Hernquist L., 2012, ApJ, 746, 108

Tremmel M., Governato F., Volonteri M., Quinn T. R., 2015, Monthly Notices of the Royal Astronomical Society, 451, 1868

Tremmel M., Karcher M., Governato F., Volonteri M., Quinn T., Pontzen A., Anderson L., Bellovary J., 2017, Monthly Notices of the Royal Astronomical Society, 470, 1121

Tremmel M., Governato F., Volonteri M., Quinn T. R., Pontzen A., 2018a, MNRAS, 475, 4967

Tremmel M., Governato F., Volonteri M., Quinn T. R., Pontzen A., 2018b, Monthly Notices of the Royal Astronomical Society, 475, 4967

Tremmel M., et al., 2019, Monthly Notices of the Royal Astronomical Society, 483, 3336

Tremmel M., Wright A. C., Brooks A. M., Munshi F., Nagai D., Quinn T. R., 2020, Monthly Notices of the Royal Astronomical Society, 497, 2786

Tripp T. M., Savage B. D., Jenkins E. B., 2000, ApJ, 534, L1

Trump J. R., et al., 2011, ApJ, 733, 60

Tumlinson J., et al., 2011a, Science, 334, 948

Tumlinson J., et al., 2011b, Science, 334, 948

Tumlinson J., et al., 2013, ApJ, 777, 59

Tumlinson J., Peeples M. S., Werk J. K., 2017, Annual Review of Astronomy and Astrophysics, 55, 389

Van Wassenhove S., Volonteri M., Mayer L., Dotti M., Bellovary J., Callegari S., 2012a, ApJ, 748, L7

Van Wassenhove S., Volonteri M., Mayer L., Dotti M., Bellovary J., Callegari S., 2012b, ApJ, 748, L7

Vasiliev E., Antonini F., Merritt D., 2015, ApJ, 810, 49

Veilleux S., Maiolino R., Bolatto A. D., Aalto S., 2020, A&ARv, 28, 2

Virtanen P., et al., 2020, Nature methods, 17, 261

Vogelsberger M., Genel S., Sijacki D., Torrey P., Springel V., Hernquist L., 2013, MNRAS, 436, 3031

Vogelsberger M., Marinacci F., Torrey P., Puchwein E., 2020, Nature Reviews Physics, 2, 42

Voit G. M., 2021, The Astrophysical Journal Letters, 908, L16

Voit G. M., Donahue M., 2015, The Astrophysical Journal Letters, 799, L1

Voit G. M., Bryan G. L., OShea B. W., Donahue M., 2015, The Astrophysical Journal Letters, 808, L30

Volonteri M., 2012, Science, 337, 544

Volonteri M., Haardt F., Madau P., 2003, ApJ, 582, 559

Volonteri M., Dubois Y., Pichon C., Devriendt J., 2016, MNRAS, 460, 2979

Volonteri M., et al., 2020, MNRAS, 498, 2219

Volonteri M., Pfister H., Beckmann R., Dotti M., Dubois Y., Massonneau W., Musoke G., Tremmel M., 2022a, MNRAS, 514, 640

Volonteri M., Pfister H., Beckmann R., Dotti M., Dubois Y., Massonneau W., Musoke G., Tremmel M., 2022b, MNRAS, 514, 640

Wadsley J. W., Stadel J., Quinn T., 2004, New astronomy, 9, 137

Wadsley J., Veeravalli G., Couchman H., 2008, Monthly Notices of the Royal Astronomical Society, 387, 427

Wadsley J. W., Keller B. W., Quinn T. R., 2017, Monthly Notices of the Royal Astronomical Society, 471, 2357

Walter F., Weiss A., Scoville N., 2002, ApJ, 580, L21

Weinberger R., et al., 2017, MNRAS, 465, 3291

Weinmann S. M., Van Den Bosch F. C., Yang X., Mo H., 2006, Monthly Notices of the Royal Astronomical Society, 366, 2

Werk J. K., Prochaska J. X., Thom C., Tumlinson J., Tripp T. M., O'Meara J. M., Peeples M. S., 2013, ApJS, 204, 17

Werk J. K., et al., 2016, The Astrophysical Journal, 833, 54

Werner N., Mernier F., 2020, Reviews in Frontiers of Modern Astrophysics: From Space Debris to Cosmology, pp 279–310

Werner N., et al., 2014, Monthly Notices of the Royal Astronomical Society, 439, 2291

Westmoquette M. S., Smith L. J., Gallagher J. S. I., Trancho G., Bastian N., Konstantopoulos I. S., 2009, ApJ, 696, 192

Wolf C., Wisotzki L., Borch A., Dye S., Kleinheinrich M., Meisenheimer K., 2003, A&A, 408, 499

Xu W., Ramos-Ceja M. E., Pacaud F., Reiprich T. H., Erben T., 2022, Astronomy & Astrophysics, 658, A59

Xu H., et al., 2023a, Research in Astronomy and Astrophysics, 23, 075024

Xu H., et al., 2023b, Res. Astron. Astrophys., 23, 075024

Yang K. Z., Mandic V., Scarlata C., Banagiri S., 2020, Mon. Not. Roy. Astron. Soc., 500, 1666

Yang X., et al., 2021, The Astrophysical Journal, 909, 143

Yang K. Z., Suresh J., Cusin G., Banagiri S., Feist N., Mandic V., Scarlata C., Michaloliakos I., 2023, Phys. Rev. D, 108, 043025

Yun K., et al., 2019, MNRAS, 483, 1042

Zahedy F. S., Chen H.-W., Johnson S. D., Pierce R. M., Rauch M., Huang Y.-H., Weiner B. J., Gauthier J.-R., 2019, Monthly Notices of the Royal Astronomical Society, 484, 2257

Zic A., et al., 2023, arXiv e-prints, p. arXiv:2306.16230

Zivancev C., Ostriker J., Küpper A. H. W., 2020, Monthly Notices of the Royal Astronomical Society, 498, 3807

van de Voort F., Schaye J., Booth C. M., Haas M. R., Dalla Vecchia C., 2011, MNRAS, 414, 2458

van de Voort F., Springel V., Mandelker N., van den Bosch F. C., Pakmor R., 2019, Monthly Notices of the Royal Astronomical Society: Letters, 482, L85

Appendix A

Additional Information

All codes used in this dissertation are available upon request. This includes the code for Chapter 3 as well as codes used for all analyses. The analyses were performed using the Python programming language (Python Software Foundation) and following packages: Numpy Harris et al. (2020), Matplotlib Hunter (2007), Pynbody (Pontzen et al., 2013b), SciPy (Virtanen et al., 2020), Tangos (Pontzen & Tremmel, 2018), and XIGrM (XIGrM documentation). The galaxy database and particle data for Romulus simulations are available upon request from Michael Tremmel.